The Microvascular Control of Insulin Action and Insulin Resistance in Skeletal Muscle

By

Ian Miller Williams

Dissertation

Submitted to the Faculty of the

Graduate School of Vanderbilt University

In partial fulfillment of the requirements

For the degree of

DOCTOR OF PHILOSOPHY

in

Molecular Physiology and Biophysics

August 31, 2018

Nashville, Tennessee

Approved:

Ambra Pozzi, Ph.D.

David G. Harrison, M.D.

Owen P. McGuinness, Ph.D.

Jamey D. Young, Ph.D.

David H. Wasserman, Ph.D

ACKNOWLEDGEMENTS

I am deeply grateful for the people who have contributed to my scientific, professional, and personal development over the last five years. The Wasserman laboratory has been an ideal environment to become an independent scientist, utilize state-of-the art techniques, and learn about many different aspects of physiology. I would like to sincerely thank my mentor, Dr. David Wasserman, for his invaluable contributions to my development as a scientist. David is always able to offer sage advice on matters including experimental design, grantsmanship, navigating peer review, and connecting with other scientists. There is no doubt in my mind that David's mentorship has prepared me for a successful career in biomedical research. I would also like to recognize past and present members from the Wasserman laboratory: Deanna Bracy, Jeff Bonner, Mickael Goelzer, Clinton Hasenour, Curtis Hughey, Freyja James, Li Kang, Louise Lantier, Dan Lark, Mason McClatchey, Elijah Trefts, Ashley Williams, and Karen Yang. It has truly been an honor to spend the last five years with this remarkable group of individuals. I would especially like to thank Deanna Bracy for her unending generosity and assistance as well as Elijah Trefts for his friendship during this process.

In addition to the Wasserman laboratory, there are many people who have contributed to my thesis work and scientific development. Foremost is Dr. K. Sam Wells, who has been an incredible mentor and was instrumental in helping me develop an intravital microscopy technique. As anyone who has interacted with Sam can attest, he is a truly brilliant individual. I am deeply grateful for the time and effort Sam spent to teach me, a naïve graduate student biologist, about quantitative fluorescence microscopy and experimental design. I was also very fortunate to work with Dr. Amy Arnold during the early stages of my graduate training. Amy provided invaluable mentorship and taught me how to manage projects and write manuscripts.

The members of Thesis Committee, including Drs. Ambra Pozzi, Owen McGuinness, Jamey Young, and David Harrison, have been instrumental in helping me develop my thesis work. I especially appreciate Ambra's insights on project and career strategies, Owen's impressive ability to teach physiology and interpret complex cardiometabolic phenotypes, Jamey's patience as he taught me mathematical modeling, and David's astute suggestions regarding nitric oxide biology. I would also like to thank the wonderful people from the Mouse Metabolic Phenotyping Center, Cell Imaging Shared Resource, Diabetes Center, Hormone Assay Core, Mass Spectrometry Research Center, and Flow Cytometry Shared Resource at Vanderbilt. The selflessness and generosity of the people who work in Vanderbilt Core facilities to serve the research community never ceases to amaze me. I also greatly appreciate Dr. Raymond Mernaugh for his generous assistance with protein conjugation and his insights on science. Finally, I would like to thank Adam Mezo, Francisco Valenzuela, and Doraiswami Ramkrishna for their contributions to the development of the intravital microscopy technique.

The undertaking of completing a PhD is an exciting journey filled with ups and downs. I would like to sincerely thank my family as well as friends from Petaluma, UCLA, and Vanderbilt for their personal support. Over the last five years, I have been fortunate enough to learn more than I could have ever envisioned, interact with brilliant individuals on a daily basis, make biological discoveries, embrace personal challenges, and make new memories with lifelong friends. I cannot imagine a fuller life experience. For this, I am truly grateful.

TABLE OF CONTENTS

LIST OF FIGURES

LIST OF TABLES

CHAPTER I

INTRODUCTION

The Insulin Resistance Epidemic

Obesity and insulin resistance

Starting at various points during the middle of the 20th century, humans got progressively fatter. In 1960, when the Center for Disease Control first started collecting data on obesity rates, just 13% of adults were obese (Body Mass Index > 30 kg/m^2) (1). The most recent National Health and Nutrition Examination Survey indicates that 40% of adults in the United States are now obese (2). This rapid rise in obesity rates has occurred not only in the United States but also worldwide (3). Perhaps even more concerning is that obesity has become a pediatric disorder, as 19% of children under the age of 18 are obese (2). Obesity has clearly reached pandemic proportions. The causes of obesity are multi-faceted. While obesity certainly has a strong heritable component, genetics alone cannot explain the rapid rise in obesity in the span of less than a generation. Clearly, changes in environmental exposures have contributed to the recent rise in obesity rates. Excessive caloric intake, sedentary lifestyle, changes in dietary composition, reduced sleep duration and quality (4), antibiotic treatment (5), anti-psychotic medications (6), and chronic psychological stress (7) all contribute to the development of obesity. Obesity has detrimental effects on health. It increases the risk of developing Type II diabetes, cardiovascular disease, many forms of cancer, Alzheimer's disease, asthma, arthritis, and chronic pain (8). Substantial biomedical research efforts have been focused on determining how obesity increases risk for these diseases. One potential driver of obesity-associated comorbidities is insulin

resistance. The expansion of adipose tissue, especially in visceral locations, is strongly associated with impaired responsiveness to the effects of insulin (9–11). It is important to note that about 30% of obese individuals have normal insulin sensitivity and ~15% of normal weight individuals are insulin resistant (12). These findings highlight the importance of abdominal adiposity, rather than body weight, in promoting insulin resistance. Regardless, obese individuals are more likely to develop insulin resistance, a condition that afflicts nearly 1 out of 3 adults in the United States (13).

Insulin action and insulin resistance

Insulin is an anabolic hormone that is involved in many physiological processes. Nearly every cell type in the body expresses the insulin receptor (14) and is sensitive to insulin's effects. The focus of this Dissertation is on the glucose-lowering and vascular effects of insulin. The effects of insulin on lipid (15, 16) and protein (17) metabolism, energy balance (18), cognition (19), reproduction (20), the sympathetic nervous system (21), immune function (22), mitogenicity (23) and electrolyte homeostasis (24) have been reviewed elsewhere.

The most well known effect of insulin is to lower blood glucose. This is achieved by suppression of hepatic glucose production and stimulation of glucose disposal into peripheral tissues. When tissues become resistant to insulin, its hypoglycemic effects become less potent. Namely, insulin resistance results in an impaired ability of insulin to suppress hepatic glucose production and to promote peripheral glucose disposal. The impact of insulin resistance – enhanced hepatic glucose production and reduced peripheral glucose uptake – is hyperglycemia.

There are several different types of insulin resistance. While most forms are pathological, others are temporary responses to normal physiological conditions. For instance, insulin

resistance develops during pregnancy to meet fetal metabolic needs and also as a response to long-term fasting (25). Pathophysiological insulin resistance is observed in obesity, polycystic ovarian syndrome (26) severe inflammatory conditions such as sepsis (27), and other rare endocrinological disorders (28). While the focus of this Dissertation will be on obesity-induced insulin resistance, it is important to consider molecular similarities between various insulin resistant states as they may elucidate important underlying mechanisms of insulin resistance.

The deleterious impact of insulin resistance on health

The detrimental effects of insulin resistance on health are profound. It is most well-known for being a driver of Type 2 diabetes (29, 30). In fact, 5-10% of insulin resistant humans will progress to overt Type 2 diabetes within a year (31). In healthy individuals, pancreatic β cells can compensate for insulin resistance by secreting more insulin to restore normoglycemia (32). However in certain individuals, β cells fail to compensate for insulin resistance and hyperglycemia ensues (33). Alternatively, it has been hypothesized that prolonged hyperinsulinemia drives insulin resistance by desensitizing tissues to the effects of insulin (34). Regardless, insulin resistance leads to the development of hyperglycemia and Type 2 diabetes, which afflicts nearly 10% of people in the United States (13). Prolonged Type 2 diabetes and hyperglycemia increase risk for cardiovascular disease, blindness, kidney failure, and limb amputation (35).

Insulin resistance is not only a disorder of glucose metabolism. More broadly, insulin resistance is thought to underlie the metabolic syndrome, or syndrome X as originally defined by Gerald Reaven (36). The metabolic syndrome is a constellation of metabolic and vascular abnormalities that frequently accompany obesity. It is defined as the co-occurrence of abdominal

adiposity, glucose intolerance, low concentrations of high-density lipoprotein, increased plasma triglyceride levels, hypertension, and elevated levels of proinflammatory and prothrombotic factors. As insulin resistance can contribute to these lipid, vascular and inflammatory abnormalities (37), it is a major independent risk factor for cardiovascular disease (38, 39). Insulin resistance and the metabolic syndrome have also been linked to other seemingly disparate diseases such as cancer (40) and Alzheimer's disease (41). It is clear, then, that the metabolic and vascular chaos resulting from obesity-induced insulin resistance has severely detrimental impacts on health. Given the pervasive nature of insulin resistance, it is difficult to estimate its economic burden. The total direct and indirect costs of Type 2 diabetes are estimated to be $245 billion, (42), and those of cardiovascular disease are $316 billion (43). Needless to say, insulin resistance is a major driver of chronic disease and a serious economic drain on the health care system. Thus, reducing the burden of insulin resistance is a major public health goal.

Skeletal Muscle Insulin Resistance

Why study muscle insulin resistance?

Insulin stimulates glucose uptake, oxidation, and storage in skeletal muscle. Skeletal muscle comprises the majority of insulin sensitive tissue by mass. Following an oral glucose load, as during a meal, 26% of the ingested glucose is taken up by skeletal muscle (44). This value is ~85% during hyperinsulinemic-euglycemic clamps (insulin clamps)* (45). Skeletal muscle is the largest glucose storage depot in the body, as it stores roughly 80% of total body glycogen (46). Given its major role in removing glucose from the circulation, skeletal muscle insulin action is a key contributor to maintenance of normoglycemia. As such, skeletal muscle

*Hyperinsulinemic-euglycemic clamps involve a continuous intravenous insulin infusion to achieve physiological hyperinsulinemia. Exogenous glucose is also infused to maintain euglycemia. The rate at which glucose must be infused to maintain euglycemia is an indicator of steady-state insulin action.

insulin resistance is a major site of obesity-induced insulin resistance (47) and a central defect in the progression of Type 2 diabetes (48). Furthermore, skeletal muscle insulin resistance appears to precede the development of hepatic insulin resistance (49, 50), underscoring its importance to the earliest stages of Type 2 diabetes.

Lifestyle modifications that induce weight loss reverse insulin resistance and prevent the development of Type 2 diabetes (51, 52). However, lifestyle modifications are ineffective due to low adherence. In the absence of lifestyle modifications, it is important to have therapies that can treat or reverse skeletal muscle insulin resistance. Such drugs may be able to reverse the metabolic syndrome and its associated comorbidities. Thiazolidinediones, a class of drugs that act as agonists of peroxisome-proliferator-activated receptor-γ, have direct and indirect insulin-sensitizing effects on adipose tissue and skeletal muscle, respectively. While these drugs do prevent Type 2 diabetes in individuals with impaired glucose tolerance, they do not reduce cardiovascular events and actually increase heart failure incidence (53). Thus, better insulin-sensitizing drugs are needed to prevent Type 2 diabetes and its comorbidities. It is interesting to speculate whether drugs specifically targeting skeletal muscle insulin resistance, which is an early defect in the pathogenesis of Type 2 diabetes, may be more effective in reducing Type 2 diabetes-associated cardiovascular events. In order to design pharmaceuticals with direct insulin-sensitizing effects on skeletal muscle, it is imperative to understand the molecular etiology of skeletal muscle insulin resistance.

What causes muscle insulin resistance?

Since obesity-induced skeletal muscle insulin resistance was first described by Rabinowitz and Zierler in 1962 (47), the mechanism by which skeletal muscle becomes resistant

to insulin has been studied extensively. The vast majority of these studies have explored potential defects at the myocellular level. In order to fully appreciate the cellular mechanisms of skeletal muscle insulin resistance, it is important to understand skeletal muscle insulin action during normal physiological conditions. The initiating event of myocellular insulin action is the binding of insulin in the interstitial fluid to the insulin receptor on the surface of myocytes. Receptors for insulin are formed from homo or heterodimerization of the two insulin receptor isoforms, insulin receptor A and B (54). Additionally, insulin – insulin-like growth factor 1 hybrid receptors can also bind insulin (54). Binding of insulin to these receptors activates the phosphatidylinositol-3-kinase / protein kinase B pathway (PI3K/Akt) pathway (Reviewed in Ref 54). Briefly, insulin binding to the insulin receptor activates the receptor tyrosine kinase which then phosphorylates both the insulin receptor itself and the insulin receptor substrate (IRS) proteins. Subsequently, PI3K is activated through binding to phosphorylated IRS proteins. Activated PI3K then phosphorylates phosphatidylinositol bisphosphate to generate phosphatidylonisotol trisphosphate (PIP_3) at the plasma membrane. Increased plasma membrane PIP_3 recruits phosphoinositide-dependent kinase, which activates Akt. Akt can then phosphorylate a number of downstream targets including Akt substrate of 160kDa (AS160), mechanistic target of rapamycin (mTOR), and glycogen synthase kinase-3β (GSK-3β). The cellular results of insulin signaling, as they relate to glucose disposal, include 1) translocation and insertion of glucose transporter type 4 (Glut4) into the plasma membrane thereby enhancing glucose transport (56) 2) increased activity of hexokinase II which phosphorylates glucose and traps it inside of the cell (57) and 3) activation of GSK-3β which promotes glycogen storage. In summary, insulin promotes myocyte glucose transport, intracellular phosphorylation and utilization through PI3K/Akt signaling events.

Defects in insulin-stimulated glucose transport (58, 59), intracellular phosphorylation (60, 61), oxidation (62, 63), and glycogen synthesis (64, 65) have been observed in the setting of insulin resistance and Type 2 diabetes. For decades, investigators have searched for molecular explanations for these impairments. Obesity-induced insulin resistance and Type 2 diabetes have been associated with defects in the insulin-stimulated PI3K/Akt signaling pathway (66). This reduction in insulin signaling may be caused by antagonistic signaling from other cascades, altered subcellular distribution of signaling proteins, or single nucleotide polymorphisms (66).

It is clear that defects at the level of the muscle cell are associated with obesity-induced skeletal muscle insulin resistance. Many investigators have wondered what molecular aspects of obesity cause these defects in insulin signaling. This question in particular has been studied extensively. Some of the more prominent hypotheses for defective insulin signaling include 1) accumulation of toxic lipid species (67) 2) low-grade inflammation (68) 3) mitochondrial dysfunction and excess generation of reactive oxygen species (69) or 4) extracellular matrix (ECM) accumulation and integrin activation (70). Each of these processes are induced by obesity and antagonize PI3K/Akt signaling by activating signaling cascades such as protein kinase C (PKC), c-Jun, N-terminal kinases (JNK), and IκB kinase (IKK) (55).

Thus far, I have focused on the myocellular aspects of insulin action and insulin resistance. An equally important, yet underappreciated, aspect of skeletal muscle insulin action is the vascular delivery of glucose and insulin to the surface of myocytes. Before the myocytes can respond to insulin or transport glucose, these molecules must travel from the portal circulation to the muscle microcirculation. In fact, the delivery of glucose and insulin are rate-limiting to insulin-stimulated glucose uptake (71–73). These aspects of insulin action highlight the inseparable nature of microvascular function and metabolism. The vascular regulation of insulin

action must be studied in intact organisms because the influence of the vasculature is eliminated in experiments utilizing isolated tissues or cells in culture. As I discuss below, the journey of insulin and glucose from their initial entry into the portal circulation to their final destination at the surface of the myocyte is complex and subject to many levels of regulation.

The Journey of Insulin and Glucose from the Portal Circulation to Skeletal Muscle

In order to put the delivery of insulin and glucose to skeletal muscle into the context of whole-body physiology, I will first describe how these molecules reach the muscle microcirculation following an oral glucose challenge.

Glucose-stimulated insulin secretion

Insulin is stored in β cells which reside in islets of the endocrine pancreas. It is stored vesicularly in dense granules as a hexamer and is released in response to various stimuli, most notably an increase in portal vein glucose concentrations. Dietary glucose is initially absorbed by the small intestine and transported into the portal circulation. β cells sense the rise in portal glucose through increased cellular glucose metabolism and respond by secreting insulin in a biphasic manner (74). In response to a 75g oral glucose challenge, pancreatic islets from healthy adults will secrete ~70 nmol of insulin with a peak secretion rate of 600 pmol/min (75).

First-pass hepatic insulin and glucose extraction

Upon secretion into the portal vein, insulin becomes monomeric and primed for biological activity. Insulin in the portal vein first encounters the liver where it acts through the insulin receptors on hepatocytes to stimulate glucose uptake and suppress glycogenolysis (76).

These concerted actions of insulin convert the liver from a net producer of glucose during fasting to a glucose consumer after feeding (77). The liver microvasculature is characterized by discontinuous sinusoids that allow for free access of circulating macromolecules to hepatocytes. As such, a significant portion of insulin secreted from β cells is extracted on the first pass through the liver. Liver insulin extraction is a regulated process and can range from negligible to 75% of secreted insulin (78, 79). While the mechanisms regulating hepatic insulin clearance are not well understood, it has been shown that first-pass hepatic insulin extraction is reduced in obese subjects (80, 81). In addition to clearing a significant proportion of the secreted insulin, the liver also extracts roughly 33% of ingested glucose for utilization and storage as glycogen (82). In summary, the liver's physical positioning makes it a crucial first-responder to the appearance of glucose and insulin in the portal circulation.

Systemic insulin and glucose distribution

The remaining insulin (~50%) and glucose (~67%) that survives first pass hepatic extraction then enter the inferior vena cava and are delivered to the right atrium of the heart. Deoxygenated blood carrying insulin and glucose moves through the pulmonary circulation before being returned to the left atrium. Very little insulin is cleared by the lung (83). After entering the left atrium, insulin and glucose are then distributed to the systemic and coronary circulation by contraction of the left ventricle. The postprandial rise in glucose and insulin appear to increase cardiac output without altering mean blood pressure (84). Following systemic distribution, insulin and glucose enter peripheral circulatory beds including those of skeletal muscle, adipose tissue, brain, kidney, and the digestive tract.

Clearance of insulin by other organs

As discussed above, the majority of insulin is cleared by the liver through first-pass metabolism. Roughly 50% of the remaining insulin that enters the peripheral circulation is then cleared by the kidney by both receptor and non-receptor mediated mechanisms (85). Of note, insulin extraction by the kidney is highly variable and its regulation is poorly understood (86). Following hepatic and renal clearance of insulin, ~25%, or 17.5 nmol, of the initially secreted insulin remains available for skeletal muscle, heart, brain, and adipose tissue. Compared to the liver and kidney, insulin clearance by these organs is low. This low extraction is rather remarkable when considering the potent effects of insulin on skeletal muscle and adipose tissue. It is possible that secondary messenger systems amplify insulin's signal in these organs. The low clearance of insulin in skeletal muscle, adipose tissue, and brain is most likely related to the continuous nature of capillaries in these tissues. Continuous capillaries are comprised of endothelial cells adjoined by tight junctions and, thus, do not readily transport plasma proteins. This is in contrast to the kidney and liver which have fenestrated and discontinuous capillaries, respectively, which allow for freer access of plasma contents to the underlying parenchymal cells.

Hemodynamic Actions of Insulin

Effect of insulin on muscle blood flow

After insulin has been distributed to the systemic circulation, it interacts with the endothelium of arteries and arterioles in skeletal muscle. William B Hood Jr. and colleagues first demonstrated an increase in muscle blood flow, as measured by microsphere deposition, during insulin clamps in dogs (87). Similar observations were made in humans (88). These findings

were extended to hypothesize that the perfusion-enhancing effects of insulin were important for its metabolic effects (89, 90). However, many other investigators were unable to detect an effect of insulin on muscle blood flow (88). As such, there has been significant controversy regarding the existence and physiological relevance of insulin-stimulated increases in muscle blood flow (91). One concern is that, in studies where insulin stimulation did produce an increase in muscle blood flow, these effects were only observed after prolonged administration (2-6 hours) of high doses of insulin (91). Furthermore, insulin increases muscle glucose uptake much more rapidly than it augments muscle blood flow. Thus, the physiological relevance of insulin's effects on bulk muscle blood flow and their importance to muscle glucose uptake are questionable.

Microvascular flow distribution

The laboratories of Michael Clark, Eugene Barrett, and Stephen Rattigan began using techniques to measure microvascular flow distribution rather than bulk muscle blood flow. They first demonstrated that insulin increased the metabolism of 1-methylxanthanine (1-MX) across the rat hind limb and human forearm (92, 93). 1-MX is a substrate for xanthine oxidase, an enzyme expressed mostly by the endothelium of capillaries and arterioles. As such, the disappearance of 1-MX across the hind limb is an indicator of endothelial surface area which itself is an index of microvascular flow distribution. Thus, the 1-MX studies suggested that insulin increases the endothelial surface area available for flow. This phenomenon was termed capillary recruitment. That is to say, at rest there are a significant number of capillaries which are under-perfused. Upon insulin stimulation, flow to these capillaries is "recruited" and the distribution of microvascular flow is increased **(Figure 1.1)**.

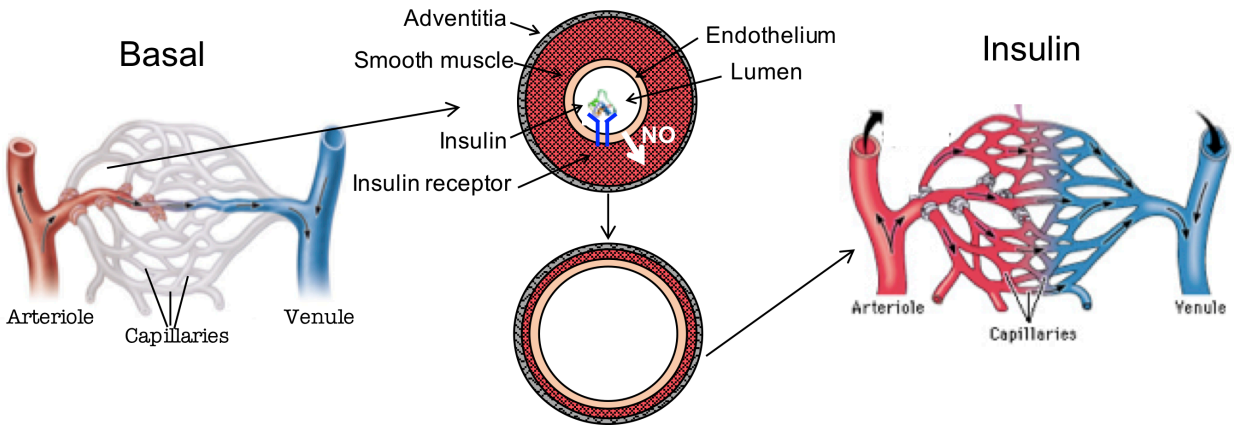

Figure 1.1: Insulin-stimulated capillary recruitment. Under basal conditions (left), muscle microvascular perfusion is low and a minority of capillaries are perfused. Upon insulin binding to its receptor, the endothelium produces NO causing resistance arterioles to dilate (middle). This vasodilation results in a recruitment of previously under-perfused capillaries (right). NO – nitric oxide. Image of capillary bed on left adapted from *Human Anatomy & Physiology 9th Edition* (Marieb EN & Hoehn KN). Image of capillary bed on right adapted from Addison-Wesley Longman, Incorporated.

Subsequently, these investigators utilized contrast-enhanced ultrasound to assess microvascular hemodynamics and flow distribution (94). With contrast-enhanced ultrasound, relative microvascular volume is estimated by measuring the intensity of sound waves reflected from 1-5μm microbubbles injected intravenously. This measurement reflects the microbubble distribution volume and its relationship to microvascular volume depends on the assumption that all microbubbles are retained intravascularly. In addition to microvascular volume, flow velocity can be determined by rupturing the microbubbles with a high intensity ultrasound pulse and then measuring the rate at which the signal recovers. As microvessels fill more slowly than larger conduit arteries, the slower of the microbubble recovery rates is assumed to represent microvascular flow velocity. Due to the limited spatial resolution of ultrasound, it is unclear whether the microvascular flow velocity measurement represents capillary or venous flow velocity, or a combination of both. Using contrast-enhanced ultrasound, these investigators showed that, in human forearm muscle, 4 hours of physiological insulin infusion increases microvascular volume while decreasing microvascular flow velocity (93). Furthermore they demonstrated that insulin's ability to increase microvascular volume occurs 1) prior to insulin-stimulated muscle glucose uptake (95) and 2) during physiological conditions such as a mixed meal tolerance test (96). Furthermore, Rattigan and Clark have suggested that insulin enhances the proportion of microvascular flow that is distributed to "nutritive" routes which allow for more rapid exchange of plasma-borne molecules with the interstitial space (97). Thus, capillary recruitment and more efficient microvascular flow distribution appear to be early physiological responses to insulin stimulation which increase the surface area for glucose and insulin exchange. Of note, whether increases in microbubble distribution volume represent bona fide capillary recruitment has been questioned. Using intravital microscopy to directly visualize

capillaries, David Poole and colleagues have observed that over 80% of capillaries are already perfused at rest (98). As such, it is unclear whether the insulin-stimulated increase in microbubble distribution volume represents a recruitment of capillaries or distension of other microvessels. The longstanding debate regarding muscle capillary recruitment is beyond the scope of this discussion and has been covered elsewhere (98, 99).

Vasodilatory effects of insulin

The ability of insulin to increase microvascular perfusion has been attributed to vasodilatory effects on both large conduits and smaller resistance vessels. Using pulse wave analysis, Yki-Järvinen and colleagues demonstrated that aortic compliance was increased after an hour of an insulin clamp (100). This suggests that insulin dilates large blood vessels. Additionally, other investigators have demonstrated that insulin relaxes skeletal muscle arterioles at physiological concentrations (101–103). Interestingly, one of these studies showed that when intravenous glucose infusion is used to elicit hyperinsulinemia, pre-capillary arterioles constrict rather than dilate (101). Furthermore, Eringa et al. did not observe a change in cremaster muscle arteriolar diameter with insulin stimulation alone (104). Only after inhibition of endothelin receptors was insulin able to induce arteriolar dilation. These findings suggest that the effects of insulin on vascular tone are highly dependent on the local balance of constrictors and dilators. While there have been relatively few studies on the effects of insulin in the venous circulation, there is evidence that insulin causes dilation of dorsal hand veins in humans (105, 106). In summary, physiological insulin levels appear to cause vasodilation at all levels of the vasculature under most conditions.

Molecular determinants of insulin's hemodynamic effects

The molecular effects of insulin on endothelial cells have been studied extensively in cell culture and to a lesser extent *in* vivo. Several investigators have demonstrated that the ability of insulin to stimulate vasodilation, capillary recruitment, or blood flow can be blocked by nitric oxide synthase (NOS) inhibitors (95, 102, 107). These findings suggested that nitric oxide (NO), the prototypical vasodilator, is involved in the dilator effects of insulin. Indeed Michael Quon and colleagues demonstrated that insulin stimulates NO production from human umbilical vein endothelial cells (HUVECs) (108). An extensive characterization of HUVECs by this group revealed that insulin signaling through the PI3K/Akt pathway is required for NO production (109). More specifically, Akt phosphorylates endothelial NOS (eNOS) at Ser^{1177} and activates it independently of classical calcium-dependent eNOS activation. Endothelial-derived NO can then diffuse to nearby smooth muscle cells to activate soluble guanylyl cyclase which causes smooth muscle relaxation through cyclic guanosine monophosphate signaling (110). As alluded to above, insulin also stimulates the production of endothelin-1, a vasoconstrictor (111). Insulin-stimulated endothelin-1 production is thought to occur through a separate mitogen-activated protein kinase (MAPK)-dependent insulin signaling pathway (109). Thus, the vascular effects of insulin depend on whether the AKT-NO or MAPK-endothelin-1 signaling cascades are activated by insulin.

It is important to keep in mind that much of the work on the molecular mechanisms of insulin action in the endothelium has been performed in cultured endothelial cells. While we have gained considerable understanding of insulin action from these studies, cultured endothelial cells are very different from vessels *in vivo* (see "***Technical difficulties...***" below for further discussion). For instance, while the insulin receptor and associated insulin signaling machinery

is certainly present in HUVECs, bovine aortic endothelial cells, and bovine retinal capillary endothelial cells, it is unclear whether skeletal muscle capillary or arterial endothelial cells express the insulin receptor. To the best of my knowledge, this has never been shown definitively *in vivo*. These would be the cells of interest in determining insulin's hemodynamic effects in skeletal muscle.

Physiological Glucose Delivery to Skeletal Muscle

Distributed control of glucose uptake

Glucose uptake in skeletal muscle involves microvascular delivery of glucose to the interstitial space, transport of glucose across the plasma membrane, and finally intramyocellular phosphorylation **(Figure 1.2)** (71). Previous experiments from our laboratory have demonstrated that the relative importance of delivery, transport, and phosphorylation steps to muscle glucose uptake are context-dependent. For instance, at rest the permeability of the muscle plasma membrane to glucose is very low making glucose transport the main barrier to glucose uptake (112). Upon insulin stimulation, membrane glucose permeability is increased through the insertion of Glut4, and glucose delivery and phosphorylation become more limiting to glucose uptake (112). These findings suggested an important role for the muscle vasculature in the control of insulin-stimulated muscle glucose uptake.

Bulk muscle blood flow and glucose uptake

Before glucose can be taken up by muscle, it must be delivered through the vasculature to the interstitial space which bathes myocytes. There are several vascular parameters, both structural and dynamic, to consider when determining how the vasculature may control glucose

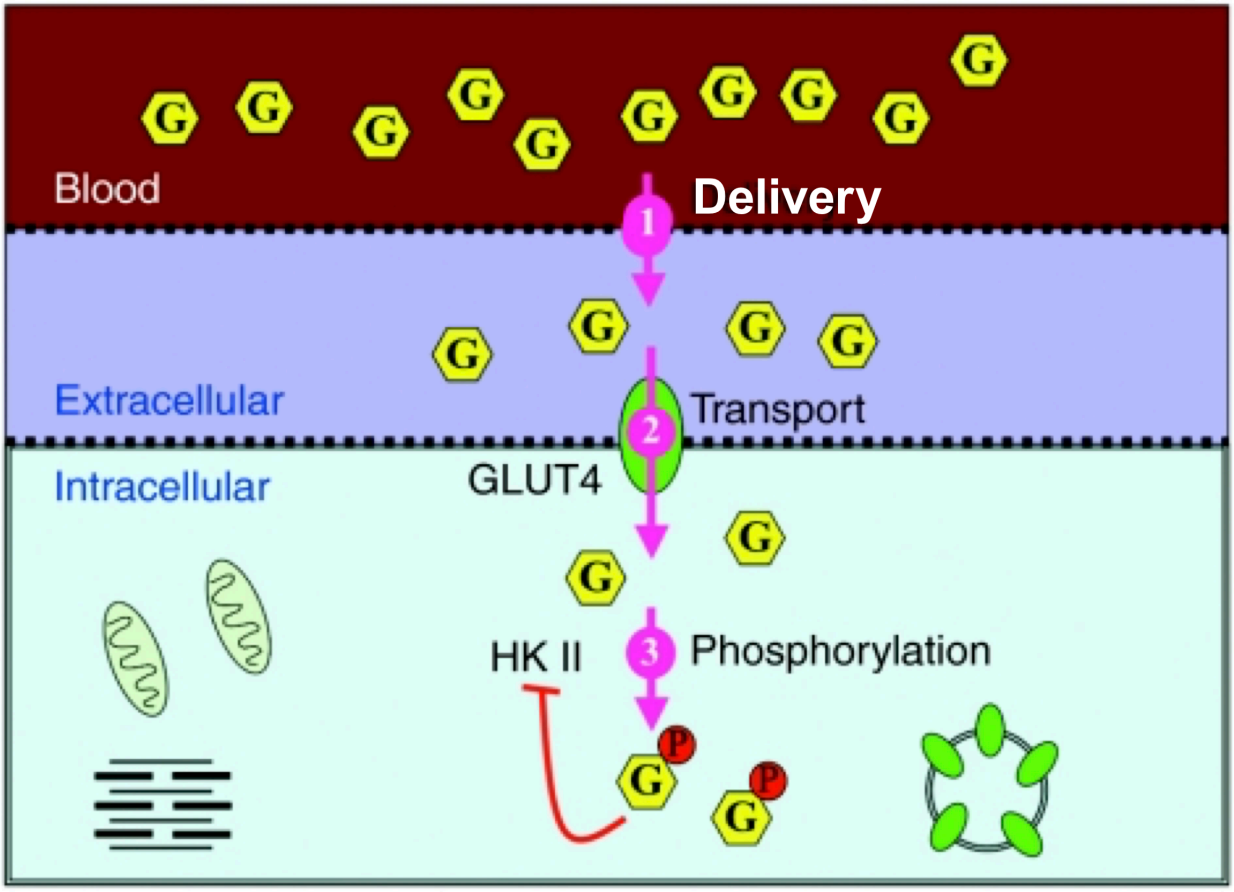

Figure 1.2: Barriers to muscle glucose uptake. Before glucose can be utilized, it must first be delivered from the plasma to the interstitial fluid (Step 1). Subsequently, glucose must be transported across the plasma membrane by facilitative glucose transporter such as Glut4 (Step 2). Finally, glucose is phosphorylated by HKII and trapped intracellularly (Step 3). Yellow hexagons labeled with a "G" represent glucose. Red circles labeled with "P" indicate phosphorylation sites. Glut4 – glucose transporter type 4, HK II – hexokinase 2. Figure adapted from Wasserman et al. (71).

delivery and uptake. The first is bulk muscle blood flow. If bulk flow were an important contributor to insulin-stimulated muscle glucose uptake, then experimentally increasing it should augment glucose uptake. Such studies have produced conflicting results. Two independent laboratories have shown that infusing either adenosine, sodium nitroprusside (SNP) or bradykinin during insulin clamps augments muscle blood flow but does not increase muscle glucose uptake in healthy or hypertensive patients (113–116). Conversely, infusing angiotensin II reduces muscle blood flow, but also did not alter muscle glucose uptake (117). These findings would seem to suggest that bulk muscle blood flow is not a major determinant of muscle insulin action. On the contrary, Baron and colleagues have shown that increasing bulk flow with methacholine enhances muscle glucose uptake and reducing bulk flow with L-N^G-monomethyl arginine acetate, a NOS inhibitor, impairs glucose uptake (118, 119). As discussed above, insulin does not increase muscle blood flow unless it is administered for several hours. Thus, the role of bulk muscle blood flow as an independent contributor to insulin-stimulated muscle glucose uptake is questionable. When considering the implications of these studies for the importance of glucose delivery to glucose uptake, it is important to remember that changes to bulk blood flow do not necessarily indicate changes in glucose delivery. In fact, none of the aforementioned studies actually measured glucose delivery. It is possible that the interventions described above may have altered bulk flow without changing the distribution of flow or glucose delivery.

Microvascular perfusion and glucose uptake

As discussed previously, insulin dilates resistance arterioles and increases muscle microvascular volume (120). These vascular effects would be predicted to increase the endothelial surface area for glucose exchange and enhance glucose delivery. Perhaps due to the

difficulty of measuring glucose delivery, this hypothesis has not been explicitly tested. Furthermore, it relies on the assumption that microbubble distribution volume, as measured by contrast-enhanced ultrasound, reflects that of plasma, the carrier for glucose. Bergman and colleagues demonstrated that insulin increased the interstitial distribution volume of inulin, an inert ~6000 Da molecule, without altering intravascular volume (121). These data indicate that insulin either increased the trans-endothelial transport of inulin or directed blood flow to vessels that more easily equilibrate with the interstitial space. Interestingly, these effects of insulin were not observed in humans (122). Whether insulin also increases the interstitial distribution volume of glucose, a much smaller molecule (180 Da), is unknown.

Findings from Barrett and colleagues do suggest that the microvascular effects of insulin are important for muscle glucose uptake. Importantly, the microvascular effects of insulin occur before stimulation of muscle glucose uptake (95). This temporal arrangement of events suggests that the vascular effects of insulin are necessary for its metabolic effects. Furthermore, treatment of rats with L-N^G-nitroarginine methyl ester (L-NAME; NOS inhibitor) blocked the insulin-stimulated increase in microvascular volume and, subsequently, muscle glucose uptake (95). Conversely, angiotensin-(1-7) [Ang-(1-7)], a peptide hormone of the renin angiotensin system, increases both microvascular perfusion and insulin action (123). While glucose delivery was not measured in these studies, these findings suggest a tight coupling between muscle microvascular volume and glucose uptake.

Vascular architecture and glucose delivery

In addition to hemodynamics, vascular architecture is also important for efficient glucose delivery. The most basic descriptor of vascular structure is the number of capillaries in a given

tissue. Given that capillaries are the main sites of plasma to muscle glucose exchange, capillary density represents the surface area available for exchange. The surface area for glucose exchange should correlate positively with glucose delivery and muscle insulin sensitivity. Indeed, skeletal muscle capillary density is positively associated with skeletal muscle insulin sensitivity (124, 125) in humans. Previous studies from our laboratory utilized a mouse model in which vascular endothelial growth factor (VEGF) was deleted specifically from muscle (126). As VEGF is a critical pro-angiogenic factor, loss of VEGF in these mice results in a 60% reduction in muscle capillary density. As would be expected, these mice displayed impaired insulin-stimulated muscle glucose uptake as measured during an insulin clamp. When soleus muscles from these mice were isolated and stimulated with insulin *ex vivo*, glucose uptake was not impaired, indicating normal myocellular insulin action. In this case, muscle insulin resistance was generated through a reduction in capillary density rather than through a myocellular defect. While capillary density is positively correlated with insulin-stimulated glucose uptake, it remains to be determined whether this correlation is driven by glucose delivery per se. It is possible that changes in capillary density could alter insulin delivery or muscle metabolism. Finally, an understudied aspect of vascular structure that may contribute to glucose delivery is the topology of microvascular networks. That is to say, certain spatial arrangements and connectivity patterns of arteries, capillaries and venules may minimize diffusion distances and allow for the most efficient delivery of glucose (127).

Endothelial glucose permeability and interstitial glucose dispersion

A final consideration in the delivery of glucose to muscle is the permeability of the endothelium and the interstitial space to glucose. Glucose is a small (~7Å) hydrophilic molecule

and, as such, is thought to either a) diffuse passively through inter-endothelial junctions (128) or b) be transported by endothelial Glut1 (129). Despite the small size of glucose compared to the width of inter-endothelial junctions (~50Å), basal muscle interstitial glucose is ~60-70% of plasma glucose in humans (130, 131). There appears to be species differences in the trans-endothelial glucose gradient as plasma and interstitial glucose concentrations are more similar in rats (132). When insulin was infused into these rats, muscle interstitial glucose fell to a greater extent than did plasma glucose, indicating that it increased the trans-endothelial glucose gradient (132). Whether the dynamics of trans-endothelial glucose transport constitute a significant barrier to muscle glucose uptake is unclear. Another aspect of glucose delivery is the movement of glucose within the interstitial space. The muscle interstitial space is a hydrogel consisting of various ECM proteins and glycosaminoglycans such as hyaluronan (133). It is possible that the interstitial milieu may hinder the access of interstitial glucose to GLUTs located on the surface of the myocyte. Whether the interstitial ECM constitutes a significant barrier to muscle glucose uptake is unknown.

In summary, glucose delivery is an important regulator of insulin-stimulated muscle glucose uptake. While the physiological relevance of total muscle blood flow to glucose uptake is questionable, it appears that insulin induces a more efficient distribution of flow. These hemodynamic effects of insulin may contribute to muscle glucose uptake. The contributions of microvascular network topology, trans-endothelial glucose transport, and interstitial glucose dispersion as barriers to glucose uptake warrant further investigation. Furthermore, future studies of glucose delivery would be improved by measuring interstitial glucose levels using interstitial sampling methods or intravital imaging techniques.

Physiological Insulin Delivery to Skeletal Muscle

The trans-endothelial insulin gradient

The hypothesis that insulin delivery may be limiting to peripheral insulin action was first proposed by Reubin Andres and colleagues (134). These investigators noticed that, during a continuous insulin infusion intended to produce hyperinsulinemia, plasma insulin levels peaked almost instantaneously whereas it took considerably longer for glucose utilization to reach its maximum. These findings suggested that there was a disconnect between plasma insulin and insulin action in the periphery. Using compartmental modeling, these investigators described an interstitial compartment with which plasma insulin equilibrated slowly that was important for peripheral glucose utilization. They hypothesized that lower permeability of some tissue vascular beds may impede insulin's delivery to this interstitial compartment. A few years earlier, Eugenio Rasio and colleagues had observed that, following an intravenous glucose bolus, insulin appeared rapidly in the hepatic lymph, indicating extensive insulin clearance by the liver (135). However, the amount of insulin in the lymph draining the leg was much lower and its appearance less rapid. Assuming that the majority of leg lymph drains skeletal muscle, these findings suggest a relatively low extraction of insulin by muscle. Consistent with this observation, Richard Bergman and colleagues measured a considerable gradient between plasma and thoracic duct insulin following an intravenous glucose bolus (136). Direct measurements of muscle interstitial insulin concentrations by microdialysis confirmed that levels of insulin in the plasma were roughly twofold higher than in the interstitial space (137). In summary, these early studies demonstrated that plasma insulin equilibrates slowly with the muscle interstitial space. Based on these findings, investigators hypothesized that the low permeability microvasculature of skeletal muscle may restrict insulin's access to muscle.

The endothelium is rate-limiting for muscle insulin action

While measuring the dynamics of lymph insulin appearance, Richard Bergman and Jerrold Olefsky's groups noticed that the kinetics of muscle insulin action were strongly correlated with its appearance in the lymph (72, 138). Namely, the timing of insulin-stimulated insulin receptor kinase activity (138) and glucose disposal (72, 138) is the same as insulin appearance in the lymph. This suggested that the movement of insulin across the endothelium is rate-limiting to muscle insulin action. To more directly test this hypothesis, Bergman and colleagues injected insulin directly into the muscle interstitial space, thereby bypassing the endothelial barrier (73). In contrast to the slow increase in glucose uptake caused by intravenously administered insulin, intramuscular insulin injection stimulated maximal glucose uptake within 10 minutes. This finding was strong evidence that the rate-limiting step to muscle insulin action is the trans-endothelial transport of insulin.

Characteristics of muscle capillary endothelium

The capillary endothelium comprises roughly 85% of all endothelial surface area (139). As such, capillary networks provide a vast surface area for fluid and solute exchange between the plasma and the underlying tissue parenchyma. The endothelium lining capillaries forms a semi-permeable barrier which limits trans-capillary exchange. The properties of this barrier depend on the tissue in which it is located. There are 3 main types of capillary endothelia: discontinuous, fenestrated, and continuous (140). Discontinuous endothelia are characterized by large distances (~100 nm) between adjacent endothelial cells and allow free exchange of circulating blood cells and plasma constituents with the underlying tissue parenchyma. Such vessels include the sinusoids of the liver and bone marrow. Fenestrated endothelium, as found in the kidney, contain

pores ranging from 6-15nm in diameter. While fenestrated endothelia are relatively impermeable to cells, they do allow free exchange of large plasma proteins. Finally, continuous endothelia, as found in the muscle, adipose tissue, and brain are comprised of endothelial cells adjoined by either zona occludens (brain) or macula occludens (adipose, skeletal muscle) inter-endothelial junctions. The capillary inter-endothelial junctions in these tissues range from <1nm in brain to ~2-5nm in skeletal muscle and do not leak plasma proteins. These characteristics of muscle capillaries are in agreement with the findings discussed above which showed that the endothelium restricts insulin's access to muscle. Given that insulin's diameter is ~3nm and inter-endothelial junctions range from ~2-5nm, it is feasible that insulin may access inter-endothelial junctions. Another consideration is that the glycocalyx, a layer of negatively charged glycoproteins that extrudes from the luminal endothelial surface, may sterically hinder insulin's access to the inter-endothelial junction. Furthermore, as insulin is negatively charged at physiological pH, the glycocalyx may impede trans-endothelial insulin efflux through charge selectivity. In summary, the muscle capillary endothelium presents barriers to trans-endothelial insulin transport. Whether insulin is able to access inter-endothelial junctions is unclear from structural considerations alone.

Endothelial transport mechanisms

In addition to passive movement through inter-endothelial junctions, macromolecules can also be actively transported by endothelial cells. Using electron microscopy, George Palade and colleagues observed that the very thin endothelium of muscle capillaries contain vesicles, termed plasmalemmal vesicles or caveolae, that span roughly 70nm in diameter. (141). These vesicles can contribute to molecular exchange by either 1) fusing to form transient trans-endothelial

channels which allow for passive movement of plasma constituents to the interstitial space (142, 143) or 2) actively transport macromolecules through a process termed transcytosis (144). Transcytosis begins with endocytosis of caveolae which are fused with the luminal endothelial plasma membrane and open to circulating plasma. Caveolae contain a number of receptors, including the insulin receptors (at least in adipocytes) (145), and thus can concentrate specific cargo for transport. These vesicles are internalized through a mechanism that involves dynamin-mediated scission (146). Subsequently, the free vesicle is translocated across endothelial microtubules with assistance from motor proteins such as kinesin and dynein (146). Finally, the free vesicle utilizes soluble N-ethylmaleimide-sensitive factor attachment protein receptor (SNARE) machinery to dock with the abluminal plasma membrane and release its contents into the interstitial space (146). Of note, there has been considerable controversy regarding the extent to which transcytosis, endothelial pores, or inter-endothelial junctions mediate trans-endothelial solute transport **(Figure 1.3)**. The specifics of this debate are beyond the scope of this discussion and have been covered elsewhere (147, 148).

How does insulin cross the capillary endothelium in skeletal muscle?

In the previous sections I discussed the evidence which shows that the endothelium restricts insulin's access to skeletal muscle and that there are multiple endothelial protein transport mechanisms. These observations led investigators to examine the molecular mechanism of trans-endothelial insulin transport in skeletal muscle. This issue has generated considerable debate over the last 30 years. Some studies have suggested that insulin is actively transported across the endothelium by saturable insulin receptor-mediated transcytosis whereas others have shown that insulin diffuses

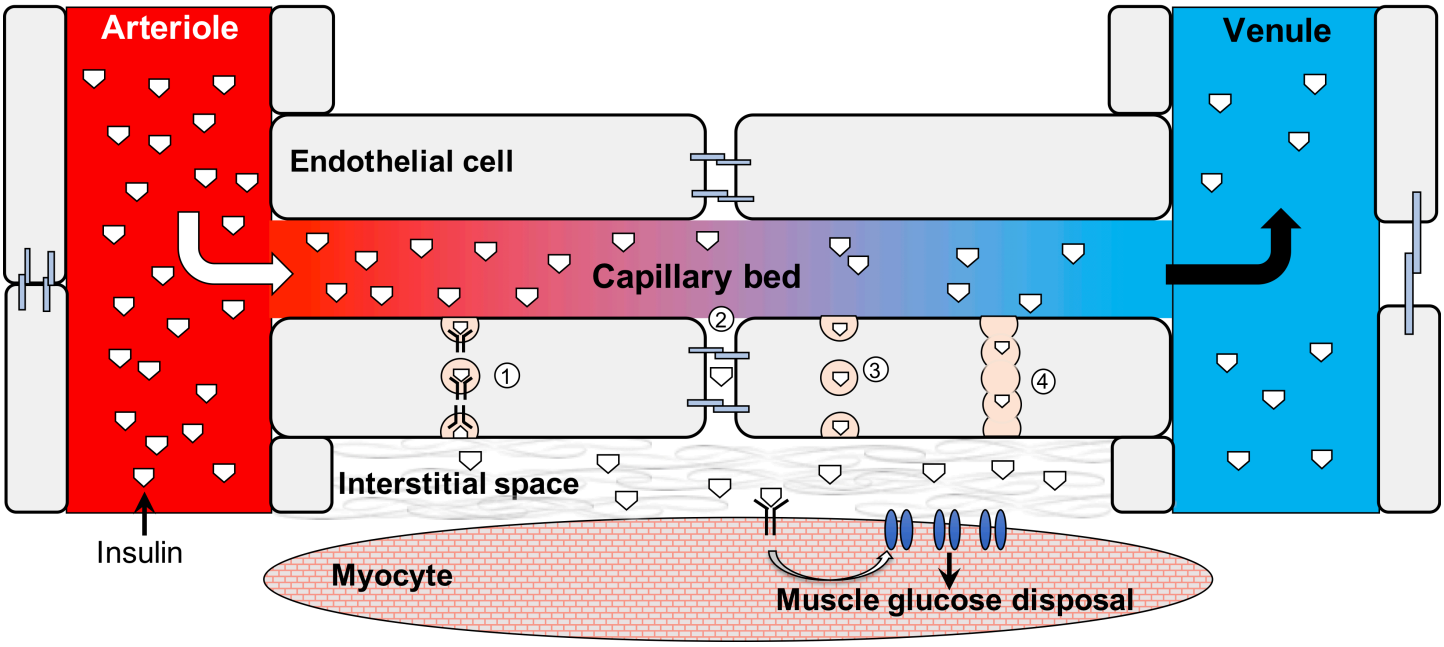

Figure 1.3: Potential mechanisms of trans-endothelial insulin transport. Insulin is delivered to muscle capillary beds through the arterial circulation. Subsequently, insulin may be transported across the endothelium either by 1) receptor-mediated transcytosis 2) movement through inter-endothelial junctions 3) non-saturable vesicular transcytosis or 4) movement through trans-endothelial channels formed by fusion of endothelial vesicles. After insulin crosses the endothelium and enters the interstitial space it can bind to the insulin receptor on the surface of myocytes and stimulate glucose uptake.

passively across the endothelium **(Figure 1.3)**. Below I will review the evidence for each hypothesis.

Evidence that insulin moves across the endothelium by saturable insulin receptor-mediated transcytosis

The notion that insulin may be trafficked across the endothelium by a receptor-mediated process began with the demonstration that cultured HUVECs contain insulin receptors (149). The expression of insulin receptors in various cultured endothelial cells has now been demonstrated extensively. George King and colleagues then showed that antibodies against the insulin receptor inhibited the movement of ^{125}I-insulin across a monolayer of bovine retinal capillary endothelial cells *in vitro* (150). This suggested that insulin was being trafficked across cultured endothelial cells by an insulin receptor-mediated process. Using an *ex vivo* perfused heart preparation, Bar and colleagues demonstrated that the appearance of ^{125}I-insulin in heart tissue sections could be reduced by unlabeled insulin and an antibody against the insulin receptor (151). These *ex vivo* findings indicated that in heart, which contains continuous capillaries, endothelial insulin receptors can control the delivery of insulin. Continuing along this line of investigation, Eugene Barrett and colleagues used immunohistochemistry to show that fluorescein isothiocyanate (FITC)-labeled insulin accumulates in the endothelium of arterioles and venules (152). Given that capillaries are the main sites of insulin exchange, the role of venular and arteriolar insulin accumulation is unclear. In the same study, these investigators also observed that, in the endothelium, the insulin receptor co-localized with caveolin-1, the main structural component of caveolae. Two separate studies in cultured endothelial cell monolayers showed that disrupting caveolae inhibited insulin uptake, indicating that caveolae may mediate

the transport of insulin (153, 154). On the contrary, Klip and colleagues found that *in vitro* endothelial insulin transport was mediated by a clathrin-dependent mechanism (155). Finally, in a tour de force study, Kubota et al. observed a reduction in interstitial insulin delivery in mice lacking endothelial insulin receptor substrate 2. These findings indicated that endothelial insulin signaling was necessary for insulin delivery (156). The most commonly accepted model, based on the studies discussed above, is that 1) insulin binds to the insulin receptor located in caveolae, 2) caveolae are then translocated across the EC by transcytosis and 3) insulin is released in the interstitial space where it can then stimulate muscle glucose uptake. It is important to note that in none of the aforementioned studies was skeletal muscle trans-endothelial insulin transport measured directly *in vivo*.

Evidence that insulin transport across the endothelium is not receptor-mediated

To test whether trans-endothelial insulin transport were saturable in dogs, Bergman and colleagues infused physiological and pharmacological doses of insulin and measured its appearance in the lymph (157). They reasoned that if trans-endothelial insulin transport were saturable, then the appearance of insulin in the lymph should plateau with increasing levels of plasma insulin. However, they found that the appearance of insulin was not saturable even with very high doses of insulin. These findings indicated that insulin delivery was not saturable *in vivo*, as would be expected for a receptor-mediated process. Subsequently, Kahn and colleagues generated a mouse that lacked the insulin receptor in endothelial cells (158). They found that this mouse had normal glucose homeostasis, suggesting that the insulin receptor was not involved in trans-endothelial insulin transport. It should be noted, however, that this same group made a second endothelial-specific insulin receptor knockout mouse using a different promoter to drive

the endothelial expression of Cre recombinase (159). These mice displayed delayed insulin-stimulated muscle insulin signaling and glucose uptake suggesting that the insulin receptor does regulate insulin delivery. In summary, there is *in vivo* evidence that trans-endothelial insulin transport is not saturable and does not require the insulin receptor. These studies are limited by their measurement of insulin delivery which is controlled by both perfusion and trans-endothelial insulin transport. Thus, it is unclear whether changes in insulin delivery are caused by altered muscle perfusion, trans-endothelial insulin transport, or a combination of both.

Technical difficulties in assessing capillary trans-endothelial insulin transport

Two main approaches have been used to study trans-endothelial insulin transport, both of which have their limitations. The first such approach is the use of techniques which measure total insulin delivery. Such methods include microdialysis (156), lymph sampling (157), and the autoradiographic approach used by Bar et al. (151). The delivery of insulin to the muscle interstitial space is regulated by two main factors: 1) muscle perfusion, or the surface area for capillary insulin exchange and 2) trans-endothelial transport. Thus, when using these techniques to measure total insulin delivery, it is unclear whether perturbations cause a change in perfusion, trans-endothelial insulin transport or both. This limitation is further complicated by the fact that insulin itself increases microvascular perfusion. Thus, these techniques do not directly measure trans-endothelial insulin transport but rather an index of insulin delivery. Another issue with microdialysis is temporal resolution. With microdialysis, equilibration of the interstitial fluid with the microdialysis probe may take up to 20 minutes (160). Thus, more rapid interstitial insulin dynamics may be missed. Finally, the use of lymph as a surrogate for interstitial fluid is

limited because lymphatic function can vary during disease conditions (161). Thus, changes in lymph flow may confound the relationship between interstitial fluid and lymph.

The majority of studies investigating trans-endothelial insulin transport have been performed in cultured endothelial cells *in vitro*. While we have gained valuable information from these studies, they have several limitations. The first issue is the source of endothelial cells. Many studies have utilized macrovascular endothelial cells such as HUVECs or bovine aortic endothelial cells (149, 154). Given the phenotypic heterogeneity between endothelial cells at different levels of the vasculature (162), it is problematic to draw conclusions about capillaries *in vivo* from cultured macrovascular endothelial cells. Some studies have utilized "microvascular" endothelial cells (150, 153, 155). The term microvascular refers to a range of vessels including arterioles, venules, and capillaries, all of which have different properties (162). Thus, the extent to which microvascular endothelial cells are representative of capillaries is questionable. The second issue with cultured endothelial cells is the organ from which they are isolated. Studies of trans-endothelial insulin transport have utilized endothelial cells from retina (150), aorta (152, 154), adipose tissue (155), or lung (153). It is becoming increasingly appreciated that endothelial cells in different tissue beds have very different properties (163). Whether endothelial insulin transport in other organs is representative of skeletal muscle is unclear. To the best of our knowledge, there have been no studies of trans-endothelial insulin transport in endothelial cells isolated from skeletal muscle capillaries.

In addition to endothelial heterogeneity, using cultured endothelial cells is problematic for several reasons. First, immediately upon isolation the endothelial proteome changes significantly. Namely, Schnitzer and colleagues analyzed the proteome of freshly cultured endothelial cells and endothelial membranes isolated *in vivo* to show that 40% of proteins

expressed *in vitro* are not expressed *in vivo* (164). Especially relevant to the current discussion, endothelial monolayers can be up to 100 times more permeable to plasma proteins than intact vessels (165). This makes trans-endothelial transport studies in cultured endothelial cells problematic. Finally, and perhaps most importantly, endothelial cells in static culture lack the complex milieu of the *in vivo* environment. *In vivo*, endothelial cells are in contact with one another, attached to a complex basement membrane, continuously exposed to shear stress from capillary plasma and red blood cells, and receive a myriad of biochemical signals from both the circulation and underlying tissue parenchyma. These features of endothelial cells *in vivo* are very difficult to replicate *in vitro*.

An ideal technique for the measurement of trans-endothelial transport in skeletal muscle capillaries would be 1) conducted *in vivo* with minimal physiological perturbations 2) able to measure both plasma and interstitial insulin as a function of time and 3) able to account for perfused capillary surface area. Such a technique would require high sensitivity for the measurement of insulin, sufficient spatial resolution to differentiate between plasma and interstitial space, and adequate temporal resolution to track rapid insulin dynamics.

The lack of methodology available for the study of trans-endothelial insulin transport was the impetus for **Aim 1 (Chapter III)**. Namely, we sought to develop a technique to directly measure trans-endothelial insulin efflux in skeletal muscle capillaries *in vivo*. Furthermore, we wanted to use this technique to determine the mechanism of trans-endothelial insulin efflux in skeletal muscle capillaries *in vivo* **(Aim 2, Chapter IV)**.

Interstitial movement of insulin

A final consideration in the delivery of insulin to the insulin receptor located on the surface of myocytes is the movement of insulin within the interstitial space. As discussed above, this space is replete with glycosaminoglycans which may sterically hinder insulin's access to the myocyte. As of yet, it is unknown whether interstitial ECM proteins form a major barrier to the movement of insulin in the interstitium. Additionally, myofibers contain deep invaginations known as t-tubules, which contain insulin receptors (166). Lauritzen and colleagues used an elegant microscopy approach to demonstrate that it takes ~10 minutes for insulin to diffuse from the surface of the myocyte to deep within the t-tubules (167). Thus, the t-tubular space appears to be a barrier to muscle insulin action.

Glucose and Insulin Delivery in Insulin Resistance

The notion that glucose and insulin delivery regulate muscle insulin action raised the intriguing possibility that these processes may contribute to insulin resistance. Below I will discuss the evidence that microvascular dysfunction contributes to muscle insulin resistance.

Muscle microvascular dysfunction accompany obesity and insulin resistance

Given that insulin stimulates muscle perfusion, it was reasonable to hypothesize that impairments in insulin's vasodilatory effects may contribute to insulin resistance. Alain Baron and colleagues demonstrated that the ability of insulin to stimulate leg blood flow was impaired in obese, insulin resistant humans (168). These findings have been supported by some (169), but not all (47), studies. On the other hand, several studies have shown that obese humans and animal models have a diminished response to endothelial-dependent vasodilators and an

exaggerated response to vasoconstrictors (170, 171). Interestingly, basal muscle perfusion is comparable between lean and obese humans (171). Furthermore, the blood flow response to SNP, an NO donor, is preserved in obesity, indicating that smooth muscle relaxation is not impaired (168). A fascinating study by Jonathan Lindner and colleagues, using contrast-enhanced ultrasound in monkeys, showed that during the development of obesity-induced insulin resistance, the primary muscle vasodilatory mechanism switches to eicosanoid-based vasodilation as NO bioavailability declines (172). Thus, it appears that obesity results in alterations to the endothelial production of and response to vasoactive compounds. With respect to microvascular perfusion Eugene Barrett and Michael Clark's groups have demonstrated that insulin-stimulated microvascular perfusion is also impaired in obese, insulin resistant humans and animal models (173, 174). Not only do obese subjects have a reduction in muscle microvascular volume, but their microvascular flow is also more heterogeneous (175). At a structural level, muscle capillary density is lower in obese and insulin resistant humans (124, 176). Interestingly, we have not observed any difference in muscle capillary density between lean and obese mouse models (177). In summary, obesity and insulin resistance are strongly associated with both structural and hemodynamic vascular dysfunction. These vascular defects may contribute to muscle insulin resistance through a reduction in glucose and insulin delivery.

Insulin resistance, endothelial dysfunction, and nitric oxide bioavailability

As discussed above, obesity and insulin resistance are associated with impaired endothelium-dependent vasodilation **(Figure 1.4)**. Investigators studying coronary artery disease had also observed this phenomenon in patients at risk for developing atherosclerosis (178). They

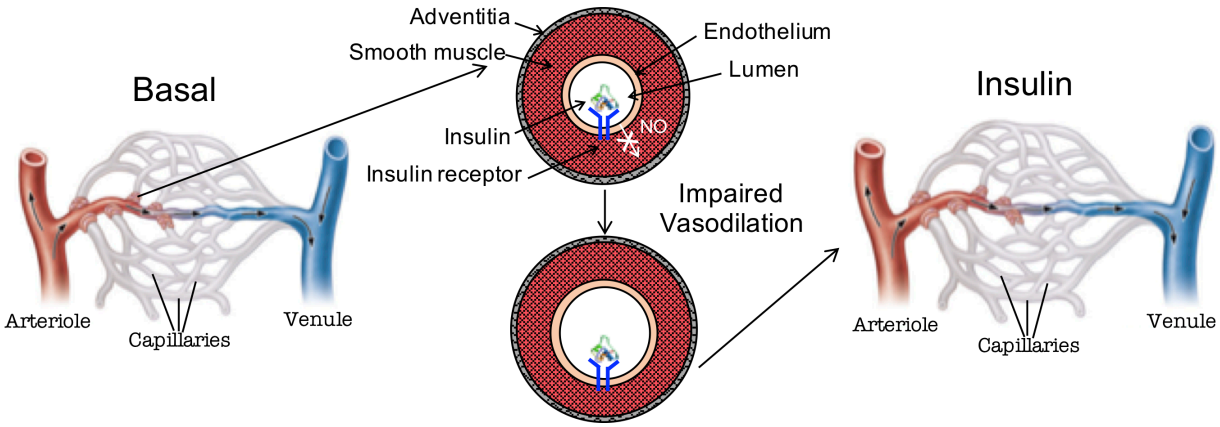

Figure 1.4: Endothelial dysfunction and impaired insulin-stimulated vasodilation in obesity. Under basal conditions (left), muscle microvascular perfusion is low and a minority of capillaries are perfused. In obese subjects, insulin-stimulated NO production from the arterial endothelium is impaired. As such, terminal arterioles are unable to relax (middle) and microvascular flow distribution is reduced (right). This reduction in capillary recruitment may reduce the surface area for glucose and insulin exchange. NO – nitric oxide. Image of capillary bed adapted from *Human Anatomy & Physiology 9th Edition* (Marieb EN & Hoehn KN).

termed this impairment in endothelium-dependent vasodilation "endothelial dysfunction." At the molecular level, endothelial dysfunction, or endothelial activation, is characterized by reduced NO bioavailability, increased production of reactive oxygen species and enhanced expression of inflammatory mediators (179). These molecular defects have been also been observed in the endothelium of insulin resistant humans and animal models (180). Most notably, obesity and insulin resistance are frequently associated with reduced endothelial NO bioavailability (181). The diminishment of endothelial NO is caused by a variety of factors including reduced endothelial NOS (eNOS) expression and activity, eNOS uncoupling, and enhanced scavenging of NO by oxidant species such as superoxide (181). An interesting study from Francis Kim and colleagues demonstrated that, in a mouse model of obesity, reduced aortic NO production occurs before the development of muscle insulin resistance. This suggests that reduced endothelial NO bioavailability may play a causative role in the development of muscle insulin resistance (182).

Endothelial function is governed, in large part, by the bioavailability of nitric oxide (NO). In arterioles, NO produced by endothelial cells causes smooth muscle relaxation thereby reducing resistance to flow and increasing muscle perfusion (110). Furthermore, NO has complex effects on capillary barrier function. Namely, under normal, basal conditions NO maintains endothelial barrier function (183, 184) whereas under inflammatory conditions NO can produce vascular leakiness (185). Given its effects on both perfusion and capillary permeability, endothelial NO is well-positioned to be a key regulator of glucose and insulin delivery to muscle.

Endothelial NO bioavailability may directly regulate muscle insulin delivery by modulating either muscle perfusion or trans-endothelial insulin transport. Several groups have demonstrated that pharmacological reduction of NO during steady-state hyperinsulinemia diminishes muscle perfusion and glucose uptake in both humans and rats (95, 119, 186, 187).

Furthermore, mice lacking eNOS display peripheral insulin resistance and impaired muscle perfusion (188, 189). These findings demonstrate that reduction of endothelial NO can limit muscle perfusion and steady-state muscle insulin action. Whether reducing NO alters trans-endothelial insulin transport remains to be determined.

With respect to insulin transport, Barrett and colleagues showed that NO promotes the uptake of FITC-labeled insulin into cultured bovine aortic endothelial cells (190). The implication of these findings is that NO may promote the movement of insulin across the endothelium. However, these studies should be interpreted with caution given the limitations of studying endothelial transport function *in vitro* discussed above. In contrast to these *in vitro* experiments, several *in vivo* studies have shown that inhibition or genetic deletion of NOS actually increases microvascular permeability (183, 184). Thus, the effect of varying endothelial NO levels on the movement of insulin across the skeletal muscle capillary endothelium *in vivo* remains unclear. The experiments described in **Aim 4 (Chapter VI)** address the role of NO in insulin movement across the endothelium of skeletal muscle capillaries *in vivo*.

Glucose delivery and insulin resistance

As alluded to previously, the muscle perfusion defects associated with obesity and insulin resistance may lead to a reduction in glucose delivery. To the best of my knowledge, insulin-stimulated glucose delivery has not been directly measured in obese, insulin resistant humans. However, it has been demonstrated that the glucose permeability – surface area product, an index of glucose delivery, is reduced in Type II diabetes (191). Furthermore, our laboratory utilized an isotopic countertransport technique to show that delivery of glucose is impaired in a rat model of diet-induced insulin resistance (192). On the other hand, when insulin resistance was created

with a lipid infusion in humans, interstitial glucose delivery was actually increased during an oral glucose tolerance test (193). Thus, the relationship between insulin resistance and glucose delivery is complex and may depend on obesity, plasma lipids, glycemia, and other factors.

If impaired glucose delivery were a component of muscle insulin resistance, one would expect that experimentally increasing delivery would correct insulin resistance. The majority of studies have shown that this is not the case. Ferrannini and colleagues showed that treating insulin resistant humans with either SNP or adenosine increased muscle blood flow but did not improve insulin sensitivity during an insulin clamp (115, 116). These findings were corroborated by an independent laboratory using bradykinin to augment muscle blood flow (194). Furthermore, studies from our laboratory demonstrated that treating obese mice acutely with sildenafil (a phosphodiesterase-5a inhibitor which increases NO bioavailability) or relaxin (an endothelium-dependent vasodilator) does not increase muscle insulin sensitivity (195, 196). These findings show that increasing perfusion acutely does not correct muscle insulin resistance. This evidence contradicts the hypothesis that impaired glucose delivery contributes to skeletal muscle insulin resistance. However, it is possible that the vasodilators described above, while increasing blood flow, did not produce efficient microvascular flow distribution or nutritive flow (197). It is also possible that the trans-endothelial movement of glucose or its diffusion through the interstitial space is restricted in obese subjects. In fact, our lab and others have shown that ECM components, such as collagens and hyaluronan, accumulate in the muscle of obese mice and humans (198–200). Thus, ECM accumulation in the interstitial space or the glycocalyx lining endothelial cells may restrict glucose's movement across the endothelium or its diffusive capacity in the interstitial space.

In contrast to the finding that acute vasodilation does not increase insulin sensitivity, our laboratory has found that chronic treatment of insulin resistant mice with vasodilators does improve muscle insulin action. Namely, treating mice with sildenafil for 12 weeks concurrently with high fat feeding prevented diet-induced muscle insulin resistance (195). Similarly, 3 weeks of relaxin treatment following 10 weeks of high fat diet restored skeletal muscle insulin sensitivity (196). The mechanism by which chronic vasodilator treatment improves muscle insulin sensitivity has yet to be determined.

This effect of chronic vasodilator treatment has also been observed to a certain extent in humans. Namely, hypertensive patients, who are frequently obese, treated with drugs that block the actions of angiotensin II (Ang II) have a lower incidence of Type II diabetes (201). These drugs, including angiotensin converting enzyme inhibitors (ACEis) and Ang II receptor blockers (ARBs) are vasodilators and improve endothelial function (202–205). ACEis and ARBs, in addition to blocking the formation and activity of Ang II, increase the formation and activity of Angiotensin-(1-7) [Ang-(1-7)], another peptide hormone of the renin angiotensin system (206). Ang-(1-7) is a vasodilatory peptide that counterbalances Ang II (206). Liu and colleagues showed that Ang-(1-7) causes a dose-dependent increase in insulin-stimulated microvascular perfusion and glucose uptake in lean mice (123). Ang-(1-7) treatment also improves glucose homeostasis in rodent models of obesity and insulin resistance (207–209). Whether this peptide may be used to specifically treat skeletal muscle insulin resistance is unknown. Furthermore, it is an ideal peptide to investigate mechanisms by which chronic vasodilator treatment restores insulin sensitivity in obese subjects. In **Aim 5 (Chapter VII)**, I will test the hypothesis that chronic treatment of obese mice with Ang-(1-7) will restore muscle insulin sensitivity.

Insulin delivery, trans-endothelial insulin transport, and insulin resistance

Given that obese and insulin resistant subjects display endothelial dysfunction, it is reasonable to hypothesize that they also have impaired muscle insulin delivery. Indeed, several investigators have demonstrated that the delivery of insulin to the muscle interstitial space is reduced in humans and animal models of insulin resistance. Using microdialysis during insulin clamps and glucose tolerance tests, Lönnroth and colleagues showed that the appearance of insulin in the interstitial space is delayed in obese, insulin resistant humans (210, 211). These findings were supported by experiments utilizing animal models of obesity and insulin resistance (156, 212). Not all studies have arrived at the same conclusion, however. During insulin clamps in a cohort of obese humans, Lillioja et al. did not find any changes in the ratio of arterial to lymph insulin, an index of insulin delivery (213). Furthermore, lipid-induced insulin resistance in lean subjects does not appear to impair the access of insulin to skeletal muscle (193, 214). As with glucose delivery, the precise relationship between obesity, insulin resistance and insulin delivery is complex and further investigation is warranted.

As discussed previously, delivery of insulin to the muscle interstitial space is a function of both microvascular perfusion and trans-endothelial insulin transport **(Figure 1.5)**. Using microdialysis or lymph sampling, it is not possible to determine whether changes in total insulin delivery are due to microvascular perfusion, trans-endothelial insulin transport, or both. As of yet, no direct measurements of trans-endothelial insulin transport in the setting of obesity and insulin resistance have been made. The experiments in **Aim 3 (Chapter V)** are designed to test whether trans-endothelial insulin transport is delayed in a mouse model of obesity and insulin resistance.

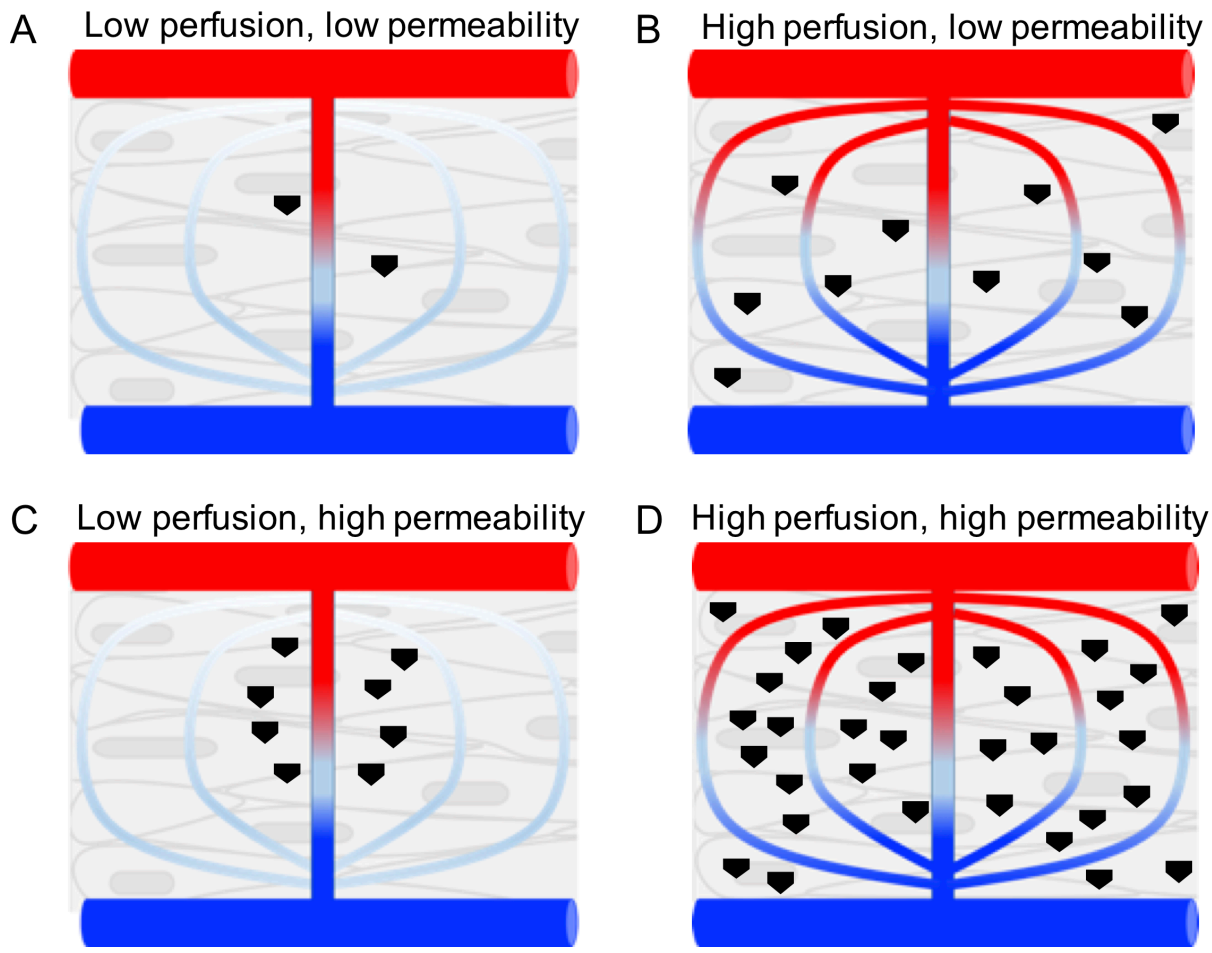

Figure 1.5: Microvascular perfusion and capillary permeability to insulin control muscle insulin delivery. Schematic illustrating the effects of perfusion and capillary permeability on insulin (black pentagons) delivery to the muscle. **A)** In a low perfusion, low permeability state, there is relatively little insulin delivered to the muscle. With isolated increases in either **B)** perfusion or **C)** capillary permeability to insulin, insulin delivery is increased. Insulin delivery is enhanced even further by **D)** concomitant increases in both perfusion and capillary permeability. Of note, interstitial sampling techniques which measure muscle insulin delivery are unable to deconvolve the contributions of perfusion and permeability to delivery.

Once insulin crosses the endothelium, it must navigate the interstitial space to find insulin receptors on the surface of myocytes. As discussed previously, the interstitial ECM (70), t-tubule geometry (167), or interstitial fluid flux may alter interstitial insulin's access to the myocyte. Bergman and colleagues performed a fascinating study whereby they injected insulin directly into the interstitial space of lean and obese dogs and measured its appearance in the lymph and vein (215). They found that, in obese dogs, the interstitially injected insulin was reabsorbed into the venous circulation whereas it had appeared mostly in the lymph in lean dogs. These findings raise the intriguing possibility that insulin's dispersion within the interstitial space may contribute to insulin action and insulin resistance.

Aims and Hypotheses

The aims of this Dissertation are to:

1. *Develop a technique to directly measure trans-endothelial insulin transport in skeletal muscle capillaries in vivo.*
2. *Test the hypothesis that trans-endothelial insulin transport occurs by a saturable, insulin receptor-mediated process.*
3. *Investigate the effects of pharmacologically manipulating nitric oxide levels on trans-endothelial insulin transport.*
4. *Determine whether trans-endothelial insulin transport is impaired in a mouse model of obesity and insulin resistance.*
5. *Determine the effects of treating obese mice chronically with Ang-(1-7), a vasodilatory peptide of the renin-angiotensin system, on skeletal muscle insulin sensitivity.*

I hypothesize that insulin is transported across the endothelium by a saturable process that involves the insulin receptor and is positively regulated by NO. Furthermore, I hypothesize that trans-endothelial insulin transport is impaired in skeletal muscle capillaries of obese, insulin resistance mice. Finally, I expect that treating obese mice chronically with Ang-(1-7), a vasodilatory peptide of the renin-angiotensin system, will restore skeletal muscle insulin sensitivity by improving microvascular function.

CHAPTER II

RESEARCH METHODS AND MATERIALS

Mouse Models

All animal protocols were approved by the Vanderbilt Institutional Animal Care and Use Committee and conducted in Association for Assessment and Accreditation of Laboratory Animal Care-accredited facilities. C57Bl/6J mice were used for all experiments. Mice were housed in a temperature and humidity-controlled facility and maintained on a 12-hour light/dark cycle. All mice were purchased from The Jackson Laboratory with the exception of the mice used for intravital microscopy experiments in **Chapter V**, which were bred and maintained at Vanderbilt University. Breeding pairs housed in the Vanderbilt University mouse colony were fed a "breeder chow" diet (**Table 2.1**). Pups were weaned at 3 weeks of age, separated by sex, and switched to a standard chow diet (5001 Purina Laboratory Rodent Diet; **Table 2.1**). At 6 weeks of age, male and female mice were fed either a chow or high fat diet (HFD; F3282 BioServ; **Table 2.1**) *ad libitum* for 16 weeks. These mice were subsequently used for intravital microscopy in **Chapter V**. For the experiments in **Chapter VII**, 6 week-old male mice were purchased from Jackson Laboratory and either fed a chow or HFD for 11 weeks.

Diet	Fat (%kcal)	Carbohydrate (%kcal)	Protein (%kcal)
Breeder chow	25.3%	54.9%	19.8%
Chow	13.3%	57.9%	28.7%
High fat	59.0%	26.0%	14.9%

Table 2.1. Mouse diet macronutrient composition.

Carotid Artery and Jugular Vein Catheterization

A detailed protocol describing the procedure for catheterization of the carotid artery and jugular vein in mice is available on the Vanderbilt Mouse Metabolic Phenotyping Center website (https://labnodes.vanderbilt.edu/resource/view/id/10764/community_id/1418) (216). All equipment and surgical spaces were sterilized prior to catheterization surgeries. Surgeries were performed on mice anesthetized with 2% isofluorane administered continuously through a nose cone.

The intrascapular and neck regions were first shaved and sterilized with betadine and 70% ethanol. A small vertical midline incision was made 5mm cephalic to the sternum. The left carotid artery was then isolated by folding back the sternomastoid muscle, removing connective tissue from the artery, and gently separating the artery from the vagus nerve. The cephalic end of the carotid artery was then ligated with silk suture. To open the artery for catheter insertion, the caudal end of the carotid artery was clamped with micro-serrefine and a small incision was made just below the cephalic ligation. Subsequently, a polyethylene catheter was inserted into the carotid artery and advanced to the aortic arch. Finally, the caudal end of the carotid artery was ligated and the catheter sampling ability was confirmed.

To expose the right jugular vein, a second incision was made 5mm to the right of the midline and 2mm caudal to the first incision. Subsequently, the right jugular vein was isolated by blunt dissection. After ligating the cephalic end of the right jugular vein, a small incision was made in the vein just below the cephalic ligature. A Silastic catheter was then inserted into the jugular vein and the caudal end of the vein was ligated with silk suture. Finally, the sampling ability of the venous catheter was confirmed.

In order to exteriorize the catheters, they were tunneled under the skin and through a small incision between the shoulder blades. The ventral incisions made for catheter insertion were then closed with nylon suture. The tunneled catheters were connected to the steel tubing of a MASA™, a device which allows the exteriorized catheters to protrude outwards from the mouse's shoulder blades. The MASA™ was then implanted in the incision between the mouse's shoulder blades and the incision was closed with nylon suture. Finally, the patency of both catheters was re-confirmed and catheters were flushed with 10U/ml heparinized saline.

Following catheterization, mice were placed in a clean cage on a heating pad. Mice were allowed to recover for at least 3 days following jugular vein catheterizations and at least 5 days following combined carotid artery and jugular vein catheterization. Recovery from catheterization surgeries was deemed adequate if mice lost no more than 10% of their pre-operative body weight and if their behavior was normal.

In Vivo Glucose Metabolism Experiments

Hyperinsulinemic-euglycemic clamps (insulin clamp)

Insulin clamps were performed in conscious, unstressed mice as described in detail previously **(Figure 2.1)** (216). At least 5 days before experiments, carotid artery and jugular vein catheters were implanted for blood sampling and infusions, respectively. Mice were fasted for 5 hours prior to starting the insulin clamp. A primed, continuous infusion of [3-^{3}H]glucose (0.04μCi·min^{-1}; Perkin Elmer) was started at t=-90 min to determine basal rates of plasma glucose appearance (R_a) and disappearance (R_d). Basal arterial samples were collected to measure glucose specific activity (t=-15 and -5 min), insulin (t=-5 min), and non-esterified fatty acids (NEFA; t=-15 and -5 min; average value reported). At t=0 min, continuous insulin

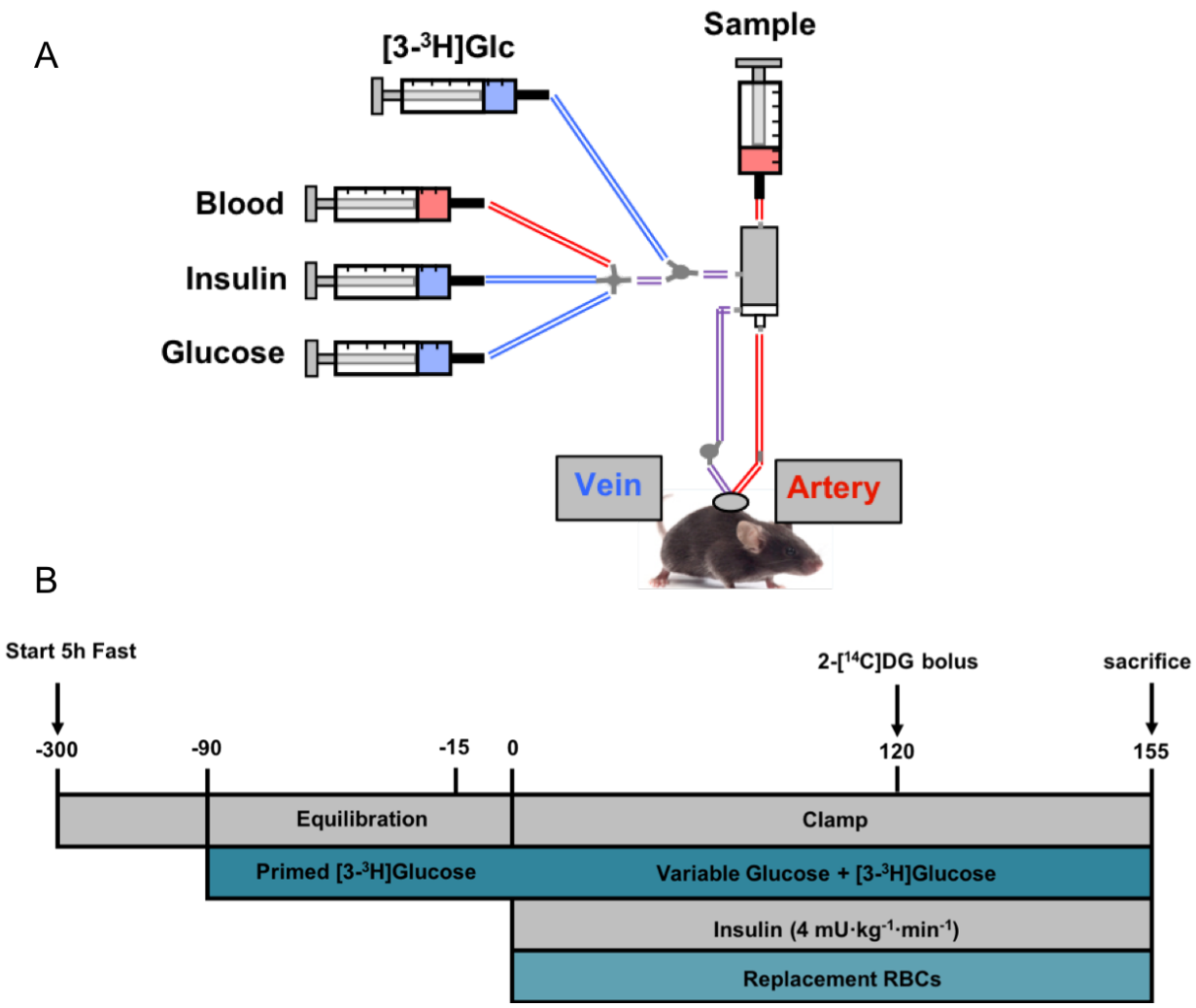

Figure 2.1 Experimental setup for the hyperinsulinemic-euglycemic clamp. A) Schematic depicting the jugular vein infusion and arterial sampling arrangement. Modified from: Glucose Clamping the Conscious Mouse (Vanderbilt MMPC 2005). **B)** Insulin clamp protocol.

(4mU·kg^{-1}·min^{-1}; Humulin R; Eli Lilly) and variable glucose (D50 + 50μCi[3-^{3}H]glucose) infusions were initiated. For the insulin clamps in **Chapter IV**, we used either unlabeled insulin or insulin labeled with Alexa Fluor 647 to assess the bioactivity of insulin-647 (INS-647). Donor erythrocytes were infused throughout the insulin clamp to prevent a fall in hematocrit. From time t=0 to 120 min, arterial glucose was measured every 10 min and the exogenous glucose infusion rate (GIR) was adjusted to maintain euglycemia (130-150 mg/dl). Steady-state GIR and [3-^{3}H]glucose kinetics were determined from t=80 to 120 min. During the clamp, arterial samples were collected for the measurement of glucose specific activity (t = 80, 90, 100, 110, 120 min), insulin (t=100 and 120 min) and NEFA (t=80 and 120 min; average value reported). At t=120 min, mice received an intravenous bolus of 2[^{14}C]deoxyglucose (2[^{14}C]DG; 13μCi; Perkin Elmer) to determine the glucose metabolic index (R_g), a measure of tissue-specific glucose uptake (217). Blood samples were obtained at t = 2, 7, 15, 25, and 35 min after the bolus to measure plasma 2[^{14}C]DG disappearance. At t = 155min, mice were sacrificed by intravenous injection of sodium pentobarbital. Tissues were immediately freeze-clamped and stored at -80ºC for biochemical analysis or incubated in 10% neutral buffered formalin followed by 70% ethanol for histological analysis.

Insulin tolerance tests

In **Chapter IV**, we performed insulin tolerance tests to assess the *in vivo* bioactivity of INS-647. Insulin tolerance tests were performed under anesthesia as to mimic the conditions of the *in vivo* imaging experiment. At least 5 days prior to the day of the study, mice had indwelling catheters implanted in the jugular vein for infusions of insulin, isotopic glucose tracers, and anesthetics (216). After a 5 hour fast, mice were anesthetized with an intravenously administered

ketamine / xylazine / acepromazine (KXA) cocktail (7.9/1.6/0.2 mg/kg). Booster doses of KXA were given as needed throughout the remainder of the study. Depth of anesthesia was ensured by assessing the response to a toe pinch. Basal glucose was measured (Accu-Chek Aviva) from the tail vein at 15 and 5 minutes prior to the start of the experiment. At t=0 min a 1U/kg bolus of either insulin or INS-647 together with 2[^{14}C]DG (13μCi) was administered. Subsequently, tail vein glucose levels were measured at t= 3, 6, 9, 12, 15, 20, 25, and 30 min following the insulin bolus. Mice were euthanized by cervical dislocation immediately following the experiment and tissues were harvested for further analysis. The glucose disappearance rate was calculated as the rate of fall of glucose over the first 15 minutes of the experiment (218).

In **Chapter VI**, we performed frequently sampled intravenous insulin tolerance tests in conscious, chronically catheterized mice to test the effects of acute L-NAME treatment on insulin sensitivity. At t = -15 min, mice received an intravenous bolus of either 30mg/kg L-NAME or an equivalent volume of saline (50μL). At t = 0 min mice received a 25mU/kg intravenous bolus of insulin (Novolin R; Novo Nordisk) diluted in 0.1% bovine serum albumin (Sigma Aldrich) in 0.9% saline. Arterial whole blood glucose was measured at t = – 5, 1, 2, 3, 4, 5, 6, 7, 8, 9, 10, and 15 min (Contour; Bayer) following the insulin bolus.

Fluorescent Probes for Intravital Microscopy

Insulin-647 synthesis and analysis

The conjugation of Alexa Fluor 647 to insulin follows a modified version of a procedure described previously (219). Diisopropylethylamine (DIPEA, 7 mmol, 1.22 mL, 40 eq) was initially added to a solution of biosynthetic human insulin (BHI, 0.2 mmol, 1.16 g) dissolved in DMSO (15 mL). Boc-OSu (0.445 mmol, 95.7 mg, 2.5 eq) was then dissolved in DMSO (2 mL)

and added slowly to the BHI solution over 5 min. After 40 min, the reaction was quenched with TFA (100 µL) and diluted with 0.1 N HCl (150 mL). The reaction mixture was purified by reverse phase-HPLC (RP-HPLC; Waters 19x300 mm SymmetryPrep C18) using gradients of acetonitrile in water with 0.1% TFA. Fractions containing the desired product as determined by LC-MS were pooled and lyophilized to provide a white powder (647.3 mg). The calculated molecular weight was 6,007.8 Da, and the electrospray mass spectrometry observed average mass was 6,006.7 Da. This intermediate product was a BHI conjugate containing t-Boc protecting groups on the A1 and B29 position of BHI (A1,B29-Bis-Boc-BHI).

To conjugate Alexa Fluor 647 to the protected BHI intermediate, Alexa Fluor 647–NHS ester (2 mg; Life Technologies) was dissolved in DMSO (20 µl) and added slowly to a dimethylformamide solution (500 µl) containing A1,B29-Bis-Boc-BHI (20 mg) and DIPEA (17 µl, 30 Eq). The reaction mixture was wrapped in aluminum foil, agitated for 5 hours, and then quenched with acetic acid (200 µl), diluted with water (10 ml), and lyophilized. The Boc groups were removed by treatment with a mixture of TFA/water/triisopropylsilane (92:4:4, vol/vol) for 1 hour at room temperature, and the material was then precipitated with cold diethyl ether and centrifuged at 2,147 x *g* for 5 minutes. The blue pellet was resuspended in acetonitrile/water (1:1, vol/vol) and purified to 98.9% by RP-HPLC (Waters 7.8 × 300 mm SymmetryPrep C18) using gradients of 0.01% HCl/acetonitrile in water. Fractions containing the desired product, INS-647, were pooled and lyophilized to provide a blue powder (8 mg). The calculated molecular weight was 6,646.6 Da, and the electrospray mass spectrometry observed average mass was 6,648.3 Da. The location of the Alexa Fluor 647 label was confirmed at the B1 position by digestion of 100 µg of product with Glu-C endoproteinase (P6181-50UG, Sigma-Aldrich; 10 µg) and analysis of the fragments by LC-MS.

To determine the affinity of INS-647 for the insulin receptor, we used a scintillation proximity assay (SPA) described previously (220). Briefly, membranes were prepared from HEK293 cells overexpressing the human insulin receptor. Membranes were then immobilized on polyvinyltoluene polyethyleneimine-treated Type A wheatgerm agglutinin-coupled SPA beads (GE Healthcare). Subsequently the abilities of INS-647 and BHI to compete with ^{125}I-insulin binding to insulin receptors were assessed. ^{125}I-insulin binding to the SPA beads was detected with a scintillation counter (Perkin Elmer MicroBeta Trilux). IC_{50} values for unlabeled insulin and INS-647 binding were calculated from 4-parameter logistic non-linear regression analysis. IC_{50} values were then converted to affinity values (K_i) using the Cheng-Prussoff equation $K_i = IC_{50}/(1+L/K_d)$, where L is the concentration of radioligand used in the experiment and K_d is the equilibrium binding affinity for the radioligand for the human insulin receptor (0.218nM as determined by saturation analysis). Three independent experiments were conducted with the geometric mean and standard error of the mean (SEM) reported.

Insulin and insulin-647 pharmacodynamics

Insulin and INS-647 pharmacodynamic studies were performed in mice with indwelling jugular vein and carotid artery catheters. Following a 5 hour fast, mice were anesthetized with (7.9/1.6/0.2 mg/kg) KXA through the venous catheter and placed on a heating pad. After a baseline arterial blood sample was taken, mice received a 4U/kg intravenous bolus of either insulin or INS-647. Subsequently, arterial blood samples were collected at t = 1, 3, 5, 10, 15, and 30 minutes following the bolus.

Insulin-647 stability in vivo

To assess the stability of INS-647 *in vivo* we first injected a bolus of INS-647 into anesthetized mice through an indwelling jugular vein catheter. 30 minutes later, tail vein blood was collected into heparinized capillary microtubes. Plasma was separated from erythrocytes by centrifuging whole blood at 13,000 rpm for 1 minute. Plasma was then diluted 25X with 0.9% NaCl and the total plasma fluorescence was measured in a quartz cuvette (Sterna Cells) with a FluoroMax-4 Spectrofluorometer (Horiba). Samples were excited at 633nm and emission spectra were collected from 650-750nm. Fluorescence intensity for a sample was calculated as the intensity area under the curve from 650-750nm. Background fluorescence was measured in unlabeled mouse plasma and subtracted from samples containing INS-647. After measuring total fluorescence, the plasma was separated into low (<3kDa) and high (>3kDa) molecular weight fractions using centrifugal filters with a 3kDa cutoff (Amicon Ultra, Millipore). Fluorescence was then measured in the two fractions as described above, with fractionated unlabeled mouse plasma serving as the background. Finally, the percent of fluorescence in each fraction was calculated. Fluorescence in the low molecular weight fraction was interpreted as Alexa Fluor 647 which had become separated from insulin over the course of the experiment.

Insulin-647 photostability

The rate of INS-647 photobleaching was measured in untreated glass capillary tubes on an LSM 780 laser scanning confocal microscope (Zeiss). INS-647 was imaged continuously for 5 minutes using a 633nm HeNe laser with powers ranging from 348 to 435 μW. Image acquisition parameters (i.e. size, scan speed) were set to the same values as used during *in vivo* imaging experiments. Photomultiplier tube gain and offset were set so that the histogram of

intensity values was centered in the full dynamic range for each laser power. From images for each of the different laser powers, we calculated the exponential decay constant of intensity as a function of scan number (i.e. exposure time). We then calculated the percent loss of fluorescence per scan as a function of laser power. Finally, we set a threshold of acceptable percent loss of fluorescence to photobleaching (~5-8%) and then calculated the laser power necessary to stay below this level of photobleaching during an experiment.

Insulin-647 emission spectrum

Equimolar amounts of INS-647 or free Alexa Fluor 647 were first diluted 100x in 0.9% NaCl. Probe fluorescence was then measured in a quartz cuvette with a FluoroMax-4 Spectrofluorometer. Samples were excited at 633nm and emission spectra were collected from 650-750nm. The slit width for excitation and emission was set to 1nm and the integration time for the photomultiplier tube detector was 1 second.

Fluorescent probe preparation and storage

2,000,000 Da tetramethylrhodamine-dextran (rho-dex), 3,000 Da Alexa Fluor 680-dextran, 10,000 Da Alexa Fluor 647-dextran, and Alexa Fluor 647-bovine serum albumin (BSA-647) were all purchased from Life Technologies. Lyophilized INS-647 was solubilized in a buffer containing buffer 16mg/ml glycerol, 2mg/ml m-cresol, 20mM Tris-HCl and 1% Triton X-100 to a final concentration of 1mg/ml. This is similar to the buffer used in pharmaceutical insulin preparations which prevents aggregation of INS-647. All other probes were dissolved in sterile 0.9% injectable saline to a concentration of 10mg/ml. All probes were mixed vigorously and sonicated in a water bath sonicator (Branson 2510) for 1 hour. Subsequently, probes were

centrifuged for 20 min at 13,000 rpm to remove any insoluble material. Finally, probes were visually inspected under a microscope to ensure that no aggregates were visible.

Flow cytometry of rhodamine-6G-labeled leukocytes

To determine the efficiency with which circulating blood cells were labeled by rhodamine 6G *in vivo*, anesthetized mice were injected with 0.2mg/kg rhodamine 6G through an indwelling jugular vein catheter. Blood samples were collected from an indwelling arterial catheter prior to, and 5 and 30 minutes following rhodamine 6G injection. Red blood cells were lysed with ACK lysis buffer (K D Medical). After a wash step with cold fluorescence-activated cell sorting (FACS) buffer (PBS, 1% FBS, 2mM EDTA), the remaining leukocytes were incubated in an Alexa Fluor 647-labeled anti-CD45 antibody (2.5 μg/ml; BioLegend, Cat: 103123, Clone 30-F11) for 30 minutes at room temperature. Cells were then washed twice and resuspended in cold FACS buffer containing 0.2 μg/ml DAPI. Appropriate single-color controls were also prepared (unstained, DAPI, Rhodamine6G, and Alexa Fluor 647 only). Samples were injected into a 5-laser BD LSRII flow cytometer following daily Cytometer Setup and Tracking quality control. Samples were analyzed using FACS DiVa software version 8.

Intravital Microscopy

Gastrocnemius preparation

Mice were first anesthetized with (7.9/1.6/0.2 mg/kg) KXA through an indwelling venous catheter and placed on a heating pad. After assuring an appropriate depth of anesthesia, hair was removed from the left leg with an electric razor. A small notch was made in the skin covering the lateral ankle. The skin was then removed from the lower leg to reveal the lateral gastrocnemius

(Figure 2.2A). Finally, the fascia covering the lateral gastrocnemius was carefully removed to uncover the fibers of the lateral gastrocnemius **(Figure 2.2B)**. Extensive care was taken to minimize perturbations to the muscle fibers and to avoid severing any blood vessels. After preparing the lateral gastrocnemius, the mouse was transferred to the custom stage mount for subsequent imaging.

Custom stage mount construction

Stage mounts were constructed with the lid of a standard plastic 96 well plate and a coverglass. Briefly, a rectangular opening was cut into the 96 well plate lid with a heated scalpel. Then, a 22mm x 50mm #1.5 cover glass (Fisher) was sealed on top of the rectangular opening using nail polish and silicone medical adhesive (Factor II, Inc). A 1-200μL pipette tip was fixed onto the stage mount with the silicone adhesive to serve as a port for removing fluids off of the coverslip.

Physiological monitoring and maintenance

Body temperature was measured with a rectal probe and maintained at 37°C using a feedback controller system connected to an electric blanket (Harvard Apparatus). To maintain the hydration and physiological stability of the exposed gastrocnemius, the tissue was continuously irrigated with a bicarbonate-buffered physiological saline solution composed of (in mmol/L)132 NaCl, 4.7 KCl, 2 $MgSO_4$, 1.2 $CaCl_2$, and 18 $NaHCO_3$ (221). This solution was maintained at 37°C and bubbled continuously with 95%N_2/5%CO_2 to maintain pH at 7.4. The saline solution was continuously circulated over the exposed tissue with a peristaltic pump (inflow) and a vacuum trap (outflow).

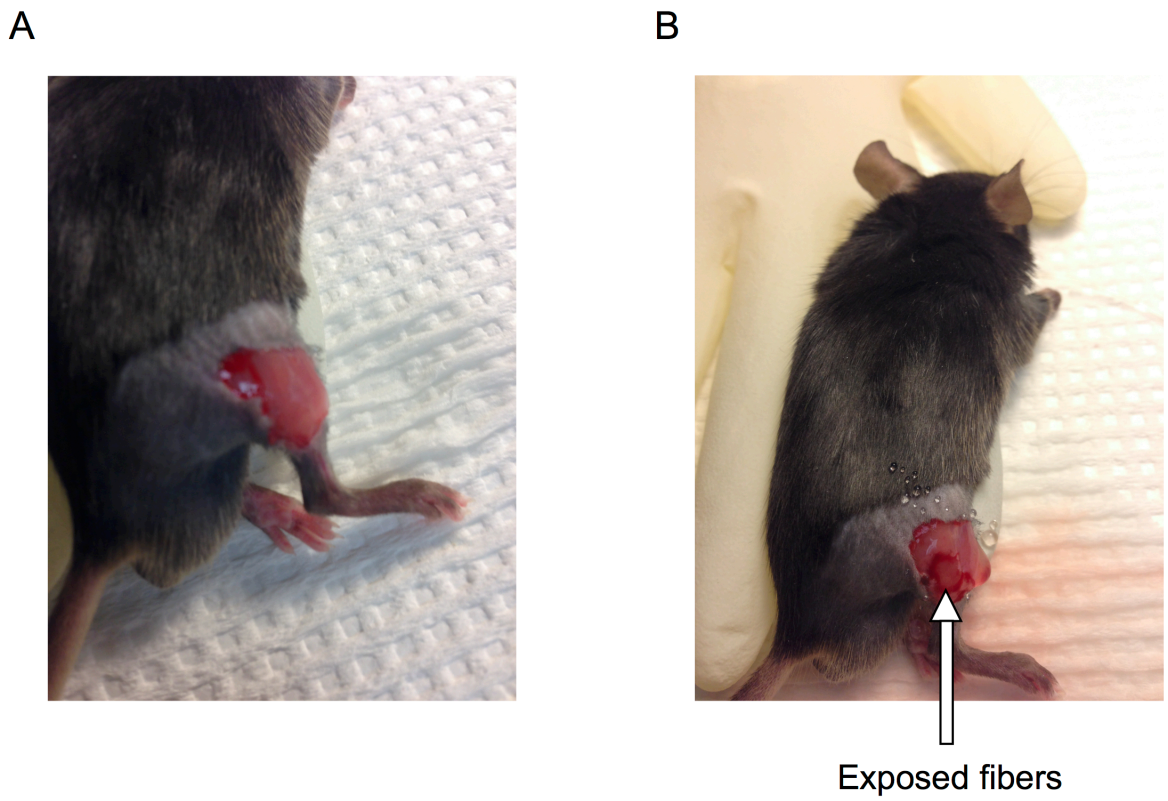

Figure 2.2: Method for exposing the gastrocnemius for intravital fluorescence microscopy. **A)** Image depicting the lateral gastrocnemius after the skin has been removed. **B)** Image showing the exposed gastrocnemius fibers following careful removal of the overlying fascia.

Selection of imaging region

The quality of the gastrocnemius preparation was visualized using tissue autofluorescence. Light from a 120W mercury arc lamp (XCite® 120) was sent through a bandpass filter (Zeiss Filter Set 10; Excitation: 450-490nm, FT: 510nm, Emission: 515-565nm) onto the exposed gastrocnemius. With this filter, blood vessels are visible as dark structures against autofluorescence emanating from the tissue. First, we ensured that fibers were sufficiently exposed and that no hairs were in potential fields of view. After ensuring the quality of the preparation, 50μg rho-dex was infused into the animal. The filter set was then switched (Zeiss Filter Set 43 HE; Excitation: 550/25nm, FT:570nm, Emission: band pass 605/70) to visualize rho-dex fluorescence emanating from blood vessels. The field of view was selected from a capillary bed emanating from the external sural artery and based on the following criteria: 1) the presence of a sufficient number of clearly visible capillaries 2) the absence of large vessels in the nearby area and 3) the absence of capillaries immediately adjacent to one another.

Molecular efflux imaging

All imaging was performed on an inverted Zeiss LSM 780 microscope (Zen software) with a 20X 0.8NA Plan-Apochromat air objective. For imaging of trans-endothelial molecular efflux (INS-647, BSA-647, dextrans), rho-dex fluorescence was excited using light from a 561nm solid-state laser and detected on a multichannel photomultiplier tube. The near infrared fluorophores were excited using a helium-neon 633nm laser and emitted light was detected using a GaAsP detector. For both rho-dex and the near-infrared fluorophores, excitation and emission light were passed through an MBS 488/561/633 dichroic. A confocal pinhole was set to give an optical section of 8μm (+/- 4μm about the focal plane). Imaging of the rho-dex and near-infrared

fluorophores was performed using two-channel sequential excitation and detection to prevent bleed through. We switched between channels every line to minimize channel mis-registration due to intra-scan motion artifacts. 8-bit intensity, 1024x1024 pixel images were acquired with unidirectional scanning. For each time point, a 4-"slice" z-stack was acquired in each channel using a step size of 4μm to avoid aliasing. Photomultiplier tube detector settings were adjusted to maximize the dynamic range of the detector and kept constant for each given experiment to allow for quantitative comparisons.

Following the selection of an imaging region but prior to administration of the probes, a background image was acquired. Subsequently, INS-647, 3kD dextran-680, 10kD dextran-647, or BSA-647 were infused through the indwelling vein catheter and followed with a 20μl pulse of saline. For the experiments in **Chapter III** and **IV**, images were then acquired using the procedure described above at t=0, 1, 2, 3, 4, 5, 6, 7, 8, 9, 10, 12.5, 15, 20, 30 min following probe injection. For mice receiving 2U/kg INS-647 in **Chapter IV**, images were collected every minute for 15 minutes. For the mice receiving 4U/kg INS-647 in Chapter **V** and **VI**, images were acquired every minute for 15 minutes.

The image acquisition procedure for mice receiving 0.5U/kg or 1U/kg INS-647 was modified slightly in order to increase sensitivity. Namely, the laser power was doubled to image the low level of INS-647. In order to keep the total laser dose similar to other INS-647 imaging experiments, we reduced the number of scans per experiment. To do this, we acquired only 2 slices per z-stack and reduced the number of time points at which images were collected (t= 0, 1, 2, 3, 4, 5, 7.5, 10, 15 min following injection). Furthermore, the pixel dwell time for each scan was increased to enhance signal detection.

In vivo imaging of capillary leukocyte and platelet adhesion

The gastrocnemius preparation for *in vivo* imaging was performed as described above. 0.2mg/kg of rhodamine-6G (Sigma) was injected into mice and allowed to circulate for 5 minutes to accumulate in leukocytes (222). At this time, images were acquired to determine the basal level of capillary leukocyte adhesion. Rhodamine-6G fluorescence was excited with light from a 514nm Argon laser passed through an MBS 458/514 dichroic beam splitter. Emitted light was passed through an open pinhole (145μm) and detected with a multichannel photomultiplier tube. 512x512 pixel single-plane images were acquired at 8-bit intensity depth using unidirectional scanning. Images were acquired continuously for a period of 2.61 minutes. To test if the laser illumination caused an increase in leukocyte adhesion, the gastrocnemius was either illuminated using the same scheme as during INS-647 imaging or not illuminated at all. Subsequently, a second round of rhodamine-6G imaging was performed as described above. Rhodamine-6G+ structures were defined as leukocytes if they were >8μm in diameter and platelets if they were <5μm in diameter. Leukocytes and platelets were deemed "adherent" if they remained in the same location along the vessel wall for >30s (223).

Phototoxicity

To determine whether the light exposure dose affected the efflux kinetics of INS-647, an experiment was performed where images were only acquired at t=0 and 30 min, thereby reducing the laser dose by ~87%. The fractional distribution of INS-647 in the intravascular and extravascular spaces was then measured at t=30min under normal INS-647 conditions and under the reduced light exposure conditions.

Intravital Microscopy Image Analysis

Intravascular and extravascular spaces were segmented in raw images using a custom ImageJ macro (**See Appendix**). A mask of vascular structures in the rho-dex channel was created using Otsu thresholding (224). This mask was then closed (dilation then erosion) and opened (erosion then dilation) with mathematical morphometric techniques. We then applied a median filter (radius = 4 pixels) to remove any remaining noise. Object recognition was then performed with the ImageJ Particle Analyzer to select vessel structures that were larger than 50μm^2 in area and having circularity from 0-0.5. The final mask of these vascular structures was then applied to the INS-647 channel to measure the intravascular intensity of INS-647. The mask was then dilated in steps of 0.5μm starting at 1μm from the capillary wall out to 3μm from the capillary wall to segment the interstitial spaces immediately adjacent to the capillary. The intensity of INS-647 was then measured in all of these extravascular segments. The contribution of INS-647 from multiple vessels to a single interstitial segment was avoided by 1) imaging regions in which capillaries are not immediately adjacent to one another (i.e. >15 μm apart in most cases) and 2) restricting analysis of the interstitial space to 3μm from the capillary wall.

Following the extraction of intravascular and extravascular INS-647 intensity vs. time profiles, a number of post-processing steps were performed. First, data were background-subtracted using intensity values from background images collected during imaging experiments. Subsequently, the loss of fluorescence due to photobleaching was corrected for each scan in the interstitial spaces. We chose not to correct the intravascular INS-647 measurements for photobleaching because intravascular INS-647 is circulating through the capillary blood stream and therefore most likely does not reside in the field of view long enough to undergo significant bleaching. The intensities from the 4 slices of the z-stack were averaged to give a single value at

each point in time and space. At this point, the contribution of free Alexa Fluor 647 to the observed kinetics of INS-647 was subtracted assuming that 10% of observed fluorescence kinetics was due to free Alexa Fluor 647 **(See Figure 3.6)**. Importantly, neither the photobleaching nor the free Alexa Fluor 647 corrections had a detectable effect on subsequent calculations. At the end of image processing, we obtained a 3D matrix describing the intensity of a given probe as a function of time after injection and distance from the capillary wall. These matrices were then used for endothelial transport parameter estimation as described below.

Intravital Microscopy Quantification

Model-independent analysis

In **Chapter V**, the clearance of INS-647 from the plasma was analyzed by fitting the first 5 minutes of the plasma INS-647 decay curve to a mono-exponential decay function. We decided to describe capillary INS-647 kinetics with mono-exponential decay as our imaging data fit this function better than bi-exponential decay (data not shown). The rate of trans-endothelial insulin efflux can be assessed by determining the rate at which insulin in the capillary equilibrates with the surrounding interstitial space. To measure this equilibration rate, we plotted the ratio of plasma to interstitial INS-647 intensity as a function of time following the INS-647 bolus. Over time, this ratio will decay as INS-647 leaves the plasma and enters the interstitial space. We quantified the gradient decay constant of the plasma/interstitial INS-647 ratio by fitting the first 5 minutes of the decay curve to a mono-exponential decay function.

To estimate an index of total INS-647 delivery to the muscle, we measured the mean INS-647 intensity in the entire extravascular space of the field of view. Extravascular INS-647 was measured by using the capillary mask from the vascular segmentation algorithm, dilating the

mask by 1μm, and then inverting the mask to measure INS-647 intensity in the entire extravascular space. In **Chapter V** and **VI**, we calculated the baseline-subtracted area under the extravascular INS-647 curve using trapezoidal integration as a measure of total insulin delivery.

Mathematical modeling

To model molecular efflux kinetics, we initially assumed that probes move through the interstitial space by diffusion. Therefore, as a base model we used the diffusion equation, a second-order partial differential equation, to describe the movement of probes through the interstitial space (Equation 1). While movement of INS-647 in the interstitial space occurs in 3 dimensions, we restricted our analysis and subsequent modeling to 1 dimension. We chose to make this dimensional reduction because it is not currently technically feasible to precisely measure the movement of INS-647 in the *z*-plane in a live animal. Therefore, we assume that the transport parameters governing INS-647 movement in 1 dimension generalize or extend to 3 dimensions. We also assumed that probes are removed from the interstitial space by a first-order, concentration-dependent process (Equation 1). The initial (IC) and boundary conditions (BCs) to the diffusion equation are as follows: IC) Prior to administration of the INS-647 bolus (i.e. t=0), INS-647 intensity is 0 for all *x*. BC1) At points infinitely far from the capillary wall INS-647 intensity is 0 for all *t*. BC2) The boundary condition describing movement of INS-647 from the plasma into the interstitial space was set to either a) the modified Fick equation to describe diffusion (Equation 2a), b) an equation describing fluid-phase transport (Equation 2b), or c) the Michaelis-Menten equation (Equation 2c). The diffusion equation (Equation 1) was solved with the aforementioned boundary and initial conditions using Laplace transforms (225) to give equations describing either diffusion (Equation 3a), fluid-phase transport (Equation 3b), or

saturable transport (Equation 3c) across the endothelium. The inputs to the equation are the independent variables *x* and *t,* the plasma INS-647 intensity as a function of time $c_p(t)$, and the adjustable parameters *D, k,* and *P* (diffusion model), *D, k,* k_L (fluid-phase transport model), or *D, k,* V_{max} and K_m (Michaelis-Menten model).

(1) $$\frac{\partial c}{\partial t} = D\frac{\partial^2 c}{\partial x^2} - kc$$

(2a) $$P\left(c_p(t) - c(0,t)\right) = -D\frac{\partial c}{\partial t}\Big|_{x=0}$$

(2b) $$k_L c_p(t) = -D\frac{\partial c}{\partial t}\Big|_{x=0}$$

(2c) $$V_{max}\frac{c_p(t)}{K_m + c_{p(t)}} = -D\frac{\partial c}{\partial t}\Big|_{x=0}$$

(3a) $$c(x,t) = h\int_0^t c_p(\tau)e^{-k(t-\tau)}\left[\sqrt{\frac{D}{\pi(t-\tau)}}e^{\frac{-x^2}{4D(t-\tau)}} - hDe^{hx+Dh^2(t-\tau)}erfc\left(\frac{x}{2\sqrt{D(t-\tau)}} + h\sqrt{D(t-\tau)}\right)\right]d\tau$$

(3b) $$c(x,t) = g\int_0^t c_p(\tau)e^{-k(t-\tau)}\sqrt{\frac{D}{\pi(t-\tau)}}e^{\frac{-x^2}{4D(t-\tau)}}d\tau$$

(3c) $$c(x,t) = a\int_0^t \left(\frac{c_p(\tau)}{K_m + c_p(\tau)}\right)e^{-k(t-\tau)}\sqrt{\frac{D}{\pi(t-\tau)}}e^{\frac{-x^2}{4D(t-\tau)}}d\tau$$

In the above equations, *c* = INS-647 intensity, *t* = time, *D* = interstitial diffusion coefficient, *x* = distance from the capillary, *k* = interstitial removal constant, *P* = permeability, k_L = the fluid-phase mass transfer coefficient, $c_p(t)$ = plasma INS-647 intensity as a function of time, *c(0,t)* = the interstitial INS-647 intensity immediately adjacent to the abluminal side of the capillary wall, V_{max} = the maximum rate of reaction, K_m = the concentration of substrate at ½ V_{max}, $h = P/D$, $g = k_L/D$, $a = V_{max}/D$, and $t - \tau$ = the convolution integral time shift.

To estimate these adjustable parameters, INS-647 intensity profiles were simulated from equations 3a-c. Parameters were estimated by minimizing the weighted sum-of-squared residuals between simulated and experimental measurements. Weighting was performed by dividing

residuals by the inverse of the intragroup standard deviation of intensity at each point in space and time. The effect of this scheme was to give more weight to the residuals at points where the confidence in the measurement was higher (i.e. low standard deviation) and vice versa. A multi-start approach was used to generate random initial parameter estimates. A trust-region-reflective search algorithm was then used to minimize the weighted sum-of-squared residuals by adjusting the parameters. Goodness of fit between experimental and simulated measurements was determined by several analyses including the sum of squares of the weighted residuals and visual analysis of the residuals. Goodness of fit was deemed to be acceptable if the weighted sum-of-squared residuals fell within the 95% confidence interval of the chi-square distribution for a certain number of degrees of freedom. Parameter estimation and goodness of fit analyses were performed using custom MATLAB scripts and functions (**See Appendix**).

Vascular parameters

Average capillary diameter was estimated using a simplified version of an algorithm developed by McClatchey et al. to measure mitochondrial width (226). Briefly, the rho-dex vascular marker channel was used to calculate the ratio of total vascular surface area to total vascular perimeter. This ratio approximates the radius of long cylindrical vessel segments. Plasma-perfused surface area was calculated from images by summing the rho-dex surface area for all 4 slices at a given time point.

In Vivo Physiological Measurements

Body composition

Body composition was measured using an mq10 nuclear magnetic resonance (NMR) analyzer. For the experiments in **Chapter VII**, body composition was measured at 16 weeks of age after 10 weeks of either chow or HFD diet and 2 weeks of either saline or Angiotensin-(1-7) treatment. In **Chapter V**, body composition was measured after 15 weeks of chow or HFD. Percent fat mass was calculated by dividing the absolute fat mass by the total mass measured by the NMR analyzer (fat mass + lean mas + free fluid mass).

Cardiac function and blood pressure

Cardiac function was assessed by transthoracic echocardiography with a Sonos 5500 system (Agilent). Parameters of cardiac function were estimated from chamber dimensions calculated from M-mode echocardiographic tracings. Blood pressure was measured through an indwelling carotid artery catheter connected to a strain-gauge transducer and a BPA-400 analyzer (Digi-Med). For the experiments in **Chapter VII**, blood pressure and heart rate were measured in conscious mice on the morning of insulin clamps, after approximately 2.5 hours of fasting. After a 15-minute acclimation period, we recorded the first five measurements taken at 10-second intervals. The average of these blood pressure and heart rate measurements was reported. In **Chapter VI**, blood pressure was measured every minute in 5 hour-fasted mice anesthetized with KXA.

Microsphere deposition

To assess muscle perfusion in **Chapter III**, we measured the deposition of intra-arterially administered microspheres. 100 µl of yellow 15-µm microspheres (Dye-Trak, Triton Technology) were injected into the carotid artery after the last sampling time point of the insulin clamp to measure regional blood flow to the hind limb. 5 minutes following microsphere administration, the hind limb (gastrocnemius, soleus, and vastus muscles) was excised, weighed and incubated in 1M KOH at 60°C overnight. Blue microspheres (10,000) were added to each sample to control for loss of microspheres during processing. The following day, samples were vortexed, 50°C ddH_2O was added, and samples were centrifuged for 15 minutes at 2623 rpm at room temperature. The supernatant was then aspirated and the pellet resuspended in Triton X-100 by sonication. This centrifugation, supernatant aspiration, resuspension sequence was repeated with 0.2% HCl in ethanol followed by ethanol alone. After aspirating the ethanol, pellets were allowed to dry overnight. To elute the dye from microspheres, pellets were incubated in *N,N*-dimethylformamide for 15 minutes. Following centrifugation for 5 min at 2623 rpm, supernatants were added to 96 well polypropylene plates and Abs_{440} and Abs_{670} were measured on a spectrophotometer. Absorbance readings were converted to microsphere numbers based on a known standard curve from the manufacturer. Arterial microsphere mixing was considered adequate if the difference in the number of microspheres deposited in the left and right kidneys was less than 15%.

Plasma Analyses

Plasma 3[^{3}H]glucose and 2[^{14}C]2deoxyglucose

To measure plasma and infusate levels of the isotopic tracers, 3[^{3}H]glucose and 2[^{14}C]DG, samples were first diluted twofold in 0.9% NaCl and then deproteinized by sequential treatment with barium hydroxide [$Ba(OH)_2$, 0.3N] and zinc sulfate ($ZnSO_4$, 0.3N]. Deproteinized plasma samples were centrifuged for 5 minutes at 13,000 rpm and 100 µl of the resulting supernatant was transferred to a glass vial. For 3[^{3}H]glucose samples, the supernatant was dried in a vacuum oven for 1 hour at 60°C followed by addition of 1 ml ddH_2O. For 2[^{14}C]2DG samples, 990 ml ddH_2O was added directly to 100ul of supernatant. Finally, 10 ml of Ultima Gold scintillation cocktail (Perkin Elmer) was added to all vials and radioactivity was measured using a Tri-Carb 2900TR liquid scintillation counter (Packard).

Plasma insulin

Plasma insulin was measured by a double antibody radio-immunoassay (Milipore Mouse/Rat Insulin RIA, see Ref (227)). Plasma samples were diluted in a buffer containing 50mM PBS (pH 7.4), 25mM EDTA, 0.08% sodium azide, and 1% BSA. Subsequently, ^{125}I-insulin and a guinea pig anti-mouse insulin antibody were added to each sample and incubated overnight at 4ºC. The antibody-bound ^{125}I-insulin was separated from free ^{125}I-insulin by adding a precipitating reagent containing goat anti-guinea pig IgG serum, 3% polyethylene glycol, and 0.05% Triton X-100 in 50mM PBS, 25mM EDTA and 0.085% sodium azide. Following a 20-minute incubation, samples were centrifuged at 2500 x *g* to separate free (supernatant) from bound (pellet) ^{125}I-insulin. ^{125}I radioactivity was then measured in the pellets using a Cobra II AutoGamma counter. Counts in the pellet were compared to a standard curve to calculate

unknown insulin concentrations in the plasma samples. If the percent of ^{125}I-insulin displaced by the unlabeled insulin was >90 % (too concentrated) or <10% (too dilute) in any given sample, plasma dilutions were adjusted and the assay was repeated.

Plasma non-esterified fatty acids

Plasma non-esterified fatty acids (NEFAs) were measured using an enzymatic colorimetric assay (HR Series NEFA-HR(2); Wako Diagnostics). Plasma samples were collected into tubes pre-treated with a lipase inhibitor, tetrahydrolipstatin, to prevent NEFA degradation during sample collection. 5μL samples were diluted 1:2 in H_2O. NEFAs were then converted to AcylCoAs by adding a solution containing AcylCoA synthetase, ATP, and CoA for 10 minutes at 37ºC. Subsequently, AcylCoAs were oxidized by adding Acyl-coenzyme A oxidase for 10 minutes at 37ºC. This reaction generates hydrogen peroxide. In the presence of peroxidase and the hydrogen peroxide, 4-aminoantipyrine and 3-methyl-N-(β-hydroxyethyl)-aniline can be oxidatively condensed to generate a purple end product. The amount of this end product formed is proportional to the amount of hydrogen peroxide generated and, thus, plasma NEFA levels. The amount of the purple end product was measured spectrophotometrically at 560nm on a SpectraMax Plus spectrophotometer. Sample absorption measurements were compared to an oleic acid standard curve to calculate NEFA levels in the unknown plasma samples. Basal and clamp NEFA levels were calculated as the average NEFA levels at t = -15 and -5 min, and t = 80 and 120 min, respectively.

Circulating angiotensin peptide levels

In **Chapter VII**, plasma Ang-(1-7) and Ang II levels were measured in a separate cohort of mice that did not undergo insulin clamps [n=6 chow-fed, vehicle; n=6 chow-fed Ang-(1-7); n=8 HFD, vehicle; n=8 HFD Ang-(1-7)]. Blood was collected in an EDTA tube containing a peptidase inhibitor to prevent degradation of Ang peptides. Plasma was separated from red blood cells and sent to the Hypertension Core at Wake Forest University for analysis as previously described (228). Briefly, plasma was homogenized in 75% ethanol/0.18M HCl and separated on a C_{18} SepPak column using high performance liquid chromatography. Radiolabeled Ang peptides were used to determine recovery efficiency. Following separation, Ang-(1-7) was measured by radioimmunoassay using a custom antibody. The minimum detectable level is 0.8 pg/tube with 8% intra-assay coefficient of variation. Ang II was measured using a commercially available radioimmunoassay kit (ALPCO Diagnostics, RK-A22). The minimum detectable level is 2.5 pg/tube with 12% intra-assay coefficient of variation.

Tissue Analyses

Tissue 2[^{14}C]deoxyglucose accumulation

To determine levels of 2[^{14}C]DG and 2[^{14}C]DG-6-phosphate (2[^{14}C]DGP), tissues were first homogenized (Bullet Blender, Next Advance) in 0.5% perchloric acid to extract metabolites. After centrifugation at 13,000 rpm for 5 minutes, the homogenate pH was adjusted to 7.5 with KOH. Radioactivity was counted in one aliquot of the neutralized homogenate to determine tissue levels of combined 2[^{14}C]DG and 2[^{14}C]DGP. A separate aliquot was treated with $Ba(OH)_2$ and $ZnSO_4$ to remove 2[^{14}C]DGP and any glycogen-incorporated radioactivity. This

sample was then counted to measure 2[^{14}C]DG. The difference in radioactivity between the first aliquot (2[^{14}C]DG + 2[^{14}C]DGP) and second aliquot (2[^{14}C]DG) is equal to 2[^{14}C]DGP.

Immunohistochemical staining

To determine muscle capillary density we performed CD31 staining on gastrocnemius sections. CD31 is an endothelial cell marker which allows for the immunohistochemical detection of blood vessels in tissue sections. Following insulin clamps, the gastrocnemius was excised, fixed in 10% neutral-buffered and embedded in paraffin. 5µm sections were cut using a microtome and mounted on charged slides. For CD31 staining, the Leica Bond Max IHC stainer was used. Epitopes were retrieved by heat-induced antigen retrieval using Epitope Retrieval 2 solution (Leica) for 20 minutes. Slides were incubated with an anti-CD31 primary antibody (1:100; Dianova; see **Table 2.1**) for 60 minutes followed by a biotinylated anti-rat antibody (1:200; Vector; **Table 2.1**) for 15 minutes. Slides were then lightly counterstained with Mayer hematoxylin solution. The EnVision+HRP/DAB System (DakoCytomation) was used to produce localized, visible staining.

In order to determine the level of Glut4 at the muscle sarcolemma, we performed a double immunostaining of Glut4 and caveolin-3 (Cav3), a sarcolemmal marker. Epitopes masked by formalin fixation were retrieved by incubating sections in a 10mM Tris buffer (pH 9) for 50 minutes at 90°C. After a brief wash in phosphate-buffered saline (PBS), non-specific secondary antibody binding was blocked for 1 hour in 5% normal goat serum (NGS; Jackson ImmunoResearch) and 'Mouse on Mouse' blocking reagent (M.O.M.; Vector) at room temperature. Then, sections were incubated overnight at 4°C in rabbit anti-Glut4 (1:200; Abcam; **Table 2.1**) and mouse anti-Cav3 (1:200; Santa Cruz; **Table 2.1**) in 5%NGS/PBS. The next day

sections were washed in PBS followed by incubation in an Alexa Fluor 647 conjugated goat anti-rabbit (1:500; Life Technologies; **Table 2.1**) and an Alexa Fluor 555 conjugated goat anti-mouse secondary antibody (1:500; Life Technologies; **Table 2.1**) in 5% NGS/PBS. Finally, sections were rinsed, mounted in 50% glycerol/H_2O, cover slipped, and stored at 4°C in the dark. Control sections stained in the same manner as described above, but lacking primary antibodies, were used to demonstrate specificity of the secondary antibodies (**Figure 2.3**). Similarly, sections stained with only one primary antibody were used to ensure that secondary antibodies only recognized the correct primary antibody (**Figure 2.3**).

Immunohistochemistry image acquisition and analysis

Following the CD31 staining, images of gastrocnemius sections were captured at 175x total magnification using a Nikon DS-Ri2 camera mounted on a Nikon AZ100M upright, wide-field microscope. At least 3 images were collected per section from 3 serial sections per mouse. Quantification of capillary density was performed by counting CD31+ structures using a custom, automated macro in ImageJ **(See Appendix)**. An investigator blind to diet and treatment performed all image acquisition and analyses.

For the Glut4/Cav3 double staining, images were acquired using an inverted Zeiss LSM 510 confocal microscope equipped with two helium-neon (HeNe) lasers (543nm and 633nm) and a 40X 1.3NA oil immersion Plan Neofluar objective (Zeiss). Alexa Fluor 555 was excited with the 543nm laser line of the HeNe laser and emitted light was collected using a 560-615nm bandpass emission filter. Alexa Fluor 647 was excited with the 633 nm laser line of the HeNe laser and emitted light was collected using a longpass 650nm filter. Sampling was performed at a resolution fulfilling the Nyquist criteria and with the pinhole set to give an optical section of

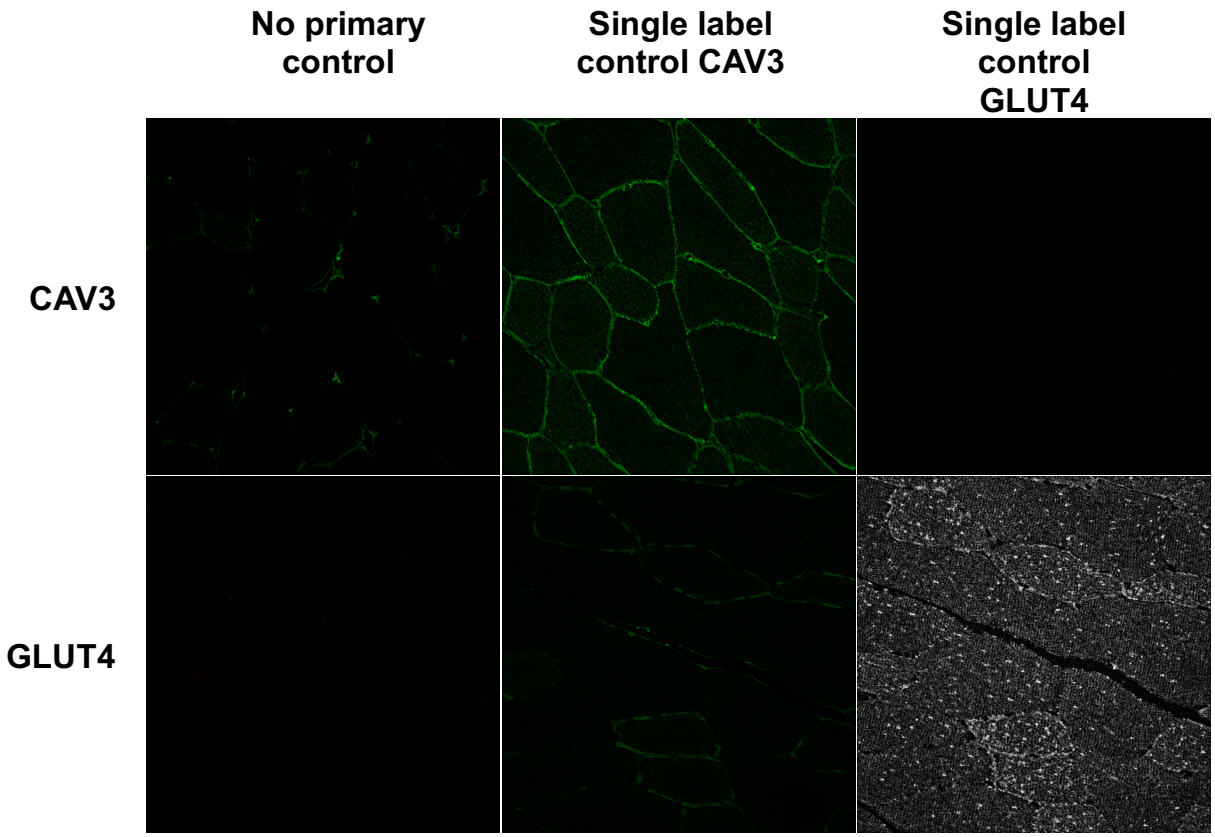

Figure 2.3 Labeling controls for Cav3/Glut4 immunofluorescence staining. Representative micrographs of gastrocnemius sections obtained following hyperinsulinemic-euglycemic clamps in high-fat fed mice. Images were obtained by confocal microscopy to demonstrate specificity of secondary antibodies for the appropriate primary antibody. All control sections were treated with both AlexaFluor555-conjugated goat anti-mouse and AlexaFluor647-conjugated goat anti-rabbit secondary antibodies. The left column represents sections not treated with any primary antibodies (no primary control). The sections in the middle and right columns were treated with either Cav3 or Glut4 primary antibodies, respectively; to ensure that secondary antibodies only recognized the correct primary antibody.

1.6μm. The two fluorophores were excited sequentially to prevent bleed-through and frame averaged 2 times. Photomultiplier tube detect settings were kept constant throughout imaging to allow for quantitative comparisons. At least 2 images were collected per section from 3 serial sections per mouse. All image analysis was performed using ImageJ software (NIH). Images were background-corrected using the rolling ball radius background subtraction method. Then, a mask of the sarcolemma was created by Otsu-based thresholding of the Cav3 channel. This mask was applied to the Glut4 (Alexa Fluor 647) channel and the mean Glut4 fluorescence intensity within this mask was measured. Image acquisition and data analysis was performed by an investigator blinded to the study design.

Immunoblotting

Gastrocnemius muscle samples were mechanically homogenized (Bullet Blender; Next Advance) in buffer containing 50mM Tris-HCl (pH 7.5), 100mM NaCl, 1mM EDTA, 1mM EGTA, 1% TritonX-100, 1mM DTT, 10% glycerol, and Halt Protease and Phosphatase Inhibitor Cocktail (Life Technologies). Samples were then centrifuged at 13,000 rpm for 20 min at 4°C. Homogenates were separated on SDS-PAGE gels and transferred to polyvinylidene fluoride membranes. Membranes were blocked with Odyssey Blocking Buffer (LI-COR) for 1 hour at room temperature. For the experiments in **Chapter VII**, membranes were probed with the following antibodies: phosphorylated Akt (Ser^{473}; Cell Signaling), total Akt (Cell Signaling), phosphorylated AS160 (Ser^{588}; Cell Signaling), and total AS160 (Millipore). In **Chapter VI**, membranes were probed with antibodies against total VASP (1:500; #3112; Cell Signaling), phosphorylated (Ser^{239}) VASP (1:500; #3114; Cell Signaling), and GAPDH (1:1000; ab9484; Abcam). Primary antibodies were detected using either 800CW goat anti-rabbit (1:5000; LI-

Antibodies:

Target	Species	Application	Dilution	Manufacturer	Ref#	Lot#
pAkt (Ser473)	Rabbit	WB	1:0000	Cell Signaling	9271	13
Akt	Rabbit	WB	1:1000	Cell Signaling	9272	25
pAS160 (Ser588)	Rabbit	WB	1:500	Cell Signaling	8730	1
AS160	Rabbit	WB	1:1000	Millipore	07-741	2455680
GAPDH	Mouse	WB	1:1000	Abcam	9484	GR174666;GR286286-12
800CW anti-Rabbit IgG	Donkey	WB	1:10,000	LI-COR	926-32213	B0228-01
680LT anti-Mouse IgG	Donkey	WB	1:10,000	LI-COR	926-68022	C50512-02
pVASP (Ser239)	Rabbit	WB	1:500	Cell Signaling	3114	6
VASP	Rabbit	WB	1:500	Cell Signaling	3112	5
800CW anti-Rabbit IgG	Goat	WB	1:5000	LI-COR	926-32211	C70620-05
680RD anti-mouse IgG	Goat	WB	1:5000	LI-COR	926-68071	C41009-01
CD31	Rat	IHC	1:100	Dianova	DIA-310	SZ31
Rat IgG	Rabbit	IHC	1:200	Vector	BA-4000	Z0612
Glut4	Rabbit	IF	1:200	Abcam	654-250	387864
Cav3	Mouse	IF	1:200	Santa Cruz	Sc-5310	B0414
Alexa Fluor 555 anti-mouse	Goat	IF	1:500	Molecular Probes	A21422	1685557
Alexa Fluor 647 anti-rabbit	Goat	IF	1:500	Molecular Probes	A21245	1700082
Alexa Fluor 647 anti-mouse CD45	Rat	Flow	2.5µg/ml	BioLegend	103123	B20144

Table 2.2. List of antibodies used. WB = western blot; IHC = immunohistochemistry; IF = immunofluorescence.

COR) or 680RD goat anti-mouse (1:10,000; LI-COR) secondary antibodies. All antibodies used for immunoblotting are shown in **Table 2.1**. Membranes were imaged with an Odyssey Imaging System (LI-COR) and quantified by densitometric analysis with ImageJ.

Transmission electron microscopy

Samples were processed for transmission electron microscopy and imaged in the Vanderbilt Cell Imaging Shared Resource – Research Electron Microscopy facility. Erythrocytes were initially rinsed from the circulation of anesthetized mice by infusing 0.1M cacodylate buffer into the vasculature through a catheter inserted into the left ventricle. Rinsing was deemed complete when perfusate leaking from an incision in the liver turned a pale pink color. Tissues were then fixed by switching the perfusate to 2.5% glutaraldehyde in 0.1M cacodylate buffer. The gastrocnemius was then excised and fixed for an additional 24h at 4°C. Tissues were subsequently postfixed with osmium tetroxide, dehydrated and embedded in Epon 812 epoxy resin. 70-80 nm sections were cut from embedded tissues and stained with 2% uranyl acetate and Reynold's lead citrate. Sections were imaged using a Philips/FEI Technai T12 electron microscope. Capillaries were identified and selected for analysis at low magnification where endothelial ultrastructure (i.e. vesicles) is not visible. This approach prevents bias in capillary selection. Subsequently, 2-4 images were acquired of each capillary at high magnification (67,000x). 6-13 capillaries were imaged per section.

Endothelial vesicular density was measured by applying a test point grid (ImageJ) to micrographs and then counting the number points residing within vesicles and within the entire endothelium (229). Endothelial vesicular density was calculated as the number of points within vesicles relative to the number of points in the endothelium as a whole. Vesicular diameter was

measured at the widest point of each vesicle. Endothelial vesicle localization was assessed by manually counting vesicles that were either facing the capillary lumen (luminal), contained within the endothelium (intracellular), or facing the interstitial space (abluminal). Basement membrane thickness was measured perpendicularly to points of intersection between a line grid applied to micrographs and the capillary endothelium.

Calculations

Whole-body glucose flux

The rates of whole-body plasma glucose appearance (R_a) and disappearance (R_d) were determined from plasma 3[^{3}H]glucose levels and calculated using non-steady state equations (230):

$$R_a = \frac{I - V_d \bullet A \bullet \frac{\partial SA}{\partial t}}{SA} \qquad R_d = R_a - V_d \bullet \frac{\partial A}{\partial t}$$

where I is the tracer infusion rate (dpm•kg^{-1}•min^{-1}), V_d is the volume of distribution (dl•kg), A is the arterial glucose (mg•dl^{-1}), ∂SA/∂t is the rate of change in glucose specific activity over 30 minutes (dpm•mg^{-1}•min^{-1}), SA is glucose specific activity (dpm•mg^{-1}), and ∂A/∂t is the rate of change in arterial glucose over 30 minutes. These equations describe the turnover of glucose in a single, well-mixed compartment. Arterial glucose and glucose specific activity used in the equations were calculated using a moving average over three consecutive time points (231). R_a and R_d were calculated at t= 90, 100, and 110 min and averaged. To calculate the endogenous rate of glucose appearance (EndoR_a), the exogenous glucose infusion rate was subtracted from total R_a. Non-steady state equations were used for all calculations; however, steady state calculations gave nearly identical rates, suggesting that steady state conditions were present.

2[^{14}C]deoxyglucose calculations

During the insulin clamps performed in **Chapter VII**, we measured the accumulation of 2[^{14}C]DG to calculate the glucose metabolic index (R_g). R_g is a measure of tissue-specific glucose uptake and was calculated using the following equation (217):

$$R_g = \frac{2[^{14}C]DGP_{tissue}}{AUC2[^{14}C]DG_{plasma}} \bullet [arterial\ glucose]$$

where 2[^{14}C]DGP$_{tissue}$ is the accumulated 2[^{14}C]DGP in tissue (dpm•mg^{-1}), AUC2[^{14}C]DG$_{plasma}$ is the area under the plasma 2[^{14}C]DG disappearance curve (dpm•ml^{-1}•min), and [arterial glucose] is the average blood glucose (mmol•L^{-1}) from t = 120 to t = 155 min of the clamp period. For the insulin tolerance tests in **Chapter V**, we measured tissue glucose clearance using the following equation:

$$K_g = \frac{2[^{14}C]DGP_{tissue}}{\int_0^{15} 2[^{14}C]DG_{plasma}}$$

where 2[^{14}C]DGP$_{tissue}$ is the accumulated 2[^{14}C]DGP in the tissue (dpm•g^{-1} tissue) and $\int_0^{15} 2[^{14}C]DG_{plasma}$ is the time-integrated 2[^{14}C]DG activity in the plasma calculated using trapezoidal integration. Finally, When using 2[^{14}C]DG during intravital microscopy experiments or for insulin tolerance tests in **Chapters III, IV, V,** and **VI**, we measured and reported the accumulation of 2[^{14}C]DG in the gastrocnemius due to the difficulty of measuring plasma 2[^{14}C]DG during intravital microscopy experiments.

Statistics

All data are presented as mean ± SEM unless otherwise noted. All statistical analysis was performed using Prism (GraphPad). Outliers were detected by Grubbs' test ($\alpha = 0.05$) and subsequently removed. Comparisons between groups were performed using either Student's t-test, one-way ANOVA, two-way ANOVA, or two-way repeated measures ANOVA where appropriate. Dunnett's tests (one-way ANOVA) or Bonferroni corrections (two-way ANOVA) were used to correct for multiple comparisons.

CHAPTER III

DEVELOPMENT OF AN INTRAVITAL MICROSCOPY TECHNIQUE TO MEASURE THE RATE OF TRANS-ENDOTHELIAL INSULIN TRANSPORT IN SKELETAL MUSCLE CAPILLARIES *IN VIVO*

Aims

Methods to measure the rates of molecular efflux across the capillary endothelium *in vivo* are lacking. Cultured endothelial monolayers, especially those using macrovascular endothelial cells, lack several key characteristics of capillaries in a live organism. On the other hand, *in vivo* interstitial sampling is limited because the number of capillaries feeding the space from which sampling is performed is unknown. Therefore, such techniques do not directly measure trans-endothelial molecular efflux but rather an index of delivery which is determined by both perfusion and transport. We sought to develop a method to directly measure capillary insulin transport that could 1) be conducted *in vivo* with minimal physiological perturbations, 2) measure the concentration of insulin in both the intravascular and adjacent interstitial spaces as a function of time, and 3) allow for determination of the capillary surface area feeding a given interstitial space. Intravital microscopy provides the necessary balance of sensitivity as well as spatial and temporal resolution to satisfy these criteria. Thus, the aim of **Chapter III** is to develop a quantitative intravital microscopy technique to directly measure the rate of movement of a fluorescently-labeled insulin probe across the endothelium in single skeletal muscle capillaries *in vivo*.

Results*

Site-specific conjugation of Alexa Fluor 647 to human insulin

The most commonly used fluorescent insulin probes are FITC-insulin conjugates. These probes can contain a heterogeneous mixture of insulin conjugate species that have lower affinity for the insulin receptor than native insulin (232, 233). Furthermore, the fluorescence intensity of FITC is sensitive to pH, falling off rapidly as the pH drops below 7 (234). Because various intracellular compartments display a range of pH values, the fluorescence intensity of FITC does not reliably reflect the concentration of the insulin probe. An ideal fluorescent insulin conjugate for in vivo imaging would be fully bioactive, have high signal-to-noise ratio in live tissue, and be unaffected by the microenvironment.

To achieve this goal, we labeled insulin in a site-specific manner with Alexa Fluor 647. We chose Alexa Fluor 647 because of its brightness and photostability (235), insensitivity to pH (234), and the lack of tissue autofluorescence in the near-infrared wavelengths. Next, we selectively labeled the N-terminal phenylalanine of the B chain (B1) of human insulin (**Figure 3.1**). We chose this site because conjugation of various molecules to B1 has little to no effect on the affinity of the resulting conjugate for the insulin receptor (232). To perform this labeling, we first blocked the reactivity of all free amines except the B1 phenylalanine using tert-butyloxylcarbonyl (t-boc) protection chemistry (**Figure 3.1**). Then we conjugated the free amine on the unprotected B1 phenylalanine to Alexa Fluor 647 succinimidyl ester (**Figure 3.1**). Finally, the t-boc groups were removed with trifluoroacetic acid to complete the synthesis of the B1-Alexa Fluor 647-insulin conjugate (INS-647) (**Figure 3.1**). Analysis of INS-647 using HPLC-

* These results have been published in: Williams IM, Valenzuela FA, Kahl SD, Ramkrishna D, Mezo AR, Young JD, Wells KS, Wasserman DH. Insulin exits skeletal muscle capillaries by fluid-phase transport. *J Journal of Clinical Investigation* 2018 Feb 1; 128(2):699-714. PMID: 29309051.

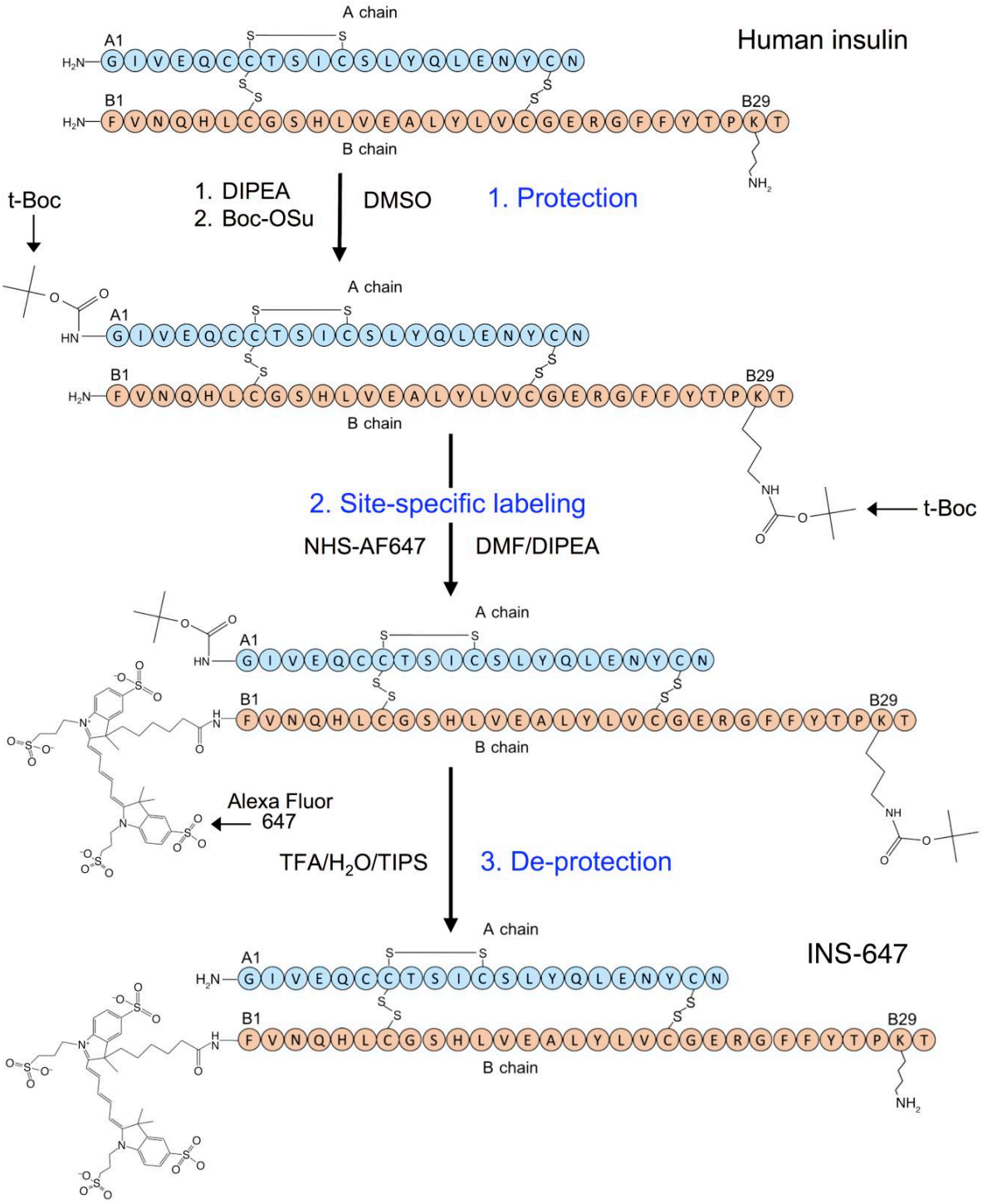

Figure 3.1: Synthesis of insulin-647, a novel fluorescent insulin probe. A) Schematic depicting the chemical synthesis of INS-647. t-Boc - tert-butyloxycarbonyl, DIPEA - *N,N*-Diisopropylethylamine; Boc-OSu - (Boc)succinimide ester; DMSO - dimethylsulfoxide; NHS-AF647 - Alexa Fluor 647 NHS ester; DMF – dimethylformamide; TFA - trifluoroacetic acid; TIPS - triisopropylsilane.

mass spectrometry (LC-MS) revealed a single conjugate species (**Figure 3.2A**) with the appropriate mass (**Figure 3.2, B and C**). Most importantly, INS-647 has unaltered affinity for the insulin receptor as determined by scintillation proximity assay-based competitive radioligand binding analysis (**Figure 3.2D)**. Moreover, during a 1U/kg insulin tolerance test in vivo, INS-647 lowered blood glucose to the same extent as unlabeled insulin (**Figure 3.3, A and B**) and fully stimulated muscle 2[^{14}C]DG accumulation (**Figure 3.3, C and D**). To assess INS-647 at a more physiological insulin level, we performed insulin clamps with insulin and INS-647 (**Figure 3.4**). During steady-state hyperinsulinemia, there was no difference in the glucose infusion rate required to maintain euglycemia using insulin or INS-647 (**Figure 3.4, A and B**). Furthermore, the rates of insulin-stimulated peripheral glucose disposal (**Figure 3.4C**) and suppression of endogenous glucose production (**Figure 3.4D**) were not different when using insulin or INS-647. Basal and clamp plasma insulin levels were also identical between groups (**Figure 3.4E**). These data indicate that INS-647 is fully bioactive at physiological concentrations. To determine whether the pharmacokinetic properties of INS-647 are similar to unlabeled insulin, we administered a 4U/kg intravenous bolus of either insulin or INS-647. Measurements of arterial plasma insulin indicated that there was no difference in arterial kinetics between insulin and INS-647 (**Figure 3.5, A and B**). INS-647 is also stable in the *in vivo* environment, with 90% of the dye remaining conjugated to insulin after 30 minutes in the circulation (**Figure 3.6**). In conclusion, we have synthesized a fully bioactive, optically optimized insulin conjugate which is well suited for *in vivo* imaging and other fluorescence-based applications.

A

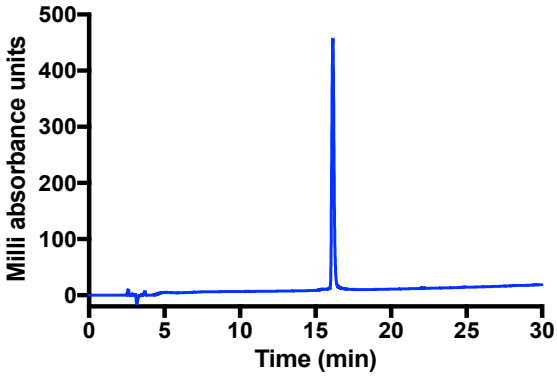

B

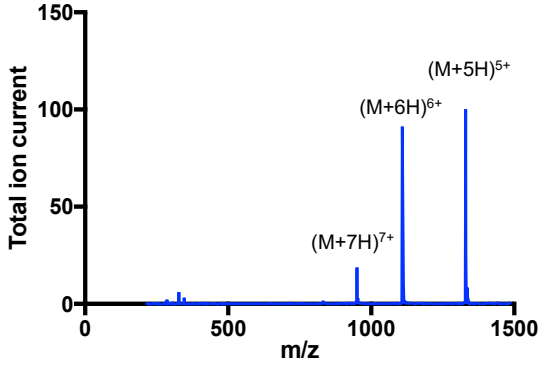

C

Ion	m/z	Deconvoluted Mass	Average Mass
$(M+5H)^{5+}$	1330.7	6648.5 Da	**6648.33**
$(M+6H)^{6+}$	1109.1	6648.6 Da	
$(M+7H)^{7+}$	950.7	6647.9 Da	

D

Insulin species	Insulin	Insulin-647
K_i (nM)	0.208 ± 0.003	0.213 ± 0.003

Figure 3.2: *In vitro* characterization of insulin-647. A) Analytical RP-HPLC trace of INS-647. **B)** Mass spectrum of INS-647. The labeled peaks indicate the three most abundant ions $(M+5H)^{5+}$, $(M+6H)^{6+}$, $(M+7H)^{7+}$. **C)** The mass of INS-647 as calculated from the m/z of the three most abundant ions $(M+5H)^{5+}$, $(M+6H)^{6+}$, $(M+7H)^{7+}$. The observed mass of INS-647 (6648.33 Da) is nearly identical to that which would be predicted (6646 Da) based on calculation derived from the molecular weight of human insulin conjugated to Alexa Fluor 647. **D)** The affinity (K_i) of unlabeled insulin and insulin-647 for the human insulin receptor determined by scintillation proximity assay-based competitive radioligand binding analysis. Data are reported as geometric mean ± standard error of the mean from n=3 experiments. m/z - mass/charge; RP-HPLC - reversed phase-high performance liquid chromatography.

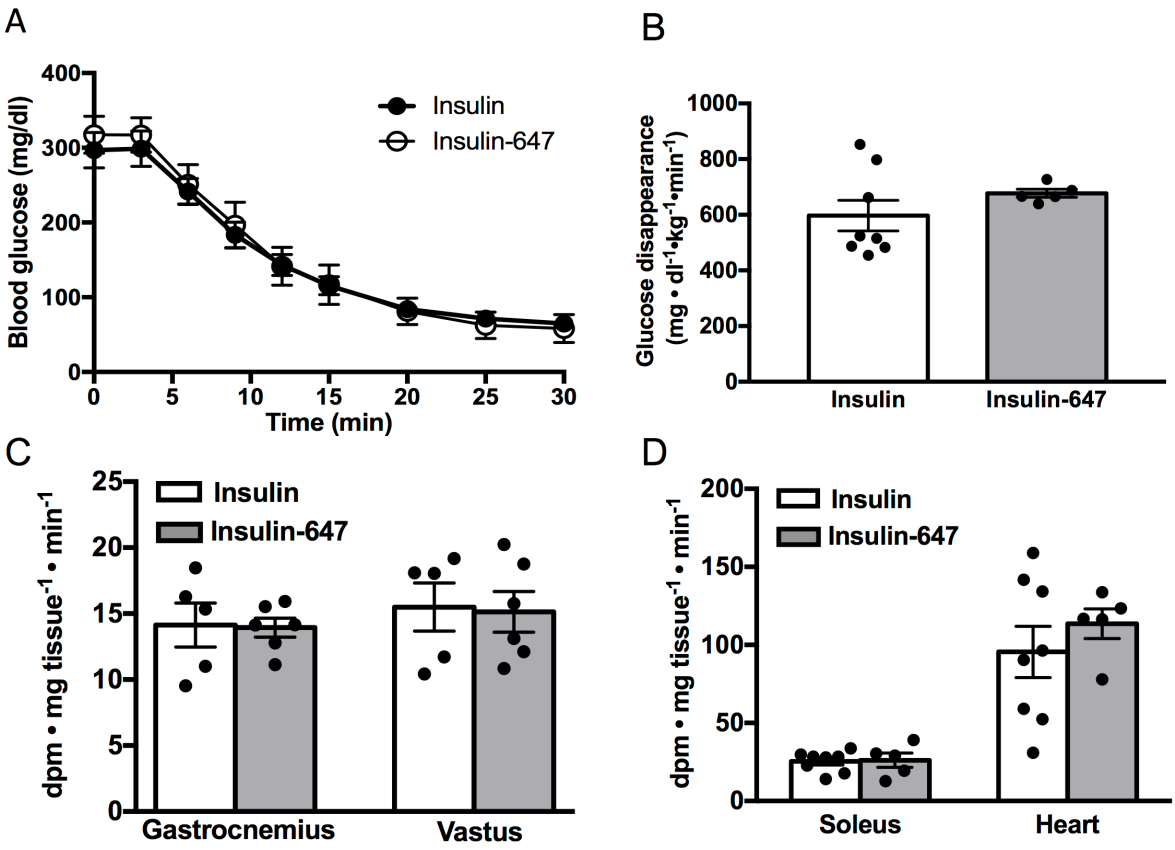

Figure 3.3: Assessment of insulin-647 bioactivity by insulin tolerance test. A) Tail blood glucose levels following a 1 U/kg intravenous bolus of either insulin (n=5) or INS-647 (n=6) in anesthetized mice. **B)** Glucose disappearance is calculated as the rate of blood glucose decrease over the first 15 minutes of the experiment. **C-D)** Accumulation of 2[^{14}C]deoxyglucose in various muscles as an index of muscle glucose uptake. A 13µCi bolus of 2[^{14}C]deoxyglucose was given in conjunction with the insulin or INS-647 bolus in **A**. Groups were compared using unpaired Student's t-test.

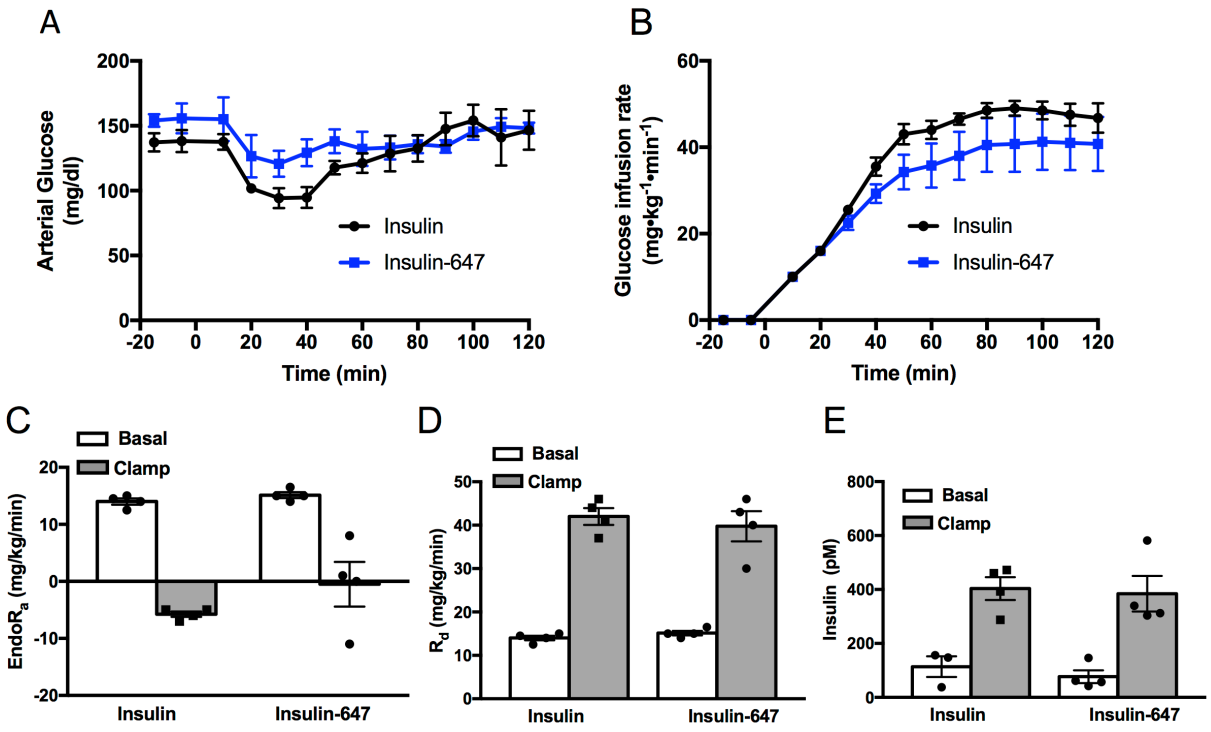

Figure 3.4: Assessment of insulin-647 bioactivity by hyperinsulinemic-euglycemic clamp. **A)** Arterial glucose levels were clamped at ~150mg/dl by variable venous infusion of 50% glucose in mice treated with unlabeled insulin (n=4) or insulin-647 (n=4). **B)** The glucose infusion rate (GIR) required to maintain euglycemia during hyperinsulinemia, a measure of insulin sensitivity. **C,D)** Basal and insulin-stimulated rates of peripheral glucose disposal (R_d) and endgoenous glucose production ($endoR_a$) as determined by steady-state plasma levels of 3[^{3}H]glucose. **E)** Basal and clamp levels of plasma insulin during hyperinsulinemic-euglycemic clamps. Groups were compared using unpaired Student's t-test.

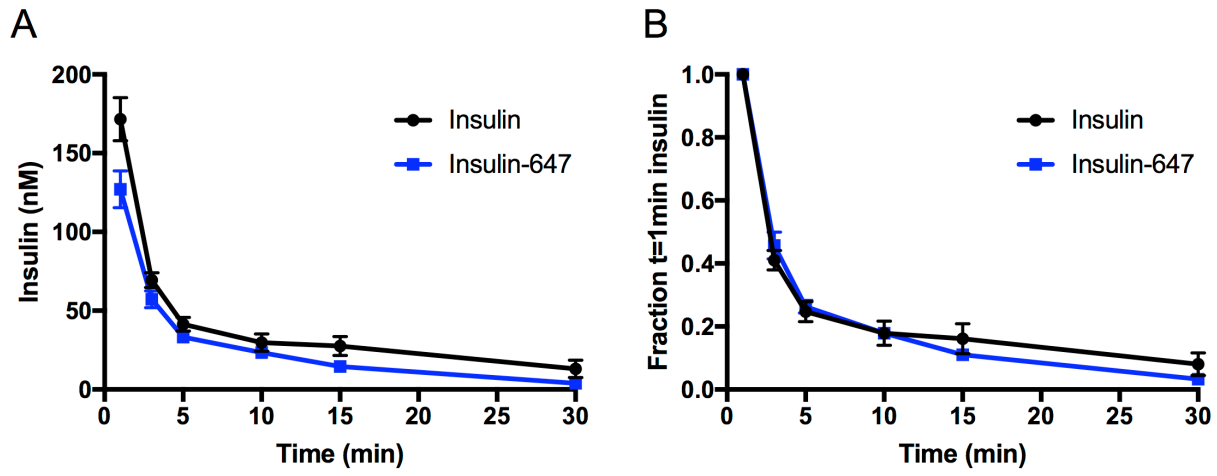

Figure 3.5: Arterial dynamics of insulin-647 and unlabeled insulin. A) Arterial plasma levels of insulin (n=6) and insulin-647 (n=6) following a 4U/kg intravenous bolus. **B)** Data in A normalized to the insulin level at t=1 min.

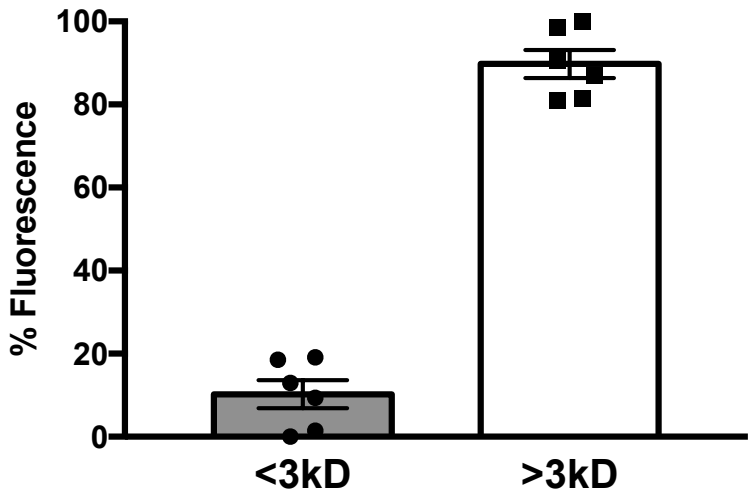

Figure 3.6: *In vivo* stability of insulin-647. Percent of total plasma INS-647 fluorescence that is in a low molecular weight fraction (<3kD) vs. a high molecular weight fraction (>3kD) 30 minutes after an intravenous bolus of INS-647 (n=6 mice). Fluorescence in the <3kD fraction is indicative of Alexa Flour 647 that is separated from INS-647 during an imaging experiment. Fluorescence in the >3kD fraction is intact INS-647.

Intravital microscopy of INS-647

Previous *in vivo* imaging examinations of skeletal muscle vascular function have used thin, translucent muscles such as the cremaster or spinotrapezius (221, 236). We sought to develop a preparation of a representative skeletal muscle that required minimal perturbations to the tissue. Therefore, we chose to study the lateral gastrocnemius muscle because it is a major site of insulin-stimulated glucose disposal. The lateral gastrocnemius fibers are exposed by carefully removing the overlying skin and fascia. The anesthetized mouse can then be simply situated on its side so that the exposed gastrocnemius is positioned against a coverslip embedded in a custom stage mount (**Figure 3.7A**). We then tested whether our gastrocnemius preparation induced an inflammatory response that might affect our measurements of capillary function. *In vivo* imaging of leukocytes and platelets labeled with rhodamine 6G (~90-95% labeling efficiency of leukocytes; **Figure 3.8, A-C**) revealed that very few leukocytes or platelets adhered to capillary walls during the course of the experiment (**Figure 3.7B**). Furthermore, BSA-647 did not leak out from gastrocnemius capillaries (**Figure 3.7C**) as it would during an inflammatory response (237). These results show that our gastrocnemius preparation maintains skeletal muscle capillaries in a near-physiological state.

To measure the rate of trans-endothelial INS-647 transport, it is imperative to be able to resolve the intravascular and interstitial spaces. In order to demarcate the intravascular space, we infused 50μg of a tetramethylrhodamine-labeled 2 megadalton dextran probe (Rho-dex) through an indwelling jugular vein catheter (**Figure 3.9**). Subsequently, the rho-dex is imaged using a confocal microscope (Zeiss LSM 780) to find a suitable region for imaging. After selecting a field of view, a 4U/kg bolus of INS-647 is injected into the mouse through the indwelling

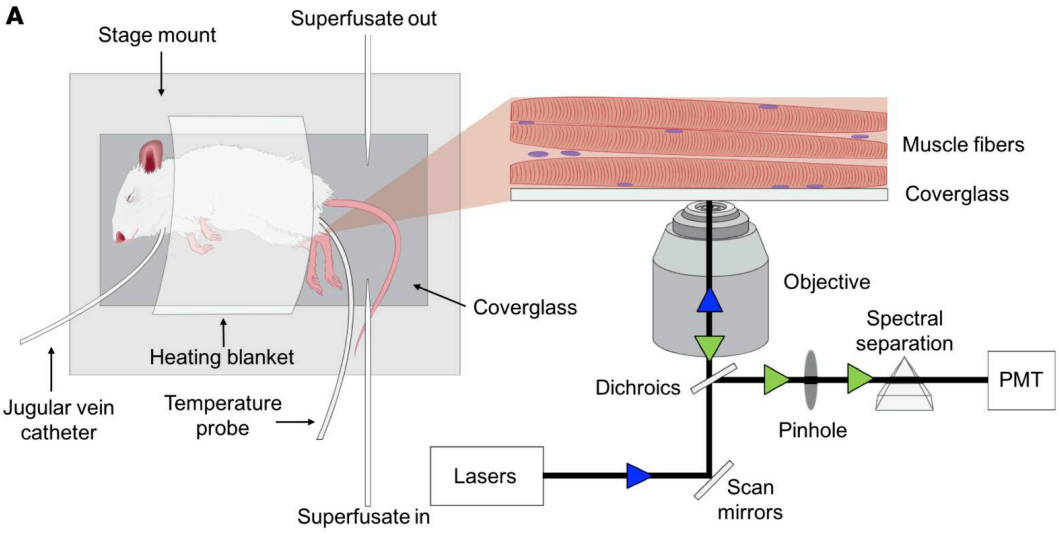
A
Stage mount
Superfusate out
Muscle fibers
Coverglass
Objective
Coverglass
Spectral separation
Heating blanket
Dichroics
PMT
Jugular vein catheter
Temperature probe
Pinhole
Lasers
Scan mirrors
Superfusate in

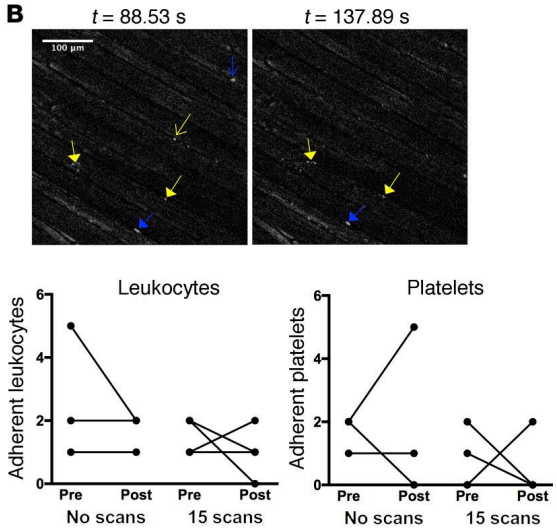
B
t = 88.53 s
t = 137.89 s
100 μm
Leukocytes
Platelets
Adherent leukocytes
Adherent platelets
Pre
Post
No scans
15 scans

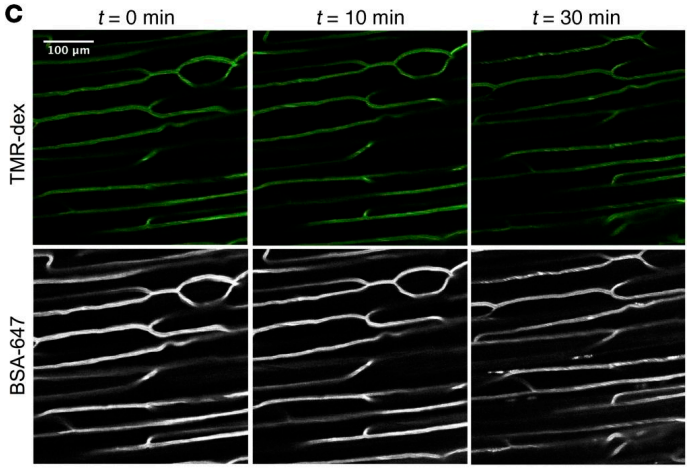
C
t = 0 min
t = 10 min
t = 30 min
100 μm
TMR-dex
BSA-647

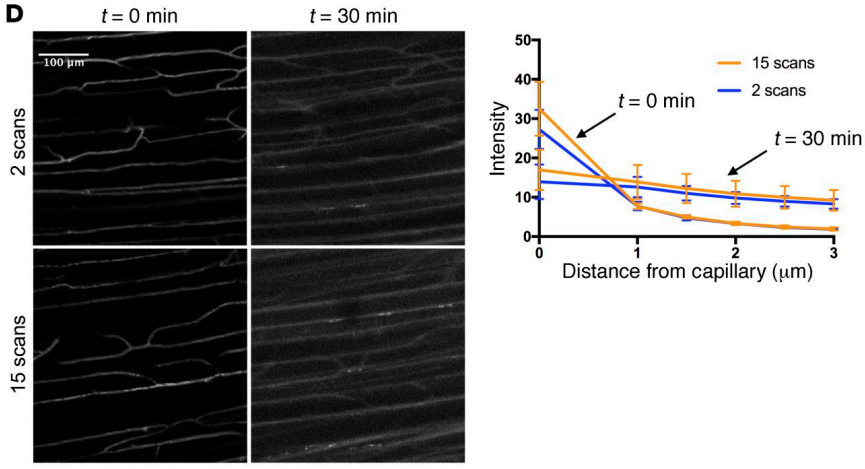
D
t = 0 min
t = 30 min
100 μm
2 scans
15 scans
15 scans
2 scans
t = 0 min
t = 30 min
Intensity
Distance from capillary (μm)

Figure 3.7: A novel gastrocnemius preparation for intravital fluorescence microscopy. A) Schematic showing the setup and mouse preparation for intravital microscopy. The left panel depicts the mouse situated on the stage mount with the necessary accessories. The inset shows a zoomed in view of the exposed gastrocnemius fibers pressed against the coverglass and a diagram of the light path for confocal microscopy. The blue and green arrows indicate incident and emitted light, respectively. **B)** *In vivo* imaging of leukocytes and platelets stained with rhodamine 6G. Background-subtracted representative images show rhodamine-6G+ structures during a typical experiment. Blue arrowheads and blue arrows indicate adherent and non-adherent leukocytes, respectively. Green arrows and arrowheads represent adherent and non-adherent platelets respectively. Graphs show the number of adherent leukocytes and platelets before and after exposure to either no light (No scans; n=3) or the same amount of light used during an insulin imaging experiment (15 scans; n=4). **C)** Imaging of albumin to test the stability of capillaries in the gastrocnemius preparation. Representative images are maximum intensity projections showing 2 megadalton tetramethylrhodamine-dextran (top) and Alexa Fluor 647-conjugated bovine serum albumin (bottom) at the indicated time points following fluorescent albumin injection. **D)** Insulin imaging with different light exposure doses to test for phototoxicity. Representative images are background-subtracted and contrast-enhanced maximum intensity projections showing INS-647 distribution at the indicated time points after 2 scans (top; n=3) or after 15 scans (bottom; n=5-6). Graph shows INS-647 intensity as a function of distance from the capillary at the indicated time points with varying light exposure doses. PMT - photomultiplier tube; TMR-dex - tetramethylrhodamine dextran; BSA-647 - Alexa Fluor 647-labeled bovine serum albumin.

A

%CD45+ R6G+ cells

Replicate	5 min	30 min
a	95.3	89.9
b	94.6	89.2
c	92.3	85.6

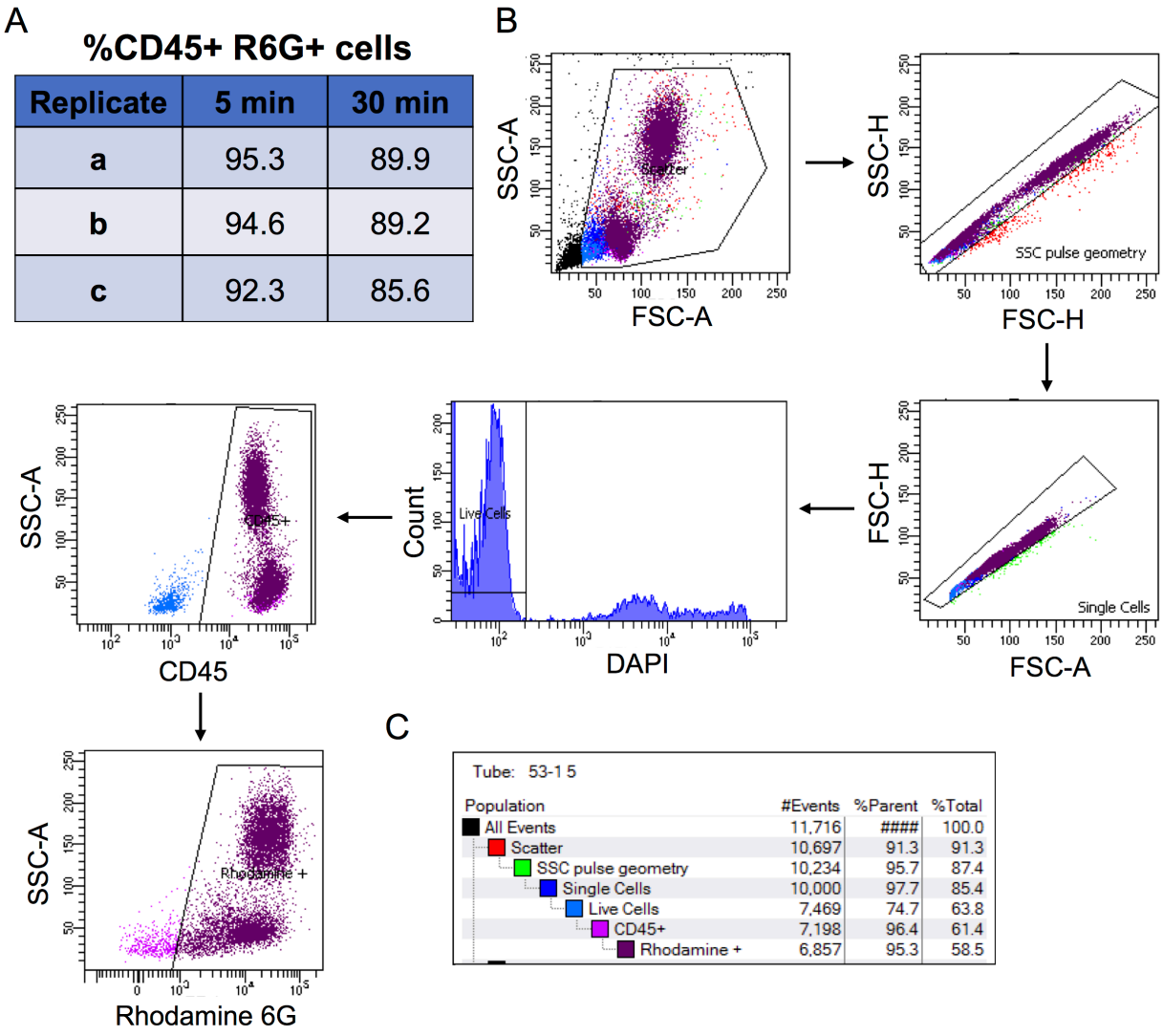

Figure 3.8: Labeling efficiency of leukocytes *in vivo* with rhodamine 6G. A) Table shows the % of live leukocytes that are stained with rhodamine 6G at two time points following rhodamine 6G injection (n=3 mice). **B)** Gating strategy for flow cytometry. In the direction of the arrows, debris were removed by size, doublets were deleted (2x), and dead cells were removed (DAPI). The remaining cells were gated for presence of CD45 to include leukocytes. **C)** Representative table showing the number and percentage of cells counted following each gating step. SSC, side scatter; FSC, forward scatter; A, area; H, height, R6G, rhodamine 6G.

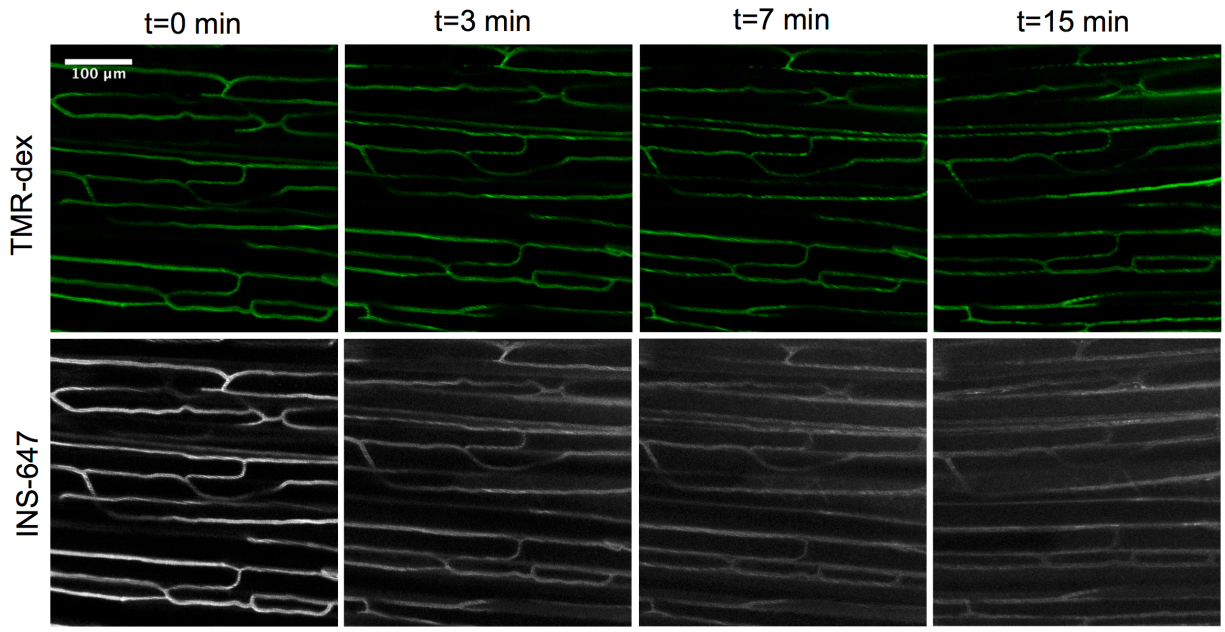

Figure 3.9: Insulin-647 imaging. Representative images (maximum intensity projections) of an INS-647 imaging experiment. The top panel shows 2 megadalton tetramethylrhodamine-dextran and the bottom panel shows INS-647 at the indicated time points following INS-647 injection.

catheter. 3D confocal images of both rho-dex and INS-647 are acquired every minute for the first 10 minutes and then at 12.5, 15, 20, and 30 minutes thereafter (**Figure 3.9**).

Imaging parameters (i.e. laser power, sampling frequency) were chosen to minimize both the photobleaching of INS-647 and phototoxicity caused by irradiating live tissue with visible light (238). We set our imaging parameters so that photobleaching would account for at most a ~5-8% loss in INS-647 fluorescence intensity during an experiment (**Figure 3.10, A-C**). Furthermore, the amount of light used during an INS-647 imaging experiment did not alter the intravascular or extravascular distribution of INS-647, (**Figure 3.7D**) accumulation of 2[^{14}C]DG, (**Figure 3.11**), or leukocyte adhesion (**Figure 3.7B**). These findings suggest that our experimental imaging conditions do not induce any detectable photodamage. Finally, the conjugation of Alexa Fluor 647 to insulin caused a very slight red shift in its emission spectrum (**Figure 3.10D**). However, this shift was not significant enough to alter the excitation or detection strategy for INS-647 compared to Alexa Fluor 647. In summary, our quantitative, intravital image acquisition design allows us to collect spatial and temporal information regarding the levels of rho-dex and INS-647 in the gastrocnemius of live mice without causing any major perturbations to the tissue.

Quantitative Image Analysis

To estimate endothelial transport parameters, the levels of INS-647 as a function of time in both intravascular and interstitial spaces must be measured. To obtain this information, we developed an Otsu-based (224) automated vascular and interstitial segmentation algorithm using ImageJ (**Figure 3.12A**; see **Research Materials and Methods**). This algorithm is used to generate intensity-time profiles of INS-647 in the intravascular and interstitial spaces (**Figure**

3.12B). To test the performance of our vascular segmentation algorithm we compared it against a manual segmentation of 192 images. We found that while our algorithm was able to capture most of the vascular spaces outlined manually, it overestimated the area of vascular space by ~45% (**Figure 3.13, A and B**). While this led to a slight underestimation of INS-647 levels (**Figure 3.13, C and D**), it did not significantly alter any transport parameter estimates (**Figure 3.13, E-H**) nor did it change model-independent efflux parameters (**Figure 3.13I**). Because the method of image segmentation did not affect the final results, we think that the benefits of automating image analysis (enhanced reproducibility, removal of user bias, faster processing speeds) outweigh the small reduction in segmentation accuracy.

After obtaining the capillary and interstitial INS-647 curves, we sought to quantify the endothelial transport parameters that control the movement of INS-647 from the plasma to the interstitial space. The transport parameters of interest depend on the mechanism by which a molecule traverses the continuous endothelium. For instance, if INS-647 crosses the endothelium by a receptor-mediated process, as has been hypothesized for insulin (150, 239), then the parameters of interest are the Michaelis-Menten parameters, K_m and V_{max}. If instead INS-647 leaks out of capillaries through inter-endothelial junctions, then the parameters of interest are either permeability of the vessel to INS-647 (diffusion), or the mass transfer coefficient (fluid-phase transport).

To make this determination, we fit our experimental data to 3 different mathematical models. As the base model, we described INS-647 movement within the interstitial space by the diffusion equation and assumed 1^{st} order removal of INS-647 from this space (**Figure 3.14;** see **Research Materials and Methods** for extended equations). A pertinent aspect of the model is the boundary condition describing movement of INS-647 from the plasma to the interstitial space

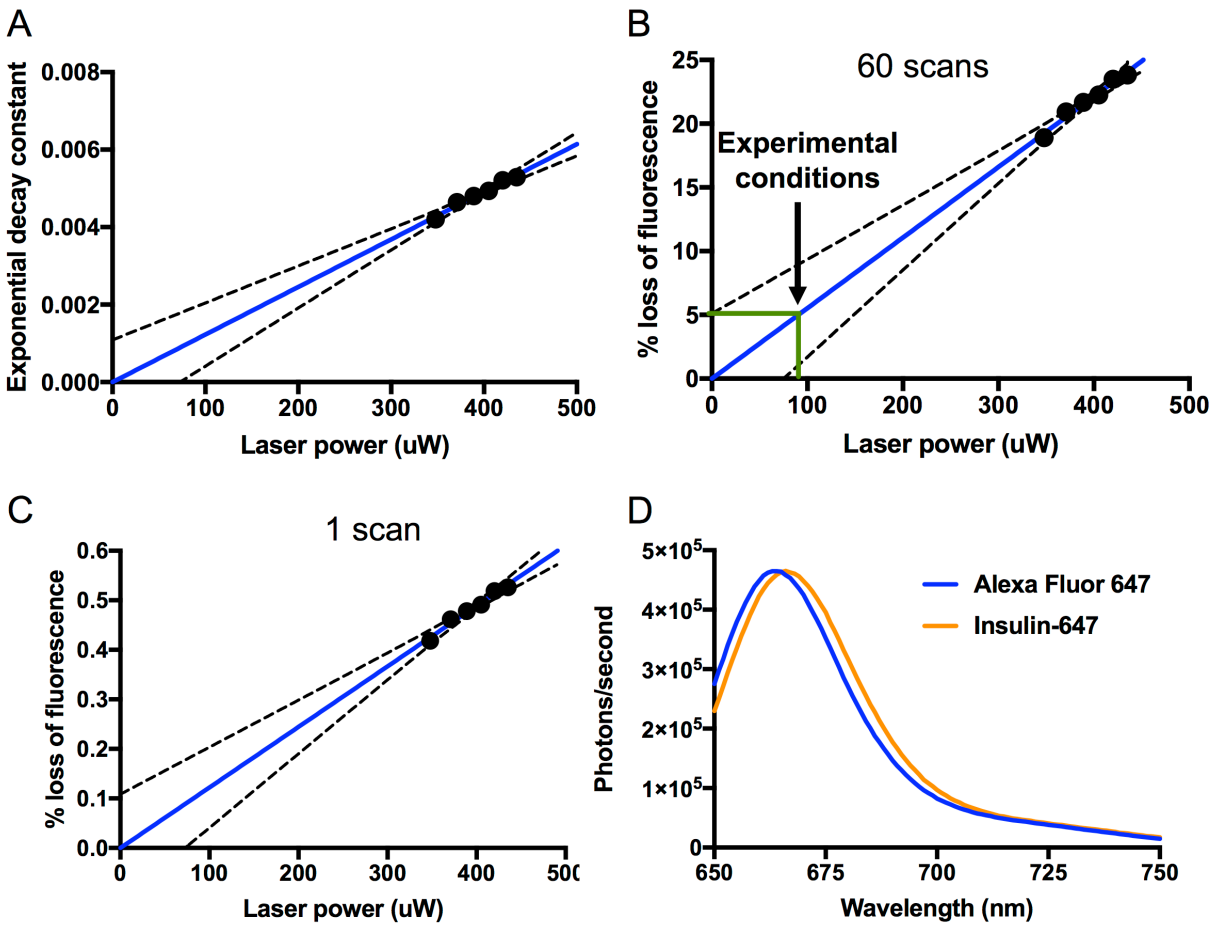

Figure 3.10: Photostability and optical properties of insulin-647. A) The rate of decay of insulin-647 fluorescence as a function of incident laser power. The blue line shows the linear regression of these two variables and the dotted lines show the 95% confidence intervals of the regression. **B)** Percent loss of fluorescence after 60 scans, the same number of scans as during an insulin imaging experiment. The green lines indicate the maximum usable laser power at which the acceptable photobleaching rate (5%) is achieved. **C)** Percent loss of fluorescence per scan. **D)** Emission spectra of equimolar amounts of Alexa Fluor 647 or insulin-647 after excitation with 633nm light.

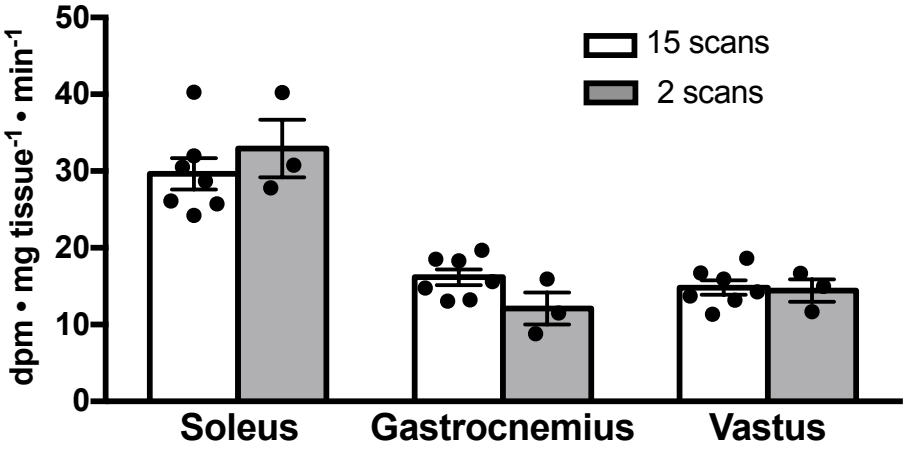

Figure 3.11: Effect of varying light exposure on insulin-stimulated muscle glucose uptake. Accumulation of 2[^{14}C]deoxyglucose in various tissues during insulin-647 imaging with either 2 (n=3) exposures or 15 exposures (n=7).

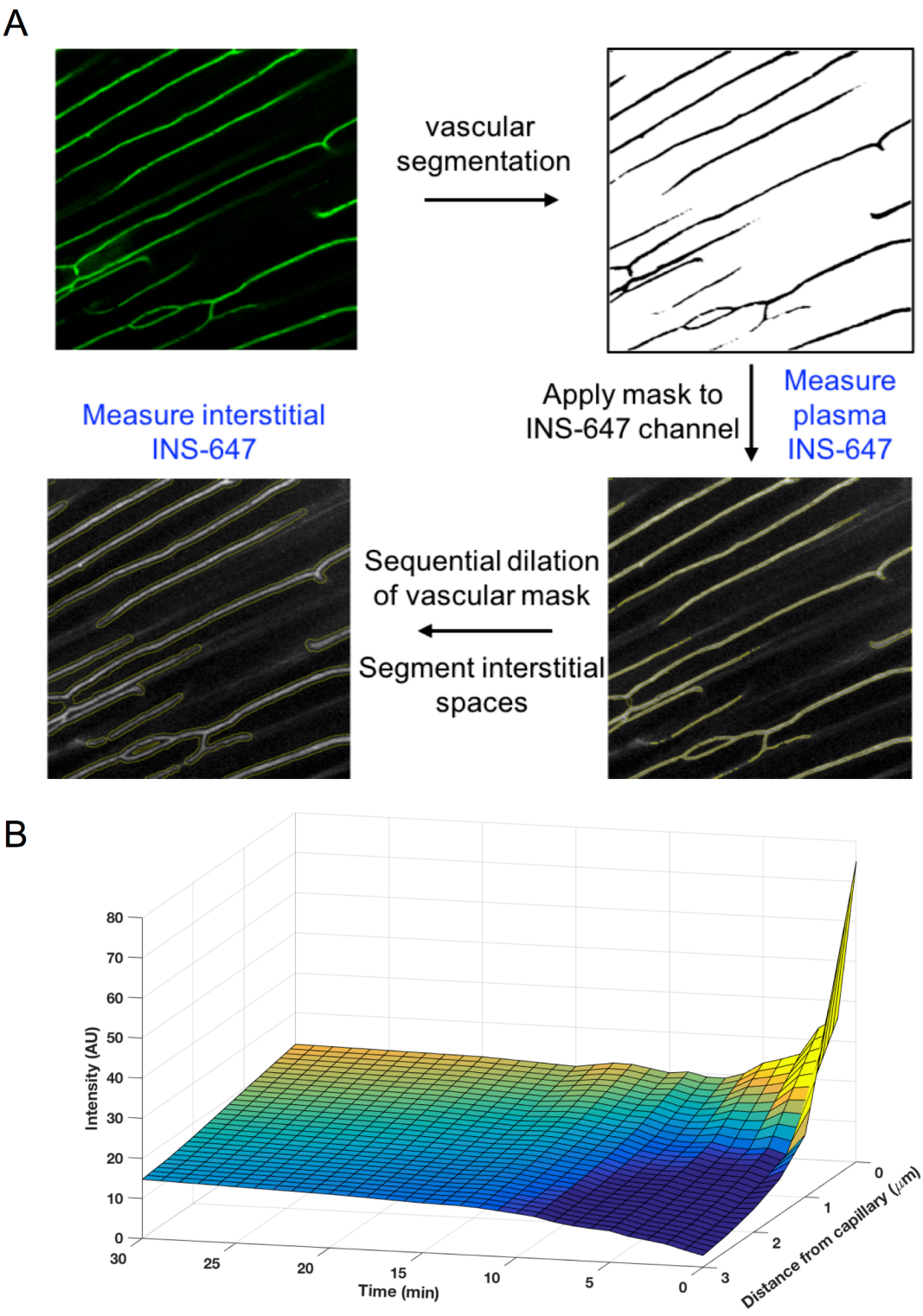

Figure 3.12: Insulin-647 image analysis. A) General workflow for image analysis. **B)** Representative 3D plot of INS-647 intensity (z-axis) as a function of distance from the capillary (y-axis) and time (x-axis).

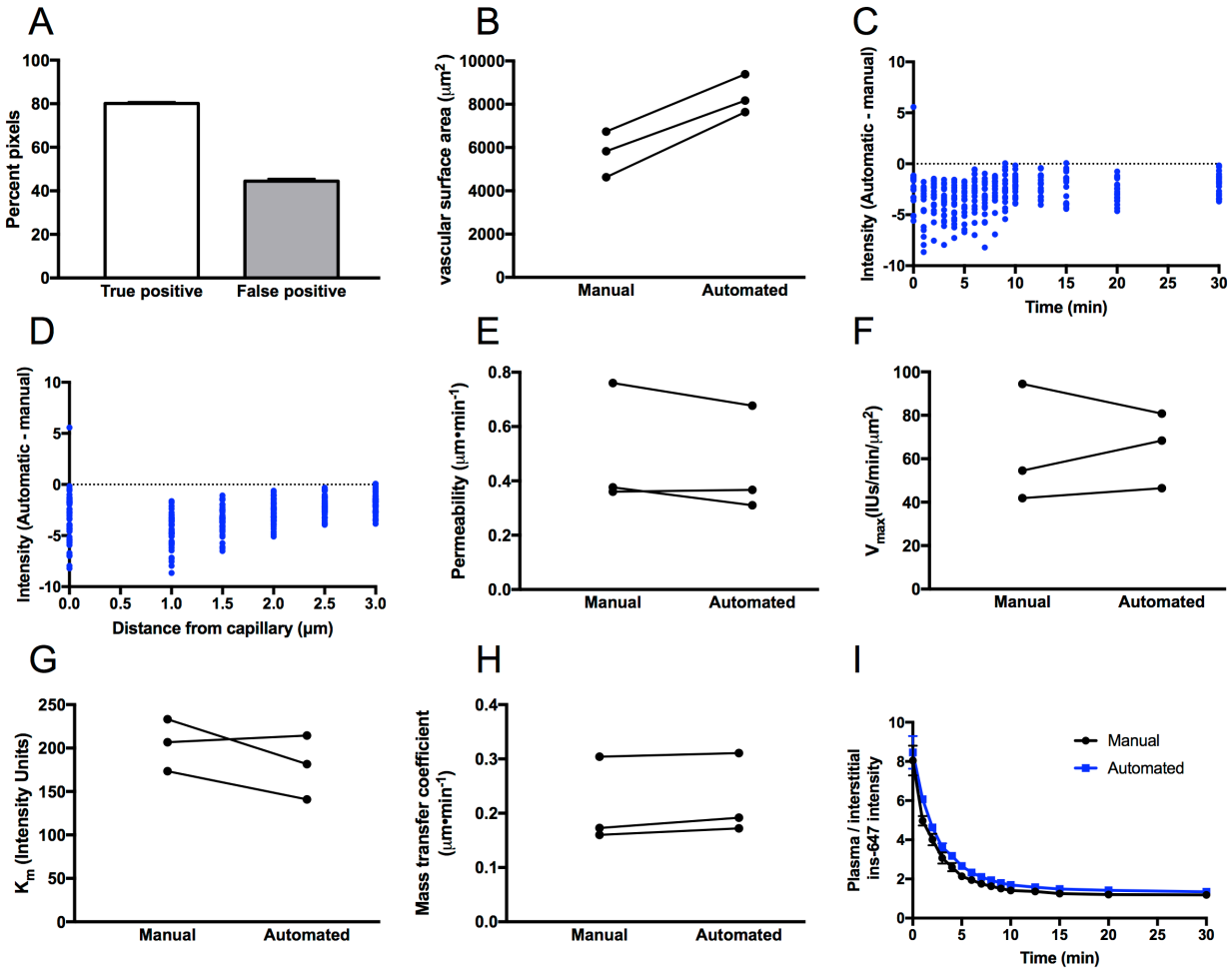

Figure 3.13: Performance of an automated vascular segmentation algorithm. The segmentation performance of an automated algorithm was compared against manual segmentation for all images from n=3 experiments. **A)** Percent of manually outlined pixels that were also outlined by the algorithm (True positive) and percent of pixels outlined by the algorithm that were not outlined by the manual segmentation (False positive). **B)** Total vascular surface area segmented by manual and automated segmentation. **C,D)** Difference in INS-647 intensity as a function of **C)** time or **D)** distance from the capillary when using automated versus manual segmentation. **E-H)** Best fit model parameter estimates using manual or automated segmentation. **I)** Ratio of plasma to interstitial INS-647 intensity as a function of time following ins-647 injection using manual and automated segmentation.

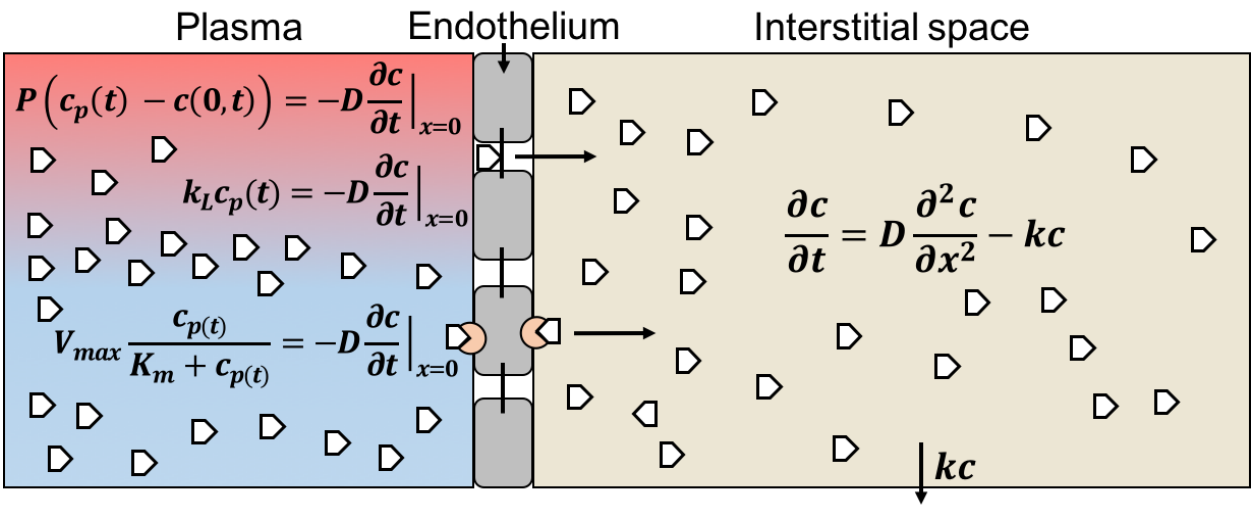

Figure 3.14: Mathematical model of trans-endothelial insulin efflux. Schematic of the mathematical models used to estimate endothelial transport parameters. White pentagons represent insulin. In the plasma compartment (red/blue), insulin is shown exiting the capillary through interendothelial junctions or by a receptor-mediated process. The equations used to describe these behaviors are the diffusion equation (top), fluid-phase transport equation (middle) and Michaelis-Menten equation (bottom). See **Research Materials and Methods** for details regarding equations and symbols.

We described the boundary behavior of INS-647 with equations describing either diffusion (240), fluid-phase transport (241), or Michaelis-Menten kinetics. We then solved the diffusion equation with the different boundary conditions to generate models that described these potential mechanisms of INS-647 transport. Experimental data were fit to these models using weighted non-linear least squares regression in MATLAB. This allows us to estimate the following parameters: permeability for the diffusion model, mass transfer coefficient for the fluid-phase transport model, and K_m and V_{max} for the Michaelis-Menten model. All models allowed for estimation of the interstitial diffusion coefficient and removal constant of INS-647. Finally, the goodness of fit of the experimental data to the models was determined by analyzing the sum of the weighted residuals.

Method validation

The rate of trans-endothelial efflux of molecules decreases with increasing molecular size (242). To validate our measurements and demonstrate that we can reproduce this phenomenon with our technique, we imaged fluorescently-labeled dextrans of sizes 3kDa and 10kDa and INS-647, which is 6.6kDa (**Figure 3.15A**). Visually, one can see that the smaller molecules leak out of capillaries much faster than the larger ones (**Figure 3.15A**). Mathematical modeling showed that the extravasation of these probes occurred by fluid-phase transport (**Figure 3.16, A-D and Chapter IV**). Mass transfer coefficient estimates show that efflux rates decrease as probe molecular weight increases (**Figure 3.15B**). Furthermore, the kinetics of capillary / interstitial gradient dissipation were slower with increasing molecular weight, as predicted (**Figure 3.15C**). Therefore, we are confident in the accuracy of our measurements and our ability to resolve differences in trans-endothelial efflux parameters.

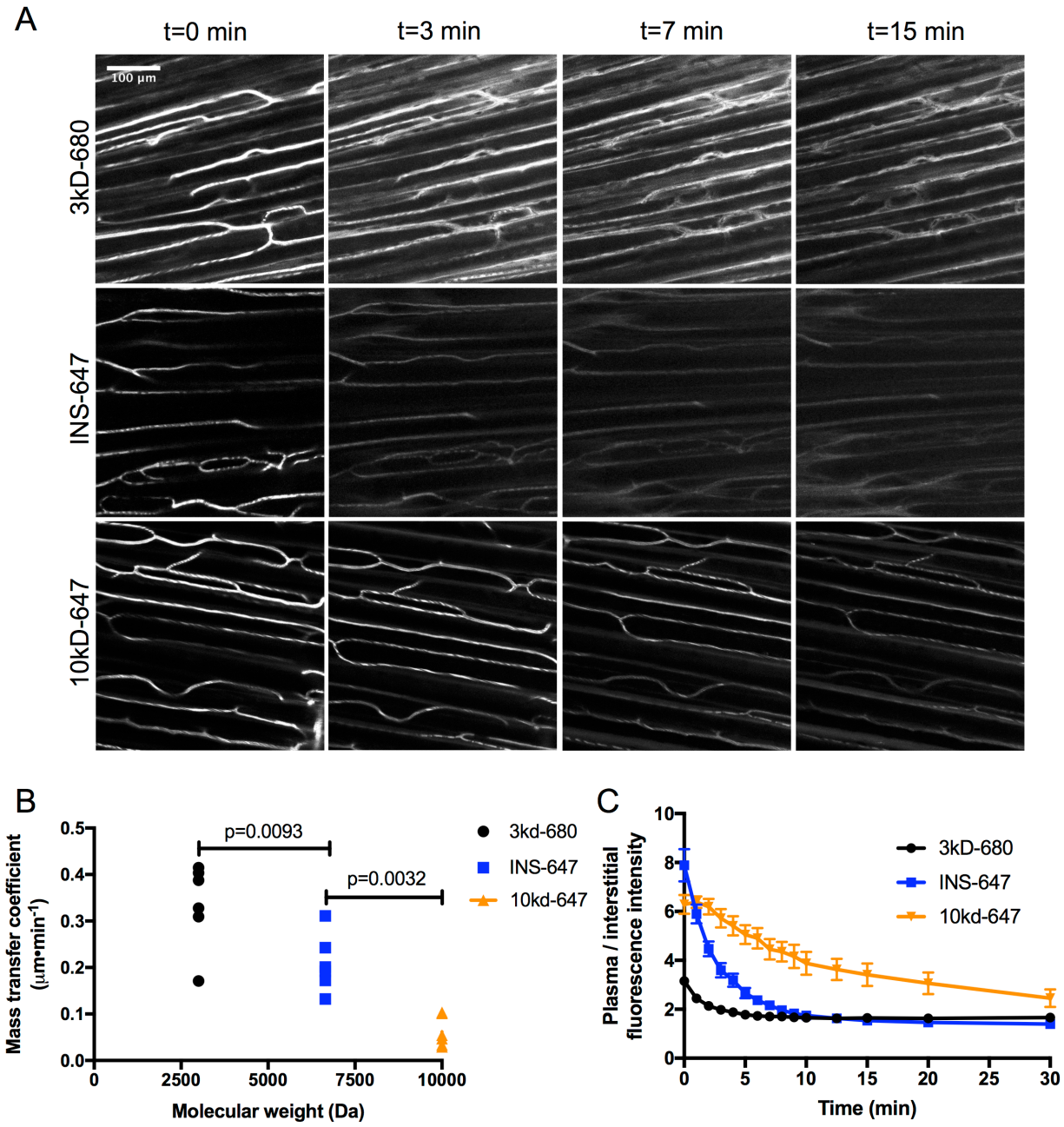

Figure 3.15: Validation of intravital fluorescence microscopy for resolving differences in trans-endothelial molecular efflux. A) Representative images (max intensity projections) of 3kD dextran-Alexa Fluor 680 (n=6), INS-647 (n=6), and 10kD dextran-Alexa Fluor 647 (n=6) distribution at the indicated time points following injection. **B)** Best-fit model estimates of the mass transfer coefficient for the probes in **A** displayed as a function of molecular weight. **C)** Ratio of plasma/interstitial fluorescence intensity as a function of time following injection for the indicated probes. Groups were compared using ANOVA with a Bonferroni correction for multiple comparisons.

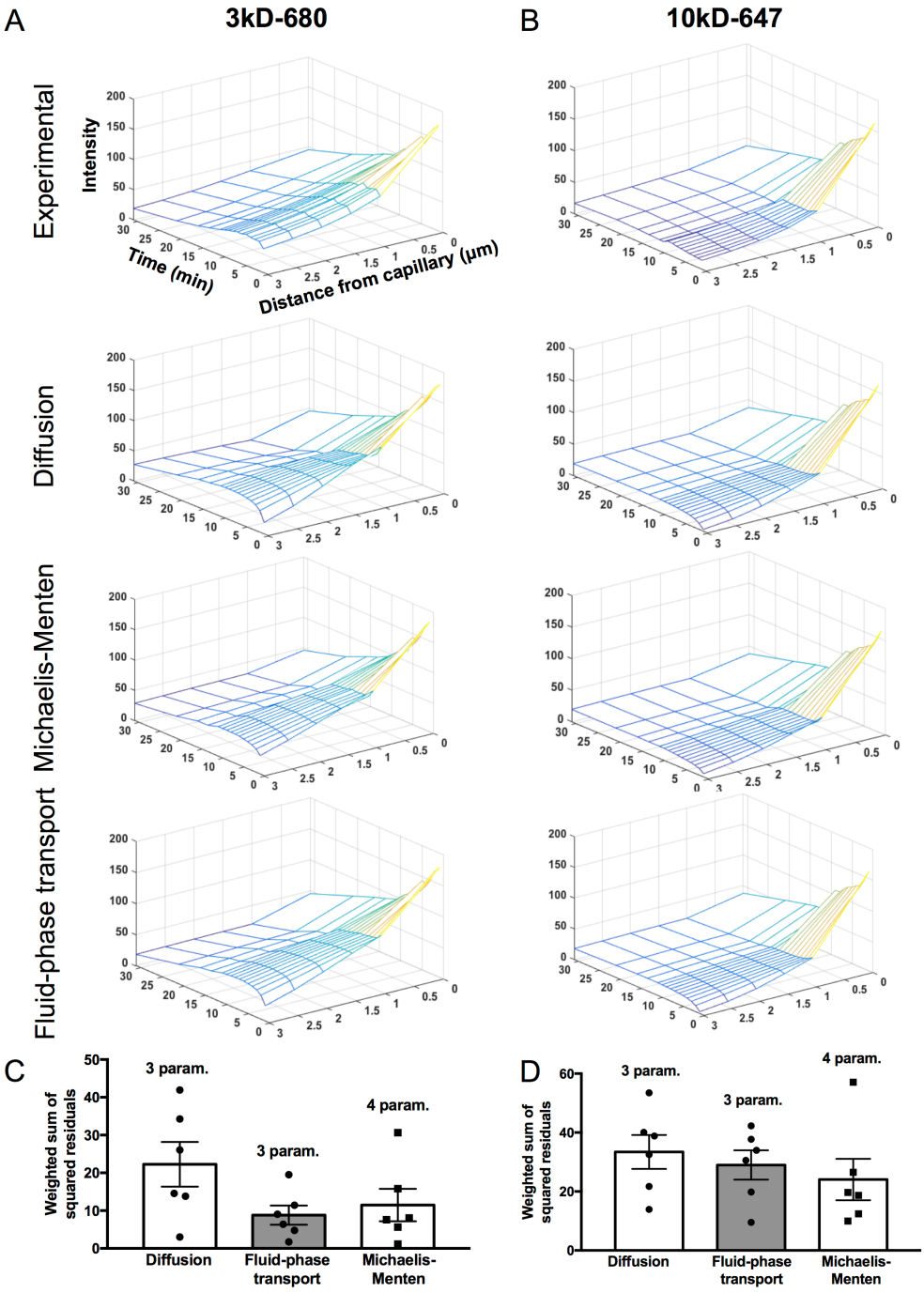

Figure 3.16: Model fit analysis of dextran imaging data. Plots show experimental data and "Diffusion," "Michaelis-Menten," or "Fluid-phase transport" model simulations for **A)** 3kD dextran-Alexa Fluor 680 and **B)** 10kD dextran-Alexa Fluor 647 probe. **C,D)** Weighted sum of squared residuals for each of the different model simulations as compared to the experimental data for **C)** 3kD dextran-Alexa Fluor 680 (n=6) and **D)** 10kD dextran-Alexa Fluor 647 (n=6). The number of variable parameters are indicated above the bar for each model. Param – parameters.

Discussion

We have developed an intravital imaging technique to measure to the flux of insulin across the endothelium of individual skeletal muscle capillaries. To accomplish this, we 1) synthesized a fluorescent, bioactive insulin probe, 2) developed a novel gastrocnemius preparation 3) developed an automated vascular segmentation algorithm and 4) fit data to mathematical models to estimate transport parameters. Notably, our measurement of the steady-state plasma/interstitial insulin gradient with intravital microscopy is similar to measurements made by both lymph sampling (157) and microdialysis (137). This observation supports the accuracy of our method. Our *in vivo* imaging technique makes major advances in other key areas. INS-647 is a suitable fluorescent insulin probe in that it is homogenous, fully bioactive, insensitive to changes in pH, photostable, and stable in the *in vivo* environment. This is an improvement over the use of FITC-insulins, which do not bind the insulin receptor with the same affinity as insulin, are very sensitive to changes in pH, and spectrally overlap with endogenous tissue fluorescence. Finally, our novel gastrocnemius preparation does not require any exteriorization or major manipulation of the tissue and maintains the skeletal muscle capillaries in a near-physiological state.

CHAPTER IV

INSULIN EXITS SKELETAL MUSCLE CAPILLARIES BY FLUID-PHASE TRANSPORT

Aims

As discussed in the **Introduction**, there is disagreement regarding the mechanism by which insulin is transported across the skeletal muscle capillary endothelium. The most commonly accepted hypothesis is that insulin is transported across the endothelium by a saturable, insulin receptor-mediated mechanism. However, there have been no direct measurements of trans-endothelial insulin transport in skeletal muscle capillaries *in vivo*. The aim of **Chapter IV** is to determine the mechanism of trans-endothelial insulin transport in skeletal muscle capillaries *in vivo*. To accomplish this goal, we will utilize the intravital microscopy technique described in **Chapter III** combined with mathematical modeling and pharmacological interventions.

Results[*]

Mathematical modeling: Trans-endothelial INS-647 transport data are best described by a fluid-phase transport model

To determine the mechanism by which insulin transits the endothelium, we initially fit our experimental INS-647 imaging data (**Figure 4.1A**) to models describing either diffusion, fluid-phase transport, or Michaelis-Menten kinetics. Both visual (**Figure 4.1, B-D**) and residual

[*]These results have been published in: Williams IM, Valenzuela FA, Kahl SD, Ramkrishna D, Mezo AR, Young JD, Wells KS, Wasserman DH. Insulin exits skeletal muscle capillaries by fluid-phase transport. *J Journal of Clinical Investigation* 2018 Feb 1; 128(2):699-714. PMID: 29309051.

(**Figure 4.1E)** analysis of best-fit model simulations revealed that INS-647 transport kinetics fit the fluid-phase transport and Michaelis-Menten models better than the diffusion model. Therefore, we rejected the diffusion model. We then compared the fluid-phase transport model to the Michaelis-Menten model. The INS-647 imaging data fit the fluid-phase transport model slightly better than the Michaelis-Menten model (weighted sum of squared residuals: 81.6 fluid-phase transport vs. 88.0 Michaelis-Menten). Furthermore, the fluid-phase transport model contains one less variable parameter than the Michaelis-Menten model. Finally, the estimate of the Michaelis constant, K_m, (226 intensity units; **Figure 4.2**) is twofold higher than INS-647 levels ever reach in the capillary plasma. This indicates that the Michaelis-Menten model essentially predicts a linear relationship between capillary INS-647 and INS-647 transport rates. This relationship is more compatible with fluid-phase transport than a receptor-mediated process. A true receptor-mediated process would be expected to have a K_m that is in the same range as the plasma levels of INS-647. Therefore, based on goodness of fit, the principle of parsimony, and the reasonability of parameter estimates we rejected the Michaelis-Menten model in favor of the fluid-phase transport model. The best-fit fluid-phase model parameter estimates are shown in **Figure 4.1F**. The decision to reject the Michaelis-Menten model was substantiated by results described in the following section.

To test whether the changing levels of glucose or insulin had effects on insulin efflux kinetics, we modeled temporal subsets of our data. Namely, we modeled data from t = 0 to either t = 5, 7, 10, 12.5, 15, 20, or 30 mins (**Figure 4.3**) to determine whether the mass transfer coefficient estimate varied at these time points. We found that the mass transfer coefficient estimate did not change when restricting analysis to earlier time points, although the variability in the estimate did increase (**Figure 4.3**). This suggests that the mass transfer coefficient is

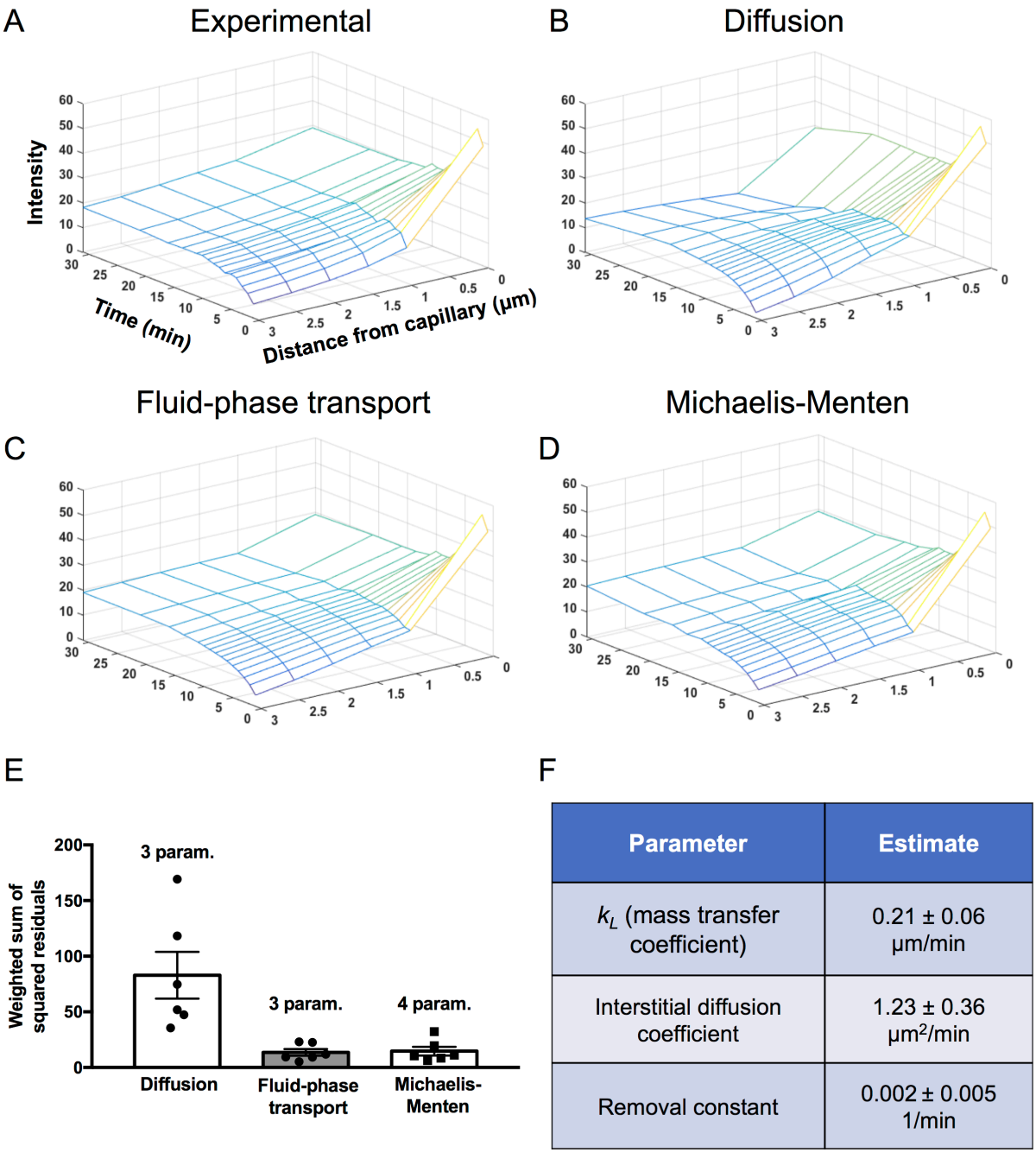

Parameter	Estimate
k_L (mass transfer coefficient)	0.21 ± 0.06 μm/min
Interstitial diffusion coefficient	1.23 ± 0.36 μm^2/min
Removal constant	0.002 ± 0.005 1/min

Figure 4.1: Mathematical modeling predicts that insulin exits skeletal muscle capillaries by fluid-phase transport. A) Data from an INS-647 imaging experiment. **B-D)** Results from fitting experimental INS-647 imaging data to mathematical models describing diffusion, fluid-phase transport, or Michaelis-Menten transport kinetics. Plots are model simulations based on best-fit parameter estimates. **e)** Weighted sum of squared residuals for each of the different model simulations as compared to the experimental data for a group of n=6 mice. The number of variable parameters are indicated above the bar for each model. **f)** Best-fit fluid-phase transport model parameter estimates for a cohort of n=6 mice. Data are mean ± SEM. Param - parameters.

Parameter	Estimate
K_m	222.1 ± 25.8 IU
V_{max}	77.2 ± 13.5 IU/min/μm^2
Interstitial diffusion coefficient	1.64 ± 0.16 μm^2/min
Removal constant	0.056 ±0.003 1/min

Figure 4.2: Michaelis-Menten model parameter estimates. A) Best-fit Michaelis-Menten model parameter estimates for a cohort of n=6 mice. Data are mean ± SEM. K_m - substrate concentration at which the reaction rate is half of V_{max}. V_{max} – maximum reaction rate.

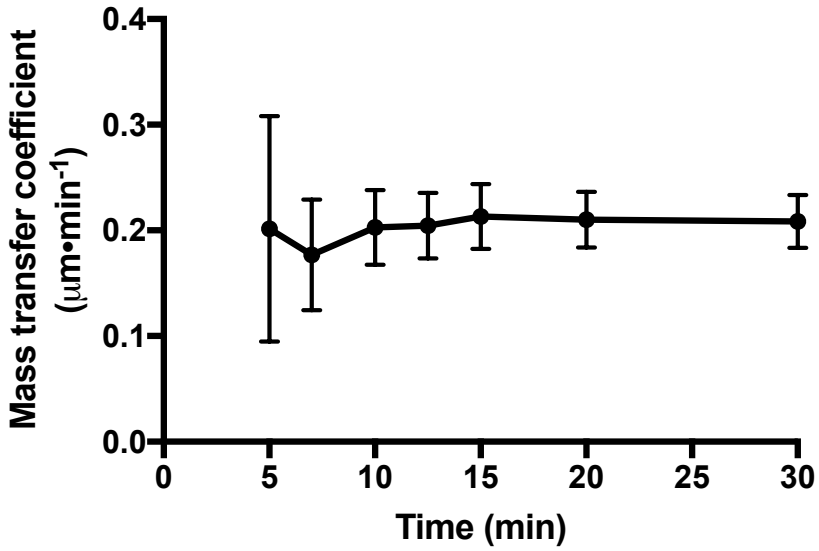

Figure 4.3: Temporal stability of the mass transfer coefficient. Best-fit mass transfer coefficient estimates from temporal subsets of INS-647 imaging experiments (n=6 mice). The x-axis represents the final time point included in subsequent mathematical modeling.

relatively constant over the course of experiment. Because insulin and glucose change over the course of the experiment while the mass transfer coefficient remains stable, this implies that the mass transfer coefficient is independent of glucose and insulin levels. Moreover, these data provide a foundation for shortening the data acquisition time window in future experiments.

Trans-endothelial insulin transport is non-saturable and does not require the insulin receptor

To test the model prediction that insulin efflux is not receptor-mediated, we treated mice with S961, a peptide insulin receptor antagonist that has nearly the same affinity for the insulin receptor as insulin (243). 10 minutes prior to the INS-647 bolus, mice were treated with 168 nmol/kg of S961 (7-fold molar excess over insulin). Subsequently, *in vivo* imaging of INS-647 was performed as described above. S961 effectively blocked both the insulin-induced lowering of blood glucose (**Figure 4.4A**) and insulin-stimulated muscle 2[^{14}C]DG accumulation (**Figure 4.4B**), suggesting that insulin receptors were successfully inhibited. However, we found that S961 had no effect on insulin transport kinetics (**Figure 4.5A**). Namely, S961 had no effect on either the mass transfer coefficient estimate (**Figure 4.5B**), the dissipation of the capillary / interstitial insulin gradient following INS-647 injection (model-independent parameter; **Figure 4.5C**) nor the capillary and interstitial behavior of INS-647 (**4.6A-D**). These findings demonstrate that the insulin receptor does not mediate the transit of insulin across the capillary wall in skeletal muscle.

We then tested whether the movement of insulin across the endothelium was saturable. To do this, we treated mice with either 0.5U/kg INS-647, 1U/kg INS-647, 2U/kg INS-647, 4U/kg INS-647, 4U/kg INS-647 and 4U/kg unlabeled insulin or 4U/kg INS-647 and 12U/kg of

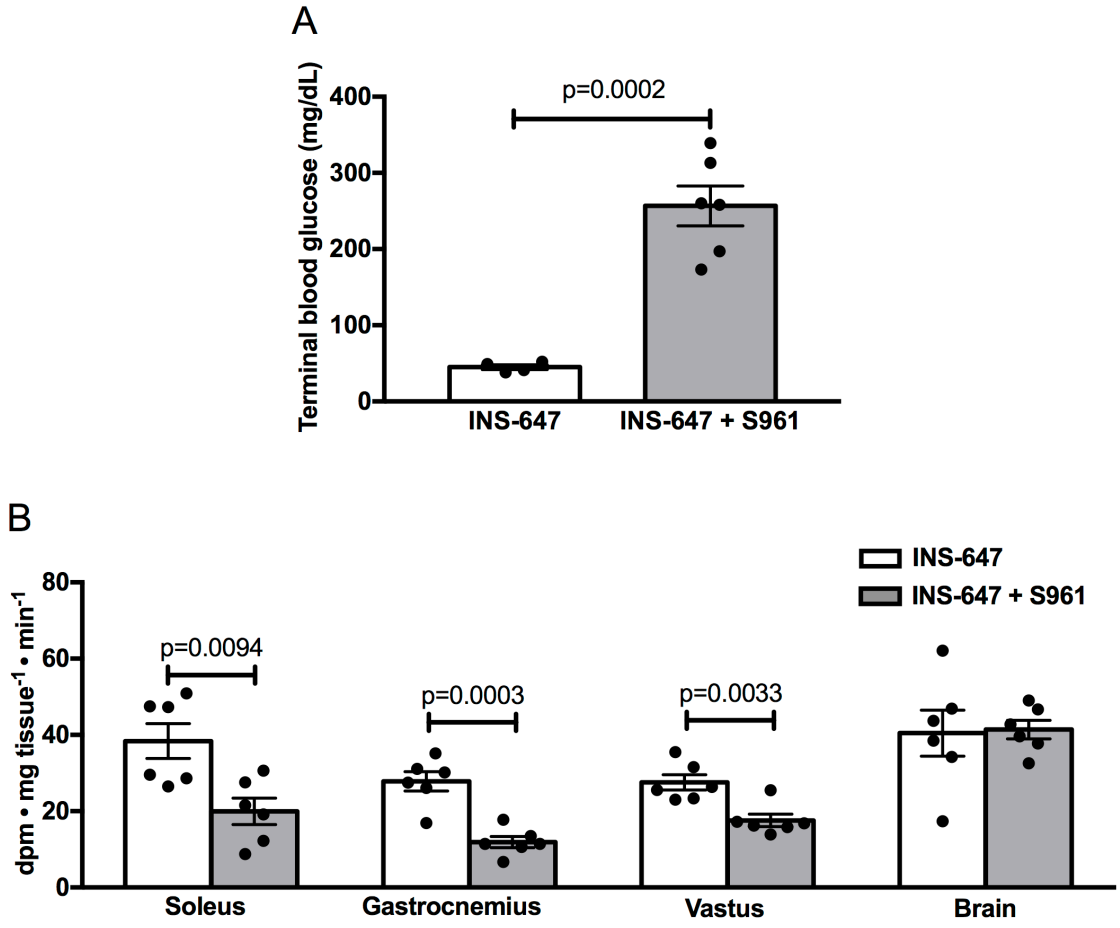

Figure 4.4: Effects of S961 on insulin-stimulated glucose kinetics. A) Tail vein blood glucose levels following an INS-647 imaging experiment in mice treated either with a 4U/kg INS-647 bolus alone (INS-647; n=4) or with an insulin receptor antagonist followed by the 4U/kg INS-647 bolus (INS-647 + S961; n=6). **B)** Accumulation of 2[^{14}C]deoxyglucose in various tissues during INS-647 imaging in mice treated with (INS-647 + S961; n=6) or without (INS-647; n=6) the insulin receptor antagonist. Groups were compared using unpaired Student's t-test.

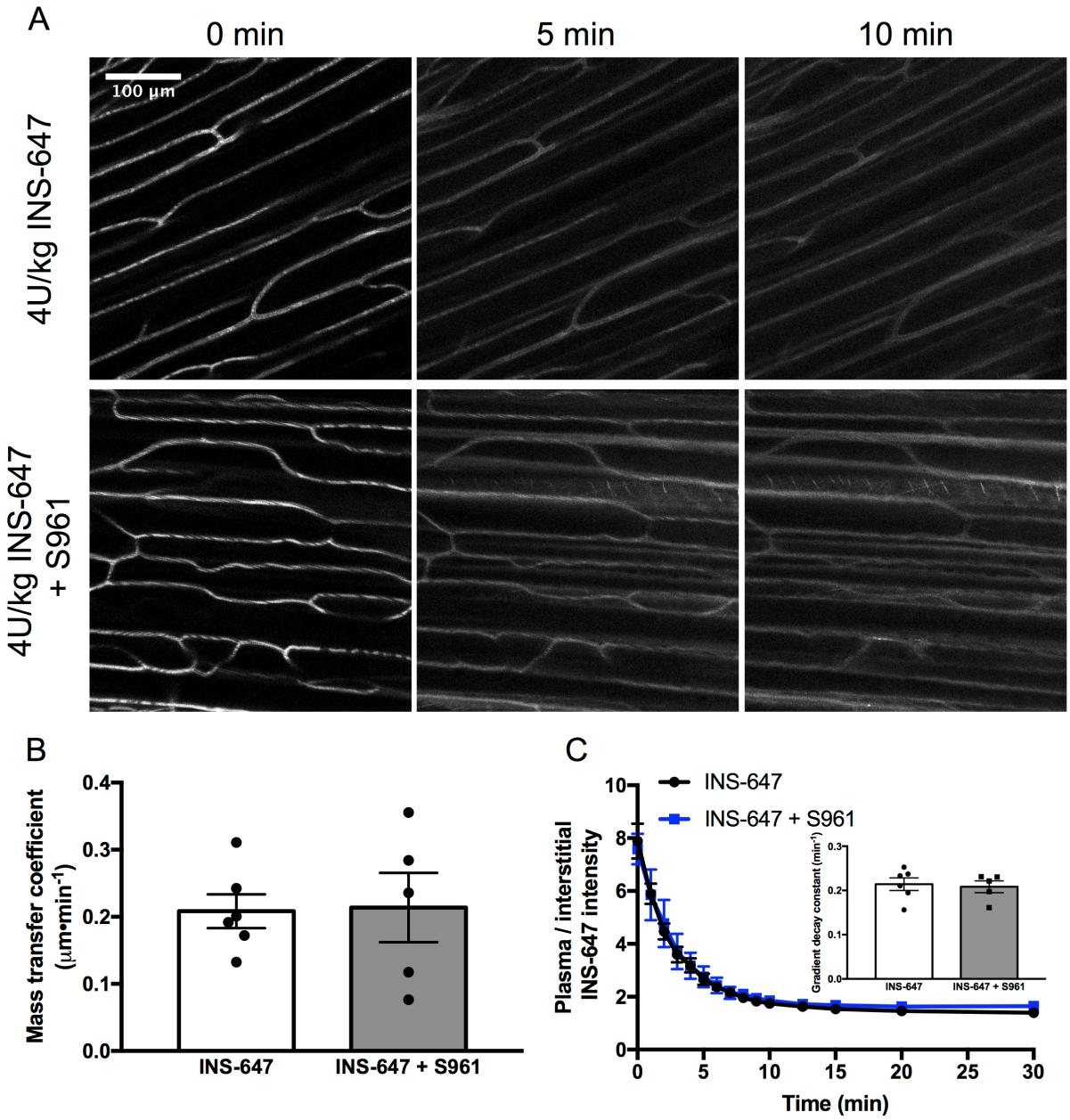

Figure 4.5: Trans-endothelial insulin efflux does not require the insulin receptor. A) Representative INS-647 images (maximum intensity projections) from mice pre-treated either with (4U/kg INS-647 + S961; 2nd from top) or without (INS-647 (4U/kg); top) an insulin receptor antagonist. **B)** Best-fit fluid-phase transport model estimates of the mass transfer coefficient in mice treated with (INS-647 + S961; n=5) and without (INS-647; n=6) the insulin receptor antagonist. **C)** The ratio of plasma to interstitial INS-647 as a function of time following injection. Interstitial INS-647 is defined as the average INS-647 intensity at 1-3µm from the capillary wall. Inset shows the exponential decay constant of the plasma to interstitial ratio, a model-independent descriptor of insulin efflux. Groups were compared using Student's t-test.

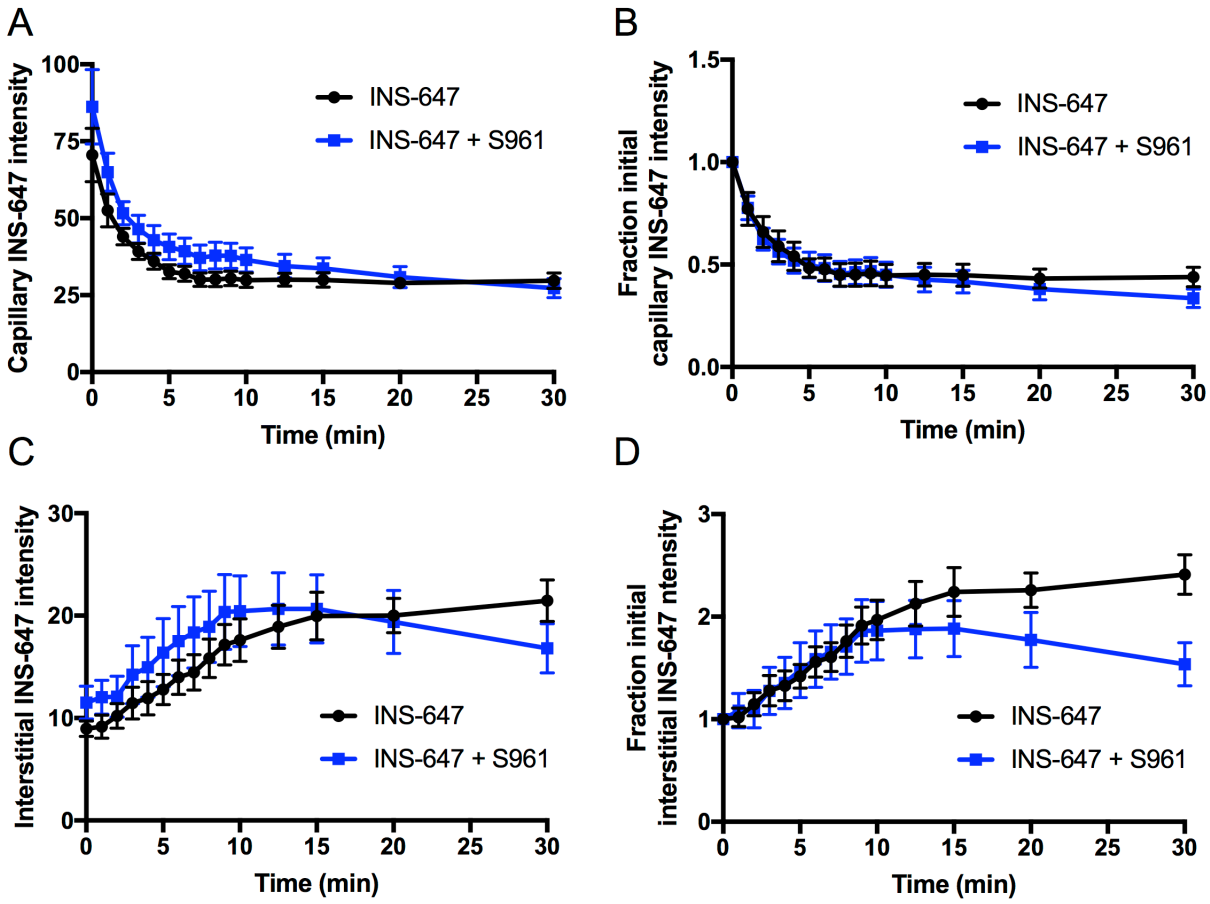

Figure 4.6 Effects of S961 on model-independent insulin efflux kinetics. A) Plasma INS-647 intensity as a function of time following 4U/kg INS-647 injection in mice treated with (INS-647 + S961; n=5) or without an insulin receptor antagonist (INS-647; n=6). **B)** Data from **a** normalized to plasma INS-647 intensity at t=0. **C)** Interstitial INS-647 intensity as a function of time following INS-647 injection. Interstitial INS-647 intensity is defined as the average INS-647 intensity between 1-3mm from the capillary wall. **D)** Data from **c** normalized to interstitial INS-647 intensity at t=0min.

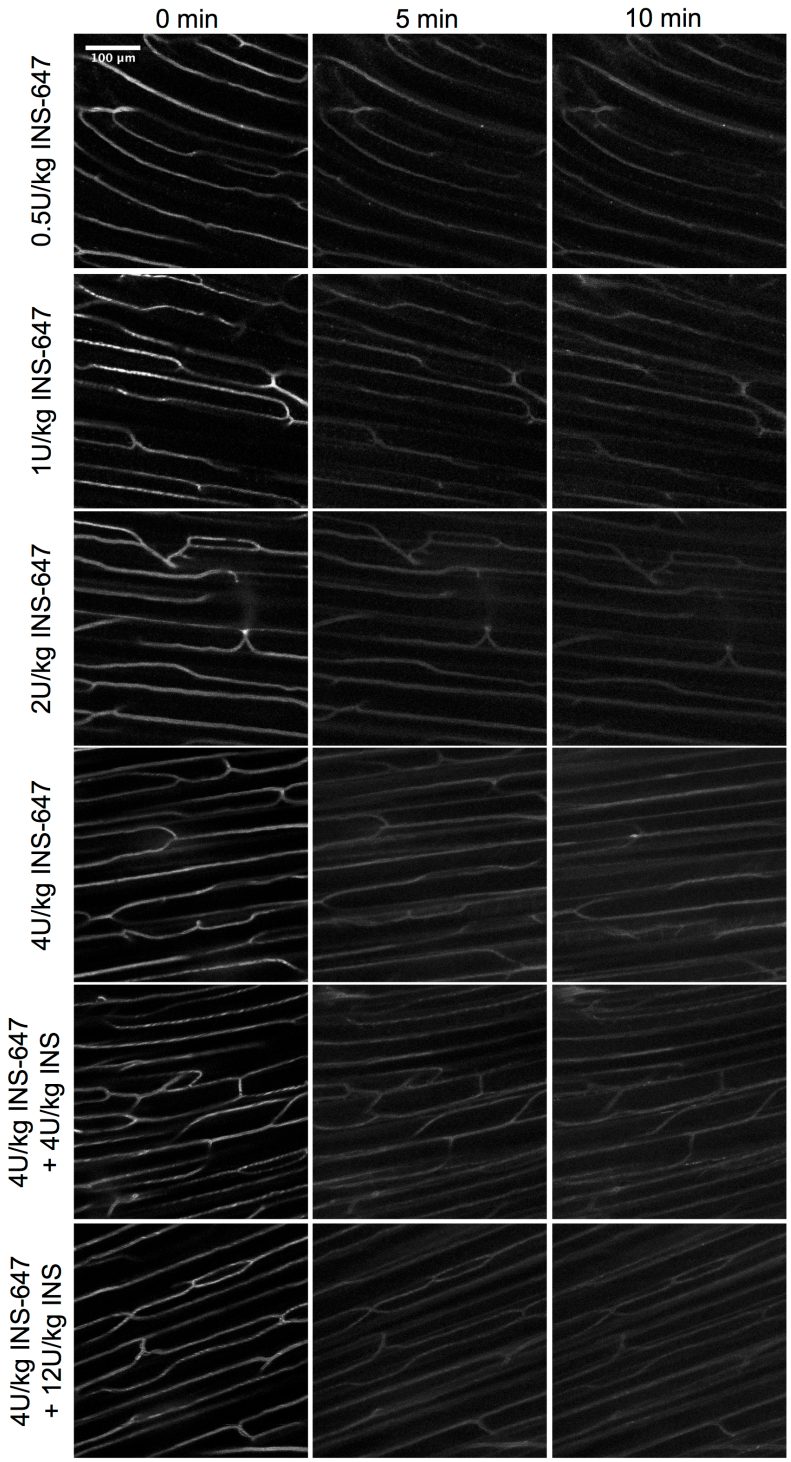

Figure 4.7: Insulin-647 imaging at different doses. Representative INS-647 images (max intensity projections) from mice treated with either 0.5U/kg INS-647 (n=7), 1U/kg INS-647 (n=7), 2U/kg INS-647, 4U/kg INS-647 (n=6), 4U/kg INS-647 + 4U/kg unlabeled insulin (n=6), or 4U/kg INS-647 + 12U/kg unlabeled insulin (n=6).

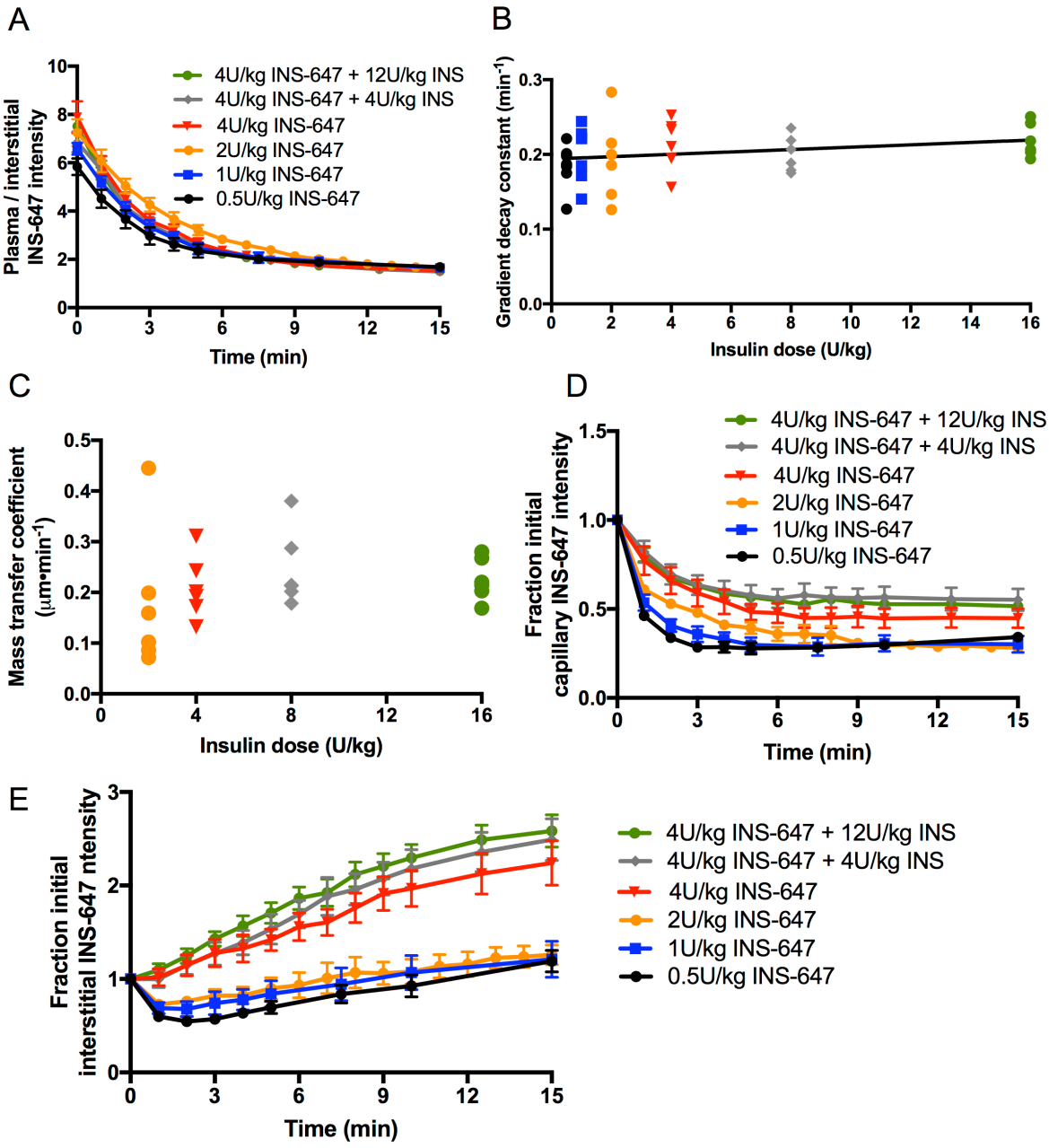

Figure 4.8: Trans-endothelial insulin efflux is not saturable. A) The ratio of plasma to interstitial INS-647 as a function of time following injection in mice treated with either 0.5U/kg INS-647 (n=7), 1U/kg INS-647 (n=7), 2U/kg INS-647 (n=6), 4U/kg INS-647 (n=6), 4U/kg INS-647 and 4U/kg unlabeled insulin (n=6), or 4U/kg INS-647 and 12U/kg unlabeled insulin (n=6). **B)** The exponential decay constant of the plasma / interstitial ratio plotted as a function of insulin dose. **C)** Best-fit fluid-phase transport model estimates of the mass transfer coefficient. For mice treated with 0.5U/kg or 1U/kg INS-647, the image signal-to-noise ratio was too low to allow for mathematical modeling. **D)** Capillary INS-647 intensity as a function of time following INS-647 normalized to capillary INS-647 at t = 0 min. **E)** Interstitial INS-647 intensity as a function of time following INS-647 injection normalized to interstitial INS-647 at t = 0 min. Interstitial INS-647 intensity is defined as the average INS-647 intensity between 1-3μm from the capillary wall.

unlabeled insulin (**Figure 4.7**). If insulin efflux were saturable, we would predict that 1) the rate at which plasma insulin equilibrates with the interstitial space would decrease with increasing doses of insulin and 2) unlabeled insulin would compete for the saturable transport machinery and reduce the apparent transport of INS-647. However, we found that the dissipation kinetics of the capillary/interstitial INS-647 gradient were the same regardless of the dose of insulin used (**Figure 4.8, A and B**). Furthermore, the mass transfer coefficient was not different for any of the doses that were amenable to mathematical modeling (**Figure 4.8C;** 2U/kg and above). Of note, low signal-to-noise ratio at doses below 2U/kg prevented stable, unique estimates of model parameters at these doses. The kinetics of INS-647 in the capillary varied depending on dose (**Figure 4.8D**), with lower doses of insulin being cleared more quickly than higher ones. These differences were also reflected in the interstitial INS-647 kinetics (**Figure 4.8E**). This finding is consistent with the notion that insulin appearance in the interstitial space is a linear function of the levels of insulin in the plasma (i.e. fluid-phase transport). Collectively, these results demonstrate that trans-endothelial insulin efflux is not saturable.

Discussion

One of insulin's key functions is to stimulate muscle glucose uptake. Before insulin can stimulate muscle glucose uptake it must first cross the endothelial barrier separating the plasma from myocytes. Previous studies have shown that insulin-stimulated muscle glucose uptake depends on the ability of insulin to cross this endothelial barrier (136). Furthermore, experiments in insulin resistant subjects have shown that impaired insulin delivery is a feature of muscle insulin resistance (156, 212, 244) which is associated with Type II diabetes. Therefore, characterizing the mechanism of capillary endothelial insulin transport is critical to

understanding the progression of insulin resistance (245). With the use of our *in vivo* imaging technique, we advance the understanding of trans-endothelial insulin efflux by showing that insulin moves across the endothelium by fluid-phase transport. Our findings extend those of Bergman and colleagues, who previously showed that the delivery of insulin to skeletal muscle is not saturable in dogs (157). Furthermore, we demonstrate that the insulin receptor is not required for the movement of insulin across the endothelium. This result is supported by experiments from Kahn and colleagues who showed that mice lacking insulin receptors on endothelial cells are fully insulin sensitive (158).

Fluid-phase transport may be accomplished by either convective movement of insulin through inter-endothelial junctions, a non-specific vesicular process, or a combination of both. Of note, Bendayan et al. used immunoelectron microscopy to show that insulin can be localized inside endothelial vesicles (246), suggesting the importance of the latter mechanism. Caveolar vesicles, which can mediate the trans-endothelial movement of macromolecules, have also been implicated in the endothelial transport of insulin (154). Future experiments will be aimed at deconvolution of these mechanisms.

One potential limitation of the current technique is measurement sensitivity. Namely, the lowest dose of INS-647 administered (0.5 U/kg) produces somewhat higher than physiological plasma insulin levels. Thus, we cannot rule out the existence of a low capacity, Michaelis-Menten-like insulin transport mechanism which operates at lower insulin levels. Such a process would be non-insulin receptor-mediated as neither insulin receptor antagonism nor unlabeled insulin had any effect on insulin transport. As of yet, there is no evidence for the existence of such a process *in vivo* or its significance. However, it is possible that there is some vesicular

compartment (e.g. caveolae) that transports insulin at low concentrations via Michaelis-Menten kinetics.

Many investigators have observed a delay between the rise in plasma insulin levels and the stimulation of glucose uptake in skeletal muscle (120). This delay has largely been attributed to the continuous endothelium of skeletal muscle capillaries, which limits the access of macromolecules to the interstitial space. Our findings regarding the mechanism of trans-endothelial insulin efflux lend insight into the characterization of the endothelial barrier. Namely, the movement of insulin from the plasma to the interstitial space may be limited by the presence of the glycocalyx, the size of inter-endothelial junctions or pores, the transmission of convective forces to the capillary, the kinetics of vesicular trafficking, or the rate at which insulin can promote capillary recruitment. A better understanding of the variables controlling trans-endothelial insulin transport will lead to improved therapeutic strategies aimed at reversing muscle insulin resistance. Such strategies might include small molecules that can enhance insulin delivery to skeletal muscle or, for diabetics, the synthesis of novel insulin analogs that can more readily access muscle.

The mechanism of endothelial insulin transport has been controversial. Studies utilizing cultured monolayers of endothelial cells have shown that trans-endothelial insulin transport is a saturable, insulin-receptor mediated process (150, 152). In contrast, we convincingly demonstrate that insulin movement across the endothelium is non-saturable and does not require the insulin receptor *in vivo*. The contrasting results likely reflect the difference in behavior between endothelial cells in culture and capillaries *in vivo.* Endothelial monolayers are 100 times more permeable to proteins than are intact vessels (165) and lack the physiological milieu that profoundly influences endothelial function in live animals (164). Furthermore, cultured

endothelial cell experiments typically use macrovascular endothelial cells such as umbilical vein or aortic endothelial cells, whereas molecular exchange occurs in the microvasculature *in vivo*. The phenotypic contrast between microvascular and macrovascular endothelial cells (162) creates difficulties in interpretation. In fact, the mechanism by which insulin is taken up by endothelial cells depends on the type of endothelial cell used (155).

In vivo examinations of insulin delivery to the skeletal muscle interstitial fluid have similarly produced conflicting results (156–159, 239). Such studies have utilized interstitial fluid sampling methods such as microdialysis and lymph sampling or measured indices of total skeletal muscle insulin delivery. These techniques are limited because the number of capillaries feeding the space from which sampling is performed is unknown. Therefore, such techniques do not directly measure trans-endothelial molecular efflux but rather a combination of both microvascular perfusion *and* endothelial transport. That is to say, any change in muscle insulin availability could be due to a change in 1) the number of perfused capillaries, 2) insulin efflux across the endothelium, or 3) a combination of both. For instance, Konishi et al. recently reported that a mouse model lacking endothelial insulin receptors have delayed muscle insulin signaling following an insulin bolus (159). The implication is that insulin delivery to muscle is impaired. It is impossible to know whether such an effect is due to impaired insulin-stimulated perfusion or insulin efflux from capillaries. Given that insulin receptor antagonism has no effect on insulin efflux, and the compelling work from several laboratories that shows insulin stimulates skeletal muscle perfusion (89, 92, 247), it is likely that the delay in skeletal muscle insulin signaling in these mice is due to a reduction in insulin-stimulated capillary recruitment. However, it is impossible to directly deconvolve perfusion and efflux from this approach. With

intravital imaging, we measure insulin efflux at the level of individual capillaries, which allows us to directly measure trans-endothelial insulin efflux.

CHAPTER V

IMPAIRED TRANS-ENDOTHELIAL INSULIN TRANSPORT IN SKELETAL MUSCLE OF OBESE MALE MICE IN VIVO

Aims

Total insulin delivery to the interstitial space is reduced in insulin resistant humans and animal models. Whether this impairment in insulin delivery is due to reduced perfusion, trans-endothelial insulin transport, or both is unknown. The aim of **Chapter V** is to utilize intravital insulin imaging to determine whether trans-endothelial insulin transport is reduced in a mouse model of obesity and insulin resistance.

Experimental Approach

Male and female 6-week old C57Bl/6J mice were fed a standard chow (5001 Laboratory Rodent Diet; Lab Diet) or HFD (60% calories from fat; Bioserv F3282) for 16 weeks. We chose this length of HFD because it induces skeletal muscle insulin resistance (248). For intravital microscopy experiments, mice were bred and housed at Vanderbilt University for the entirety of the experiment. One HFD-fed male mouse which underwent intravital microscopy was excluded due to a lack of weight gain and fat accumulation. For insulin tolerance tests and electron microscopy experiments, age-matched diet-induced obese (DIO) and lean control C57Bl/6J mice were purchased from Jackson Laboratory.

Results*

HFD impairs trans-endothelial insulin transport in male mice

We first tested the hypothesis that diet-induced obesity and skeletal muscle insulin resistance are associated with impaired trans-endothelial insulin transport. Lean and diet-induced obese (DIO) mouse models were generated by feeding male mice chow or HFD for 16 weeks. As expected, DIO mice weighed 52% more than their lean counterparts (**Figure 5.1A**) and had a 2.5-fold increase in body fat percentage (**Figure 5.1B**).

Using intravital insulin imaging, we observed that trans-endothelial insulin transport was impaired in DIO male mice (**Figure 5.2**). Namely, the rate at which plasma INS-647 equilibrated with the interstitial space was ~15% lower in DIO mice compared to lean mice (**Figure 5.2, B and C, Figure 5.3**). This indicates that trans-endothelial insulin transport is slower in DIO male mice. Following the INS-647 bolus, capillary INS-647 levels were consistently higher in DIO male mice (**Figure 5.4A**). The clearance rate of plasma INS-647, however, was not significantly different between groups (**Figure 5.4, A and B**). Consistent with higher levels of plasma INS-647, DIO male mice also had higher absolute levels of interstitial INS-647 (**Figure 5.4C**). The rate of interstitial INS-647 appearance, however, was slightly, but non-significantly, lower in the DIO male mice (**Figure 5.4D**). Furthermore, the magnitude of the increased interstitial INS-647 in DIO male mice (**Figure 5.4C**) was lower than that of the increase in plasma INS-647 (**Figure 5.4A**). These findings indicate that, while DIO male mice had higher levels of plasma INS-647, a lower fraction of the plasma INS-647 was able to access the interstitial space. This demonstrates an impairment in trans-endothelial insulin transport.

* These results are described in a manuscript which is in preparation for submission: Williams IM, McClatchey PM, Bonner JS, Valenzuela FA, Wasserman DH. Trans-endothelial insulin efflux is impaired in skeletal muscle of obese mice.

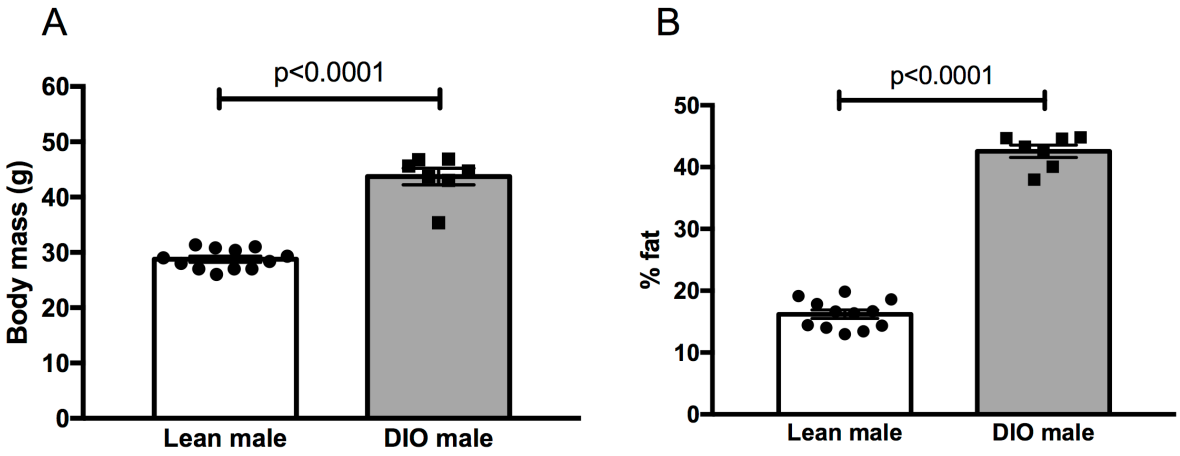

Figure 5.1: Effect of HFD on body mass and composition in male mice. A) Body mass and **B)** percent body fat in lean (n=12) and DIO (n=7) male mice undergoing intravital microscopy. DIO – diet-induced obese, HFD – high fat diet. Groups were compared using Student's t-test.

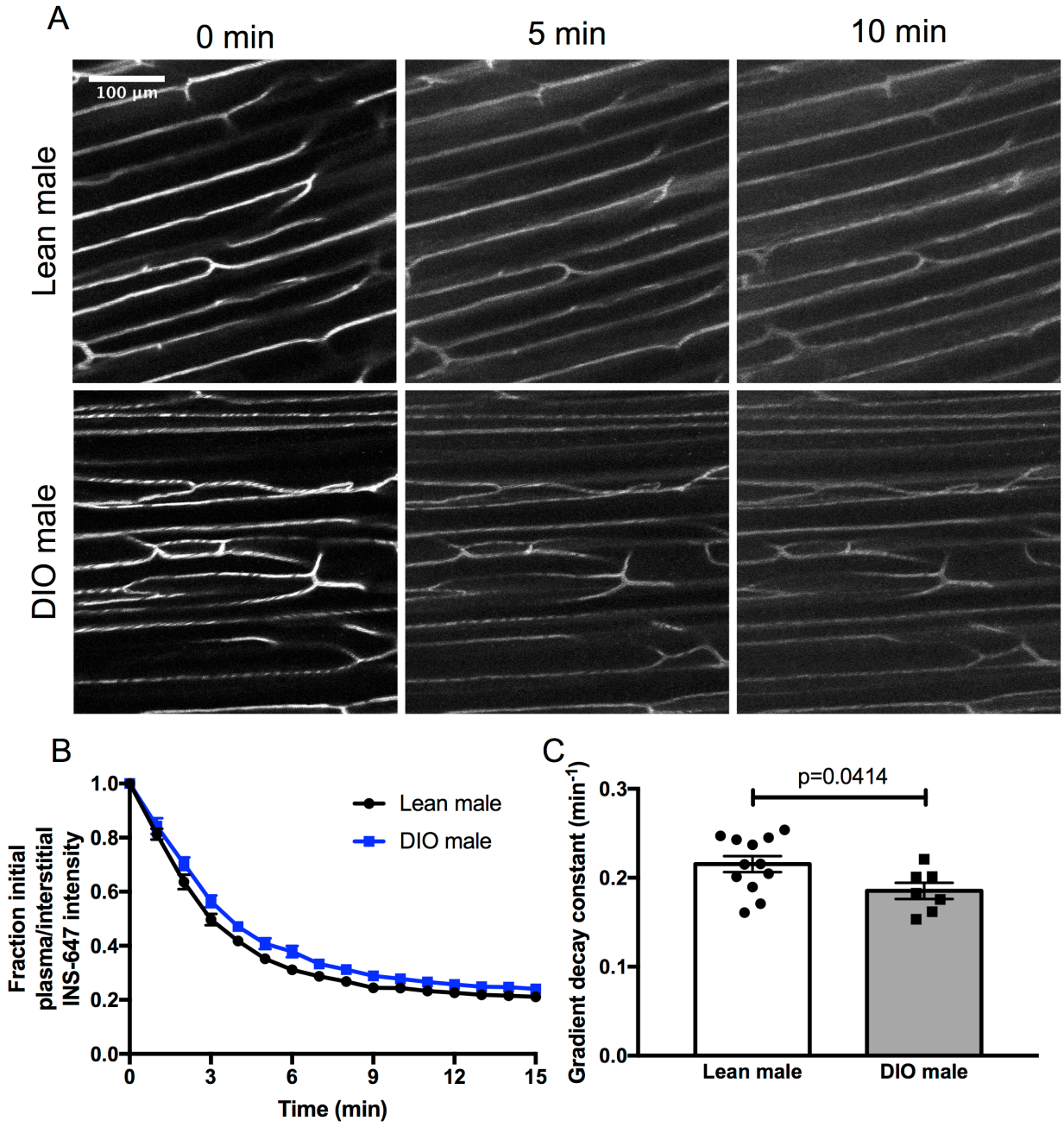

Figure 5.2: Obese male mice have impaired trans-endothelial insulin efflux in skeletal muscle capillaries. A) Representative INS-647 images (maximum intensity projections) in lean (n=12) and DIO (n=7) male mice. **B)** The ratio of plasma to interstitial INS-647 as a function of time following INS-647 injection, normalized to the ratio at t = 0 min. **C)** Decay constant of the plasma / interstitial INS-647 ratio, a measure of trans-endothelial insulin efflux kinetics. INS-647 – insulin-647, DIO – diet-induced obese. Groups were compared using Student's t-test.

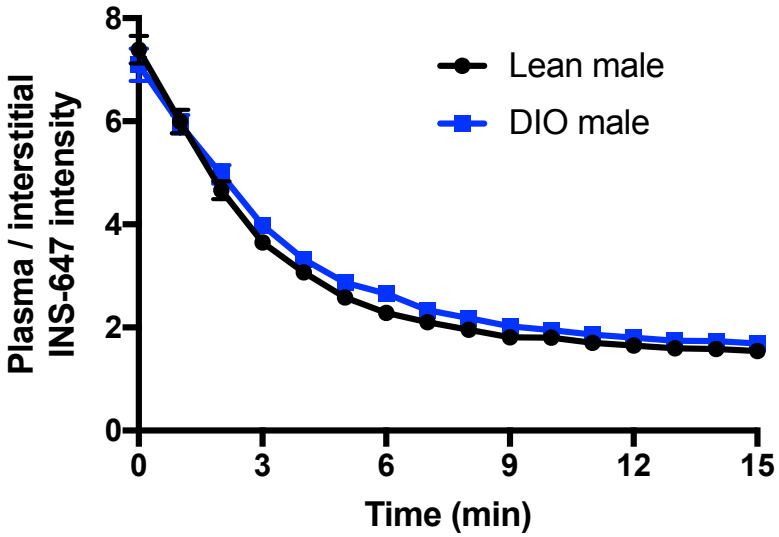

Figure 5.3: Trans-endothelial insulin efflux kinetics in lean and DIO male mice. The ratio of plasma to interstitial INS-647 intensity following INS-647 injection, a measure of trans-endothelial insulin efflux. INS-647 – insulin-647.

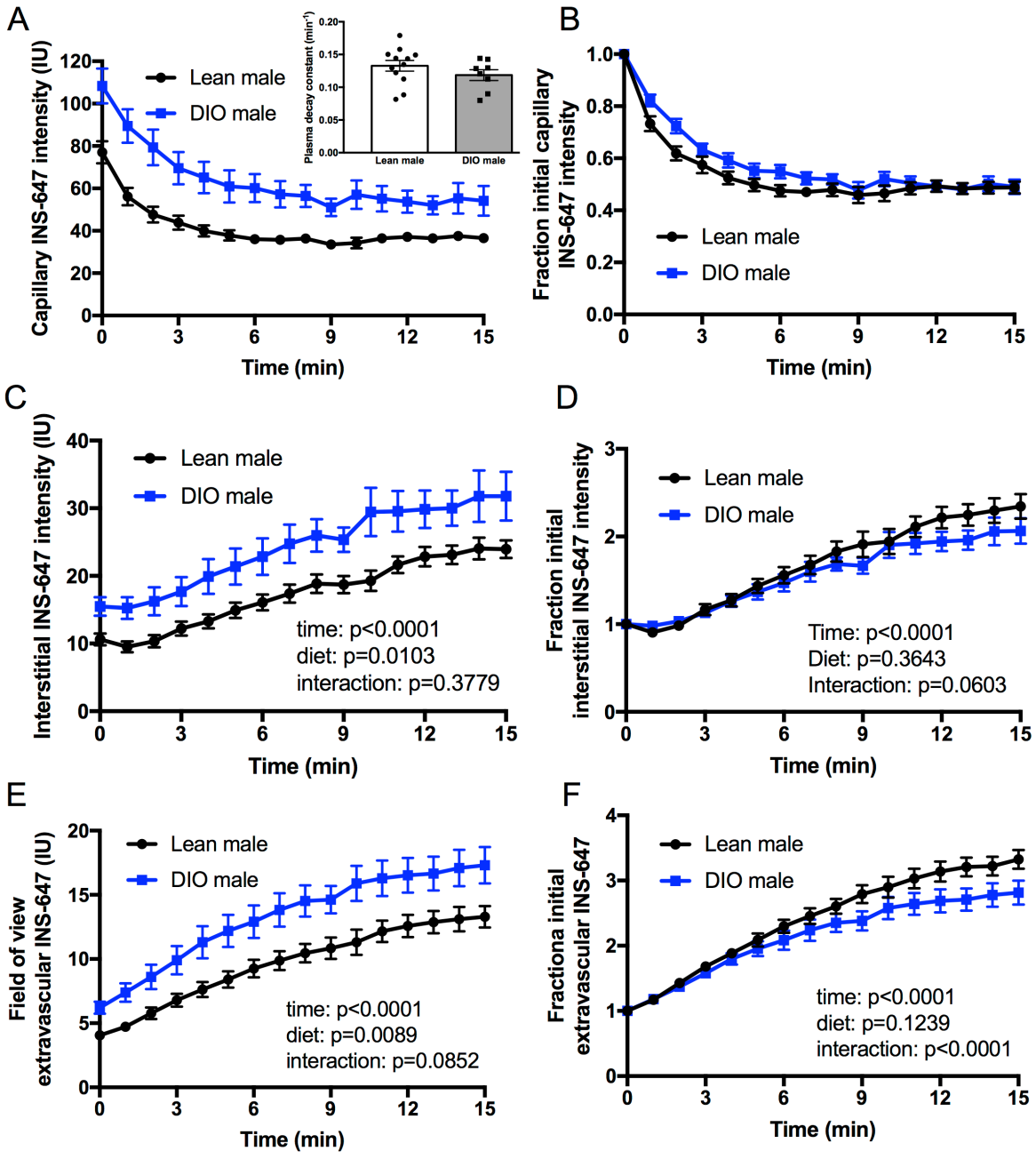

Figure 5.4: Effects of HFD on plasma insulin clearance, interstitial appearance, and insulin delivery in male mice. A) Capillary plasma INS-647 intensity as a function of time following injection in lean (n=12) and DIO (n=7) male mice. Inset shows the decay constant of capillary INS-647. **B)** Data in **A** normalized to the capillary INS-647 intensity at t = 0 min. **C)** Interstitial INS-647 intensity as a function of time following injection. The interstitial space is defined as the region emanating 1-3μm from the capillary wall. **D)** Data in **C** normalized to the interstitial INS-647 intensity at t = 0 min. **E)** Total extravascular INS-647 in the field of view as a function of time following injection. **F)** Data in **E** normalized to the extravascular INS-647 intensity at t = 0 min. Groups were compared either by Student's t-test or by two-way repeated measures ANOVA. IU – intensity units, HFD – high fat diet.

Trans-endothelial insulin transport is one of three variables, including plasma insulin concentration and the capillary surface area for insulin exchange, that control muscle insulin delivery. We found that neither plasma-perfused surface area (**Figure 5.5, A and B**) nor capillary diameter (**Figure 5.5, C and D**) were affected by HFD. This suggests that the surface area for insulin exchange was the same in lean and DIO males. To determine whether the reduced trans-endothelial insulin transport in DIO males affected total insulin delivery, we measured INS-647 in the entire extravascular space. We found that, while the extravascular INS-647 levels were consistently higher in DIO male mice, (**Figure 5.4E**), the rate of INS-647 appearance in the extravascular space was reduced (**Figure 5.4F**). These findings indicate that the kinetics of insulin delivery to skeletal muscle are impaired in DIO male mice.

Following intravital microscopy experiments, we observed that DIO male mice had higher blood glucose levels (**Figure 5.6A**) and lower accumulation of the isotopic glucose tracer 2[^{14}C]DGP in the gastrocnemius (**Figure 5.6B**). These findings indicate that DIO male mice have whole-body and skeletal muscle insulin resistance. To confidently ensure that muscle insulin resistance could be detected using the same conditions as intravital microscopy experiments, we performed insulin tolerance tests with isotopic glucose tracers in a separate cohort of DIO male mice (**Figure 5.7**). This cohort of HFD-fed male mice also weighed more (**Figure 5.8A**) and had a higher percentage of body fat (**Figure 5.8B**) than their chow-fed counterparts. As expected, DIO male mice had a significantly impaired glucose-lowering response to insulin (**Figure 5.7, A and B**). Furthermore, the clearance of 2[^{14}C]DG by the soleus, gastrocnemius, and vastus lateralis muscles was reduced in DIO male mice (**Figure 5.7 C**). These results confirm that DIO male mice display muscle insulin resistance. Therefore, muscle

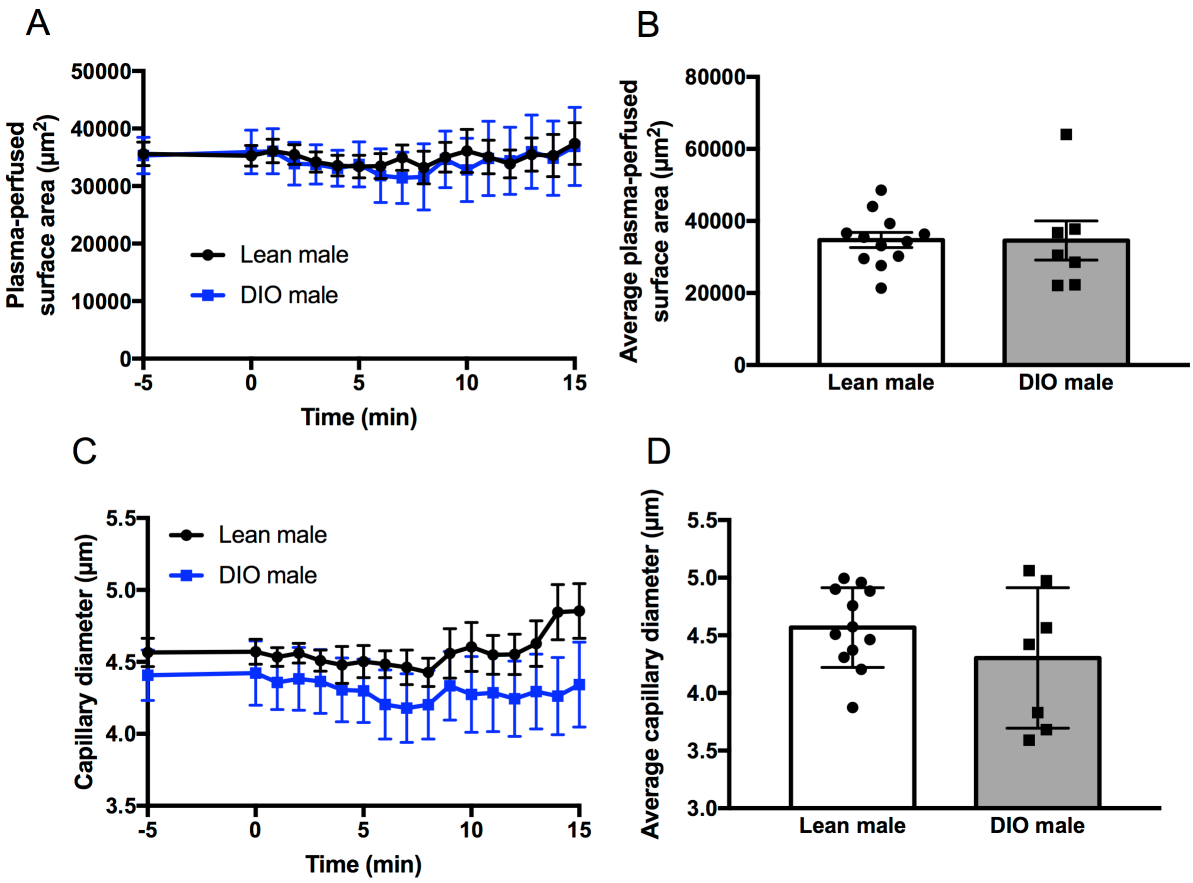

Figure 5.5: HFD has no effect on plasma-perfused surface area or capillary diameter in male mice. A) Vascular cross-sectional surface area, as determined by the area of rhodamine dextran (vascular marker), as a function of time in lean (n=12) and DIO (n=7) male mice. INS-647 was injected at t = 0 min. **B)** Average plasma-perfused surface area throughout the course of the intravital microscopy experiment. **C)** Capillary diameter as a function of time during intravital microscopy experiments. INS-647 was injected at t = 0 min. **D)** Average capillary diameter throughout the intravital microscopy experiment. Groups were compared using Student's t-test.

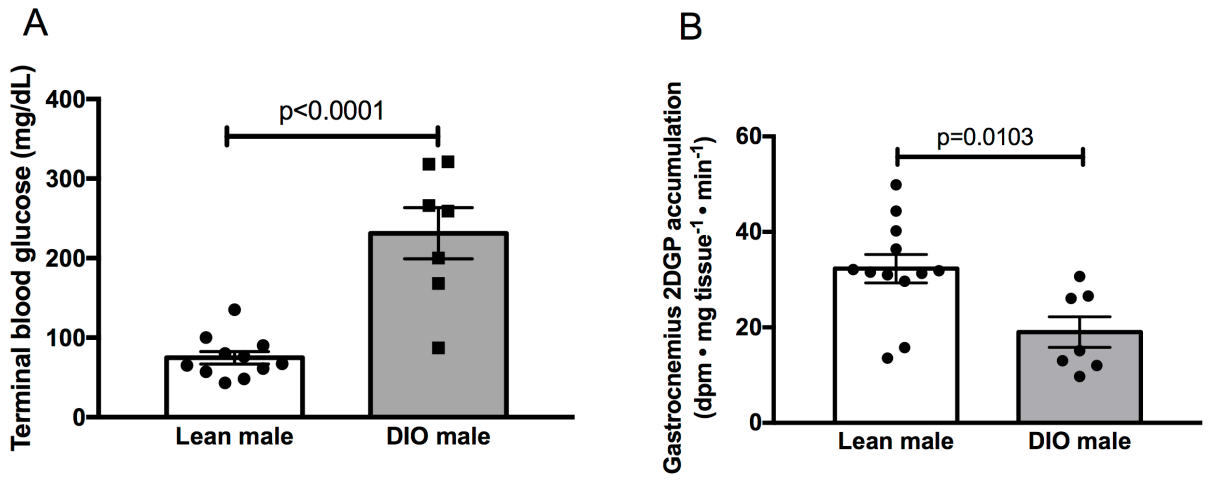

Figure 5.6: HFD causes skeletal muscle insulin resistance in male mice. A) Terminal blood glucose following intravital microscopy experiments in lean (n=11) and DIO (n=7) male mice. **B)** Accumulation of the isotopic glucose tracer, 2[^{14}C]2deoxyglucose-6-phosphate, in the gastrocnemius during intravital microscopy experiments. Groups were compared using Student's t-test. 2DGP - 2[^{14}C]2deoxyglucose-6-phosphate, dpm – disintegrations per minute.

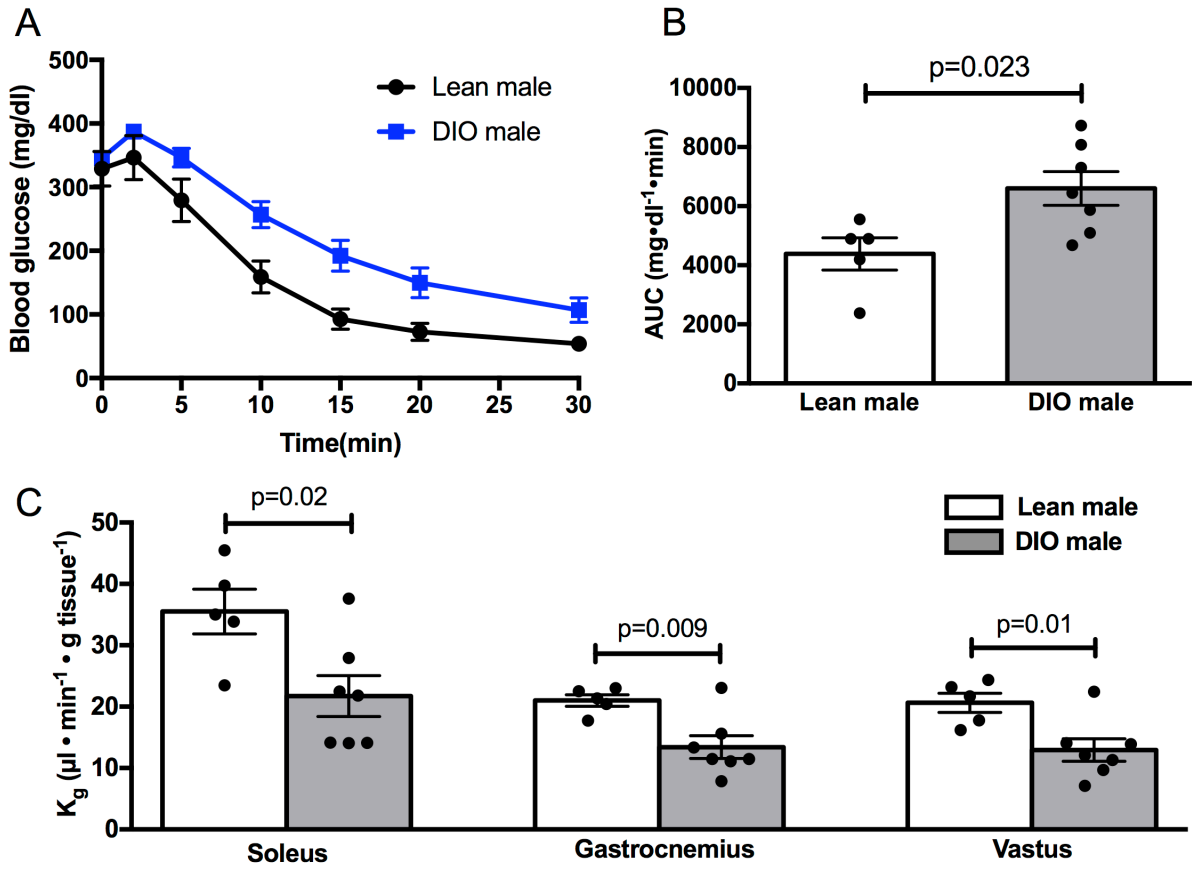

Figure 5.7: DIO male mice display skeletal muscle insulin resistance. A) Glucose excursions in anesthetized lean (n=5) and DIO (n=7) male mice following a 4U/kg intravenous insulin bolus. **B)** Area under the glucose excursion curves in **A**. **C)** Clearance of 2[^{14}C]2deoxyglucose during the insulin tolerance tests by the soleus, gastrocnemius, and vastus muscles. Groups were compared using Student's t-test.

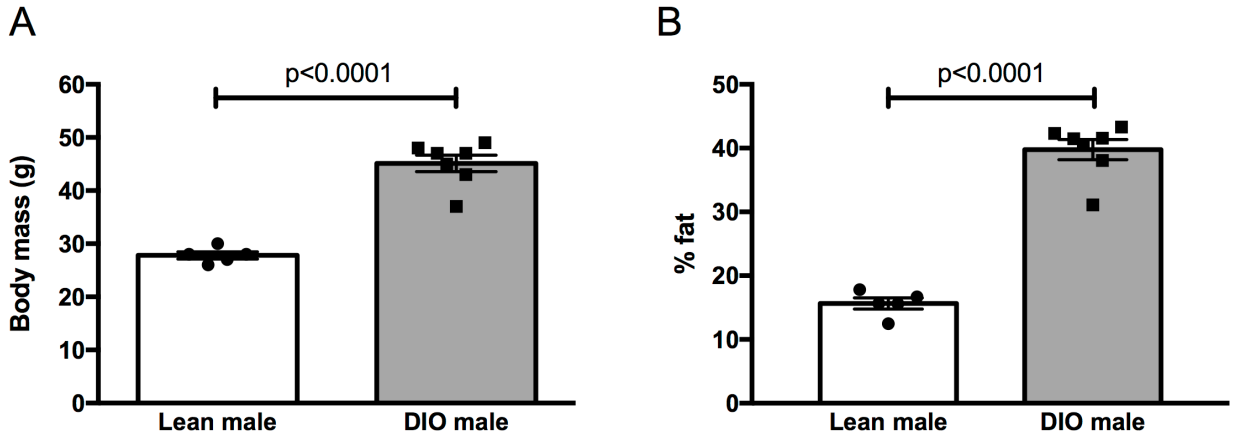

Figure 5.8: Effects of HFD on body mass and composition in male mice. A) Body mass and **B)** percent body fat in lean (n=5) and DIO (n=7) male mice undergoing insulin tolerance tests. Groups were compared using Student's t-test.

insulin resistance is associated with impaired trans-endothelial insulin transport in DIO male mice.

HFD causes ultrastructural defects in the skeletal muscle capillary endothelium of male mice

In light of the finding that trans-endothelial insulin transport is delayed in DIO male mice, we hypothesized that this impairment would be associated with changes to the skeletal muscle capillary endothelium. To test this hypothesis, we assessed capillary endothelial ultrastructure with transmission electron microscopy (**Figure 5.9**). We observed that the density of vesicles in the endothelium was reduced by ~45% in DIO male mice (**Figure 5.9, A-C**). Neither the diameter of vesicles (**Figure 5.9D**), nor the localization of vesicles within the endothelium (**Figure 5.9E**), however, were altered in DIO male mice. Furthermore, the basement membrane thickness was not different between groups (**Figure 5.9F**). The reduction in endothelial vesicles observed in DIO males, which can serve as macromolecular transporters (146), may explain the impairment in trans-endothelial insulin transport.

HFD does not alter trans-endothelial insulin efflux in females

We next tested whether the effects of HFD on trans-endothelial insulin transport were similar in female mice. Female mice fed HFD for 16 weeks weighed 30% more than their chow-fed counterparts (**Figure 5.10A**). Interestingly, HFD-fed females did not have a significantly higher percentage of body fat than chow-fed mice (**Figure 5.10B**). We did not observe a difference in trans-endothelial insulin transport between chow and HFD-fed females (**Figure 5.11**). Namely, there was no change in the dissipation of the plasma/interstitial INS-647 gradient (**Figure 5.11, B and C, Figure 5.12**). Similar to HFD-fed males, plasma INS-647 levels were

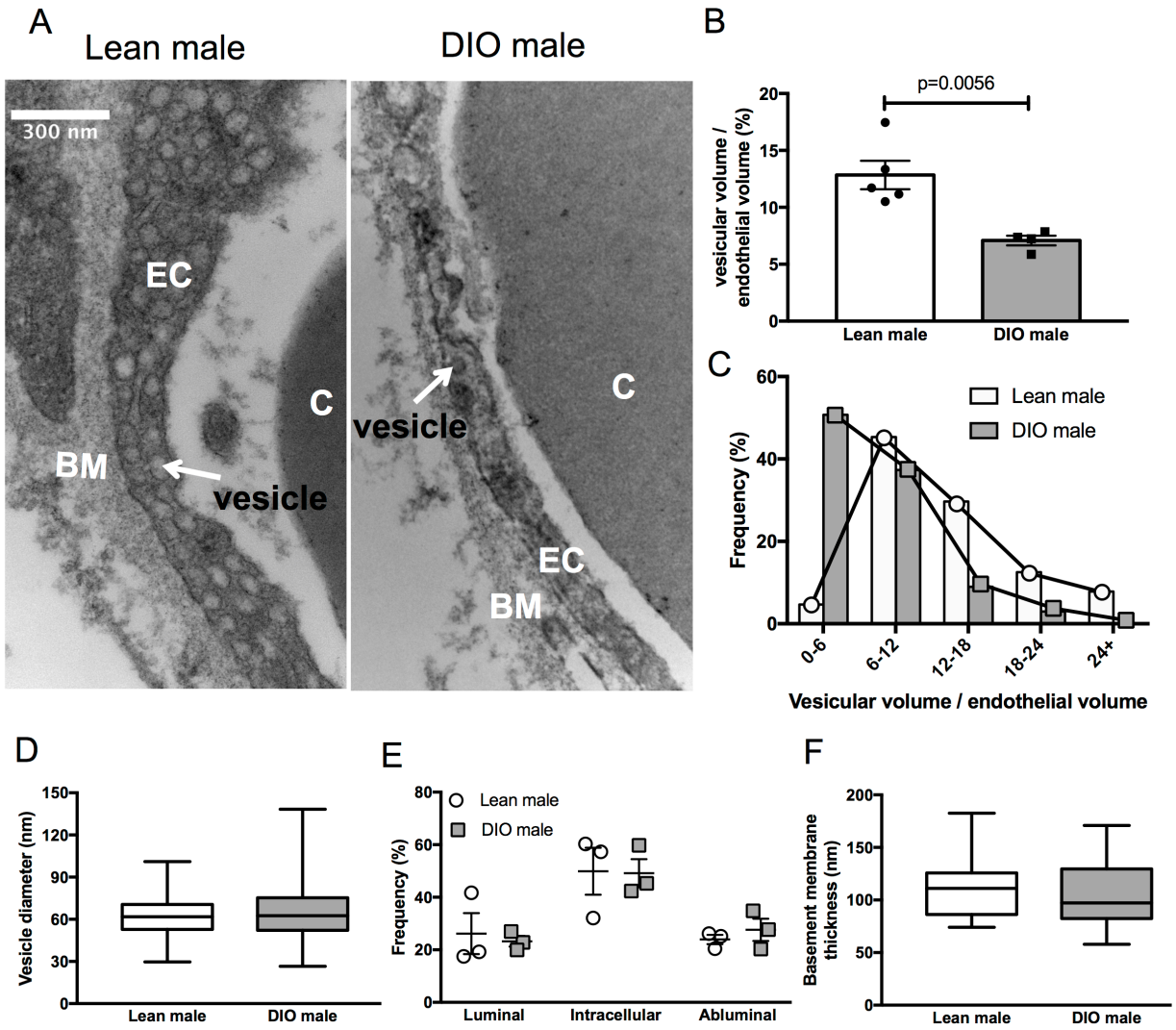

Figure 5.9: Skeletal muscle capillaries of DIO male mice contain fewer endothelial vesicles. **A)** Representative electron micrographs of the capillary endothelium in the gastrocnemius of lean and DIO male mice. **B)** Volume of vesicles relative to total endothelial volume in chow (n=5) and DIO (n=4) male mice. **C)** Frequency distribution of relative vesicular volume in all capillaries from chow (n=64) and DIO male mice (n=66). **D)** The average diameter of all endothelial vesicles in chow (n=227) and DIO (n=116) male mice. **E)** Frequency distribution of the localization of vesicles in the capillary endothelium. **F)** Average basement membrane thickness in capillaries from chow (n=31) and DIO male mice (n=31). In the box and whisker blots, the box extends from the 25th to the 75th percentiles and the whiskers indicate the range. Groups were compared using Student's t-test.

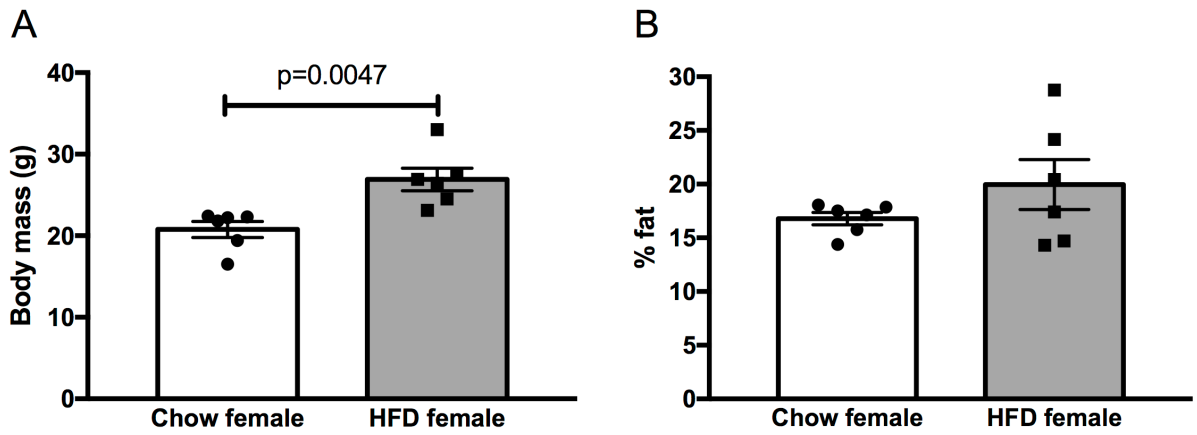

Figure 5.10: Effects of high fat feeding on body mass and composition in female mice. A) Body mass and **B)** percent body fat in chow (n=6) and HFD-fed (n=8) female mice undergoing intravital microscopy. Groups were compared using Student's t-test.

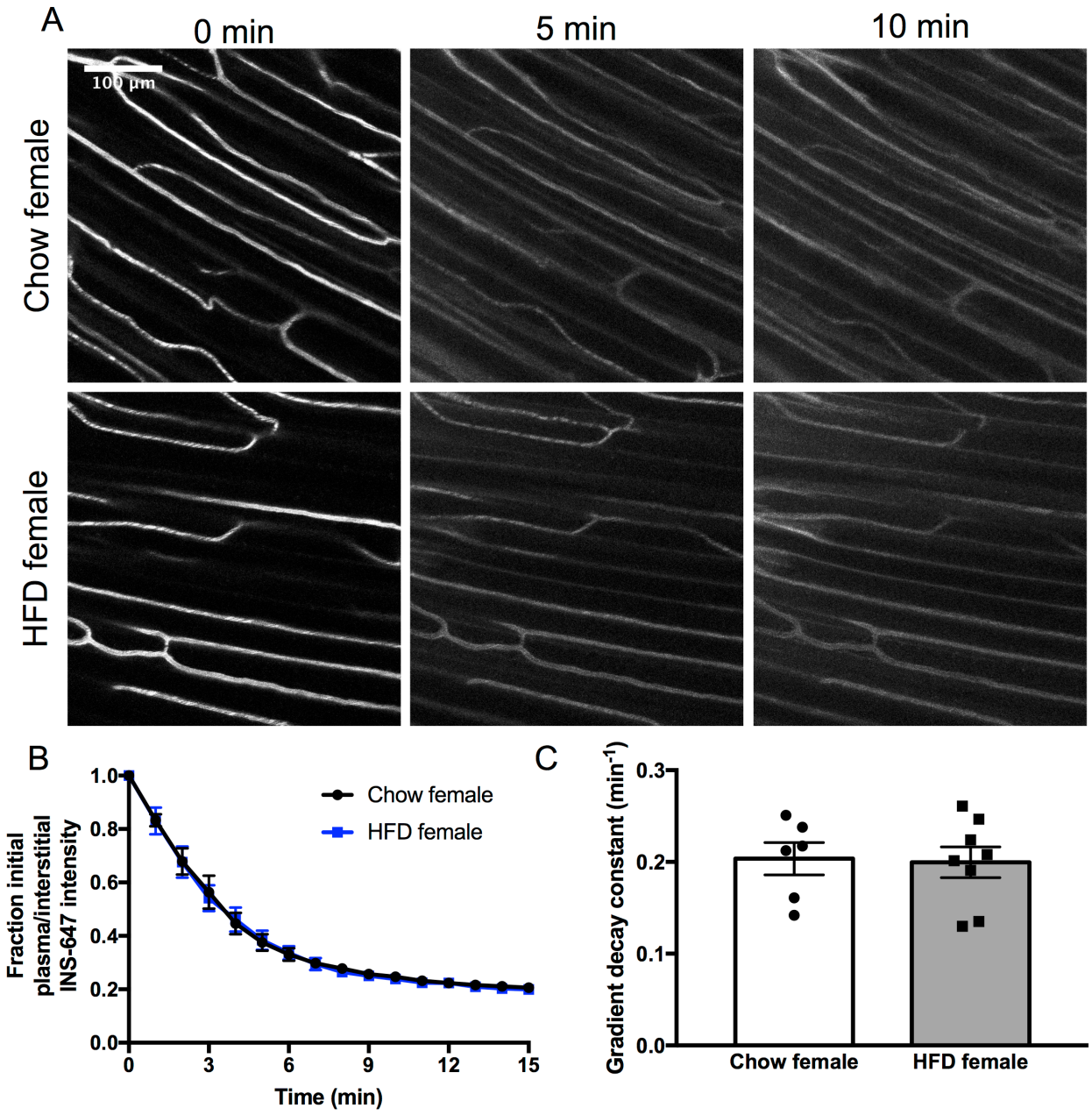

Figure 5.11: HFD does not alter trans-endothelial insulin efflux in females. A) Representative INS-647 images (maximum intensity projections) in chow (n=6) and HFD-fed (n=8) female mice. **B)** The ratio of plasma to interstitial INS-647 as a function of time following INS-647 injection, normalized to the ratio at t = 0 min. **C)** The gradient decay constant of the plasma to interstitial INS-647 ratio as a function of time. Groups were compared using Student's t-test.

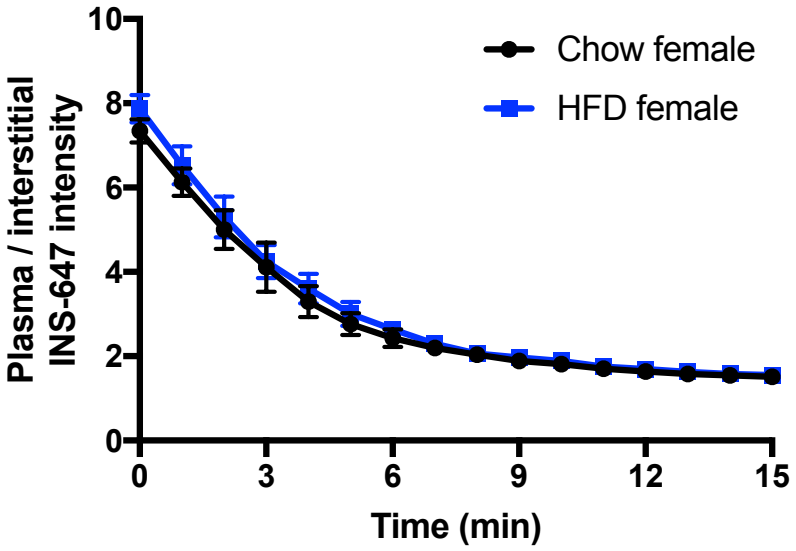

Figure 5.12: Trans-endothelial insulin efflux kinetics in chow and HFD-fed female mice. The ratio of plasma to interstitial INS-647 intensity as a function of time following INS-647 injection, a measure of trans-endothelial insulin efflux.

higher in HFD-fed females following the INS-647 bolus (**Figure 5.13A**). However, the rate of INS-647 clearance from the plasma was not different between the two groups (**Figure 5.13, A and B**). HFD-females tended to have higher levels of interstitial INS-647 (**Figure 5.13C**) as expected from their higher levels of plasma INS-647. However, there was no difference in the rate of interstitial INS-647 appearance between chow and HFD-fed females (**Figure 5.13D**).

With respect to microvascular hemodynamic indices, we did not observe any difference in either average plasma-perfused surface area (**Figure 5.14, A and B**) or capillary diameter (**Figure 5.14, C and D**). As expected from the lack of differences in capillary surface area (**Figure 5.14B**) and trans-endothelial insulin transport (**Figure 5.11C**), there was no change in total extravascular INS-647 delivery (**Figure 5.13, E and F**) in HFD-fed females. Following the intravital microscopy experiments, we did not observe any difference in terminal blood glucose **(Figure 5.15A)**. HFD-fed females did have a 27% reduction in 2[^{14}C]DGP accumulation in the gastrocnemius (**Figure 5.15B**), although this difference was not statistically significant. These findings suggest that, in contrast to males, 16 weeks of HFD does not alter trans-endothelial insulin transport and only causes mild skeletal muscle insulin resistance in females.

Discussion

In this study, we show for the first time that DIO male mice with skeletal muscle insulin resistance have an impairment in the movement of insulin across the skeletal muscle capillary endothelium *in vivo*. This delay in trans-endothelial insulin transport is associated with a loss of vesicles in the skeletal muscle capillary endothelium. Interestingly, female mice were protected from the effects of HFD on trans-endothelial insulin transport and skeletal muscle insulin resistance. These findings reveal a novel contributor to skeletal muscle insulin resistance in DIO

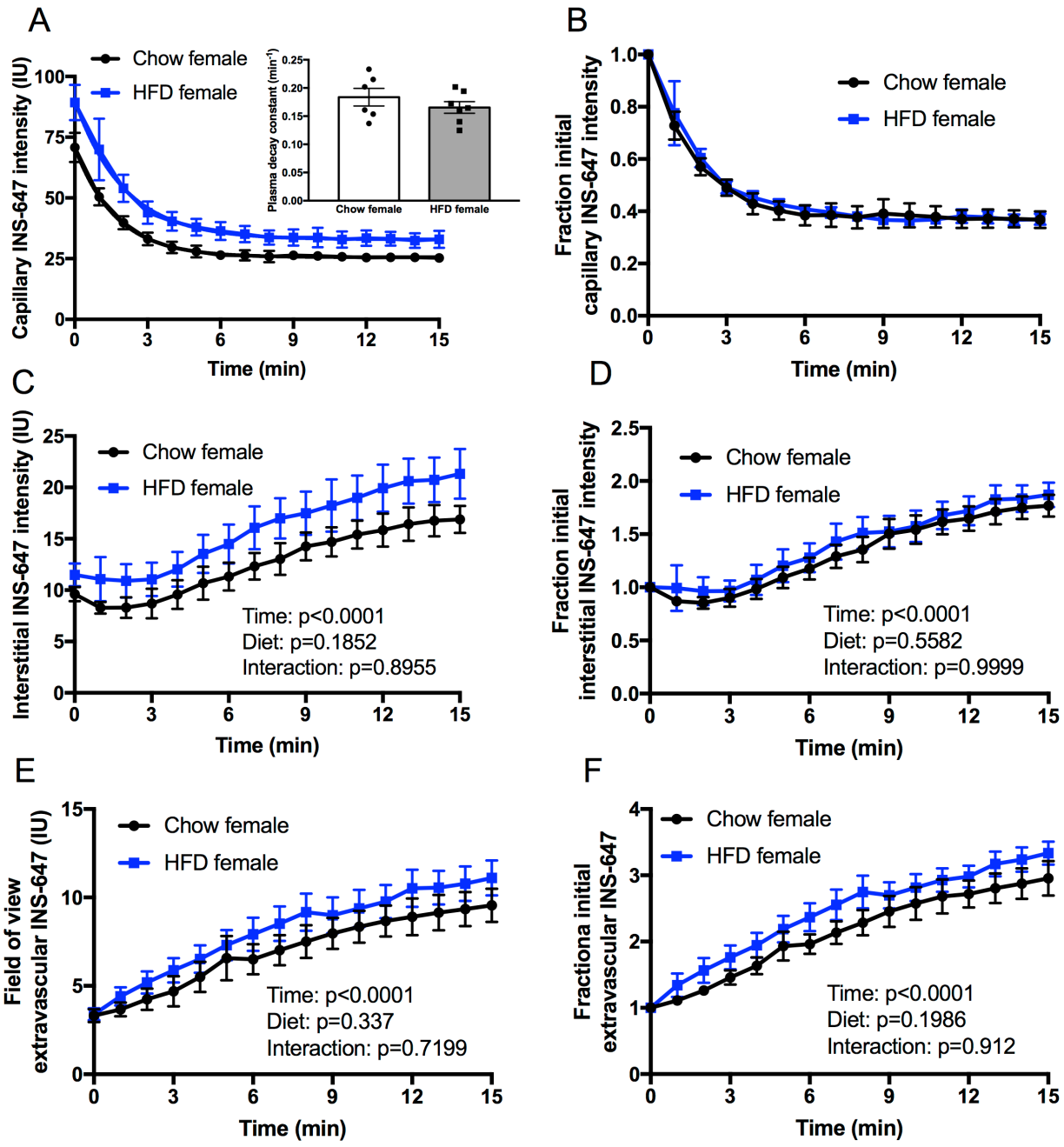

Figure 5.13: Effects of HFD on plasma insulin clearance, interstitial appearance, and total insulin delivery in female mice. A) Capillary INS-647 as a function of time following injection in female mice fed chow (n=6) or HFD (n=8). Inset shows the plasma INS-647 decay constant. **B)** Data in **A** normalized to the capillary INS-647 intensity at t = 0 min. **C)** Interstitial INS-647 as a function of time following injection. The interstitial space is defined as the region emanating 1-3µm from the capillary wall. **D)** Data in **C** normalized to the interstitial INS-647 intensity at t = 0 min. **E)** Total extravascular INS-647 in the field of view as a function of time following injection. **F)** Data in **E** normalized to the extravascular INS-647 at t = 0 min. Groups were compared either by Student's t-test or two-way repeated measures ANOVA.

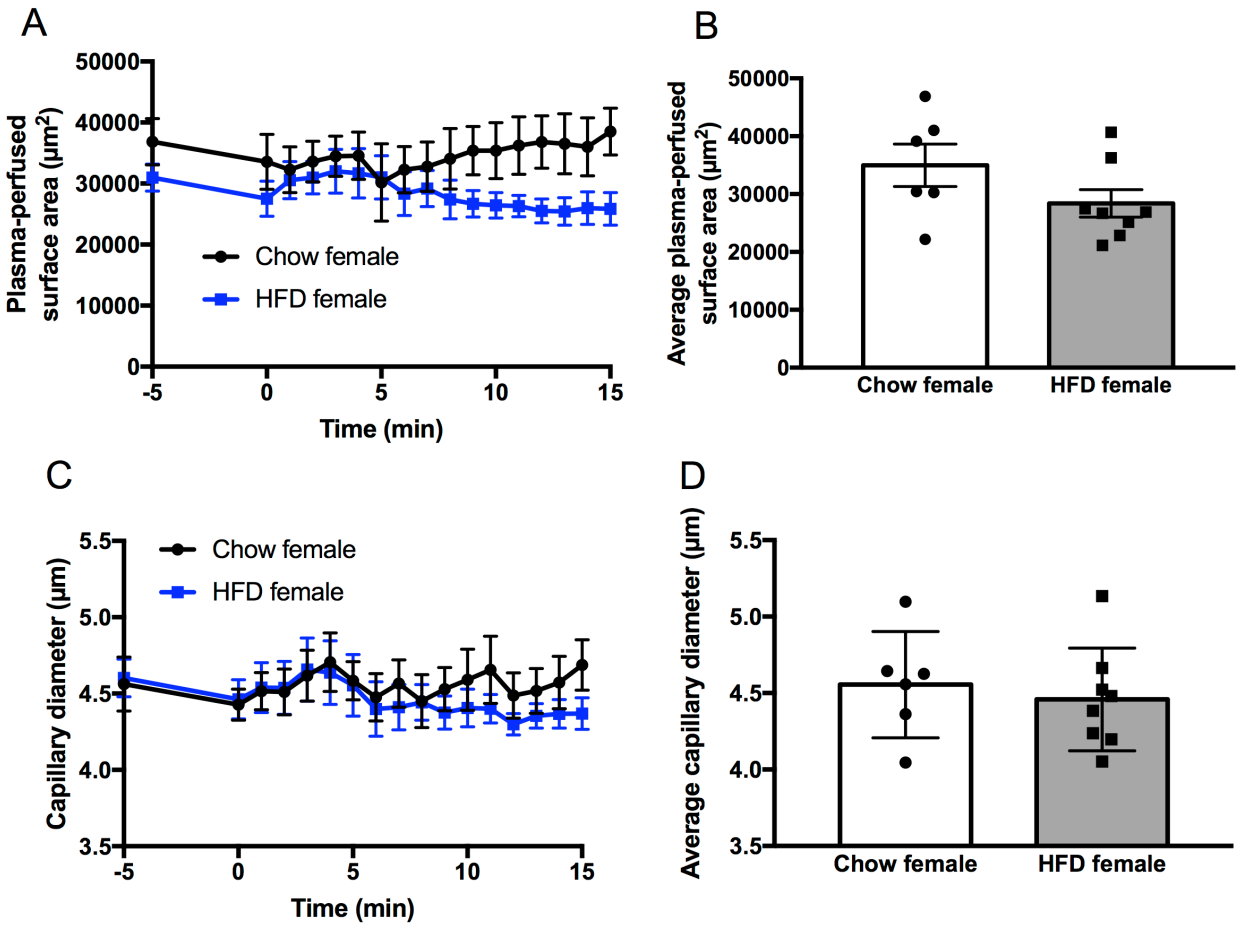

Figure 5.14: Effects of HFD on microvascular parameters in female mice. A) Vascular cross-sectional surface area, as determined by the area of rhodamine dextran (vascular marker), as a function of time in chow (n=6) and HFD-fed (n=7) female mice. INS-647 was injected at t = 0 min. **B)** Average plasma-perfused surface area throughout the course of the intravital microscopy experiment. **C)** Capillary diameter as a function of time during intravital microscopy experiments. INS-647 was injected at t = 0 min. **D)** Average capillary diameter throughout the intravital microscopy experiment. Groups were compared using Student's t-test.

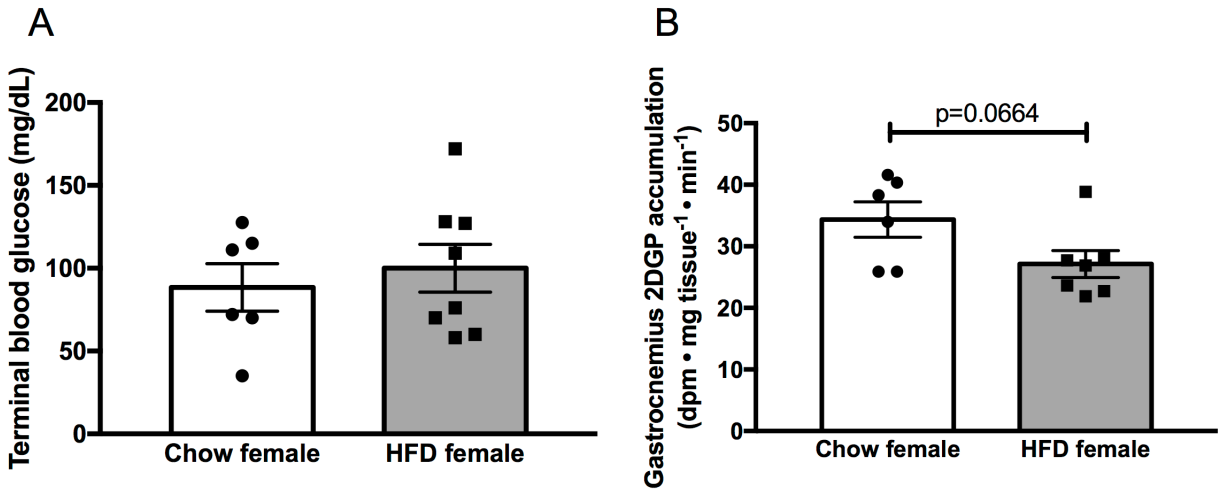

Figure 5.15: Effects of HFD on glucose metabolism in female mice. A) Terminal blood glucose following intravital microscopy experiments in chow (n=6) and HFD-fed (n=7) female mice. **B)** Accumulation of the isotopic glucose tracer, 2[^{14}C]2deoxyglucose-6-phosphate, in the gastrocnemius during intravital microscopy experiments. Groups were compared using Student's t-test.

male mice. Namely, skeletal muscle insulin resistance may be due, in part, to an inability of insulin to cross the capillary endothelium and access myocytes. A critical and yet unresolved question is whether impaired trans-endothelial insulin transport contributes to skeletal muscle insulin resistance (245, 249). Most previous studies, but not all (213), have demonstrated that the delivery of insulin to skeletal muscle interstitial space is reduced in obese humans (244) and animal models (156, 212, 250). The delivery of insulin to skeletal muscle depends on both the capillary surface area for insulin exchange and the rate at which insulin moves across the capillary endothelium. Many studies have shown that insulin-stimulated skeletal muscle perfusion is reduced in obesity (89, 156, 173, 251). The contribution of trans-endothelial insulin transport to the reduced insulin delivery observed in obesity, however, has been unclear due to the lack of direct measurements *in vivo*. We utilized the intravital microscopy technique described in **Chapter III** to directly visualize and quantify the movement of insulin across the endothelium of individual skeletal muscle capillaries *in vivo* (252). This method has major advantages over *in vitro* studies of cultured endothelial cells. Namely, cultured endothelial cells are very different than capillaries *in vivo* with respect to microenvironment, protein expression, permeability, and the mechanism of insulin transport (164, 165, 252, 253). Utilizing direct measurements of trans-endothelial insulin transport *in vivo*, we demonstrate that the movement of insulin across the endothelium is impaired in the skeletal muscle of DIO male mice.

We observed a 15% reduction in trans-endothelial insulin transport in DIO male mice. The implication of this reduction in trans-endothelial insulin transport would presumably be a reduction in total delivery of insulin to skeletal muscle. Interestingly, we found that absolute extravascular levels of insulin were actually increased in DIO male mice. A limitation of this measurement is that it is made in a very small volume and may not reflect insulin delivery at the

whole muscle level. Regardless, this finding demonstrates, perhaps obviously, that in addition to surface area for insulin exchange and trans-endothelial insulin transport, plasma insulin concentration is an important determinant of muscle insulin delivery. In the current study, the higher plasma insulin levels in DIO male mice compensate for the reduced trans-endothelial insulin transport to maintain extravascular insulin delivery. Plasma insulin levels were most likely higher in DIO mice because the dose of INS-647 was normalized to total body mass and plasma volume does not scale with body mass in obese mice (254). Thus, the plasma insulin concentration was likely higher in DIO male mice because a greater amount of insulin was administered into a similar plasma volume. Nonetheless, the higher levels of plasma insulin alone would not be expected to affect trans-endothelial insulin transport because 1) insulin efflux is not saturable (252) and 2) HFD-female mice also have higher levels of plasma insulin but no change in trans-endothelial insulin transport. Furthermore, these experimental conditions recapitulate the hyperinsulinemia observed in obesity. We hypothesize that such hyperinsulinemia may be a compensatory mechanism to overcome defects in trans-endothelial insulin transport and maintain insulin levels at the myocyte. Despite the higher levels of extravascular insulin in the DIO male mice, they still displayed skeletal muscle insulin resistance. This indicates cellular insulin resistance at the level of the myocyte. Thus, defects in trans-endothelial insulin transport compound with myocyte insulin resistance to severely impair insulin action in skeletal muscle during obesity.

The reduction of trans-endothelial insulin transport in DIO male mice is associated with a profound reduction in the density of endothelial vesicles. This is consistent with a previous finding from Bagi and colleagues who showed that the number of endothelial vesicles in coronary arterioles was reduced in humans with established Type 2 diabetes (255). Endothelial

vesicles can serve as macromolecular transporters (146) which may carry insulin (246). It is unclear whether these vesicles are distinct, transcytotic carriers or if they represent pores in the endothelium (147). We hypothesize that these capillary endothelial vesicles are likely components of pore networks for two reasons. First, trans-endothelial insulin efflux is not saturable *in vivo* (252). Assuming these vesicles do indeed carry insulin (246), the transport of insulin through endothelial pores is more compatible with the non-saturable nature of insulin transport. The presence of a non-saturable yet active, energy-requiring transcytotic transport mechanism seems unlikely. Furthermore, if individual vesicles were actively taking up macromolecules and being transcytosed across the endothelium, we would expect to see molecular accumulation in the capillary endothelium. However, unlike studies utilizing cultured endothelial cells (233), we have never observed the accumulation of any fluorescent molecule (dextrans, albumin, transferrin, insulin) in the endothelium of skeletal muscle capillaries. We do see uptake and accumulation of these molecules in the cells lining arterioles and venules, indicating that vesicular transcytosis may be a more relevant transport mechanism in larger blood vessels. Thus, we hypothesize that, in DIO male mice, the number of capillary endothelial pores available for insulin exchange is reduced, thereby impairing trans-endothelial insulin transport.

It should be noted that the magnitude in reduction of endothelial vesicles (45%) was much larger than the impairment in trans-endothelial insulin transport (15%). We have two hypotheses for this discrepancy. First, there may be an excess of endothelial pore surface area available for insulin exchange in healthy, lean mice. Thus, a more significant reduction in endothelial vesicular density may be required to severely limit trans-endothelial insulin transport. An alternative possibility is that paracellular permeability, as governed by the width of inter-endothelial junctions, increases in DIO male mice to compensate for the reduction in

transcellular (i.e. vesicular pores) permeability. Indeed, there is considerable crosstalk between transcellular and paracellular transport pathways (256). Given the importance of fluid and macromolecular delivery, it would be expected that compensatory mechanisms exist to maintain these functions. Finally, we cannot exclude the possibility that the paracellular movement of insulin through inter-endothelial junctions is a greater determinant of trans-endothelial insulin transport than transcellular insulin movement.

Using our intravital microscopy technique, we also measured plasma-perfused surface area and capillary diameter, indices of microvascular structure and hemodynamics. We did not observe any difference between lean and DIO male mice in either of these parameters. Furthermore, the administration of insulin did not appear to have any effect on plasma-perfused surface area. This suggests that there was no effect of HFD on the capillary surface area available for insulin exchange. These findings are seemingly in contrast to previous studies utilizing contrast-enhanced ultrasound which concluded that 1) that insulin increases muscle microvascular perfusion (120, 156) and 2) insulin-stimulated muscle perfusion is reduced in obesity. The use of contrast-enhanced ultrasound to measure the distribution volume of ~1-3μm microbubbles gives an index of red blood cell distribution volume. This is different from our measurement of the distribution volume of a rhodamine-labeled plasma marker, 2MDa dextran. As insulin exists in plasma and not red blood cells, the measurement of plasma-perfused surface area is more relevant for assessing the surface area available for insulin exchange. Thus, it is possible that insulin and HFD have divergent effects on red blood cell and plasma distribution. Namely, while insulin increases and obesity decreases microbubble distribution volume (120), neither insulin nor obesity alter plasma-perfused surface area in skeletal muscle. Given that insulin and HFD alter microbubble velocity (120), it is likely that they also alter plasma velocity.

Regardless, changes in plasma velocity would not be predicted to alter trans-endothelial insulin transport as insulin is a relatively slowly equilibrating molecule (257).

In contrast to male mice, we found that female mice were protected from the deleterious effects of HFD on trans-endothelial insulin transport. The most likely explanation for this finding is that, while HFD-fed female mice were heavier than chow-fed mice, they did not have a significantly higher percentage of body fat. This observation is mostly consistent with a previous study which showed that 15 weeks of HFD causes weight gain but only a small increase in body fat percentage in female mice (258). Thus, HFD in the absence of obesity does not cause impaired capillary insulin transport in female mice. Consistent with the unaltered trans-endothelial insulin transport, skeletal muscle insulin sensitivity, as measured by 2[^{14}C]DGP accumulation, was only slightly and non-significantly reduced in HFD-fed females. This contrasts with male mice which develop severe skeletal muscle insulin resistance when fed a HFD. It is also conceivable that sex differences in microvascular function (259, 260) protect female mice from the endothelial dysfunction associated with HFD.

In summary, we have shown for the first time that the movement of insulin across the endothelium in skeletal muscle capillaries is impaired in a mouse model of diet-induced obesity and insulin resistance. This impairment in trans-endothelial insulin transport is associated with a reduction in endothelial vesicles. These findings demonstrate that capillaries contribute to skeletal muscle insulin resistance. Treatments that increase trans-endothelial insulin transport may be useful in enhancing the delivery of insulin to skeletal muscle for the treatment of insulin resistance or in generating fast-acting insulin analogs for diabetics.

CHAPTER VI

ACUTE NITRIC OXIDE SYNTHASE INHIBITION ACCELERATES TRANS-ENDOTHELIAL INSULIN TRANSPORT *IN VIVO*

Aims

Several studies have demonstrated that endothelial NO is positively correlated to skeletal muscle insulin action through its ability to increase microvascular perfusion. NO also regulates endothelial barrier permeability. This raises the possibility that NO may also regulate skeletal muscle insulin action through its effects on trans-endothelial insulin transport. The aim of **Chapter VI** is to investigate the effects of pharmacologically manipulating endothelial NO levels on trans-endothelial insulin transport *in vivo*.

Experimental Approach

To determine the effects of acutely modulating NO and blood pressure on trans-endothelial insulin transport and glucose metabolism, mice were treated with either L-NAME (NOS inhibitor), SNP, (NO donor), phenylephrine, or hydralazine. Phenylephrine and hydralazine are direct smooth muscle acting drugs that raise and lower blood pressure, respectively (261, 262). For each individual drug treatment, the same protocol was used for intravital microscopy, blood pressure measurements, and insulin tolerance experiments. For the L-NAME experiment, mice were administered a 30 mg/kg i.v. bolus (50μL volume) of L-NAME or an equivalent volume of saline 15 minutes prior to the beginning of experiments (**Figure 6.1A**). This timing and dose of L-NAME was chosen because it was previously shown to increase blood pressure (i.e. inhibit NOS) in rats (263). For SNP experiments, mice were treated

with a continuous infusion of either SNP (100μg/kg/min) or saline beginning 15 minutes before the experiment and continuing throughout the course of the study (**Figure 6.6A**). This dose was based on a previous study which showed that a 37μg/kg/min infusion lowered blood pressure within 15 minutes (264). We increased this dose to ensure that SNP would be effective in anesthetized mice. Phenylephrine and hydralazine were administered as primed, continuous infusions starting at 5 minutes prior to experiments and continuing throughout the study (**Figure 6.10A**). Mice were given a 300μg/kg or 1mg/kg bolus followed by a 300μg/kg/min or 1mg/kg/min continuous infusion of phenylephrine or hydralazine, respectively. These doses were chosen based on their ability to raise (phenylephrine) or lower (hydralazine) blood pressure (265, 266). Control mice were treated with equivalent infusion rates and volumes of saline.

Results*

Acute L-NAME treatment accelerates trans-endothelial insulin transport

We first tested the hypothesis that acutely reducing NO would impair insulin transport as suggested by studies in cultured bovine aortic endothelial cells (190). To reduce endothelial NO levels, we treated mice with L-NAME. L-NAME is an arginine-based inhibitor of all 3 isoforms of NOS and therefore reduces endothelial NO production (267). Mice received a 30 mg/kg i.v. bolus of L-NAME 15 minutes prior to intravital insulin imaging. As expected, treatment of mice with L-NAME increased blood pressure by ~30 mmHg throughout the course of the experiment (**Figure 6.1, A and B**). L-NAME treatment also reduced capillary diameter by ~0.4μm both prior to (**Figure 6.1, C and D**) and following the insulin bolus (**Figure 6.1C**). Finally, vascular NO signaling was dampened by L-NAME treatment as evidenced by lower levels of

* These results are described in a manuscript which has been accepted for publication: Williams IM, McClatchey PM, Bracy DP, Valenzuela FA, Wasserman DH. Acute nitric oxide synthase inhibition accelerates trans-endothelial insulin efflux *in vivo*. *Diabetes* 2018. *In press.*

phosphorylated vasodilator-stimulated phosphoprotein (VASP) in the gastrocnemius (**Figure 6.1, E-I**). Taken together, these results suggest that vascular NO levels were effectively reduced by L-NAME treatment.

After confirming that L-NAME reduced NO levels, we performed *in vivo* insulin imaging as described above. Interestingly, acute reduction of NO with L-NAME accelerated the kinetics of trans-endothelial insulin transport by ~30% (**Figure 6.2**). Namely, L-NAME increased the dissipation rate of the plasma/interstitial INS-647 gradient, indicating a more rapid movement of insulin across the endothelium (**Figure 6.2, B and C, Figure 6.3A**). This increase in trans-endothelial insulin transport was not due changes in clearance of insulin from the plasma, which reflects whole body insulin clearance, (**Figure 6.2D**) but rather increased appearance of insulin in the muscle interstitial space (**Figure 6.2E**). Furthermore, there was no difference in plasma-perfused surface area between saline and L-NAME-treated mice (**Figure 6.3B**). Therefore, L-NAME, which increased capillary permeability to insulin without altering the surface area for insulin exchange, enhanced total extravascular insulin delivery (**Figure 6.3, C and D**). Thus, acute reduction of systemic NO by L-NAME accelerates the movement of insulin across the endothelium and increases total insulin delivery.

Acute L-NAME treatment enhances the kinetics of insulin-induced glucose lowering

Following the 4U/kg INS-647 bolus during intravital microscopy experiments, we observed that the blood glucose in L-NAME-treated mice was ~55mg/dl lower than in saline-treated mice (**Figure 6.4A**), reflecting an increase in insulin sensitivity. Furthermore, L-NAME treatment resulted in a non-significant 35% increase in the accumulation of 2[^{14}C]DGP, an isotopic glucose tracer, in the gastrocnemius (**Figure 6.4B**). These results suggest that acute

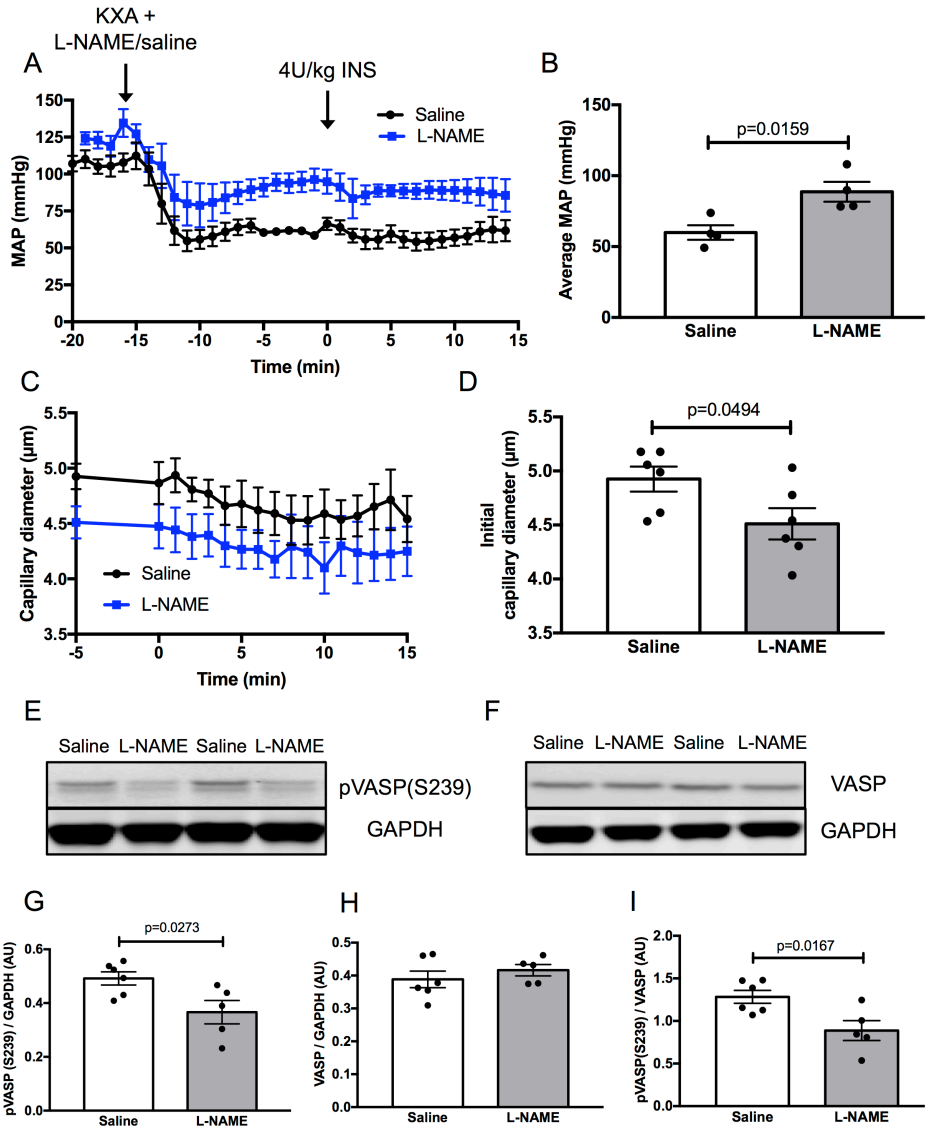

Figure 6.1: Acute L-NAME treatment increases blood pressure, reduces capillary diameter and decreases NO signaling. A) Mean arterial blood pressure measured through an indwelling carotid artery catheter in saline (n=4) and L-NAME-treated (n=4) mice. Mice were anesthetized with KXA and treated with either saline or 30mg/kg L-NAME at t= - 15 min. At t = 0 min, mice were administered a 4U/kg insulin bolus, as during the imaging experiments. **B)** Average MAP from t = - 10 to 15 min. **C)** Capillary diameter as a function of time during INS-647 imaging experiments. **D)** Average diameter of capillaries (rhodamine dextran-labeled vascular structures) at t = - 5 min. **E)** Representative immunoblots of phosphorylated VASP (S239) and GAPDH in gastrocnemius homogenates. **F)** Representative immunoblots of total VASP and GAPDH in gastrocnemius. **G-I)** Levels of **(G)** phosphorylated VASP (S239), **(H)** total VASP and **(I)** the ratio of pVASP/VASP as determined by densitometric analysis of immunoblots in saline (n=6) and L-NAME-treated (n=5) mice. Groups were compared using Student's t-test. KXA – ketamine/xylazine/acepromazine cocktail, MAP – mean arterial pressure, L-NAME – L-N^G-Nitroarginine methyl ester, VASP – vasodilator-stimulated phosphoprotein, GAPDH – glyceraldehyde 3-phosphate dehydrogenase.

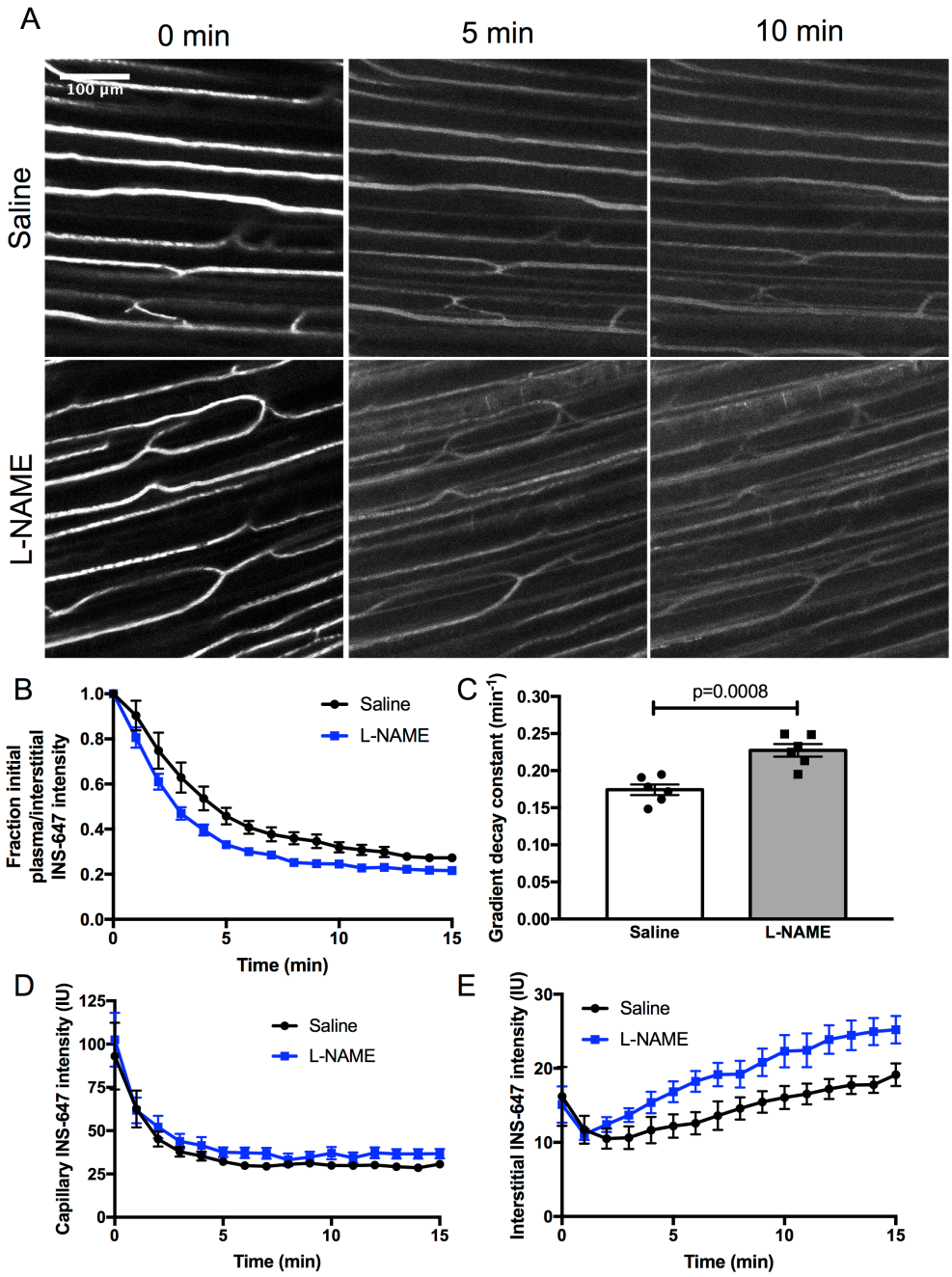

Figure 6.2: Acute inhibition of nitric oxide synthase by L-NAME enhances trans-endothelial insulin efflux. **A)** Representative INS-647 images (max intensity projections) from mice treated with either saline (n=6) or L-NAME (30 mg/kg i.v.; n=6) 15 minutes prior to the 4U/kg INS-647 bolus. **B)** The ratio of plasma to interstitial INS-647 as a function of time following injection normalized to the ratio at t = 0 min. **C)** The exponential decay constant of the plasma / interstitial INS-647 ratio, a measure of insulin efflux kinetics. **D)** Capillary INS-647 intensity as a function of time following INS-647 injection. **E)** Interstitial INS-647 as a function of time following INS-647 injection. Interstitial INS-647 intensity is defined as the average INS-647 intensity between 1-3µm from the capillary wall. Groups were compared using Student's t-test. INS-647 – insulin 647, IU – intensity units, L-NAME – L-N^{G}-Nitroarginine methyl ester.

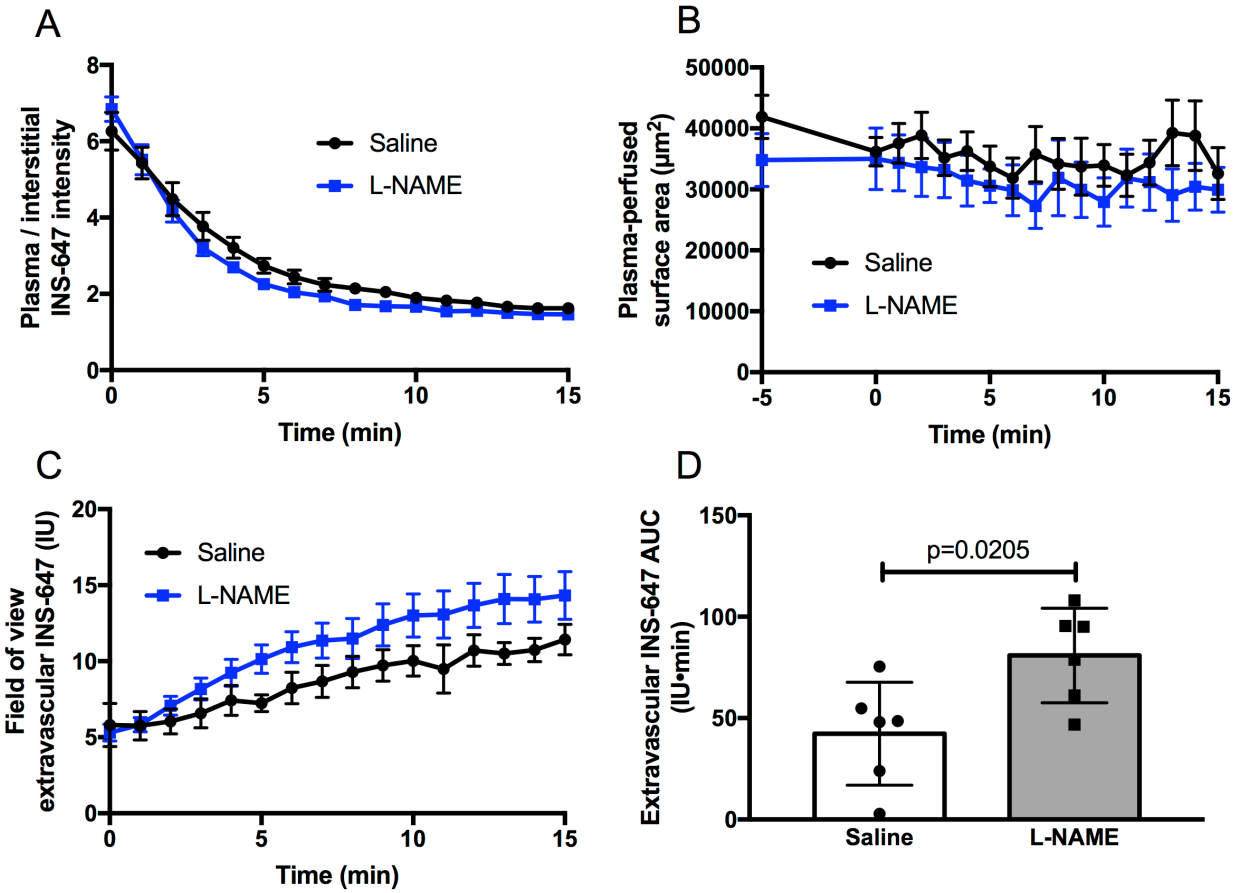

Figure 6.3: Acute L-NAME treatment increases capillary permeability to insulin and total extravascular insulin delivery. A) The ratio of plasma to interstitial INS-647 as a function of time following INS-647 injection in saline (n=6) and L-NAME-treated (n=6) mice. **B)** Vascular cross-sectional surface area over the course of the intravital microscopy experiment. INS-647 was administered at t = 0 min. **C)** Average INS-647 intensity in the entire extravascular space of the field of view. **D)** Baseline-subtracted area under the extravascular INS-647 curve. Groups were compared using Student's t-test.

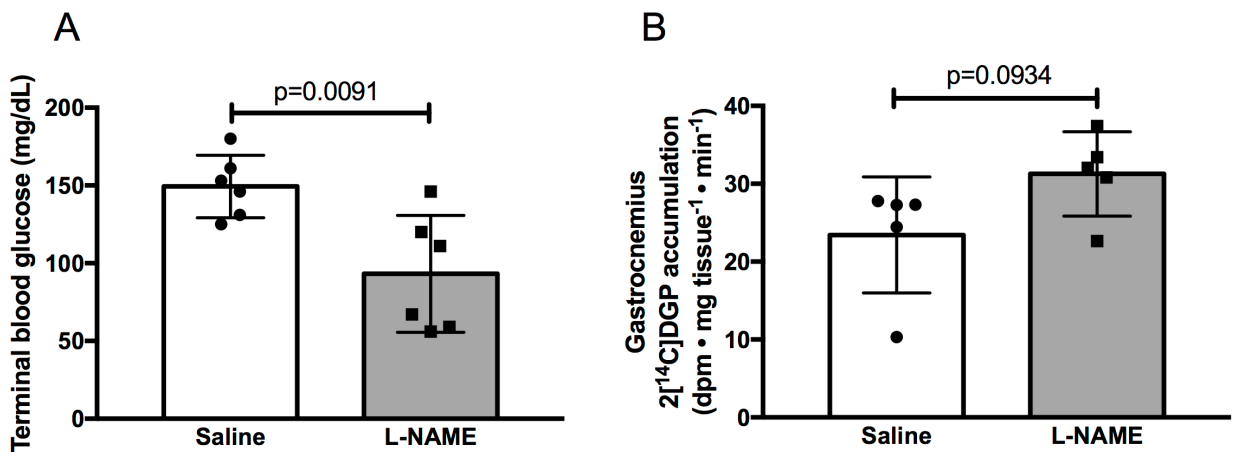

Figure 6.4: Effects of acute L-NAME treatment on insulin-induced glucose lowering and 2[^{14}C]DGP accumulation during INS-647 imaging experiments. A) Tail-vein blood glucose levels following an INS-647 imaging experiment in mice treated with either saline (n=6) or L-NAME (n=6). **B)** Accumulation of 2[^{14}C]DGP in the gastrocnemius of mice treated with either saline (n=5) or L-NAME (n=5). Groups were compared using unpaired Student's t-test. 2[^{14}C]2DGP – 2[^{14}C]deoxyglucose-6-phosphate.

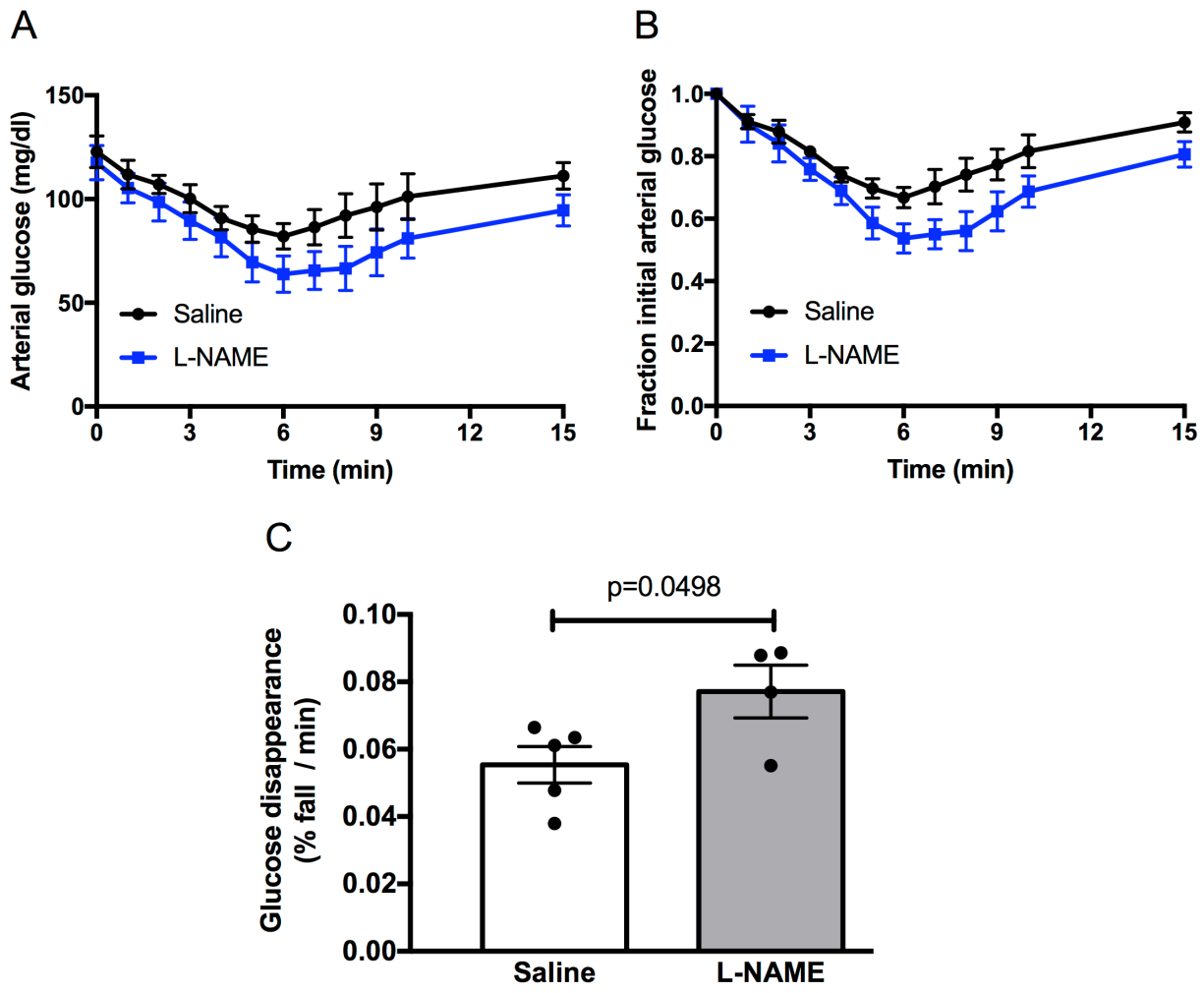

Figure 6.5: **Acute L-NAME treatment accelerates insulin-induced glucose lowering in conscious, unstressed mice. A)** Arterial glucose excursions following a 25mU/kg insulin bolus (t = 0 min) in mice treated with saline (n=5) or L-NAME (n=4) 15 minutes prior to the insulin bolus. **B)** Glucose excursions from **A** displayed as a fraction of arterial glucose levels at t = 0 min. **C)** Rate of fractional glucose disappearance from t = 0 to t = 6 min, an index of insulin sensitivity.

L-NAME treatment enhanced insulin-stimulated glucose metabolism. To more comprehensively assess the effects of L-NAME on insulin sensitivity, we performed frequently-sampled intravenous insulin tolerance tests (**Figure 6.5**). We chose to perform insulin tolerance tests as to mimic the experimental design of the intravital microscopy experiments, which also assessed the response to an insulin bolus. Following treatment with a 25mU/kg insulin bolus, L-NAME-treated mice displayed a more rapid glucose lowering than saline-treated mice (**Figure 6.5, A and B**). Namely, the fractional fall in glucose per minute was increased by ~40% with L-NAME treatment (**Figure 6.5C**). These findings demonstrate that acute L-NAME treatment accelerates glucose lowering following an intravenous insulin bolus.

Acute NO donor treatment does not affect trans-endothelial insulin transport kinetics

In light of the finding that reducing endothelial NO with L-NAME enhanced trans-endothelial insulin transport, we hypothesized that acutely raising NO would have the opposite effect. To test this hypothesis, we treated mice with a 100μg/kg/min continuous infusion of SNP, an NO donor. SNP treatment reduced blood pressure by 10mmHg during the treatment period prior to insulin stimulation (**Figure 6.6, A and B**). Interestingly, the hypotensive effect of SNP was abolished by insulin administration (**Figure 6.6, A and B**). The diameter of capillaries was unaffected by SNP treatment (**Figure 6.6, C and D)**. Finally, the ratio of phosphorylated to total VASP, an index of vascular NO signaling, was increased by ~40%, although this difference was not statistically significant (**Figure 6.6, E-I)**. These findings indicate that SNP treatment modestly elevated NO levels.

Using intravital insulin imaging we observed that SNP treatment had no effect on trans-endothelial insulin transport (**Figure 6.7**). Namely, SNP treatment did not alter the dissipation

rate of the plasma/interstitial INS-647 gradient (**Figure 6.7, B and C, Figure 6.8A**) nor the INS-647 kinetics in the plasma and interstitial space (**Figure 6.7, D and E**). Furthermore, as SNP had no effect on plasma-perfused surface area (**Figure 6.8B**), it did not change total extravascular insulin delivery (**Figure 6.8, C and D**). Consistent with the lack of an SNP effect on trans-endothelial insulin transport and insulin delivery, SNP treatment did not alter the blood glucose (**Figure 6.9A**) nor the accumulation of 2[^{14}C]DGP in the gastrocnemius following the imaging experiment (**Figure 6.9B**). Taken together, these findings suggest that acutely increasing NO with SNP, in otherwise healthy mice, does not affect trans-endothelial insulin transport.

NO-independent modulation of blood pressure does not affect trans-endothelial insulin transport kinetics

As shown above, L-NAME treatment accelerates trans-endothelial insulin transport and increases blood pressure. To test whether the effects of L-NAME on trans-endothelial insulin transport kinetics were due solely to changes in blood pressure we treated mice with either phenylephrine or hydralazine. These drugs act directly on smooth muscle to raise and lower blood pressure, respectively (261, 262). Compared to saline-treated mice, phenylephrine raised blood pressure by ~15 mmHg whereas hydralazine lowered it by the same amount (**Figure 6.10, A and B**). Phenylephrine treatment reduced the initial capillary diameter by ~0.6μm **(Figure 6.10, C and D)**, although this effect was not sustained following the insulin bolus **(Figure 6.10C)**. Hydralazine had no effect on capillary diameter **(Figure 6.10, C and D)**.

Intravital imaging of insulin efflux revealed that neither phenylephrine nor hydralazine treatment affected the rate at which insulin transited the endothelium (**Figure 6.11, B and C, Figure 6.12**). Of note, phenylephrine did appear to enhance the clearance of INS-647 from the

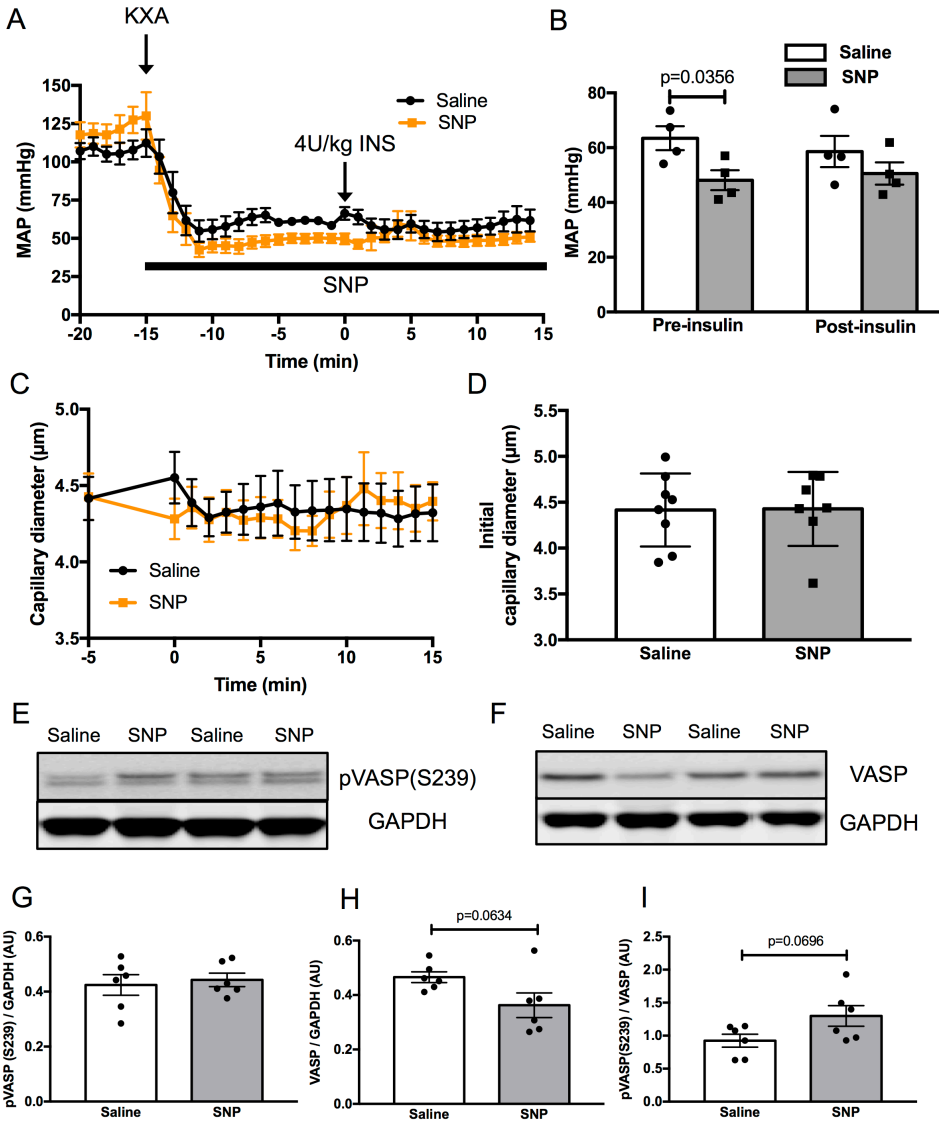

Figure 6.6: Effects of SNP on blood pressure, capillary diameter, and nitric oxide signaling. **A)** Mean arterial blood pressure (MAP) measured through an indwelling carotid artery catheter in saline (n=4) and SNP-treated (n=4) mice. Of note, the saline control group is the same as used for determination of the blood pressure effects of L-NAME **(Figure 1A)**. Mice were anesthetized with KXA and treated with a continuous infusion SNP beginning at t = - 15 min and continuing throughout the experiment. At t = 0 min, mice were administered a 4U/kg bolus of insulin, as during the imaging experiments. **B)** Average MAP during SNP or saline treatment prior to (t = - 10 min to t = 0 min) or following (t = 0 min to t = 15 min) insulin treatment. **C)** Capillary diameter as a function of time during INS-647 imaging experiments. **D)** Average diameter of capillaries (rhodamine dextran-labeled vascular structures) at t = - 5 min. **E)** Representative immunoblots of phosphorylated VASP (S239) and GAPDH in gastrocnemius. **F)** Representative immunoblots of total VASP and GAPDH in gastrocnemius. **G-I)** Levels of **(G)** phosphorylated VASP (S239), **(H)** total VASP and **(I)** the ratio of pVASP/VASP as determined by densitometric analysis of immunoblots in saline (n=6) and SNP-treatmed mice (n=6). Groups were compared using Student's t-test. SNP – sodium nitroprusside.

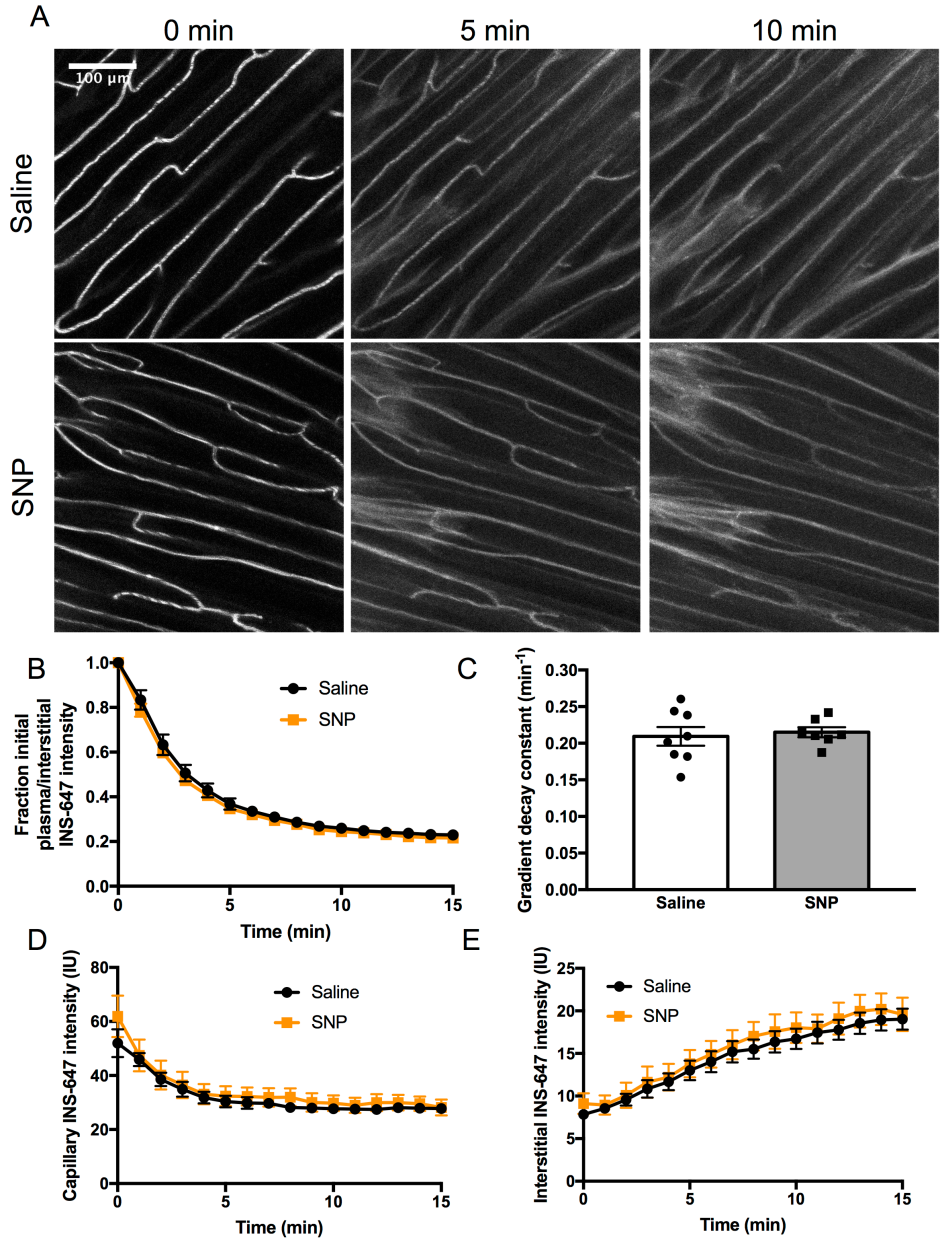

Figure 6.7: Nitric oxide donor treatment has no effect on trans-endothelial insulin efflux kinetics. A) Representative INS-647 images (max intensity projections) from mice treated with either saline (n=8) or 100µg/kg/min SNP (n=7). Continuous infusions of saline or SNP were begun 15 min prior to the INS-647 bolus and continued throughout the experiment. **B)** The ratio of plasma to interstitial INS-647 as a function of time following injection normalized to the ratio at t = 0 min. **C)** The exponential decay constant of the plasma / interstitial INS-647 ratio, a measure of insulin efflux kinetics. **D)** Capillary INS-647 intensity as a function of time following INS-647 injection. **E)** Interstitial INS-647 as a function of time following INS-647 injection. Interstitial INS-647 intensity is defined as the average INS-647 intensity between 1-3µm from the capillary wall. Groups were compared using Student's t-test. INS-647 – insulin 647, SNP – sodium nitroprusside.

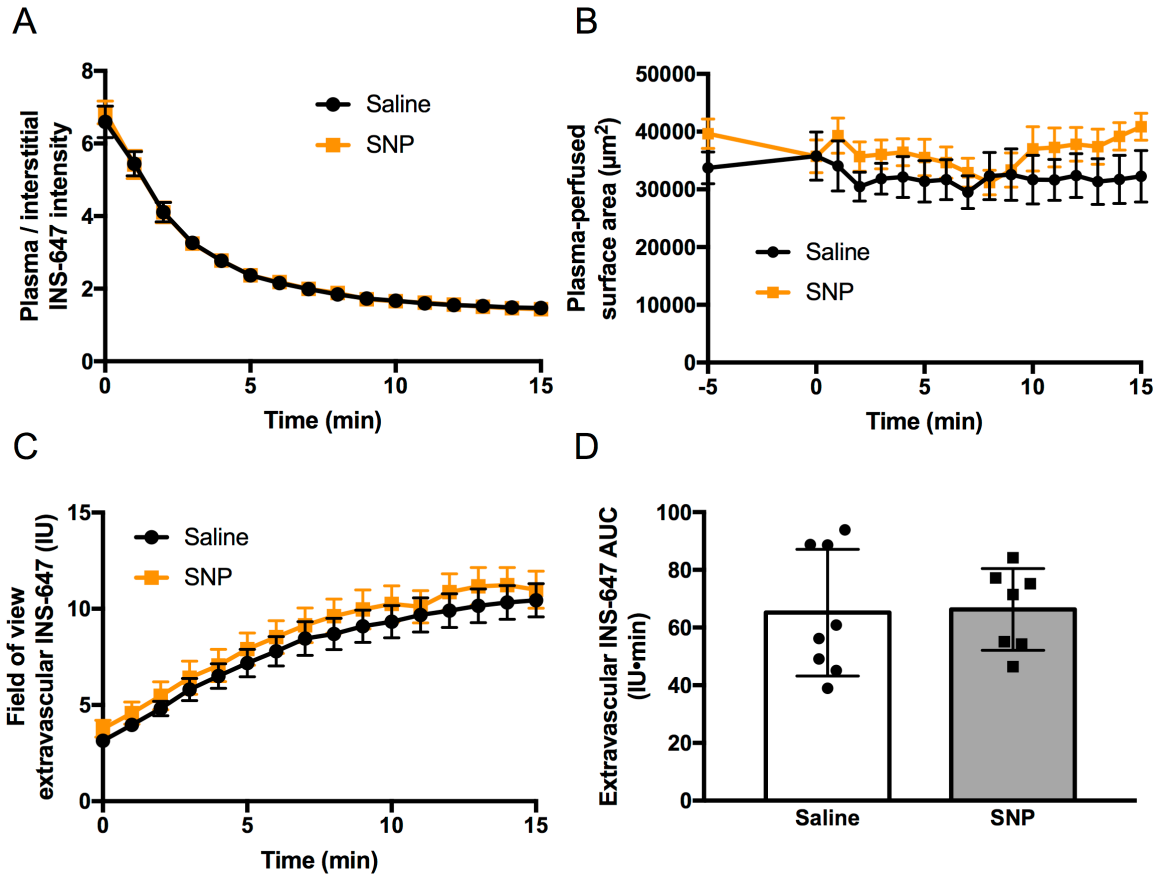

Figure 6.8: No effect of SNP treatment on gastrocnemius insulin delivery. A) The ratio of plasma to interstitial INS-647 as a function of time following INS-647 injection in saline (n=8) or SNP-treated mice (n=7). **B)** Vascular cross-sectional surface area over the course of the intravital microscopy experiment. INS-647 was administered at t = 0 min. **C)** Average INS-647 intensity in the entire extravascular space of the field of view. **D)** Baseline-subtracted area under the extravascular INS-647 curve. Groups were compared using Student's t-test.

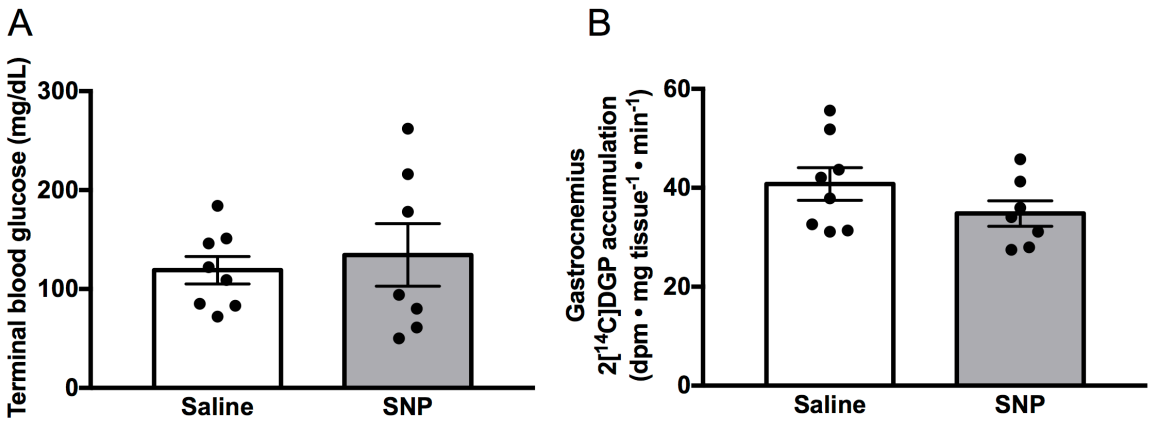

Figure 6.9: No effect of SNP treatment on insulin-induced glucose lowering and 2[^{14}C]DGP accumulation during INS-647 imaging experiments. A) Tail-vein blood glucose levels following an INS-647 imaging experiment in mice treated with either saline (n=8) or SNP (n=7). **B)** Accumulation of 2[^{14}C]DGP in the gastrocnemius. Groups were compared using unpaired Student's t-test.

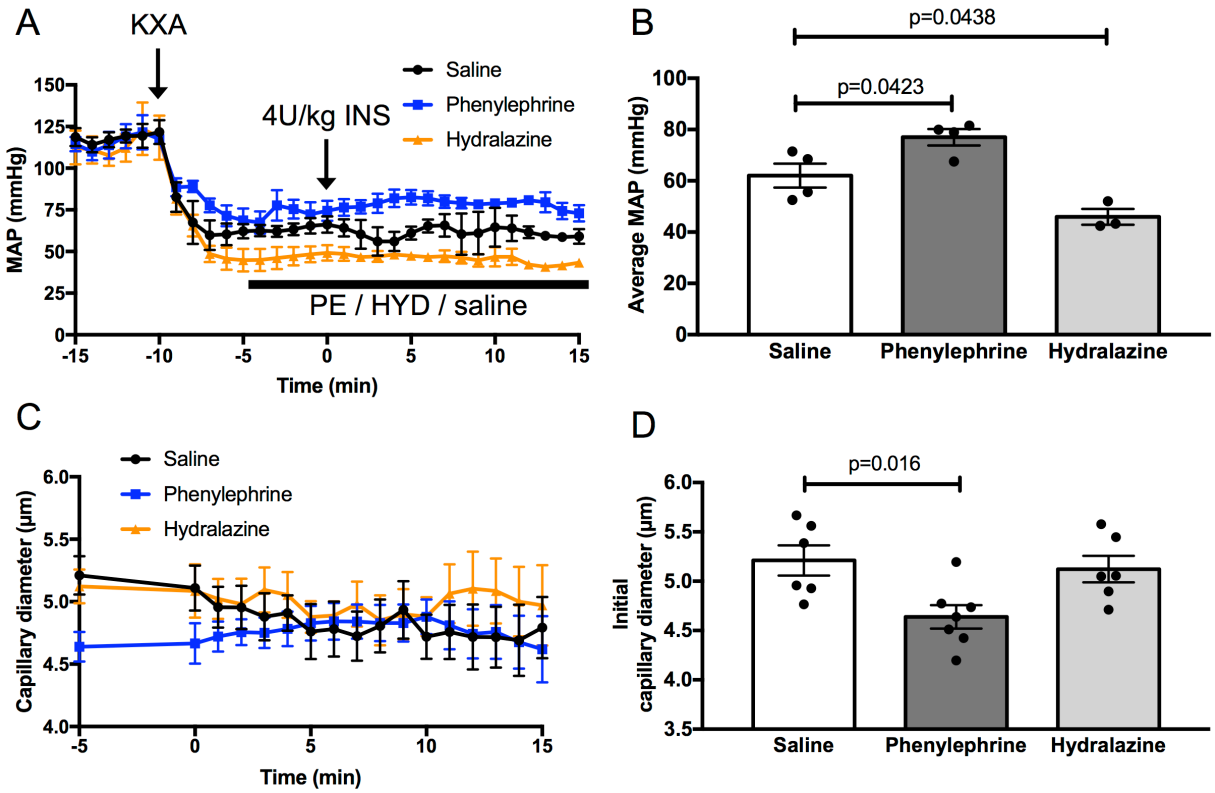

Figure 6.10: Effects of phenylephrine and hydralazine on blood pressure and capillary diameter. A) Mean arterial blood pressure (MAP) measured through an indwelling carotid artery catheter in saline (n=4), phenylephrine (n=4), or hydralazine-treated (n=3) mice. Mice were anesthetized with KXA and treated with a continuous infusion of either saline, phenylephrine, or hydralazine beginning at t = - 5 min and continuing throughout the experiment. At t = 0, mice were administered a 4U/kg insulin bolus, as during the imaging experiments. **B)** Average MAP from t = - 5 to 15 min. **C)** Capillary diameter as a function of time during INS-647 imaging experiments in mice treated with saline (n=6), phenylephrine (n=7), or hydralazine (n=6). **D)** Average diameter of capillaries at t = - 5 min. Groups were compared with a one-way ANOVA followed by Dunnett's test for multiple comparisons to a control group (saline).

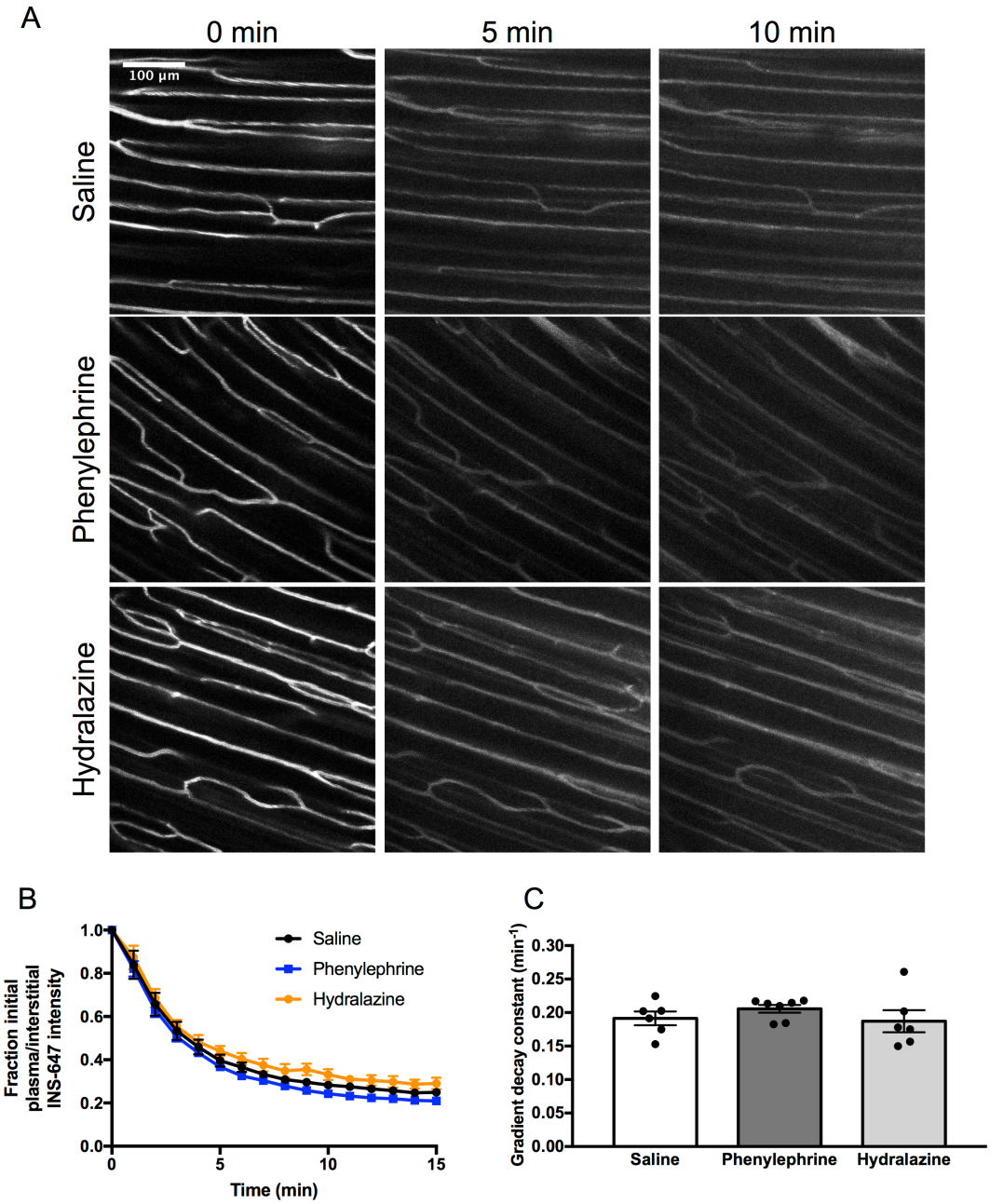

Figure 6.11: Neither a direct smooth muscle-acting vasoconstrictor nor dilator alter trans-endothelial insulin efflux.

A) Representative INS-647 images (max intensity projections) from mice treated with either saline (n=6), phenylephrine (n=7), or hydralazine (n=6). Primed, continuous infusions of saline, phenylephrine (300µg/kg bolus, 300µg/kg/min continuous infusion), or hydralazine (1mg/kg bolus, 1mg/kg/min continuous infusion) were begun 5 min prior to the INS-647 bolus. **B)** The ratio of plasma to interstitial INS-647 as a function of time following injection normalized to the ratio at t = 0 min. **C)** The exponential decay constant of the plasma/interstitial INS-647 ratio, a measure of insulin efflux kinetics. Groups were compared using one-way ANOVA followed by Dunnett's test for multiple comparisons to a control group (saline).

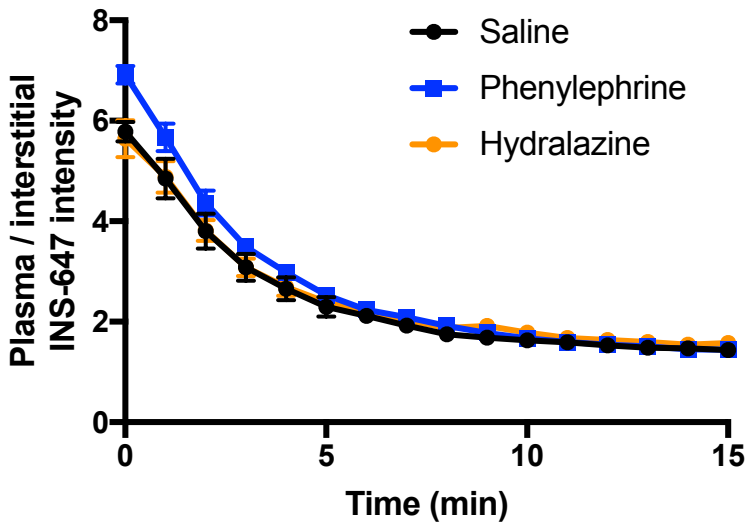

Figure 6.12: Effects of phenylephrine and hydralazine on the plasma/interstitial INS-647 ratio. The ratio of plasma to interstitial INS-647 as a function of time following INS-647 injection in mice treated with saline (n=6), phenylephrine (n=7), or hydralazine (n=6).

plasma but this was also associated with a reduced appearance of INS-647 in the interstitial space in skeletal muscle (**Figure 6.13, A-D**). This suggests that, while phenylephrine may enhance the whole-body clearance of insulin from the plasma by other organs, (**Figure 6.13B**), it does not change trans-endothelial insulin transport in skeletal muscle capillaries (**Figure 6.11C**). Phenylephrine treatment had no effect on plasma-perfused surface area (**Figure 6.13E**) and therefore, combined with its effect to dampen interstitial INS-647 appearance (**Figure 6.13C**), reduced total extravascular insulin delivery (**Figure 6.13, F and G**). Thus, it appears that while phenylephrine does not affect either trans-endothelial insulin transport or the surface area for insulin exchange, it diverts insulin away from muscle by increasing its clearance by other organs. In total, these findings indicate that increasing or decreasing blood pressure by ~15mmHg does not affect trans-endothelial insulin transport.

With respect to glucose metabolism, phenylephrine treatment resulted in a non-significant ~50mg/dl increase in glucose following intravital insulin imaging **(Figure 6.14A)**. Furthermore, phenylephrine reduced the accumulation of 2[^{14}C]DGP in the gastrocnemius indicating that it induced skeletal muscle insulin resistance **(Figure 6.14B)**. Hydralazine had no effect on either blood glucose or gastrocnemius 2[^{14}C]DGP accumulation **(Figure 6.14B)**. Taken together, these results suggest that phenylephrine induces skeletal muscle insulin resistance through a mechanism that does not involve alterations to trans-endothelial insulin transport kinetics.

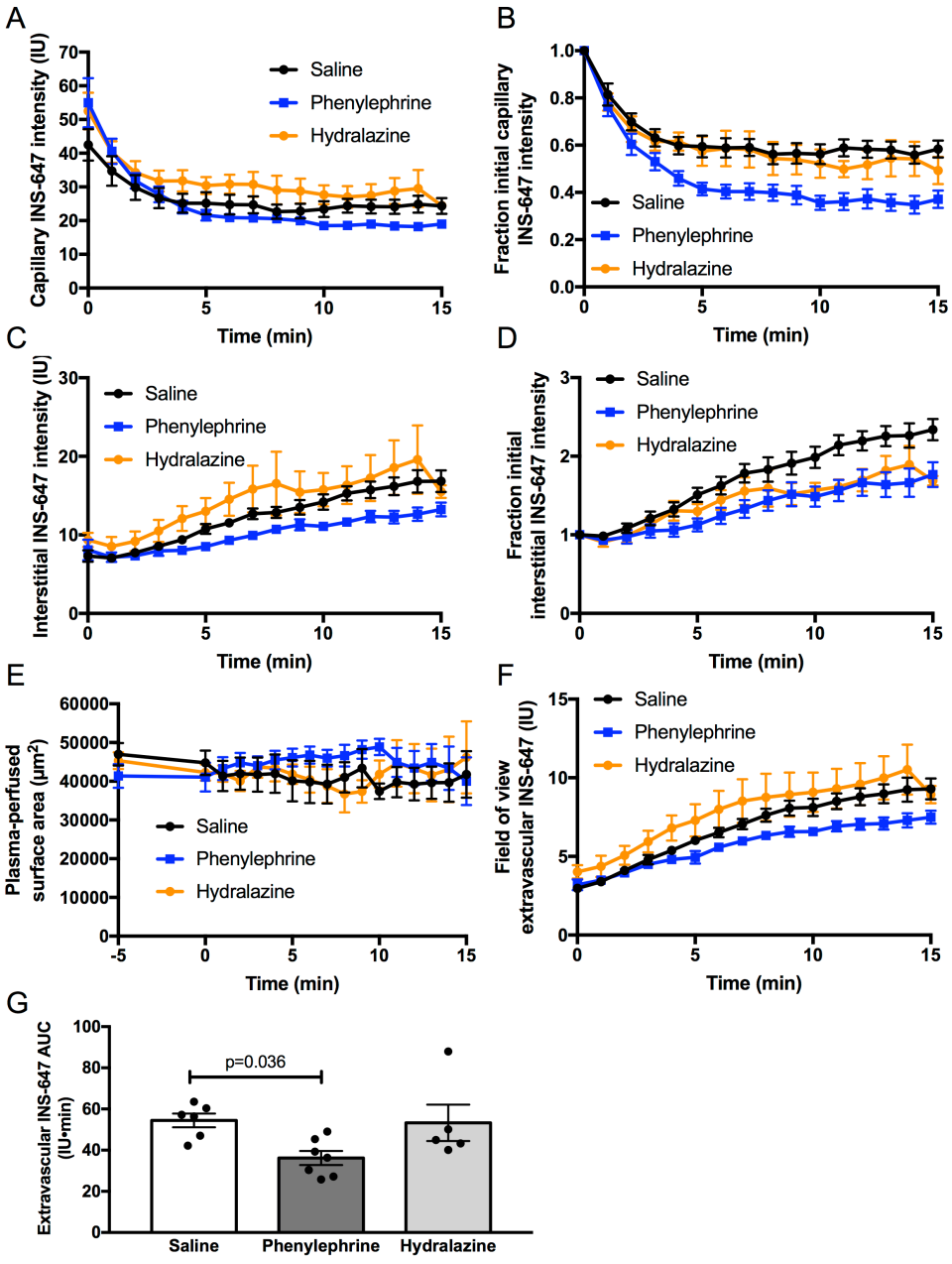

Figure 6.13: Effects of phenylephrine and hydralazine on plasma insulin clearance, interstitial appearance, and insulin delivery. A) Capillary INS-647 intensity as a function of time following INS-647 injection in mice treated with saline (n=6), phenylephrine (n=7), or hydralazine (n=6). **B)** Data in **A** normalized to capillary INS-647 at t = 0 min. **C)** Interstitial INS-647 as a function of time following INS-647 injection. Interstitial INS-647 intensity is defined as the average INS-647 intensity between 1-3μm from the capillary wall. **D)** Data in **C** normalized to interstitial INS-647 at t = 0 min. **E)** Vascular cross-sectional surface area over the course of the intravital microscopy experiment. **F)** Average INS-647 intensity in the entire extravascular space of the field of view. **G)** Baseline-subtracted area under the extravascular INS-647 curve. Groups were compared with a one-way ANOVA followed by Dunnett's test for multiple comparisons to a control group (saline).

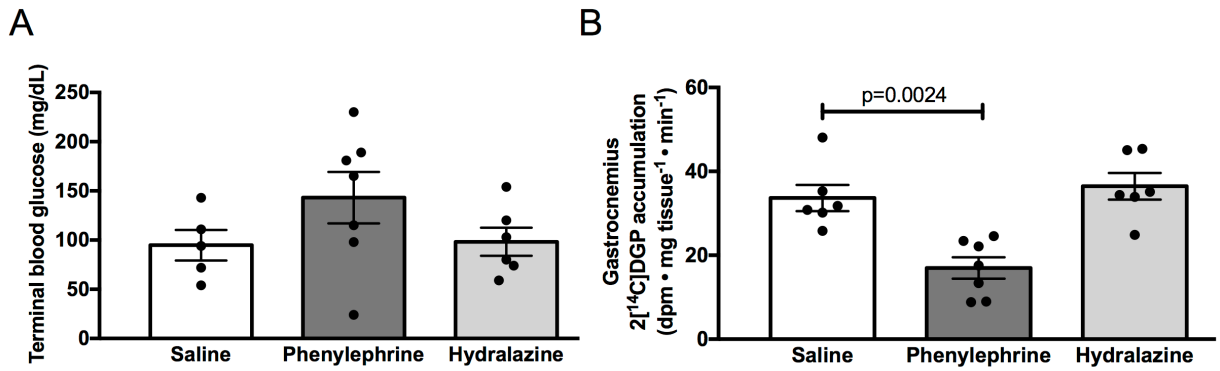

Figure 6.14: Effects of phenylephrine and hydralazine on insulin-induced glucose lowering and 2[^{14}C]DGP accumulation during INS-647 imaging experiments. A) Tail-vein blood glucose levels following an INS-647 imaging experiment in mice treated with either saline (n=5), phenylephrine (n=7), or hydralazine (n=6). **B)** Accumulation of 2[^{14}C]DGP in the gastrocnemius of mice treated with either saline (n=6), phenylephrine (n=7), or hydralazine (n=6). Groups were compared using one-way ANOVA followed by Dunnett's test for multiple comparisons to a control group (saline).

Discussion

In this study, we utilized intravital imaging of fluorescent insulin to show that acute reduction of endothelial NO with L-NAME accelerates the rate at which insulin moves across the endothelium in skeletal muscle capillaries. This increase in trans-endothelial insulin transport kinetics was also associated with increased insulin delivery and accelerated whole-body insulin action. Interestingly, treatment with SNP, an NO donor, did not alter trans-endothelial insulin transport kinetics. Furthermore, a direct-acting vasoconstrictor, phenylephrine, had no effect on trans-endothelial insulin transport kinetics, indicating that the effects of L-NAME on trans-endothelial insulin transport kinetics are not due solely to blood pressure changes. These findings demonstrate that acute pharmacological NO reduction induces changes to the skeletal muscle microvasculature which increase insulin efflux and delivery.

Several previous studies have investigated the effects of NO on microvascular permeability. With respect to insulin, Wang et al. demonstrated that inhibition of NO with L-NAME reduced the uptake of FITC-labeled insulin into cultured bovine aortic endothelial cells (190). This finding suggested that NO is a positive regulator of trans-endothelial insulin transport *in vitro*, which is seemingly at odds with the present study which shows that L-NAME enhances trans-endothelial insulin transport *in vivo*. It is conceivable that L-NAME may block the non-specific vesicular uptake of insulin into endothelial cells and thereby promote more efficient paracellular movement of insulin through inter-endothelial junctions. Additionally, the hemodynamic effects of L-NAME on the microvasculature, which are present *in vivo* but not *in vitro*, may contribute to the contrasting results. Another important consideration is that the mechanism of trans-endothelial insulin transport is different *in vivo* than in cell culture and depends on the type of endothelial cell used (155). With our intravital microscopy technique, we

can directly visualize and quantitate the movement of insulin across the endothelium in skeletal muscle capillaries *in vivo*.

Other groups have assessed the effects of modulating NO on microvascular permeability *in vivo* to macromolecules besides insulin. While the precise effects of NO on capillary permeability are still debated, it is clear that they are dependent on context (185, 268). Under basal conditions, NO reduction by NOS inhibition increases capillary permeability in a number of different species and vascular beds including skeletal muscle (183, 184, 269). On the other hand, hyperproduction of NO during pathological inflammatory states also increases capillary permeability (185). Thus, it appears that the relationship between endothelial NO production and microvascular permeability is U-shaped, with low and high levels of NO being associated with increased capillary permeability. This is consistent with the present study where we show that, during a non-inflammatory state, reduction of NO with L-NAME increases the permeability of skeletal muscle capillaries to insulin. Interestingly, increasing NO availability in otherwise healthy mice with SNP had no effect on capillary permeability to insulin. It is possible that high levels of NO only increase microvascular permeability during inflammatory conditions in which oxidant production is also elevated.

Mechanistically, we found that the effect of L-NAME on trans-endothelial insulin transport was not due to changes in blood pressure alone, as phenylephrine also raised blood pressure but did not alter trans-endothelial insulin transport. These findings suggest that L-NAME increases trans-endothelial insulin transport either through direct effects on the capillary endothelium or by altering the trans-capillary balance of Starling forces. The findings described in **Chapter IV** demonstrated that insulin moves across the capillary endothelium in skeletal muscle either by a convective paracellular route or by non-saturable vesicular transcytosis (252).

Malik and colleagues used electron microscopy to show that treatment of mice with L-NAME opens inter-endothelial junctions (183). This increased distance between endothelial cells would allow for enhanced paracellular extravasation of insulin across the endothelium, consistent with our previous findings. Furthermore, in the present study we show that L-NAME reduces capillary diameter, indicating that L-NAME treatment most likely alters capillary hemodynamics. These hemodynamic effects may alter the balance of Starling forces across the endothelium and, subsequently, the convective movement of insulin into the interstitial space. Finally, it is also conceivable that reduction of endothelial NO production affects either the abundance of endothelial vesicles or the kinetics of their trafficking.

Consistent with the increase in trans-endothelial insulin transport and insulin delivery, we found that acute inhibition of NOS with L-NAME increased the effect of insulin on whole-body glucose kinetics. This corroborates the findings of Vincent et al. who showed that, following 15 minutes of a continuous insulin and L-NAME infusion in rats, L-NAME treatment increased femoral artery blood flow without changing arteriovenous glucose difference across the hindlimb (95). This indicates that, at this early time point, insulin-stimulated muscle glucose uptake is enhanced by L-NAME treatment. Interestingly, these investigators also showed that by 30 minutes, the hindlimb arteriovenous glucose difference was reduced whereas femoral artery blood flow remained elevated in the L-NAME group, indicating a small reduction in insulin-stimulated muscle glucose uptake. Taken together, these findings suggest that L-NAME initially increases skeletal muscle insulin action whereas more prolonged administration results in skeletal muscle insulin resistance.

Previous studies in humans and rodents have generally found a negative relationship between NOS inhibition and muscle insulin sensitivity during insulin clamps (119, 186, 187). In

the present study, we show that L-NAME treatment accelerates insulin-stimulated glucose lowering during an insulin tolerance test. Differences in study design may explain these seemingly contradictory findings. Insulin clamps, as used previously, (119, 186, 187) are usually designed to assess steady-state insulin action whereas the glucose response to an insulin bolus is an indicator of the kinetics of insulin action. Thus, it is possible that L-NAME treatment enhances the kinetics of insulin action while also reducing maximal steady-state insulin-stimulated glucose disposal. These differing effects can be reconciled considering that L-NAME both increases the movement of insulin across the endothelium while also reducing skeletal muscle perfusion (95, 119). We hypothesize that the effect of L-NAME to increase capillary permeability to insulin accelerates the kinetics of insulin action. On the other hand, the L-NAME-induced reduction in muscle perfusion is most likely responsible for limiting maximal steady-state insulin action. It is interesting to speculate that these opposing effects of L-NAME may be protective, serving to buffer the muscle from changes in macromolecular delivery. Namely, when NO bioavailability and muscle perfusion are reduced, capillaries become more permeable thereby compensating for the reduced perfusion and maintaining macromolecular delivery.

Another key distinction between the present study and previous investigations (119, 186, 188, 189) is the timing and duration of NOS inhibition. Previous insulin clamp studies have typically infused NOS inhibitors after establishing steady-state hyperinsulinemia (119, 186). This is different from our experimental design, where we treated mice with L-NAME prior to insulin stimulation. Furthermore, studies utilizing genetic deletion of NOS (188, 189) assess the effects of chronic NO reduction. In the current study, we were interested in determining the acute role of

NO in the delivery of an insulin bolus to skeletal muscle. We chose to study nonsteady-state insulin action as it is more physiologically relevant than a prolonged steady-state insulin clamp.

In light of the finding that L-NAME increased trans-endothelial insulin transport, we speculated that treating mice with SNP, an NO donor, would have the opposite effect. However, we found that there was no effect of NO on either trans-endothelial insulin transport or accumulation of 2[^{14}C]DGP in the gastrocnemius. This finding is largely consistent with previous studies, which showed that SNP infusion either does not alter insulin-stimulated glucose disposal (115) or slightly reduces it (264). One limitation of our study is that, despite infusing a high dose of SNP which was previously shown to have major cardiovascular and metabolic effects (264), blood pressure was only lowered by ~10mmHg and the 40% increase in VASP activation (i.e. NO signaling) was not statistically significant. The blood pressure response to SNP may have been attenuated because mice are already hypotensive when anesthetized. Furthermore, because insulin stimulates NO production from endothelial cells (108), it is possible that NO signaling is already near-maximal in the saline-treated control mice. In this situation, SNP may have little additional effect on VASP activation. As such, we hypothesize that, under conditions where endothelial NO is sufficient, adding more NO gives no further benefit to trans-endothelial insulin transport or muscle insulin sensitivity.

As noted above, we also demonstrated that while phenylephrine and hydralazine raise and lower blood pressure, respectively, neither drug altered trans-endothelial insulin transport. These findings suggest that the L-NAME-induced increase in trans-endothelial insulin transport is not due to elevated blood pressure alone. One caveat, however, is that L-NAME treatment raised blood pressure by 30mmHg whereas phenylephrine only raised it by 15mmHg. Thus, it is possible that a more pronounced increase in blood pressure might affect trans-endothelial insulin

transport. In contrast to L-NAME, however, phenylephrine induced muscle insulin resistance during intravital microscopy experiments through a mechanism independent of trans-endothelial insulin transport. Previous studies of phenylephrine and muscle insulin sensitivity are limited, with one study in humans showing that phenylephrine has no effect on whole-body insulin sensitivity (270). However, other adrenergic receptor agonists have been shown to cause peripheral insulin resistance (271). In the current study, we showed that, although the relationship between plasma and interstitial insulin was not different with phenylephrine treatment, there was a lower total delivery of insulin to the interstitial space. It is possible that phenylephrine induced muscle insulin resistance either by diverting insulin to other organs or by limiting the microvascular delivery of glucose to muscle.

In summary, we demonstrate that reduction of endothelial NO enhances trans-endothelial insulin transport *in vivo* by a mechanism that is independent of blood pressure alone. Thus, acute reduction of NO levels has contrasting effects on microvascular perfusion and the capillary exchange of insulin, the net effect of which is to increase insulin delivery to skeletal muscle. These findings highlight the importance of considering the targeted blood vessel type (i.e. artery vs. capillary), kinetics of NO modulation, and desired microvascular exchange properties when designing NO-based therapies for metabolic disease.

Chapter VII

ANGIOTENSIN-(1-7), A VASOACTIVE PEPTIDE HORMONE, IMPROVES INSULIN SENSITIVITY IN DIET-INDUCED OBESE MICE

Aims

Our laboratory and others have found that chronic treatment of obese mouse models with vasodilators improves muscle insulin sensitivity. Ang-(1-7) is a vasodilatory peptide of the renin-angiotensin system that acutely increases insulin sensitivity and improves glucose homeostasis in rodent models of diet-induced insulin resistance. Whether chronic treatment of obese mice with Ang-(1-7) can reverse muscle insulin resistance is unknown. The aims of **Chapter VII** are to 1) determine whether Ang-(1-7) can restore skeletal muscle insulin sensitivity in a mouse model of obesity and insulin resistance and 2) investigate potential mechanisms by which chronic vasodilator therapy improves insulin sensitivity.

Experimental Approach

Male 6 week-old C57BL/6J mice (Jackson Laboratory) were fed a standard chow (5001 Laboratory Rodent Diet) or 60% HFD (Bioserv F3282) *ad libitum* for 11 weeks. After 8 weeks of diet, subcutaneous osmotic mini-pumps (Alzet Model 2004) were implanted to deliver Ang-(1-7) [400 ng/kg/min; Bachem] or saline vehicle for 3 weeks. This dosing regimen of Ang-(1-7) was chosen as it has been shown to improve endothelial function in HFD mice independent of changes in body weight (272).

Results*

Effect of Ang-(1-7) on cardiovascular indices

Plasma Ang-(1-7) was reduced in HFD versus chow-fed mice (**Table 7.1**; p=0.045 diet effect). Chronic Ang-(1-7) infusion restored HFD-induced reductions in the peptide to approximately 70% of levels seen in chow-fed mice. There were significant diet (p=0.015) and interaction (p=0.004) effects for plasma Ang II, which were driven entirely by increased Ang II levels in chow-fed mice following Ang-(1-7) treatment. HFD mice had increased systolic (p=0.001), diastolic (p=0.039) and mean (p=0.001) blood pressure, with no difference in HR (p=0.129). There was no effect of Ang-(1-7) on blood pressure or HR in chow-fed or HFD mice (**Table 7.1**).

Effect of Ang-(1-7) on metabolic indices:

Body weight and adiposity were higher in HFD mice (p=0.001 diet effect; **Table 7.2**). Ang-(1-7) did not alter body weight in HFD or chow-fed mice; however, there was a small reduction in adiposity (p=0.040 drug effect). HFD mice had higher basal arterial glucose and insulin (p=0.018 and p=0.001 diet effect, respectively), with no difference in NEFA. Ang-(1-7) tended to lower basal insulin (p=0.055 drug effect), but did not alter fasting glycemia or NEFA. During steady-state hyperinsulinemia, glucose was clamped at ~140 $mg \bullet dl^{-1}$ glucose in both HFD and chow-fed mice (**Figure 7.1, A and B**). HFD mice maintained higher insulin levels during the clamp (p=0.002 diet effect; **Table 7.2**), compared with chow-fed mice. Ang-(1-7) did not alter clamp glucose and insulin levels, but significantly enhanced insulin-mediated suppression of NEFA (p=0.001 drug effect; **Table 7.2**).

* These results have been published in: Williams IM, Otero YF, Bracy DP, Wasserman DH, Biaggioni I, Arnold AC. Chronic Angiotensin-(1-7) improves insulin sensitivity in high-fat fed mice independent of blood pressure. *Hypertension* 2016 May;67(5):983-91. PMID:26975707.

Table 7.1. Hormonal and Cardiovascular Effects of Chronic Ang-(1-7) Administration

Parameter, unit	Chow Vehicle	Chow Ang-(1-7)	HFD Vehicle	HFD Ang-(1-7)	P_{Diet}	P_{Drug}	P_{Int}
n	9	10	6	7			
Ang-(1-7), ng/ml	2.94±1.29	1.72±0.90	0.45±0.15	1.97±1.31	0.045	0.267	0.191
Ang II, ng/ml	0.16±0.06	0.51±0.14	0.18±0.02	0.09±0.03	0.015	0.074	0.004
SBP, mm Hg	123±5	128±3	143±4	143±3	0.001	0.574	0.566
DBP, mm Hg	97±5	98±4	109±3	104±3	0.039	0.658	0.515
MBP, mm Hg	110±5	113±3	126±3	123±2	0.001	0.949	0.454
Heart Rate, bpm	647±41	701±24	618±21	648±19	0.129	0.119	0.652

Data are mean±SEM and were analyzed by two-way ANOVA for diet effect (P_{Diet}), drug effect (P_{Drug}), and their interaction (P_{Int}). HFD, high fat diet; Ang, angiotensin; SBP, systolic blood pressure; DBP, diastolic blood pressure; MBP, mean blood pressure.

Table 7.2. Metabolic Effects of Chronic Ang-(1-7) Administration

Parameter, unit	Chow Vehicle	Chow Ang-(1-7)	HFD Vehicle	HFD Ang-(1-7)	P_{Diet}	P_{Drug}	P_{Int}
n	9	10	6	7			
Body Mass, g	29±1	28±1	39±2	37±1	0.001	0.321	0.981
Adiposity, %	6.7±0.7	6.5±0.2	35.6±2.6	30.1±1.4	0.001	0.040	0.056
Glucose, mg/dl							
Basal	132±7	131±7	152±13	153±7	0.018	0.969	0.923
Clamp	141±3	142±4	133±3	137±3	0.078	0.555	0.603
Insulin, pmol/l							
Basal	226±40	136±19	648±100	533±47	0.001	0.055	0.843
Clamp	585±59	569±58	1518±430	1245±290	0.002	0.549	0.480
NEFA, mmol/l							
Basal	0.81±0.12	0.62±0.13	0.57±0.10	0.37±0.08	0.055	0.129	0.947
Clamp	0.25±0.06	0.05±0.03	0.25±0.05	0.11±0.06	0.677	0.001	0.472

Data are mean±SEM and were analyzed by two-way ANOVA for diet effect (P_{Diet}), drug effect (P_{Drug}), and their interaction (P_{Int}). Metabolic hormones were measured in arterial blood at baseline (basal), and during steady state of hyperinsulinemic-euglycemic clamps (clamp). HFD, high fat diet; Ang, angiotensin; NEFA, non-esterified fatty acids.

Ang-(1-7) reverses HFD-induced skeletal muscle (skeletal muscle) insulin resistance:

The glucose infusion rate required to maintain euglycemia during steady state hyperinsulinemia, a measure of whole-body insulin sensitivity, was similar following Ang-(1-7) versus saline treatment in chow-fed mice (**Figure 7.1, C and E**; p=0.143). As expected, HFD mice had lower whole-body insulin sensitivity compared with chow fed-mice (p=0.001). Ang-(1-7) doubled the glucose infusion rate required to maintain euglycemia in HFD mice (**Figure 7.1, D and F**; p=0.017). This enhanced whole body insulin sensitivity was due to increased insulin-stimulated peripheral glucose disposal (R_d; **Figure 7.2A**; p=0.049). There was no effect of Ang-(1-7) on insulin-mediated suppression of endogenous glucose production ($Endo_{Ra}$; **Figure 7.2B**; p=0.476). Consistent with effects on peripheral glucose disposal, Ang-(1-7) augmented insulin-stimulated glucose uptake (R_g) in soleus, gastrocnemius, and vastus muscles in HFD mice, with no effect in epididymal adipose or cardiac tissue (**Figure 7.2, C and D**). Ang-(1-7) did not alter R_d, $Endo_{Ra}$ or R_g in chow-fed mice (**Figure 7.3**).

***Ang-(1-7) does not improve measures of perfusion in HFD mice**:*

To determine if the Ang-(1-7)-mediated improvement in insulin sensitivity was due to improved vascular glucose delivery, we measured indices of skeletal muscle perfusion in HFD mice. Levels of a capillary density marker (CD31) were not different in gastrocnemius muscle following Ang-(1-7) treatment **(Figure 7.4, A and B)**. Hind limb perfusion, measured by deposition of colored microspheres at the end of the insulin clamp, was not different between treatment groups (**Figure 7.4C**). Finally, Ang-(1-7) did not alter cardiac function (**Table 7.3**).

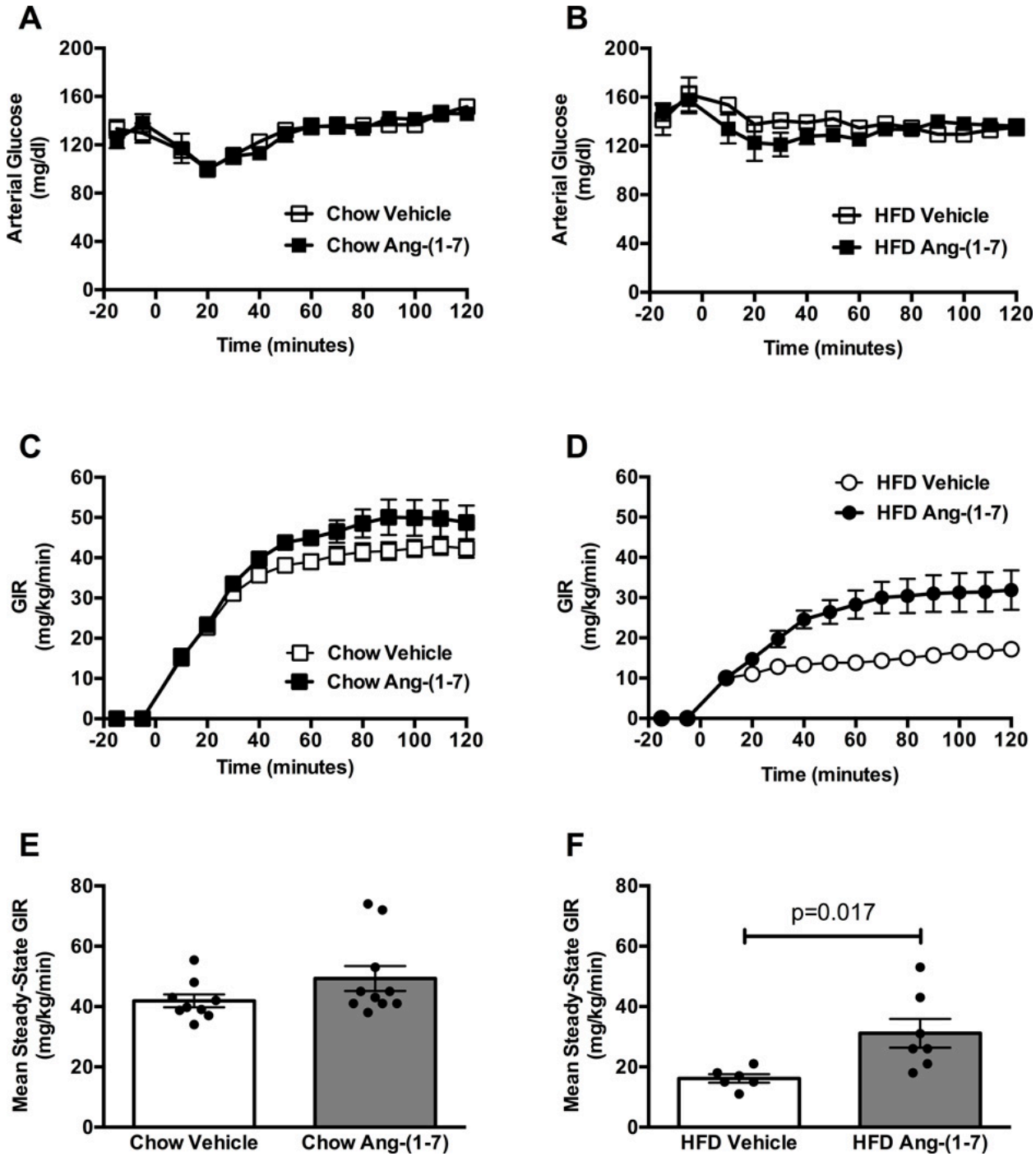

Figure 7.1: Ang-(1-7) improves whole-body insulin sensitivity in high-fat diet (HFD)-fed mice. A, B: Arterial glucose levels were maintained at ~140 mg/dl during insulin clamps by variable venous infusion of 50% glucose. **C, D:** The glucose infusion rate (GIR) needed to maintain euglycemia, a measure of whole-body insulin sensitivity, over the 120 min period of the insulin clamp. **E:** There was no effect of Ang-(1-7) on mean steady-state GIR (measured from t=80-120 min of the insulin clamp) in chow fed mice. F: Ang-(1-7) significantly increased the mean steady-state GIR in HFD mice.

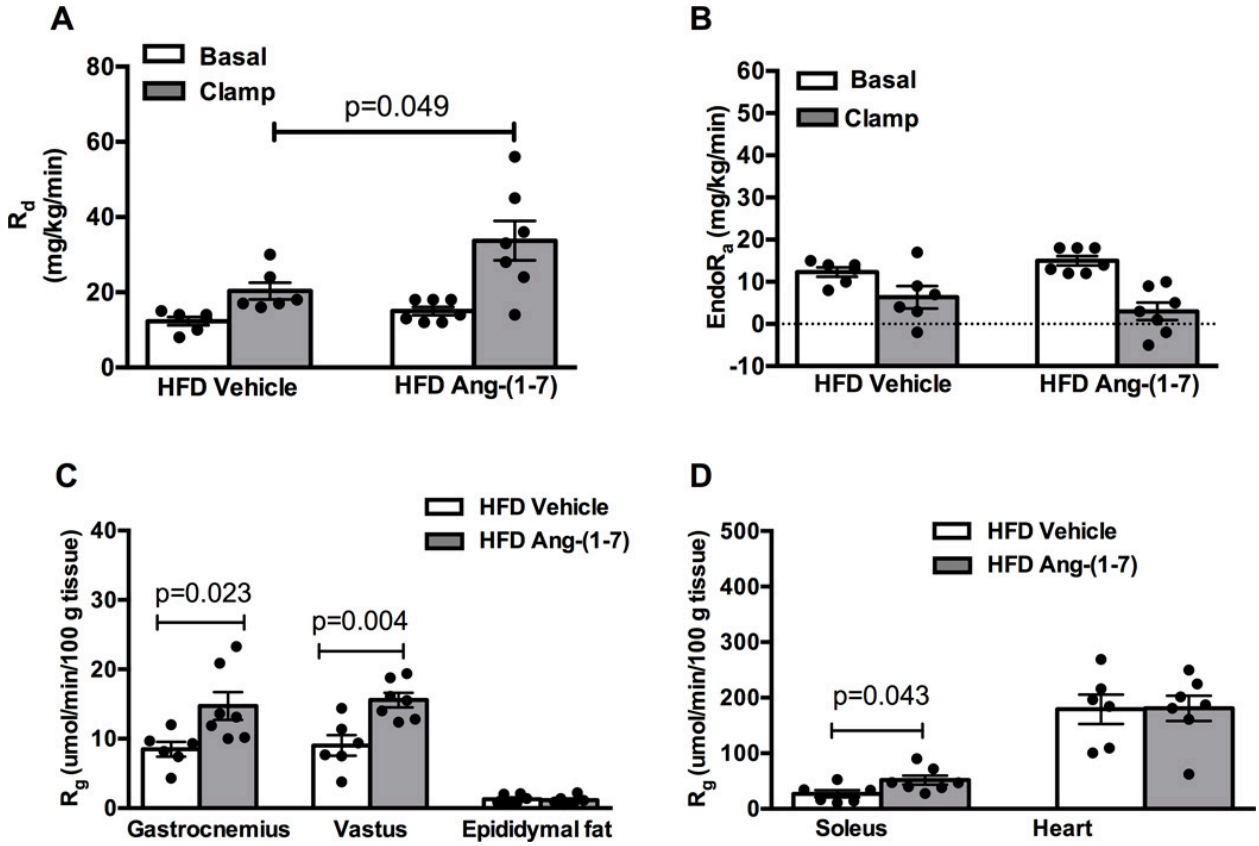

Figure 7.2: Ang-(1-7) improves insulin sensitivity in high-fat diet (HFD) mice by increasing insulin-stimulated skeletal muscle glucose uptake.

A: Ang-(1-7) increased peripheral glucose disposal (R_d) in HFD mice as determined by steadystate plasma levels of 3[^{3}H]glucose. **B:** Ang-(1-7) had no effect on the insulin-stimulated rate of endogenous glucose production ($EndoR_a$). **C, D:** Ang-(1-7) increased the glucose metabolic index(R_g) in gastrocnemius, vastus, and soleus skeletal muscles from HFD mice as determined by 2[^{14}C]deoxyglucose accumulation, with no effect in epididymal fat or heart.

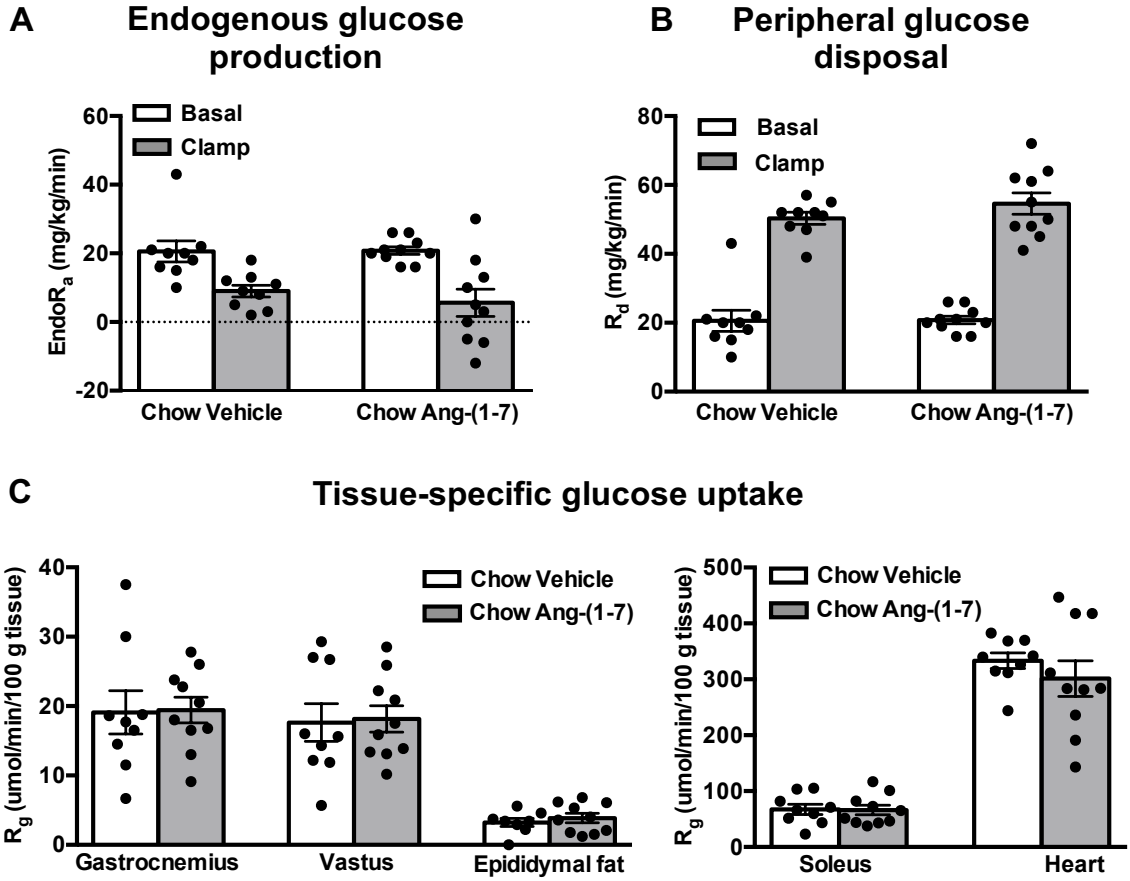

Figure 7.3: Chronic Ang-(1-7) infusion does not alter glucose turnover or tissue-specific glucose uptake in chow-fed mice. A and B: There were no differences in the basal and insulin-stimulated clamp rates of **(A)** endogenous glucose production ($EndoR_a$) or (**B)** peripheral glucose disposal (R_d) following Ang-(1-7) versus vehicle in chow fed mice. **C:** The glucose metabolic index (R_g) in various insulin-sensitive tissues was also not different between groups.

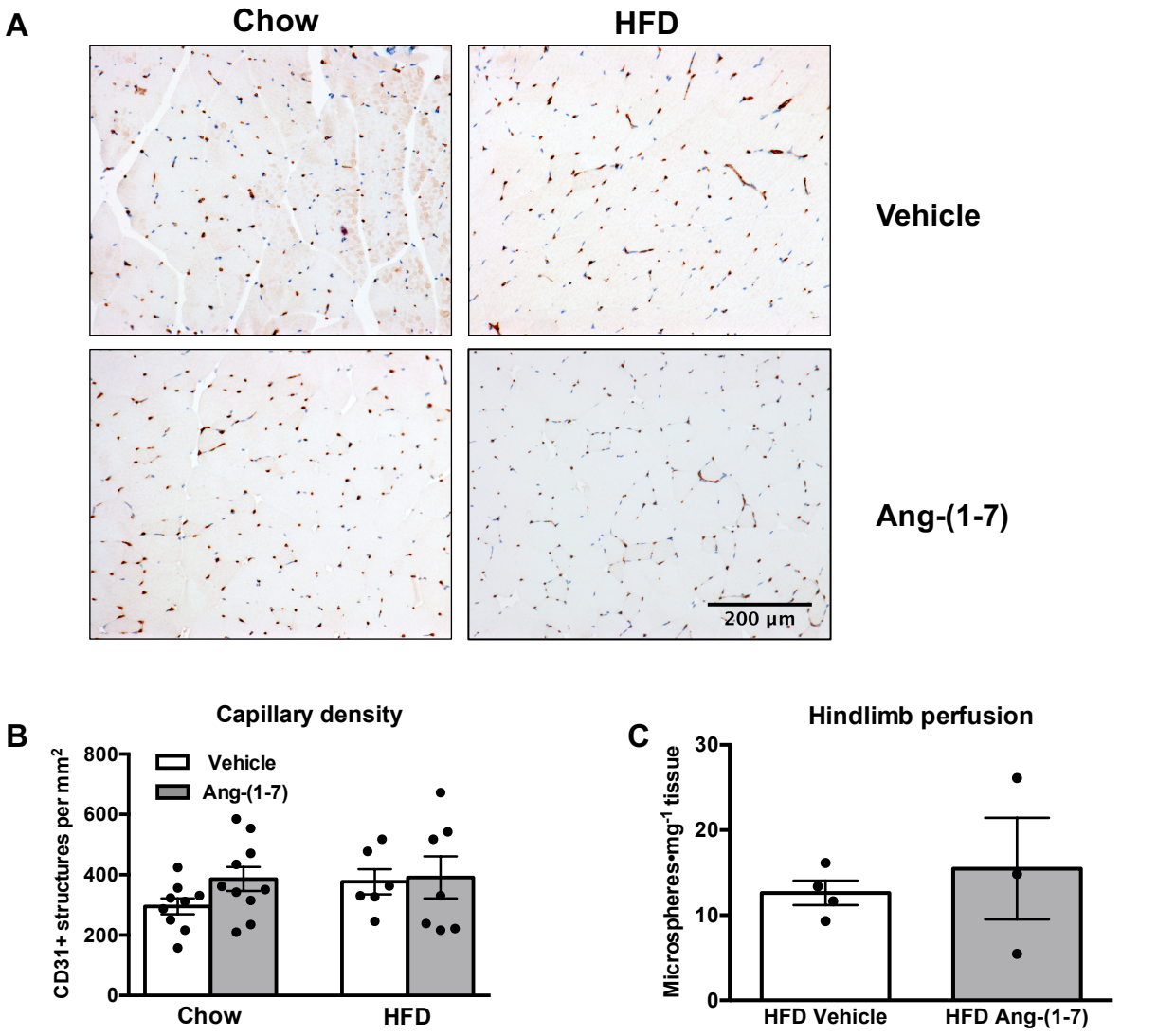

Figure 7.4: Ang-(1-7) infusion does not change capillary density or insulin-stimulated muscle perfusion in high fat diet-fed (HFD) mice. A: Representative 175X magnification micrographs of gastrocnemius sections from clamped mice stained immunohistochemically for CD31 to visualize blood vessels. **B:** The number of CD31+ structures per field of view, an index of capillary density, was not altered by Ang-(1-7) treatment in chow or HFD mice. **C:** Colored microspheres (15µm-diameter) were administered into the carotid artery at the end of hyperinsulinemic-euglycemic clamps, with their deposition measured in soleus, gastrocnemius, and vastus skeletal muscles, to obtain an index of hind limb perfusion. There was no difference in hind limb perfusion following vehicle versus Ang-(1-7) treatment in HFD mice.

Table 7.3: Effect of Ang-(1-7) on Cardiac Function in High-Fat Fed Mice

Parameter (unit)	Vehicle	Ang-(1-7)	P Value
n	6	7	
Cardiac output (ml/min)	23.2 ± 1.9	24.1 ± 1.6	0.714
Stroke volume (μl)	35.6 ± 2.9	34.3 ± 2.4	0.732
Ejection fraction (%)	78.1 ± 1.3	80.4 ± 0.5	0.146
Fractional shortening (%)	45.8 ± 1.2	47.8 ± 0.5	0.143
Left ventricular mass (mg)	102.8 ± 9.3	89.8 ± 3.9	0.226
LVIDd (mm)	3.36 ± 0.13	3.27 ± 0.09	0.592
LIVDs (mm)	1.82 ± 0.09	1.71 ±0.06	0.332
LVPWd (mm)	1.02 ± 0.09	0.92 ± 0.04	0.325
LVPWs (mm)	1.39 ± 0.10	1.34 ± 0.03	0.645
IVSd (mm)	1.03 ± 0.02	1.02 ± 0.02	0.627
IVSs (mm)	1.32 ± 0.04	1.27 ± 0.03	0.347

Data are mean ± SEM. Parameters of cardiac function were calculated from M-mode echocardiographic tracings. Ang, angiotensin; LVIDd, left ventricular internal dimension, diastolic; LVIDs, left ventricular internal dimension, systolic; LVPWd, left ventricular posterior wall, diastolic; LVPWs, left ventricular posterior wall, systolic; IVSd, interventricular septum, diastolic; IVSs, interventricular septum, systolic.

Ang-(1-7) enhances sarcolemmal Glut4 translocation in HFD mice:

A critical step in insulin-stimulated muscle glucose uptake is translocation of Glut4 from intracellular vesicles to the sarcolemma. To determine if Ang-(1-7) improves skeletal muscle insulin sensitivity by increasing sarcolemmal Glut4 levels, we measured Glut4 abundance within the region demarcated by the sarcolemmal marker Cav3 in gastrocnemius muscle (**Figure 7.5A**). Ang-(1-7) increased mean Glut4 fluorescence at the muscle plasma membrane in HFD mice (**Figure 7.5B**; p=0.011). This increased Glut4 trafficking was associated with reduced total AS160 protein, a negative regulator of Glut4 translocation (**Figure 7.5C**; p=0.034), with no effect on phosphorylated AS160 (p=0.999). Ang-(1-7) did not alter phosphorylated or total Akt in HFD mice (**Figure 7.6**).

Discussion

The main finding of this study is that chronic systemic Ang-(1-7) administration reverses HFD-induced whole-body insulin resistance by enhancing insulin-stimulated muscle glucose uptake. These insulin-sensitizing effects of Ang-(1-7) on skeletal muscle were associated with increased sarcolemmal Glut4 levels and down-regulation of AS160, a negative regulator of Glut4 translocation. Importantly, these effects occurred independent of changes in body weight, blood pressure, and measures of systemic and regional perfusion. Taken together, these findings provide evidence for blood pressure-independent effects of Ang-(1-7) on insulin action, and further support targeting this peptide to treat insulin resistance in cardiometabolic disease.

Numerous previous studies using intraperitoneal glucose and insulin tolerance tests have demonstrated that activation of the Ang-(1-7)/*mas* axis improves whole-body glucose intestinal glucose absorption, glucose-stimulated insulin secretion, insulin sensitivity, glucose

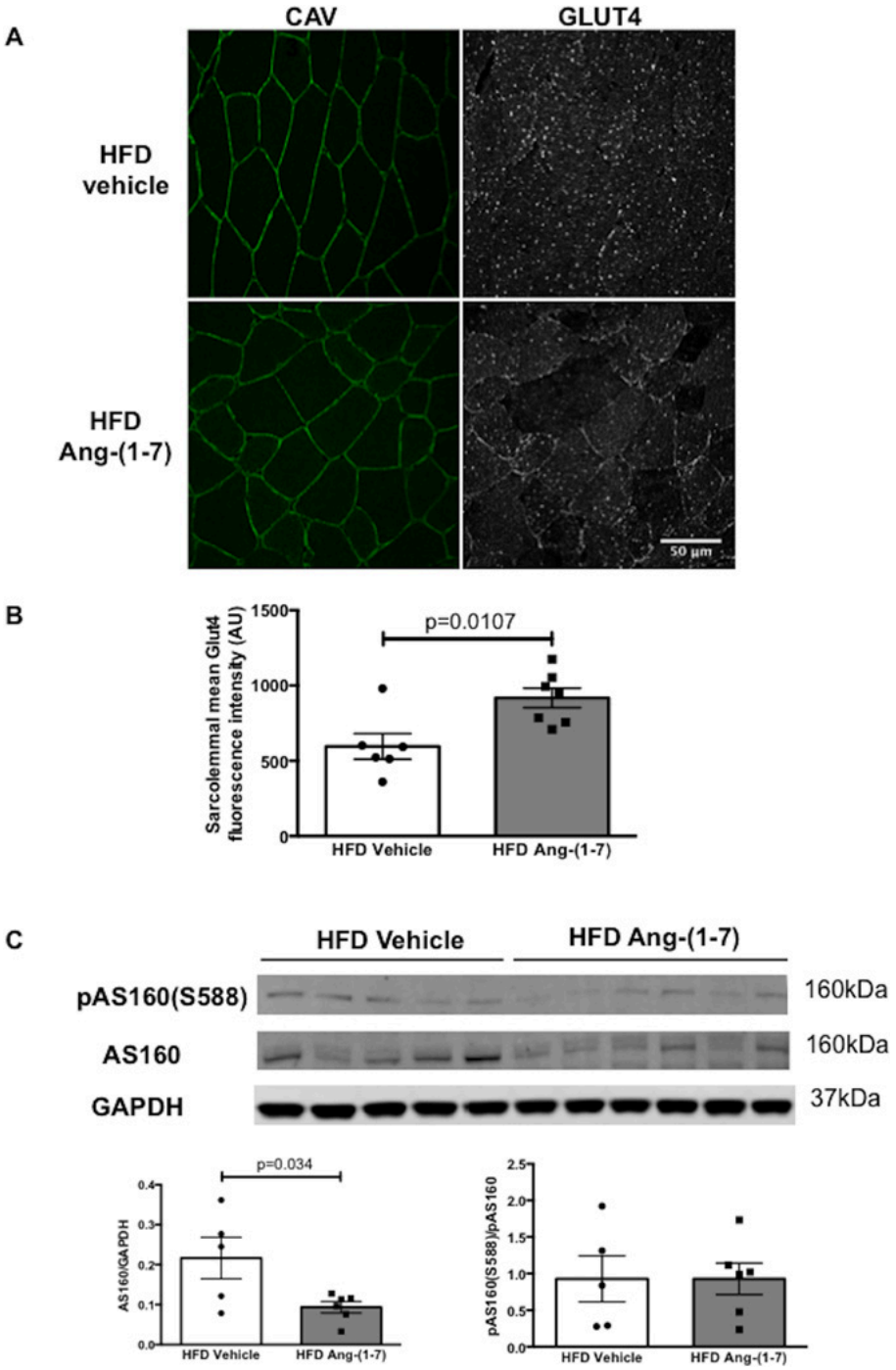

Figure 7.5: Ang-(1-7) increases sarcolemmal Glut4 in high-fat diet (HFD) mice by reducing levels of AS160, a negative regulator of Glut4 trafficking.

A: Representative 500x magnification micrographs of gastrocnemius sections from HFD mice treated with vehicle versus Ang-(1-7). Sections were stained for Cav3 (green) and Glut4 (white) and images were obtained by confocal microscopy. **B:** Ang-(1-7) increased sarcolemmal Glut4, measured as the mean Glut4 fluorescence intensity in the region demarcated by Cav3 staining. **C:** Immunoblot of gastrocnemius extracts from clamped HFD vehicle and Ang-(1-7)-treated mice. Ang-(1-7) decreased total AS160 protein levels, with no effect on phosphorylated AS160.

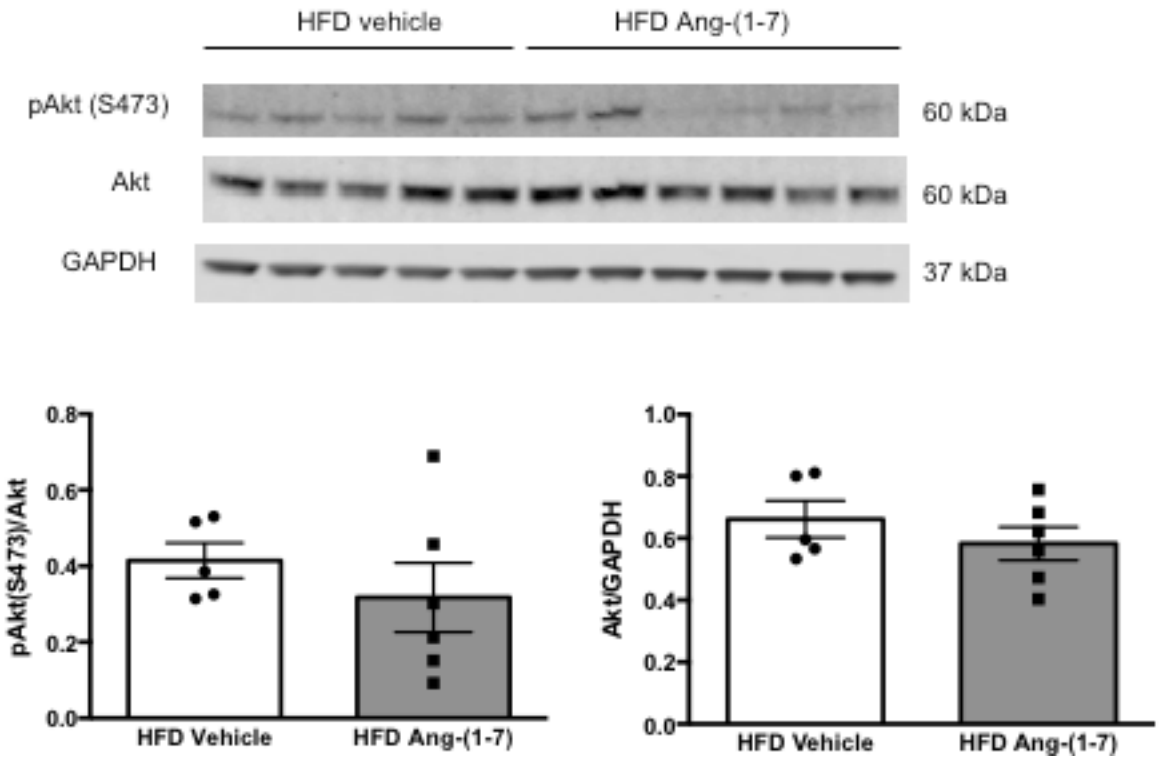

Figure 7.6: Chronic Ang-(1-7) treatment does not alter skeletal muscle Akt phosphorylation or protein levels. Immunoblot of gastrocnemius extracts from high-fat diet fed (HFD) mice treated with antibodies against total Akt, phosphorylated Akt [pAkt(S473)], and the loading control GAPDH. There was no effect of chronic Ang-(1-7) infusion on Akt or phosphorylated Akt protein levels in HFD mice.

homeostasis (207–209, 273). These tests involve a number of variables including effectiveness, and counter-regulatory responses. Here, we specifically measured the contribution of insulin sensitivity to Ang-(1-7)-induced improvements in glucose tolerance using insulin clamps. Moreover, by combining the insulin clamp with isotopic glucose tracers, as in the present study, we are able to assess tissue-specific insulin action. Using this gold standard method, we provide evidence that restoration of physiological Ang-(1-7) levels improves whole-body insulin sensitivity in a well-established animal model of cardiometabolic syndrome that exhibits mild hyperglycemia, hyperinsulinemia, insulin resistance, and modest hypertension (274). We did not observe an effect of chronic Ang-(1-7) in chow-fed mice, in contrast to reports showing acute intravenous Ang-(1-7) enhances insulin sensitivity in lean anesthetized rats (123, 275). This may reflect differences in species and methodology, as well as compensatory mechanisms to prolonged Ang-(1-7) elevation including *mas* receptor internalization (276).

Interestingly, Ang-(1-7) did not alter the mild fasting hyperglycemia induced by HFD feeding in this study. The first response, however, to increased insulin action is compensation by the endocrine pancreas. This is evidenced by an initial reduction in insulin, without changes in blood glucose or hemoglobin A1c levels (277). In our study, Ang-(1-7) treated-mice had approximately 20% lower fasting insulin levels than vehicle-treated mice. Similarly, short-term Ang-(1-7) treatment (2 to 4 weeks) lowers plasma insulin levels in fructose fed rats, but does not lower fasting glycemia (207, 209). Longer-term Ang-(1-7) treatment (8-24 weeks) lowers both fasting insulinemia and glycemia in animal models of cardiometabolic syndrome (209, 273). Thus, an improvement in insulin sensitivity precedes and contributes to normalization of glycemia. In our study, it is likely glycemia would have been lowered with more prolonged Ang-(1-7) treatment.

The reason for maintained hyperglycemia following short-term Ang-(1-7) treatment is unclear. It is conceivable that an increase in basal glucose transport and/or delivery would increase muscle glucose uptake and normalize fasting glycemia. In this study, sarcolemmal Glut4 levels and skeletal muscle perfusion were both measured under the insulin-stimulated conditions. It is not likely that the lack of effect of Ang-(1-7) on skeletal muscle perfusion in our study would contribute to the preserved basal hyperglycemia, given that an increase in glucose delivery in the absence of hyperinsulinemia has no impact on glucose uptake (278). Importantly, an improvement in insulin sensitivity alone has beneficial effects on cardiometabolic health. For example, insulin sensitivity is a stronger predictor of type 2 diabetes development compared with fasting glucose or HbA1c (279, 280). Furthermore, insulin sensitivity is a stronger risk factor for cardiovascular disease than hyperglycemia (281).

Over-activation of the renin-angiotensin system, and in particular Ang II, is associated with development of skeletal muscle and hepatic insulin resistance (282, 283). We found that chronic Ang-(1-7) infusion improves insulin-stimulated muscle glucose uptake in HFD mice. This corroborates *in vitro* studies showing that Ang-(1-7) potentiates insulin-stimulated muscle glucose uptake in normal rodents and reverses Ang II-induced muscle insulin resistance (284, 285). Ang-(1-7) did not alter basal or insulin-stimulated hepatic glucose output in HFD mice, which was normal in HFD compared with chow-fed mice. The lack of hepatic insulin resistance in HFD mice is consistent with previous reports from our group (196, 286). This is likely due to the high physiologic insulin dose infused during clamps, which could mask more subtle effects of Ang-(1-7) on hepatic insulin sensitivity. Ang-(1-7) reduced adiposity and improved insulin-stimulated suppression of lipolysis in our study, consistent with reports showing improved adipose insulin action (207, 273). Although there was no effect of Ang-(1-7) on adipose glucose

uptake during insulin clamps, one cannot rule out an indirect contribution of reduced adiposity to improved insulin sensitivity.

It is unclear to what extent the vascular effects of Ang-(1-7) contribute to its metabolic effects. Ang-(1-7) promotes endothelial-dependent vasodilation in macro- and micro-vessels (206). The improved glucose tolerance in fructose-fed rats with Ang-(1-7) was associated with blood pressure-lowering (207, 208), which could indicate vasodilation and manifest as improved glucose delivery and insulin sensitivity. Ang-(1-7) did not alter blood pressure or cardiac function, however, in HFD mice. The lack of a depressor effect in our model is consistent with accumulating evidence showing that the anti-hypertensive effect of Ang-(1-7) is not apparent in all research models. There are several potential reasons for varying blood pressure effects with Ang-(1-7) including species differences, diet, and dose, duration, and route of treatment. The discrepancy between the two previous studies and our results most likely reflects differences in animal models. Fructose-fed rats do not gain weight during the first 8 weeks of feeding and, for the most part, develop isolated systolic hypertension (287). In contrast, high fat diet-fed mice have about 5 times more adiposity than their lean counterparts, and develop both systolic and diastolic hypertension. The hypertension in these two models may therefore be driven by different mechanisms with varying sensitivity to Ang-(1-7).

Ang-(1-7) could also influence regional perfusion to improve insulin sensitivity. Indeed, acute Ang-(1-7) increases muscle microvascular perfusion in normal rats (123). We were unable to detect differences in insulin-stimulated muscle perfusion following Ang-(1-7) in HFD mice. There are several possible explanations: (1) previous studies used acute intravenous Ang-(1-7) and were performed under anesthesia (123), which alone has hemodynamic effects; (2) the ability of acute Ang-(1-7) to promote peripheral vasodilation could be lost following prolonged

exposure; (3) while microsphere deposition is the gold standard for assessing microvascular perfusion in conscious animals, it may not give the resolution necessary to detect small changes; (4) the mild hyperglycemia in HFD mice may contribute to endothelial dysfunction, thus preventing the vasodilatory actions of Ang-(1-7); and (5) Ang-(1-7) may improve other aspects of endothelial function that enhance skeletal muscle insulin action such as trans-endothelial insulin transport from capillaries to the myocyte surface.

Given that we did not observe changes in perfusion, we examined direct effects of Ang-(1-7) on skeletal muscle. A critical component of skeletal muscle insulin action is partitioning of Glut4 to the sarcolemma to enhance glucose transport (288). Chronic Ang-(1-7) potentiated insulin-stimulated Glut4 translocation in HFD mice, thereby increasing glucose transport into myocytes. This is consistent with previous reports demonstrating effects of Ang-(1-7) on Glut4. Namely, ACE2 deletion in mice reduces skeletal muscle Glut4 expression, an effect reversed by Ang-(1-7) infusion (284). Furthermore, ACE inhibition, which increases Ang-(1-7) levels, improves insulin sensitivity by enhancing Glut4 translocation (289). Insulin stimulates Glut4 translocation via activation of the PI3K/Akt pathway. Ultimately, Akt phosphorylates and inactivates AS160 to allow Glut4-containing vesicles to fuse with the sarcolemma (290). In normal and fructose-fed rats, Ang-(1-7) stimulates Akt phosphorylation in insulin-sensitive tissues (207, 291, 292). In addition, Ang-(1-7) increases AS160 phosphorylation in normal and diabetic rats (291, 293). In our study, Ang-(1-7) reduced AS160 protein levels, which functionally promotes increased Glut4 at the myocyte plasma membrane (294), independent of changes in classical Akt signaling. The precise mechanism suppressing AS160 levels is unclear, but may involve transcriptional regulation.

There are some potential limitations to these studies. We did not examine receptor and related intracellular signaling mechanisms involved in Ang-(1-7) metabolic effects. The literature suggests that most, if not all, of Ang-(1-7) actions in vivo are mediated by *mas* receptors (295). Indeed, the ability of Ang-(1-7) to augment insulin-mediated glucose disposal is *mas*-dependent in anesthetized rats (123). There is evidence, however, that AT_2 receptors participate in complex vascular effects of Ang-(1-7). Furthermore, due to limitations in blood volume sampling in mice, we were unable to measure all components of the circulating renin angiotensin system. The few studies examining Ang-(1-7) effects on renin angiotensin system components showed no effect on renin activity in lean rats (296), and reduced aldosterone in fructose-fed rats. We observed significant plasma Ang II elevations following Ang-(1-7) infusion in chow-fed mice, with no effect in HFD mice. A similar elevation was observed in lean rats and thought to reflect a homeostatic feedback response. Finally, it should be noted that the HFD has lower sodium content compared with the control diet. Despite lower sodium, HFD mice exhibited a cardiometabolic syndrome-like phenotype and did not have increased renin angiotensin system components. Furthermore, all HFD mice were fed the same diet, indicating the improved insulin sensitivity with Ang-(1-7) was sodium-independent.

In summary, these studies show that chronic Ang-(1-7) reverses diet-induced muscle insulin resistance by enhancing insulin-stimulated Glut4 translocation. Importantly, these effects occurred even when giving a dose of Ang-(1-7) that does not lower blood pressure. These findings provide evidence for divergence between Ang-(1-7) effects on blood pressure and glucose metabolism, and support the growing notion that the renin angiotensin system influences whole body physiology beyond control of blood pressure (297).

CHAPTER VIII

CONCLUSIONS AND FUTURE DIRECTIONS

Summary

The findings presented in this Dissertation greatly improve our understanding of the microvascular control of muscle insulin action. The major advance described in this work is the development of an intravital microscopy technique to directly visualize and measure the rate of insulin movement across the endothelium of muscle capillaries. These are the first direct measurements of trans-endothelial insulin transport *in vivo*. Using this technique, I discovered that trans-endothelial transport is accomplished by a fluid-phase transport mechanism that is not saturable and does not require the insulin receptor (**Figure 8.1A**). This is different than what has been observed in cell culture and highlights the importance of studying endothelial transport function *in vivo*. Furthermore, I directly show for the first time that trans-endothelial insulin transport is reduced in a mouse model of obesity and insulin resistance (**Figure 8.1B**). These novel findings reveal that the capillary endothelium is a contributor to muscle insulin resistance. I also found that reducing endothelial NO bioavailability paradoxically increases the movement of insulin across the endothelium and enhances the kinetics of insulin action. Finally, I demonstrate that chronic treatment with Ang-1-7, a vasodilatory peptide that improves endothelial function, can restore insulin sensitivity in a mouse model of diet-induced insulin resistance. Collectively, these findings demonstrate that muscle insulin action is inextricably linked to microvascular function.

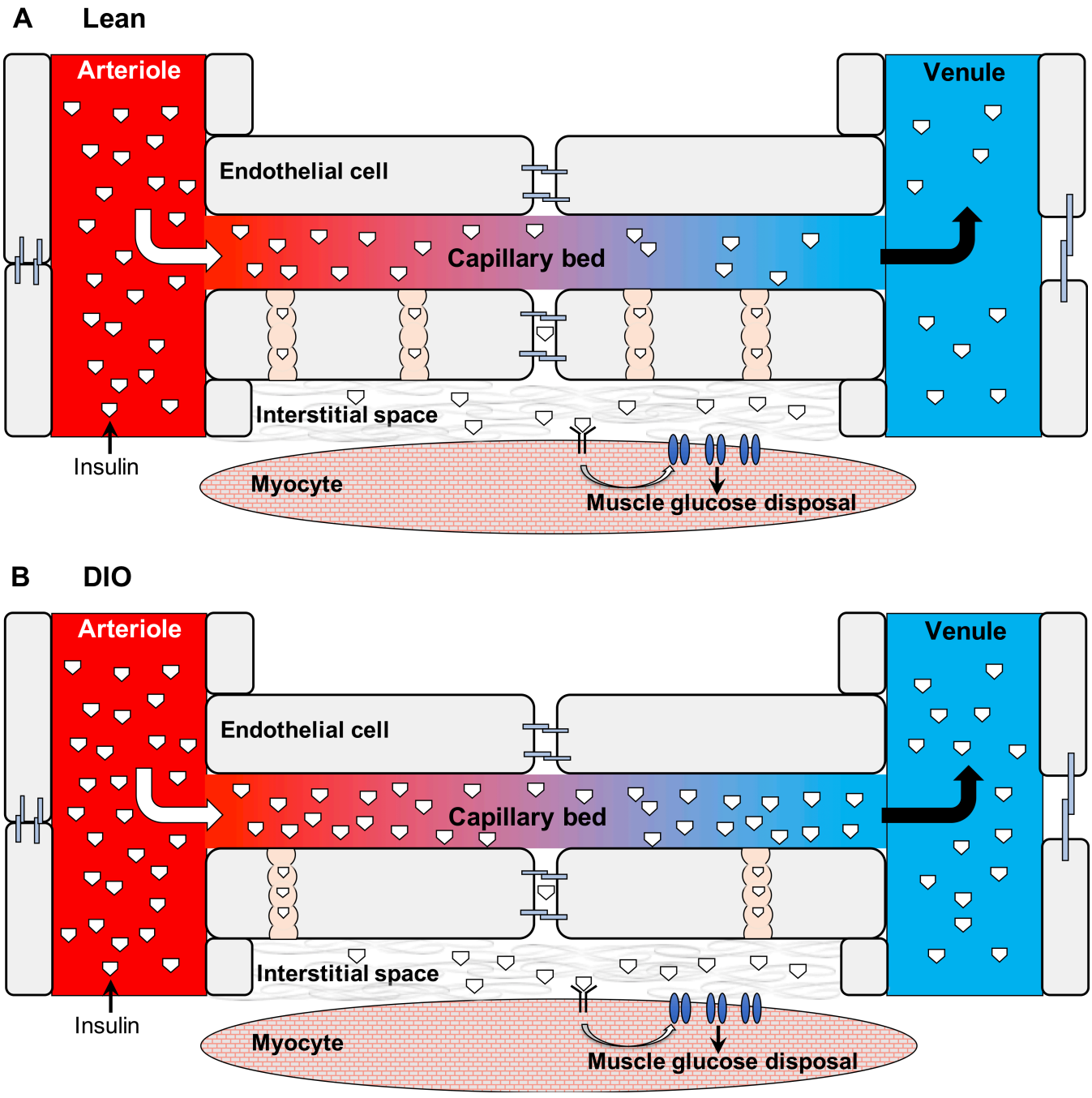

Figure 8.1: Working model of trans-endothelial insulin transport. A) Model of trans-endothelial insulin transport in lean mice. Insulin crosses the endothelium by a fluid-phase transport mechanism which is non-saturable and does not require the insulin receptor. Fluid-phase transport may involve both paracellular (inter-endothelial junctions) and transcellular (endothelial channels) mechanisms. **B)** In DIO mice, the number of endothelial vesicles is reduced and the transport of insulin is impaired. However, because DIO mice have higher capillary levels of insulin, they are able to overcome the impaired trans-endothelial insulin transport and maintain insulin levels in the interstitial space. DIO – diet-induced obese.

Implications and Hypotheses

The mechanism of trans-endothelial insulin transport

As described in **Chapter IV,** I found that the movement of INS-647 across the endothelium is not saturable nor can it be blocked by an insulin receptor antagonist. These findings suggest that insulin is transported passively across the endothelium *in vivo*. Potential passive transport mechanisms include a) diffusion of insulin down a concentration gradient b) convection, or the movement of insulin through bulk fluid filtration across the capillary wall, and c) a combination of both. In analyzing insulin imaging data, we observed that the rate of insulin appearance in the interstitial space depended solely on the concentration of insulin in the plasma rather than on the trans-endothelial concentration gradient. This suggests that insulin is being transported by convection rather than diffusion. Indeed, using mathematical modeling we demonstrated that a convection model was a better fit for the insulin transport data than a diffusion model. Thus, we initially hypothesized that insulin was most likely being moved across the endothelium by paracellular fluid flux through inter-endothelial junctions. An astute reviewer noted that insulin could also be moving through the endothelium by a non-specific, non-saturable vesicular process such as micropinocytosis. In fact, previous investigators had observed insulin inside endothelial vesicles suggesting that insulin can be transported transcellularly (246). This process cannot be distinguished from convection mathematically as both are linear functions of plasma insulin concentrations. Therefore, we concluded that insulin moves across the endothelium by fluid-phase transport, a term which encompasses both convection and micropinocytosis.

I am skeptical of the hypothesis that insulin moves across the endothelium by micropinocytosis for two reasons. Micropinocytosis, and subsequent transcytosis, would involve

an accumulation of insulin in vesicles in the endothelium. I have never observed endothelial insulin accumulation in capillaries. However, I have seen significant accumulation of INS-647 in the endothelium lining larger venules (**Figure 8.2**). Thus, if insulin were accumulating in the capillary endothelium, I would be able to see it. Second, dextran is a marker of pinocytosis. If the muscle capillary endothelium were capable of significant pinocytosis, one would expect to see dextran accumulation in the capillary endothelium. Again, I have never observed capillary endothelial accumulation of dextrans ranging in molecular weight from 3kDa to 2MDa. The 2MDa dextran does accumulate in the venular endothelium (**Figure 8.2**), suggesting that larger microvessels have a higher pinocytotic capacity than capillaries. Thus, endocytosis and vesicular accumulation of plasma molecules appear to be characteristics of venular, but not capillary, endothelium in muscle. This suggests that insulin moves across the endothelium by moving through transcellular and/or paracellular endothelial (**Figure 8.1A**).

The hypothesis that insulin moves paracellularly across the endothelium through inter-endothelial junctions is inconsistent with previous observations of insulin localized within endothelial vesicles (246). An explanation which unifies these findings is that endothelial vesicles are not discrete vesicles but rather parts of pores in the endothelium. That is to say, endothelial vesicles observed by two-dimensional electron microscopy may actually be part of 3D vesicle networks that effectively form channels through the endothelium **(Figure 8.1A)**. In fact, there is evidence that endothelial vesicles can transiently fuse to form trans-endothelial channels which support macromolecular transport (298, 299).

A limitation of our intravital microscopy technique is that we must administer high doses of fluorescent insulin due to the sensitivity of fluorescence microscopy and low circulating insulin concentrations. Klip and colleagues, studying cultured endothelial cells, raised the

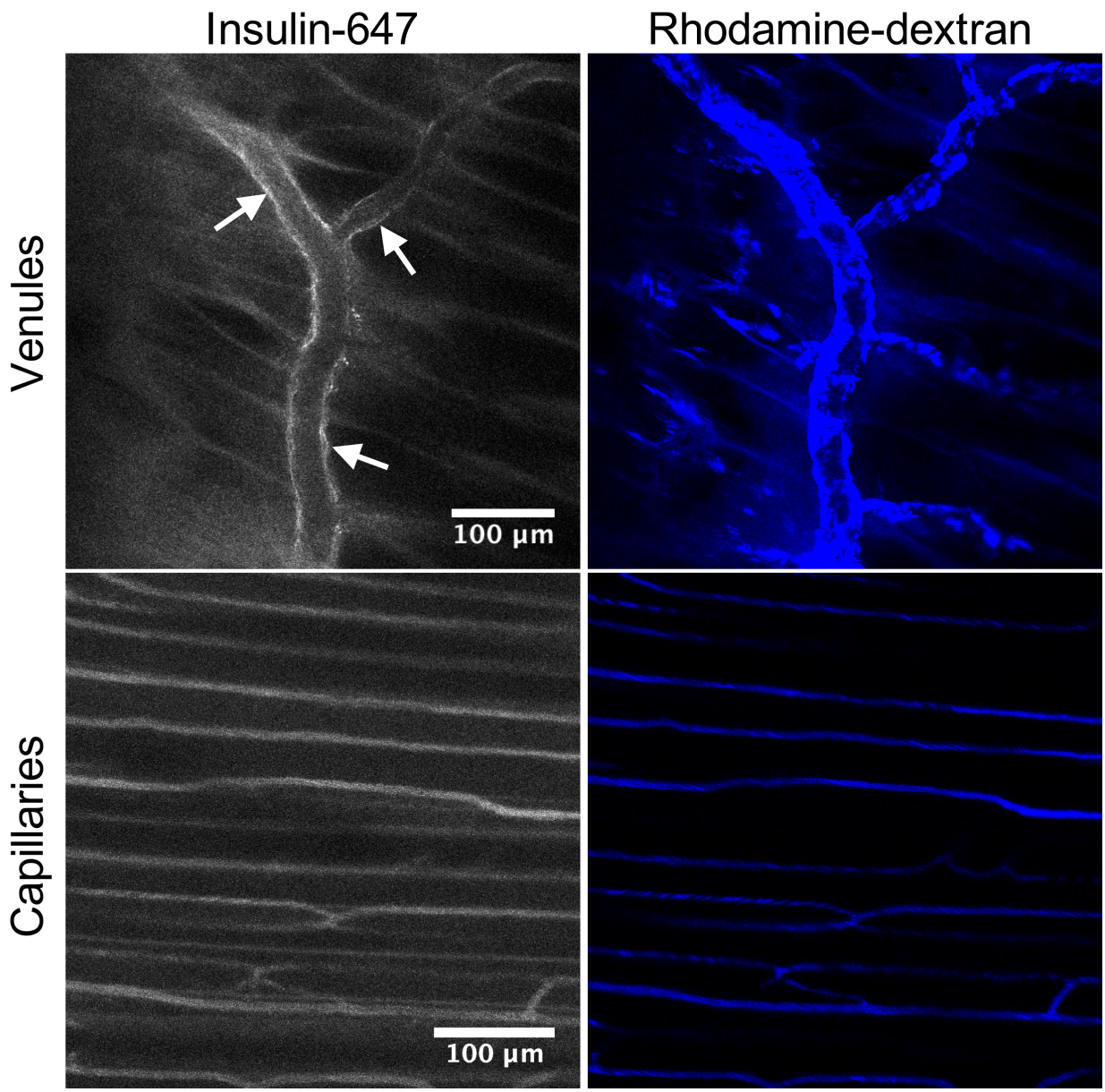

Figure 8.2: Insulin and dextran accumulate in the endothelium of post-capillary venules. Intravital microscopy images of insulin-647 (left panels) and rhodamine-labeled 2MDa dextran (right panels) in venules (top panels) and capillaries (bottom panels). Both insulin and dextran can be seen accumulating in the endothelium of venules but not capillaries. Arrows indicate regions of insulin accumulation in the endothelium.

intriguing possibility that insulin can be transported by two distinct pathways: 1) an insulin-receptor mediated transcytotic process that occurs at physiological insulin concentrations and 2) a non-saturable, micropinocytotic pathway that operates at pharmacological insulin concentrations (233). As discussed above, the lack of capillary endothelial insulin or dextran accumulation *in vivo* calls this transcytosis-based hypothesis into question. Furthermore, it is possible that the cultured endothelial cells used in by Klip and colleagues may be more representative of venules, in which case insulin accumulation would be expected. While the capillary endothelium does not accumulate insulin, it is possible that insulin binding to its receptor on the luminal endothelial surface may have important effects on vascular function and insulin action.

In summary, based on intravital imaging of trans-endothelial insulin transport and the considerations above, we hypothesize that insulin moves convectively through inter-endothelial junctions and trans-endothelial channels **(Figure 8.1A)**.

Trans-endothelial insulin transport and insulin action

Previous studies have suggested that the trans-endothelial transport of insulin is rate-limiting for insulin action in muscle (72, 73, 138). I have also observed a strong temporal correlation between the appearance of insulin in the interstitial space and whole-body insulin action. Namely, an intravenous bolus injection of insulin fully equilibrates with the muscle interstitial space in roughly 5 minutes, approximately the same period of time in which insulin-stimulated glucose lowering is maximal. Thus, our direct measurements of trans-endothelial insulin transport lend further support to the idea that the capillary endothelium governs the rate of muscle insulin action.

A major function of the endothelium, as it relates to insulin action, is to control insulin's access to muscle. Capillary permeability to insulin controls both the kinetics and absolute levels of muscle insulin exposure. The manner in which changes to trans-endothelial insulin transport affect muscle insulin exposure depends on insulin clearance by other organs. For instance, if trans-endothelial insulin transport in muscle is reduced, then first-pass insulin extraction by the muscle will also be reduced. However, if insulin clearance by other organs such as liver and kidney are also decreased, then plasma insulin will remain elevated. The muscle will be able to extract this insulin on subsequent passes. In this case, the kinetics, but not absolute levels, of insulin delivery would be delayed. On the other hand, if there is an isolated impairment in muscle insulin extraction, the liver and kidney may remove the excess insulin not extracted by muscle. In this case, the absolute delivery of insulin to the muscle would be reduced. These scenarios highlight the importance of plasma insulin concentration to muscle insulin delivery. Namely, because insulin appearance in the interstitial space is a linear function of plasma insulin and trans-endothelial insulin transport, high plasma levels of insulin can overcome defects in trans-endothelial insulin transport. This is what we observed in obese, insulin resistant mice where a 40% increase in plasma insulin levels overcame a 15% reduction in trans-endothelial insulin transport to maintain insulin delivery **(Chapter V)**. As such, the kinetics, but not absolute levels, of insulin delivery were impaired in these mice.

Trans-endothelial insulin transport and insulin resistance

The primary reason for which the present work was undertaken was to determine whether impaired trans-endothelial insulin transport contributes to skeletal muscle insulin resistance. Indeed, I observed a 15% reduction in trans-endothelial insulin transport in male mice made

obese and insulin resistant by 16 weeks of high fat feeding. Thus, in the setting of obesity and insulin resistance, the capillary endothelium limits the access of insulin to skeletal muscle. However, this reduction in capillary permeability to insulin did not reduce the absolute levels of insulin in the interstitial space. As described above, insulin in the interstitial space was actually increased in obese mice due to a 40% increase in plasma insulin levels following the intravenous insulin bolus. These findings indicate that the kinetics, but not absolute levels, of insulin delivery are impaired in obese, insulin resistant mice. A delay in trans-endothelial insulin transport would be predicted to cause a delay in muscle insulin action. Indeed, obese, insulin resistant humans require more time and insulin to dispose of an oral glucose load (300). Olefsky and colleagues utilized insulin clamps to show that this delay in whole-body insulin action was due in part to a delay in the onset kinetics of insulin-stimulated peripheral glucose disposal (300). Thus, the delay in peripheral insulin action observed in obesity may be caused by reduced capillary permeability to insulin in skeletal muscle. Delayed insulin action, especially in the context of physiological feeding, may increase the amount of time that obese individuals spend in hyperglycemia. These repeated, transient bouts of postprandial hyperglycemia may contribute to obesity-associated co-morbidities.

As trans-endothelial insulin transport was only measured at one time point during the development of diet-induced insulin resistance, it is unclear whether this process is a cause or consequence of muscle insulin resistance. It is possible that impaired trans-endothelial insulin transport occurs prior to the development of overt myocellular insulin resistance. In fact, Kim et al. observed aortic endothelial dysfunction after just 1 week of a high fat diet, prior to the development of muscle insulin resistance (182). Subsequently, hypersecretion of insulin from β-cells may be a response to overcome impaired trans-endothelial insulin transport and preserve

muscle insulin action. Alternatively, impaired trans-endothelial insulin transport may be a consequence of whole body insulin resistance. Insulin resistance at the whole body level results in a host of abnormalities including increased free fatty acids, glucose, inflammatory mediators, reactive oxygen species and extracellular matrix accumulation. The prolonged exposure of the capillary endothelium to this milieu may drive endothelial dysfunction and reduce trans-endothelial insulin transport. In support of this hypothesis, Lindner and colleagues found that microvascular hemodynamic function only declined after the development of obesity and glucose intolerance in monkeys (172). Thus, it is possible that a model of more severe insulin resistance may display a greater impairment in trans-endothelial insulin transport.

The delayed trans-endothelial insulin transport observed in obese male mice was associated with a 50% reduction in endothelial vesicles. As discussed above, these vesicles may represent channels or pores in the endothelium. If the availability of endothelial channels is reduced in obese mice, this may provide a structural basis for the reduction in trans-endothelial insulin transport. Interestingly, the reduction in endothelial vesicles (50%) was much larger than the impairment in trans-endothelial insulin transport (15%). This may reflect 1) that there is an excess of trans-endothelial channels available for insulin exchange and only a severe reduction of these channels would impact trans-endothelial insulin transport or 2) paracellular insulin transport through inter-endothelial junctions increases to compensate for reduced transcellular transport.

Collectively, my findings indicate that the endothelium delays insulin's access to skeletal muscle in a mouse model of obesity and insulin resistance. The structural determinants of this impairment, as well its chronological appearance during the development of insulin resistance, remain to be determined.

Nitric oxide and trans-endothelial insulin transport

After observing delayed trans-endothelial insulin transport in obese male mice, we considered potential molecular determinants of this defect. A likely candidate was NO. NO exerts a plethora of beneficial effects on endothelial function, is correlated positively with muscle insulin sensitivity, and has been shown to be reduced in the setting of obesity and insulin resistance. Thus, we hypothesized that a reduction in endothelial NO bioavailability caused the impaired trans-endothelial insulin transport observed in obese male mice. To explore this hypothesis, we initially tested whether pharmacologically reducing NO in lean, insulin sensitive mice would impair trans-endothelial insulin transport. To our surprise, we found the opposite to be true. Namely, reducing endothelial NO with a NOS inhibitor (L-NAME) actually increased the rate at which insulin was transported across the endothelium. Consistent with increased capillary permeability to insulin, L-NAME also enhanced the glucose-lowering effect of insulin. As discussed in detail in the **Discussion** of **Chapter VI**, these findings corroborate previously reported effects of NO reduction on vascular permeability and elucidate a novel role for NO in the control of insulin action kinetics. To the best of my knowledge, this is the first report of a pharmacological intervention which enhances the delivery of insulin to the muscle.

Given that L-NAME increases trans-endothelial insulin transport, it may be a useful tool to better understand the molecular, cellular, and structural determinants of this process. At present, the precise mechanism by which L-NAME increases capillary permeability to insulin is unclear. Based on previous work from the Granger and Malik laboratories, we hypothesize that L-NAME may increase trans-endothelial insulin transport by 3 non-mutually exclusive mechanisms. First, L-NAME may cause a widening of inter-endothelial junctions. This would result in reduced resistance to paracellular insulin flux across the endothelium. Indeed, electron

microscopic analysis of skeletal muscle capillaries revealed an opening of inter-endothelial junctions after L-NAME treatment (183). Second, given that L-NAME treatment increases blood pressure and reduces capillary diameter, it most likely has hemodynamic effects in the microvasculature. These hemodynamic effects may alter the balance of fluid pressures across the capillary wall and, subsequently, trans-capillary fluid flux. Thus, L-NAME may enhance the transport of insulin by increasing convective fluid flux. Finally, it is possible that L-NAME increases the density or stability of trans-endothelial channels which support insulin transport. Further dissection of the mechanism by which L-NAME increases trans-endothelial insulin transport would 1) afford a better understanding of the mechanism of insulin transport and 2) guide attempts to specifically reverse engineer the permeability-enhancing effects of L-NAME.

A conundrum raised by the findings described in **Chapter VI** is the connection between obesity, insulin resistance, NO bioavailability and trans-endothelial insulin transport. Many investigators have found that obesity and insulin resistance are associated with reduced NO bioavailability (181). Given these previous observations and our finding that pharmacological reduction of NO increases capillary permeability, one might predict that obese, insulin resistant mice would have increased trans-endothelial insulin transport. However, we found the opposite to be true. Before discussing potential explanations of this conundrum, it is important to note that there have been no direct measurements of muscle capillary NO production. This is the process of interest for trans-endothelial insulin transport. Most previous studies have utilized indirect measures of NO bioavailability in larger vessels. Thus, the effect of obesity and insulin resistance on NO levels in skeletal muscle capillaries is unclear.

If we assume that muscle capillary NO bioavailability is indeed reduced in DIO mice, there are two potential explanations for the counterintuitive observations that 1) reducing NO

increases trans-endothelial insulin transport 2) DIO mice have reduced endothelial NO and 3) DIO mice have impaired trans-endothelial import. First, it is possible that concurrent cellular events in the endothelium overcome the reduction in NO bioavailability to reduce permeability of capillaries to insulin. For instance, obesity and insulin resistance are associated with increased endothelial generation of superoxide, a free radical (301). Superoxide can react with NO to form peroxynitrite. Not only does this reaction inactivate NO and reduce its bioavailability, but peroxynitrite itself can form lipid and protein adducts which impart adverse effects on vascular function (302). Thus, it is possible that increased peroxynitrite generation in the endothelium of DIO mice counteracts the effects of reduced NO bioavailability and diminishes trans-endothelial insulin transport. A second possibility is that a reduction in NO bioavailability is a homeostatic feedback mechanism to maintain trans-endothelial insulin transport at a more physiological level. That is to say, the impairment in trans-endothelial insulin transport observed in obese mice may be even greater were it not for reduced endothelial NO generation.

In summary, inhibition of NOS increases trans-endothelial insulin transport and accelerates whole body insulin action. The precise mechanism by which L-NAME increases the flux of insulin across the endothelium remains to be determined. Furthermore, the relationship between obesity, endothelial NO, oxidative stress, and trans-endothelial insulin transport warrants further investigation.

Vasodilators and muscle insulin sensitivity

Previous work from our laboratory showed that chronic, but not acute, treatment of obese mice with vasodilators restores insulin sensitivity (195, 196). These findings suggested that 1) augmenting perfusion alone does not rescue muscle insulin action and 2) chronic vasodilator

treatment induces structural changes to the muscle, including increased capillarization and reduced ECM accumulation, which improve muscle insulin sensitivity. In **Chapter VII**, we treated obese mice with Ang-(1-7), a vasodilatory peptide hormone of the renin-angiotensin system which has been shown to improve endothelial function. Thus, we hypothesized that chronic Ang-(1-7) treatment would improve muscle insulin sensitivity by augmenting the access of glucose and insulin to skeletal muscle. While Ang-(1-7) treatment did restore muscle insulin action, it did so by enhancing Glut4 translocation rather than by improving muscle perfusion. Thus, chronic Ang-(1-7) treatment improves muscle insulin sensitivity by augmenting glucose transport. At present, it is unclear whether this effect of Ang-(1-7) is mediated by myocytes or the vasculature. It is possible that Ang-(1-7) treatment may improve insulin signaling and Glut4 translocation by stimulation of the *mas* receptor, which is expressed in skeletal muscle. Alternatively, it is possible that chronic vasodilation increases delivery of oxygen to muscle which may enhance muscle fat oxidation. In support of this hypothesis, we observed that Ang-(1-7) treatment caused a slight reduction in adiposity in obese mice. An elevated capacity to oxidize lipids may reduce accumulation of toxic lipid species which can impair insulin signaling. Whether the insulin-sensitizing effects of vasodilators are due to direct myocellular or vascular effects warrants further investigation.

Future Directions

Intravital microscopy and trans-endothelial insulin transport

Controversies regarding biological mechanisms are often resolved through improvements in methodology. The development of intravital microscopy to study trans-endothelial insulin transport has fundamentally changed our understanding of this process. Using this technique, we

have challenged the longstanding receptor-mediated transcytosis model of trans-endothelial insulin transport and discovered that, *in vivo*, insulin moves across the muscle capillary endothelium by convection. While intravital microscopy has afforded us the first direct measurements of trans-endothelial insulin transport, there is certainly room for improvement. One limitation of intravital fluorescence microscopy is sensitivity. In its current iteration, *in vivo* insulin imaging requires the use of high doses of fluorescent insulin due to low circulating insulin concentrations and fluorescence detection limits. While we have considerable evidence that insulin is transported across the endothelium by fluid-phase transport, it would be ideal to definitively demonstrate this at physiological insulin concentrations. The lowest dose we have imaged is 0.5U/kg. This dose would be predicted to give plasma insulin levels which start at 16nM immediately following injection and fall to 4nM after 5 minutes. Under physiological conditions, circulating insulin concentrations range from 1nM to 50pM. In order to move into the physiological range of plasma insulin concentrations, the sensitivity of fluorescent insulin detection needs to increase by ~20 fold. This may be achieved through a combination of modifications including using brighter dyes, objectives with higher light-collecting capacity, higher laser power and longer pixel dwell times, more sensitive non-descanned detectors, and computational techniques such as adaptive optics. It should be noted that increases in sensitivity may come at the expense of other parameters including imaging speed, field of view, and phototoxicity.

Another aspect of imaging on which we can improve is our understanding of the cellular and structural landscape of the tissue being imaged. Currently, we measure insulin concentrations in the intravascular and the extravascular space as indicated by the presence or absence of a rhodamine-labeled 2MDa dextran vascular marker, respectively. We assume that

the region emanating 1 – 3 μm from the capillary wall is the interstitial space. This assumption is based on electron microscopic analysis of muscle sections and the smooth exponential decay of insulin concentrations in this space. Ideally, we should validate this assumption in a more rigorous manner. For instance, we could determine the co-localization of interstitial INS-647 with a fluorescent, non-metabolizable extracellular marker such as inulin. Additionally, our two-compartment model of insulin movement is an oversimplification of the complex structure of muscle tissue. It would be useful to visualize the location of the ECM, myofibers, endothelial cells, lymphatic vessels, and pericytes in order to define muscle compartments with more granularity. These elements of muscle can be detected using a combination of second harmonic microscopy to image collagen fibers and cell type-specific expression of genetically-encoded fluorescent proteins. More sophisticated imaging of tissue structures may allow us to make detailed measurements of insulin movement through complex muscle compartments.

As with most high-resolution intravital microscopy experiments, one concern is the relevance of the small region being imaged to the behavior of the tissue as a whole. To illustrate this point, we image a 0.02 mm^3 volume of tissue which represents just ~0.04% of the entire lateral gastrocnemius. Drawing conclusions about tissue-level function from microscale measurements will require a better understanding of the intra-individual variability of trans-endothelial insulin transport. There are several layers of variability which are important to consider. First, it would be very useful to know the variability of individual capillary permeabilities. This can be accomplished by modifying my automated image analysis script to analyze trans-endothelial insulin transport on a per-capillary basis. Such data may reveal subpopulations of capillaries with varying permeabilities to insulin. Furthermore, systematic measurements of trans-endothelial insulin transport at well-defined points within the exposed

tissue would allow us to determine whether certain regions of the tissue are more preferable for comparison. It is also possible that capillaries of superficial myofibers, similar to the ones we image, have different characteristics than those located deeper in the tissue. We could use two-photon microscopy to make this determination. Finally, microvascular properties vary depending on the type of muscle (i.e. glycolytic vs. oxidative) being studied. In the work described above, we have exclusively imaged the superficial lateral gastrocnemius which is composed mostly of Type II glycolytic fibers. It would be interesting to determine whether the mechanism and regulation of trans-endothelial insulin transport is similar in Type I oxidative fibers. In summary, a better understanding the variability of trans-endothelial insulin transport on multiple scales would allow us to 1) determine the degree to which our current measurements represent all of skeletal muscle and 2) design experiments and comparisons with maximal statistical power.

All biological processes are both 1) emergent properties of events occurring at a lower scale as well as 2) individual components of higher-order processes. An ideal strategy to advance our understanding of trans-endothelial insulin transport would be to connect our intravital microscopy measurements with processes at both smaller and larger spatial scales. For instance, the use of electron microscopy to measure vesicular density and inter-endothelial junction distance would allow us to relate endothelial ultrastructure to capillary transport function. Furthermore, the development of techniques to measure whole muscle insulin clearance would allow us to determine whether changes to trans-endothelial insulin transport scale to the entire muscle. Using this approach, we would be able to discover important molecular regulators of insulin access by identifying key variables that have effects over multiple scales.

A limitation of most intravital microscopy techniques is the requirement of anesthesia to stabilize animals for imaging. To a varying degree, all anesthetics cause changes to both

cardiovascular function and metabolism. These changes could presumably alter the rate or regulation of trans-endothelial insulin transport. It should be noted, however, that our measurement of the trans-endothelial insulin gradient in anesthetized mice is similar to that of conscious humans as measured by microdialysis (137). Regardless, it would be ideal to study trans-endothelial insulin transport in the absence of anesthesia. Investigators in neuroscience have engineered miniature confocal microscopes that can be affixed to windows implanted in the skulls of mice (303). This allows for long-term subcellular resolution fluorescence microscopy in the brain of freely moving mice. Adapting this concept to the muscle, while logistically challenging, may offer an opportunity to study insulin transport in conscious, freely moving animals. Furthermore, the implantation of window chambers onto muscle would allow for repeated measurements of trans-endothelial insulin transport in the same mouse. Such experiments would give us the ability to correlate changes in trans-endothelial insulin efflux with disease progression.

Another way to improve our investigation of trans-endothelial insulin transport would be to administer insulin in a more physiological manner. Currently, we give intravenous bolus injections of insulin into the peripheral circulation which is different than the physiological secretion of insulin by β cells into the portal circulation. Infusing insulin into the portal vein, while technically challenging in mice, may reveal additional regulatory mechanisms of trans-endothelial insulin transport. An even more elegant approach would be to genetically ligate a fluorescent protein to endogenous insulin. In this case, one could measure trans-endothelial insulin transport in response to endogenously secreted insulin following physiological stimuli. However, fluorescent proteins are large and their conjugation to insulin may affect trans-endothelial insulin transport and insulin action. This technical hurdle may eventually be solved

by the development of smaller genetically-encodable fluorescent tags or other *in vivo* endogenous labeling strategies.

There are limitations to drawing conclusions about human obesity and insulin resistance from experiments in mouse models. As such, the holy grail would be ideal to directly measure trans-endothelial insulin transport in human skeletal muscle. There are a few different strategies which may afford this measurement. Schnitzer and colleagues have utilized two-photon microscopy combined with microendoscopy to measure sarcomere contractile dynamics in human skeletal muscle (304). It is feasible that his approach could be adapted to measure trans-endothelial insulin efflux. Alternatively, it is conceivable that future insulin probes may allow for non-invasive discrimination between plasma and interstitial insulin. That is to say, if an insulin probe were to behave differently in various compartments, these differences may be detected by an imaging modality such as magnetic resonance imaging. Such technical advances would allow us to determine the contribution of trans-endothelial insulin transport to muscle insulin resistance in humans.

The mechanism of trans-endothelial insulin transport

Intravital insulin imaging revealed that insulin is transported across the endothelium by a fluid-phase transport mechanism that is not saturable and does not require the insulin receptor. Moreover, a mathematical model predicted that insulin moved across the endothelium by convection rather than diffusion. This model prediction should be tested experimentally in future studies. If insulin is indeed moving convectively across the endothelium, manipulating trans-capillary fluid flux should have predictable effects on trans-endothelial insulin transport. Fluid efflux is governed by the balance of hydrostatic and oncotic pressure gradients (Starling forces)

across the capillary wall. In resting skeletal muscle, the balance of Starling forces promote net fluid efflux from the capillaries to the interstitial space (305). In preliminary studies, I administered a continuous infusion of unlabeled 70 kDa dextran in an attempt to increase plasma oncotic pressure. The predicted effect of increasing plasma oncotic pressure would be to either inhibit or reverse trans-endothelial fluid efflux. Dextran treatment slightly reduced hematocrit, indicating fluid re-absorption from the extravascular to intravascular space (data not shown). However, there was no effect of dextran treatment on trans-endothelial insulin efflux (data not shown). It is unclear whether dextran actually altered trans-capillary fluid flux in muscle. Future investigations into the convective nature of trans-endothelial insulin transport should utilize protocols which verifiably alter fluid filtration in the region of tissue being imaged. Subsequently, the effects of both increasing and decreasing fluid efflux on trans-endothelial insulin transport should be determined.

Another question regarding the mechanism of trans-endothelial insulin transport is if insulin moves paracellularly (around the endothelial cells) or transcellularly (through the endothelial cells). A paracellular process would involve insulin moving through inter-endothelial junctions. Transcellular mechanisms might include pinocytotic transcytosis or movement through endothelial pores. Several experimental strategies can be employed to distinguish between these different routes. First, one could stain muscle sections with gold-conjugated insulin antibodies to visualize the distribution of insulin at the ultrastructural level. Subsequently, the distribution of insulin located in inter-endothelial junctions (paracellular) and vesicles (transcellular) could be quantified. If insulin were found in vesicles, intravital microscopy could be used to determine the functional significance of transcytosis to trans-capillary insulin transport. As vesicular transcytosis requires the GTPase dynamin, one could use a dynamin

inhibitor such as Dyngo-4a to determine whether transcytosis is required for trans-endothelial insulin transport. Alternatively, amiloride, a purported fluid-phase endocytosis inhibitor, can be used to determine whether micropinocytosis is involved in trans-endothelial insulin transport. In addition to using these drugs in intravital insulin imaging experiments, it would be prudent to use electron microscopy to assess their effects on both endothelial ultrastructure and insulin localization. If insulin is found in vesicles but cannot be blocked by transcytosis or pinocytosis inhibitors, this would suggest that endothelial vesicles seen in 2D are actually components of 3D trans-endothelial channels. To confirm this hypothesis, one could utilize a volumetric electron microscopy technique such as focused ion beam – scanning electron microscopy or serial block-face scanning electron microscopy. On the other hand, if insulin is found exclusively in inter-endothelial junctions, then various pharmacological and genetic approaches could be used to widen these junctions. Subsequently, the effect of manipulating junction distance on trans-endothelial insulin transport could be assessed with intravital microscopy.

Another interesting observation that warrants further investigation is that insulin accumulates in the endothelium of larger microvessels such as venules (**Figure 8.2**). The function and nature of this venular insulin accumulation is unclear. The experiments which I have performed (**Chapter IV)** and proposed above could be repeated in arterioles and venules to determine the mechanism of endothelial insulin accumulation in these vessels. Given that venules are more permeable to insulin than capillaries, it is possible that venular insulin transport is an important aspect of insulin delivery and insulin action. One potential indicator of the importance of venules insulin action would be proximity to the insulin receptor and PI3K/Akt signaling machinery. Put another way, if the myocellular insulin receptor and signaling

machinery is highly clustered in regions close to venules, this may suggest that venules are an important source of insulin for the muscle.

Trans-endothelial insulin transport, nitric oxide and insulin resistance

We observed a 15% reduction in trans-endothelial insulin transport in mice fed an HFD for 16 weeks. As discussed above, it is unclear whether this impairment in trans-endothelial insulin transport is a cause or consequence of insulin resistance. Time course experiments where both muscle insulin sensitivity and trans-endothelial insulin transport are measured following various durations of HFD would allow us to make this determination. Furthermore, it would be interesting to examine other models of insulin resistance to determine whether impaired trans-endothelial insulin transport is a ubiquitous feature of insulin resistance. For instance, one could study models of acute insulin resistance such as lipid or cytokine-infused mice. Finally, utilizing mouse models with more severe insulin resistance and/or overt diabetes would inform us if microvascular defects worsen with disease progression.

While the effect of diet-induced obesity to delay trans-endothelial insulin transport is relatively low (~15%), enhancing muscle insulin delivery may still be a useful treatment strategy in overcoming insulin resistance. For instance, it would be interesting to determine whether L-NAME, which we have shown to increase trans-endothelial insulin transport, would improve trans-endothelial insulin transport and insulin action in DIO mice. Other molecules that transiently increase permeability, such as VEGF or histamine, would also be useful in testing this hypothesis. Ultimately, utilizing findings regarding the precise mechanism of trans-endothelial insulin transport in lean mice will provide the best opportunity for engineering strategies to enhance insulin delivery in DIO mice. For instance, we have observed that DIO male mice have

a 50% reduction in the density of endothelial vesicles. If experiments in lean mice indicate that these vesicles are important for trans-endothelial insulin transport, then targeted strategies could be developed to restore vesicular density in DIO mice. Alternatively, if inter-endothelial junctions are deemed to be more relevant to trans-endothelial insulin transport, then one could experimentally widen these junctions to normalize insulin delivery.

Finally, the connection between capillary NO bioavailability, trans-endothelial insulin transport, and diet-induced insulin resistance warrants further investigation. An important first step would be to determine whether muscle capillaries produce NO and if this process is impaired in DIO mice. To make these measurements, one could image fluorescent nitric oxide reporters with intravital microscopy. Furthermore, experimentally manipulating endothelial NO levels in DIO mice will allow us to determine whether NO bioavailability contributes to impaired trans-endothelial insulin transport. In **Chapter VI**, we observed that reducing NO bioavailability with L-NAME increased trans-endothelial insulin transport. It will be interesting to determine whether NOS inhibition has the same effect in DIO mice. Another potential area of exploration is the enhanced superoxide-mediated NO inactivation and peroxynitrite formation observed in obesity and insulin resistance. To determine whether this process alters trans-endothelial insulin efflux, one could treat lean mice with a peroxynitrite donor or pharmacologically reduce peroxynitrite formation in DIO mice.

Concluding Remarks

The findings presented in this Dissertation describe novel mechanisms by which the capillary endothelium regulates insulin action and insulin resistance. The major advance described herein is the development of an intravital microscopy technique to directly measure

trans-endothelial insulin transport. This is the first report of such measurements *in vivo*. Using this technique, we have discovered the mechanism of trans-endothelial insulin transport and found that impaired movement of insulin across the endothelium contributes to muscle insulin resistance. These findings support the notion that the capillary endothelium is a key regulator of muscle insulin action.

REFERENCES

1. Fryar, C. D., Carroll, M. D., and Ogden, C. L. (2016) Prevalence of Overweight, Obesity, and Extreme Obesity Among Adults Aged 20 and Over: United States, 1960–1962 Through 2013–2014. [online] https://www.cdc.gov/nchs/data/hestat/obesity_adult_13_14/obesity_adult_13_14.pdf (Accessed May 19, 2018)
2. Hales, C. M., Fryar, C. D., Carroll, M. D., Freedman, D. S., and Ogden, C. L. (2018) Trends in Obesity and Severe Obesity Prevalence in US Youth and Adults by Sex and Age, 2007-2008 to 2015-2016. *JAMA*. **319**, 1723
3. Ng, M., Fleming, T., Robinson, M., Thomson, B., Graetz, N., Margono, C., Mullany, E. C., Biryukov, S., Abbafati, C., Abera, S. F., Abraham, J. P., Abu-Rmeileh, N. M. E., Achoki, T., AlBuhairan, F. S., Alemu, Z. A., Alfonso, R., Ali, M. K., Ali, R., Guzman, N. A., Ammar, W., Anwari, P., Banerjee, A., Barquera, S., Basu, S., Bennett, D. A., Bhutta, Z., Blore, J., Cabral, N., Nonato, I. C., Chang, J.-C., Chowdhury, R., Courville, K. J., Criqui, M. H., Cundiff, D. K., Dabhadkar, K. C., Dandona, L., Davis, A., Dayama, A., Dharmaratne, S. D., Ding, E. L., Durrani, A. M., Esteghamati, A., Farzadfar, F., Fay, D. F. J., Feigin, V. L., Flaxman, A., Forouzanfar, M. H., Goto, A., Green, M. A., Gupta, R., Hafezi-Nejad, N., Hankey, G. J., Harewood, H. C., Havmoeller, R., Hay, S., Hernandez, L., Husseini, A., Idrisov, B. T., Ikeda, N., Islami, F., Jahangir, E., Jassal, S. K., Jee, S. H., Jeffreys, M., Jonas, J. B., Kabagambe, E. K., Khalifa, S. E. A. H., Kengne, A. P., Khader, Y. S., Khang, Y.-H., Kim, D., Kimokoti, R. W., Kinge, J. M., Kokubo, Y., Kosen, S., Kwan, G., Lai, T., Leinsalu, M., Li, Y., Liang, X., Liu, S., Logroscino, G., Lotufo, P. A., Lu, Y., Ma, J., Mainoo, N. K., Mensah, G. A., Merriman, T. R., Mokdad, A. H., Moschandreas, J., Naghavi, M., Naheed, A., Nand, D., Narayan, K. M. V., Nelson, E. L., Neuhouser, M. L., Nisar, M. I., Ohkubo, T., Oti, S. O., Pedroza, A., Prabhakaran, D., Roy, N., Sampson, U., Seo, H., Sepanlou, S. G., Shibuya, K., Shiri, R., Shiue, I., Singh, G. M., Singh, J. A., Skirbekk, V., Stapelberg, N. J. C., Sturua, L., Sykes, B. L., Tobias, M., Tran, B. X., Trasande, L., Toyoshima, H., van de Vijver, S., Vasankari, T. J., Veerman, J. L., Velasquez-Melendez, G., Vlassov, V. V., Vollset, S. E., Vos, T., Wang, C., Wang, S. X., Weiderpass, E., Werdecker, A., Wright, J. L., Yang, Y. C., Yatsuya, H., Yoon, J., Yoon, S.-J., Zhao, Y., Zhou, M., Zhu, S., Lopez, A. D., Murray, C. J. L., Gakidou, E., Wang, X., Weiderpass, E., Werdecker, A., Wright, J. L., Yang, Y. C., Yatsuya, H., Yoon, J., Yoon, S.-J., Zhao, Y., Zhou, M., Zhu, S., Lopez, A. D., Murray, C. J. L., and Gakidou, E. (2014) Global, regional, and national prevalence of overweight and obesity in children and adults during 1980-2013: a systematic analysis for the Global Burden of Disease Study 2013. *Lancet*. **384**, 766–781
4. Beccuti, G., and Pannain, S. (2011) Sleep and obesity. *Curr. Opin. Clin. Nutr. Metab. Care*. **14**, 402–12
5. Trasande, L., Blustein, J., Liu, M., Corwin, E., Cox, L. M., and Blaser, M. J. (2013) Infant antibiotic exposures and early-life body mass. *Int. J. Obes. (Lond)*. **37**, 16–23
6. Correll, C. U., Lencz, T., and Malhotra, A. K. (2011) Antipsychotic drugs and obesity. *Trends Mol. Med.* **17**, 97–107
7. Bose, M., Oliván, B., and Laferrère, B. (2009) Stress and obesity: the role of the hypothalamic-pituitary-adrenal axis in metabolic disease. *Curr. Opin. Endocrinol. Diabetes. Obes.* **16**, 340–6

8. Guh, D. P., Zhang, W., Bansback, N., Amarsi, Z., Birmingham, C. L., and Anis, A. H. (2009) The incidence of co-morbidities related to obesity and overweight: A systematic review and meta-analysis. *BMC Public Health*. **9**, 88
9. Karter, A. J., Mayer-Davis, E. J., Selby, J. V, D'Agostino, R. B., Haffner, S. M., Sholinsky, P., Bergman, R., Saad, M. F., and Hamman, R. F. (1996) Insulin sensitivity and abdominal obesity in African-American, Hispanic, and non-Hispanic white men and women. The Insulin Resistance and Atherosclerosis Study. *Diabetes*. **45**, 1547–55
10. Preis, S. R., Massaro, J. M., Robins, S. J., Hoffmann, U., Vasan, R. S., Irlbeck, T., Meigs, J. B., Sutherland, P., D'Agostino, R. B., O'Donnell, C. J., Fox, C. S., and Fox, C. S. (2010) Abdominal subcutaneous and visceral adipose tissue and insulin resistance in the Framingham heart study. *Obesity (Silver Spring)*. **18**, 2191–8
11. Abate, N., Garg, A., Peshock, R. M., Stray-Gundersen, J., and Grundy, S. M. (1995) Relationships of generalized and regional adiposity to insulin sensitivity in men. *J. Clin. Invest.* **96**, 88–98
12. Wildman, R. P., Muntner, P., Reynolds, K., McGinn, A. P., Rajpathak, S., Wylie-Rosett, J., and Sowers, M. R. (2008) The Obese Without Cardiometabolic Risk Factor Clustering and the Normal Weight With Cardiometabolic Risk Factor Clustering. *Arch. Intern. Med.* **168**, 1617
13. Centers for Disease Control and Prevention (2017) *National Diabetes Statistics Report, 2017.*, [online] https://www.cdc.gov/diabetes/pdfs/data/statistics/national-diabetes-statistics-report.pdf (Accessed May 21, 2018)
14. POSNER, B. I., KELLY, P. A., SHIU, R. P. C., and FRIESEN, H. G. (1974) Studies of Insulin, Growth Hormone and Prolactin Binding: Tissue Distribution, Species Variation and Characterization. *Endocrinology*. **95**, 521–531
15. Czech, M. P., Tencerova, M., Pedersen, D. J., and Aouadi, M. (2013) Insulin signalling mechanisms for triacylglycerol storage. *Diabetologia*. **56**, 949–64
16. Leavens, K. F., and Birnbaum, M. J. (2011) Insulin signaling to hepatic lipid metabolism in health and disease. *Crit. Rev. Biochem. Mol. Biol.* **46**, 200–215
17. Biolo, G., and Wolfe, R. R. (1993) Insulin action on protein metabolism. *Baillieres. Clin. Endocrinol. Metab.* **7**, 989–1005
18. Begg, D. P., and Woods, S. C. (2012) The Central Insulin System and Energy Balance. in *Handbook of experimental pharmacology*, pp. 111–129, 10.1007/978-3-642-24716-3_5
19. Zhao, W. Q., and Alkon, D. L. (2001) Role of insulin and insulin receptor in learning and memory. *Mol. Cell. Endocrinol.* **177**, 125–34
20. Sliwowska, J. H., Fergani, C., Gawałek, M., Skowronska, B., Fichna, P., and Lehman, M. N. (2014) Insulin: its role in the central control of reproduction. *Physiol. Behav.* **133**, 197–206
21. Daly, P. A., and Landsberg, L. Hypertension in Obesity and NIDDM Role of Insulin and Sympathetic Nervous System. [online] http://care.diabetesjournals.org/content/14/3/240.full-text.pdf (Accessed May 20, 2018)
22. Boutens, L., and Stienstra, R. (2016) Adipose tissue macrophages: going off track during obesity. *Diabetologia*. **59**, 879–894
23. Draznin, B. (2010) Mitogenic action of insulin: friend, foe or 'frenemy'? *Diabetologia*. **53**, 229–233
24. DeFronzo, R. A., Cooke, C. R., Andres, R., Faloona, G. R., and Davis, P. J. (1975) The effect of insulin on renal handling of sodium, potassium, calcium, and phosphate in man.

J. Clin. Invest. **55**, 845–55
25. LUNDBAEK, K. (1948) Metabolic abnormalities in starvation diabetes. *Yale J. Biol. Med.* **20**, 533–44
26. Dunaif, A. (1997) Insulin Resistance and the Polycystic Ovary Syndrome: Mechanism and Implications for Pathogenesis [1]. *Endocr. Rev.* **18**, 774–800
27. Van Cromphaut, S. J., Vanhorebeek, I., and Van den Berghe, G. (2008) Glucose metabolism and insulin resistance in sepsis. *Curr. Pharm. Des.* **14**, 1887–99
28. Tritos, N. A., and Mantzoros, C. S. (1998) Syndromes of Severe Insulin Resistance. *J. Clin. Endocrinol. Metab.* **83**, 3025–3030
29. Golay, A., Chen, Y. D., and Reaven, G. M. (1986) Effect of differences in glucose tolerance on insulin's ability to regulate carbohydrate and free fatty acid metabolism in obese individuals. *J. Clin. Endocrinol. Metab.* **62**, 1081–8
30. Weyer, C., Tataranni, P. A., Bogardus, C., and Pratley, R. E. (2001) Insulin Resistance and Insulin Secretory Dysfunction Are Independent Predictors of Worsening of Glucose Tolerance During Each Stage of Type 2 Diabetes Development. *Diabetes Care*. **24**, 89–94
31. Tabák, A. G., Herder, C., Rathmann, W., Brunner, E. J., and Kivimäki, M. (2012) Prediabetes: a high-risk state for diabetes development. *Lancet (London, England)*. **379**, 2279–90
32. Bergman, R. N. Lilly Lecture 1989 Toward Physiological Understanding of Glucose Tolerance Minimal-Model Approach. [online] http://diabetes.diabetesjournals.org/content/38/12/1512.full-text.pdf (Accessed May 21, 2018)
33. Weyer, C., Bogardus, C., Mott, D. M., and Pratley, R. E. (1999) The natural history of insulin secretory dysfunction and insulin resistance in the pathogenesis of type 2 diabetes mellitus. *J. Clin. Invest.* **104**, 787–94
34. Shanik, M. H., Xu, Y., Skrha, J., Dankner, R., Zick, Y., and Roth, J. (2008) Insulin resistance and hyperinsulinemia: is hyperinsulinemia the cart or the horse? *Diabetes Care*. **31 Suppl 2**, S262-8
35. Forbes, J. M., and Cooper, M. E. (2013) Mechanisms of Diabetic Complications. *Physiol. Rev.* **93**, 137–188
36. Reaven, G. M. (1993) Role of Insulin Resistance in Human Disease (Syndrome X): An Expanded Definition. *Annu. Rev. Med.* **44**, 121–131
37. Reaven, G. M. (1988) Banting lecture 1988. Role of insulin resistance in human disease. *Diabetes*. **37**, 1595–607
38. Yip, J., Facchini, F. S., and Reaven, G. M. (1998) Resistance to Insulin-Mediated Glucose Disposal as a Predictor of Cardiovascular Disease. *J. Clin. Endocrinol. Metab.* **83**, 2773–2776
39. Howard, G., O'Leary, D. H., Zaccaro, D., Haffner, S., Rewers, M., Hamman, R., Selby, J. V., Saad, M. F., Savage, P., and Bergman, R. (1996) Insulin Sensitivity and Atherosclerosis. *Circulation*. **93**, 1809–1817
40. Esposito, K., Chiodini, P., Colao, A., Lenzi, A., and Giugliano, D. (2012) Metabolic syndrome and risk of cancer: a systematic review and meta-analysis. *Diabetes Care*. **35**, 2402–11
41. Arnold, S. E., Arvanitakis, Z., Macauley-Rambach, S. L., Koenig, A. M., Wang, H.-Y., Ahima, R. S., Craft, S., Gandy, S., Buettner, C., Stoeckel, L. E., Holtzman, D. M., and Nathan, D. M. (2018) Brain insulin resistance in type 2 diabetes and Alzheimer disease:

concepts and conundrums. *Nat. Rev. Neurol.* **14**, 168–181
42. American Diabetes Association, A. D. (2013) Economic costs of diabetes in the U.S. in 2012. *Diabetes Care*. **36**, 1033–46
43. Benjamin, E. J., Blaha, M. J., Chiuve, S. E., Cushman, M., Das, S. R., Deo, R., de Ferranti, S. D., Floyd, J., Fornage, M., Gillespie, C., Isasi, C. R., Jiménez, M. C., Jordan, L. C., Judd, S. E., Lackland, D., Lichtman, J. H., Lisabeth, L., Liu, S., Longenecker, C. T., Mackey, R. H., Matsushita, K., Mozaffarian, D., Mussolino, M. E., Nasir, K., Neumar, R. W., Palaniappan, L., Pandey, D. K., Thiagarajan, R. R., Reeves, M. J., Ritchey, M., Rodriguez, C. J., Roth, G. A., Rosamond, W. D., Sasson, C., Towfighi, A., Tsao, C. W., Turner, M. B., Virani, S. S., Voeks, J. H., Willey, J. Z., Wilkins, J. T., Wu, J. H., Alger, H. M., Wong, S. S., Muntner, P., and American Heart Association Statistics Committee and Stroke Statistics Subcommittee, O. behalf of the A. H. A. S. C. and S. S. (2017) Heart Disease and Stroke Statistics-2017 Update: A Report From the American Heart Association. *Circulation*. **135**, e146–e603
44. Kelley, D., Mitrakou, A., Marsh, H., Schwenk, F., Benn, J., Sonnenberg, G., Arcangeli, M., Aoki, T., Sorensen, J., and Berger, M. (1988) Skeletal muscle glycolysis, oxidation, and storage of an oral glucose load. *J. Clin. Invest.* **81**, 1563–1571
45. DeFronzo, R. A., Jacot, E., Jequier, E., Maeder, E., Wahren, J., and Felber, J. P. (1981) The effect of insulin on the disposal of intravenous glucose. Results from indirect calorimetry and hepatic and femoral venous catheterization. *Diabetes*. **30**, 1000–7
46. Jensen, J., Rustad, P. I., Kolnes, A. J., and Lai, Y.-C. (2011) The role of skeletal muscle glycogen breakdown for regulation of insulin sensitivity by exercise. *Front. Physiol.* **2**, 112
47. Rabinowitz, D., and Zierler, K. L. (1962) FOREARM METABOLISM IN OBESITY AND ITS RESPONSE TO INTRA- ARTERIAL INSULIN. CHARACTERIZATION OF INSULIN RE- SISTANCE AND EVIDENCE FOR ADAPTIVE HYPERINSULINISM *. *J. Clin. Invest.* [online] https://www.ncbi.nlm.nih.gov/pmc/articles/PMC291152/pdf/jcinvest00321-0095.pdf (Accessed January 19, 2018)
48. DeFronzo, R. A., and Tripathy, D. (2009) Skeletal muscle insulin resistance is the primary defect in type 2 diabetes. *Diabetes Care*. **32 Suppl 2**, S157-63
49. Gulli, G., Ferrannini, E., Stern, M., Haffner, S., and DeFronzo, R. A. (1992) The metabolic profile of NIDDM is fully established in glucose-tolerant offspring of two Mexican-American NIDDM parents. *Diabetes*. **41**, 1575–86
50. Eriksson, J., Franssila-Kallunki, A., Ekstrand, A., Saloranta, C., Widén, E., Schalin, C., and Groop, L. (1989) Early Metabolic Defects in Persons at Increased Risk for Non-Insulin-Dependent Diabetes Mellitus. *N. Engl. J. Med.* **321**, 337–343
51. Goodpaster, B. H., Kelley, D. E., Wing, R. R., Meier, A., and Thaete, F. L. (1999) Effects of weight loss on regional fat distribution and insulin sensitivity in obesity. *Diabetes*. **48**, 839–47
52. Knowler, W. C., Barrett-Connor, E., Fowler, S. E., Hamman, R. F., Lachin, J. M., Walker, E. A., Nathan, D. M., and Diabetes Prevention Program Research Group (2002) Reduction in the incidence of type 2 diabetes with lifestyle intervention or metformin. *N. Engl. J. Med.* **346**, 393–403
53. DREAM (Diabetes REduction Assessment with ramipril and rosiglitazone Medication) Trial Investigators, Gerstein, H. C., Yusuf, S., Bosch, J., Pogue, J., Sheridan, P., Dinccag,

N., Hanefeld, M., Hoogwerf, B., Laakso, M., Mohan, V., Shaw, J., Zinman, B., and Holman, R. R. (2006) Effect of rosiglitazone on the frequency of diabetes in patients with impaired glucose tolerance or impaired fasting glucose: a randomised controlled trial. *Lancet*. **368**, 1096–1105

54. Belfiore, A., Frasca, F., Pandini, G., Sciacca, L., and Vigneri, R. (2009) Insulin receptor isoforms and insulin receptor/insulin-like growth factor receptor hybrids in physiology and disease. *Endocr. Rev.* **30**, 586–623
55. Haeusler, R. A., McGraw, T. E., and Accili, D. (2017) Biochemical and cellular properties of insulin receptor signalling. *Nat. Rev. Mol. Cell Biol.* **19**, 31–44
56. Thong, F. S. L., Dugani, C. B., and Klip, A. (2005) Turning Signals On and Off: GLUT4 Traffic in the Insulin-Signaling Highway. *Physiology*. **20**, 271–284
57. Mandarino, L. J., Printz, R. L., Cusi, K. A., Kinchington, P., O'Doherty, R. M., Osawa, H., Sewell, C., Consoli, A., Granner, D. K., and DeFronzo, R. A. (1995) Regulation of hexokinase II and glycogen synthase mRNA, protein, and activity in human muscle. *Am. J. Physiol. Metab.* **269**, E701–E708
58. Zierath, J. R., Houseknecht, K. L., Gnudi, L., and Kahn, B. B. (1997) High-fat feeding impairs insulin-stimulated GLUT4 recruitment via an early insulin-signaling defect. *Diabetes*. **46**, 215–23
59. Cline, G. W., Petersen, K. F., Krssak, M., Shen, J., Hundal, R. S., Trajanoski, Z., Inzucchi, S., Dresner, A., Rothman, D. L., and Shulman, G. I. (1999) Impaired Glucose Transport as a Cause of Decreased Insulin-Stimulated Muscle Glycogen Synthesis in Type 2 Diabetes. *N. Engl. J. Med.* **341**, 240–246
60. Bonadonna, R. C., Del Prato, S., Bonora, E., Saccomani, M. P., Gulli, G., Natali, A., Frascerra, S., Pecori, N., Ferrannini, E., Bier, D., Cobelli, C., and DeFronzo, R. A. (1996) Roles of glucose transport and glucose phosphorylation in muscle insulin resistance of NIDDM. *Diabetes*. **45**, 915–25
61. Kelley, D. E., Mintun, M. A., Watkins, S. C., Simoneau, J. A., Jadali, F., Fredrickson, A., Beattie, J., and Thériault, R. (1996) The effect of non-insulin-dependent diabetes mellitus and obesity on glucose transport and phosphorylation in skeletal muscle. *J. Clin. Invest.* **97**, 2705–2713
62. Kelley, D. E., Mokan, M., and Mandarino, L. J. (1992) Intracellular defects in glucose metabolism in obese patients with NIDDM. *Diabetes*. **41**, 698–706
63. Thorburn, A. W., Gumbiner, B., Bulacan, F., Wallace, P., and Henry, R. R. (1990) Intracellular glucose oxidation and glycogen synthase activity are reduced in non-insulin-dependent (type II) diabetes independent of impaired glucose uptake. *J. Clin. Invest.* **85**, 522–9
64. Shulman, G. I., Rothman, D. L., Jue, T., Stein, P., DeFronzo, R. A., and Shulman, R. G. (1990) Quantitation of Muscle Glycogen Synthesis in Normal Subjects and Subjects with Non-Insulin-Dependent Diabetes by ^{13} C Nuclear Magnetic Resonance Spectroscopy. *N. Engl. J. Med.* **322**, 223–228
65. Petersen, K. F., Dufour, S., Savage, D. B., Bilz, S., Solomon, G., Yonemitsu, S., Cline, G. W., Befroy, D., Zemany, L., Kahn, B. B., Papademetris, X., Rothman, D. L., and Shulman, G. I. (2007) The role of skeletal muscle insulin resistance in the pathogenesis of the metabolic syndrome. *Proc. Natl. Acad. Sci.* **104**, 12587–12594
66. Boucher, J., Kleinridders, A., and Kahn, C. R. (2014) Insulin Receptor Signaling in Normal and Insulin-Resistant States. *Cold Spring Harb. Perspect. Biol.* **6**, a009191–

a009191
67. Samuel, V. T., and Shulman, G. I. (2012) Mechanisms for Insulin Resistance: Common Threads and Missing Links. *Cell*. **148**, 852–871
68. Wu, H., and Ballantyne, C. M. (2017) Skeletal muscle inflammation and insulin resistance in obesity. *J. Clin. Invest.* **127**, 43–54
69. Muoio, D. M. M., and Neufer, P. D. D. (2012) Lipid-induced mitochondrial stress and insulin action in muscle. *Cell Metab.* **15**, 595–605
70. Williams, A. S., Kang, L., and Wasserman, D. H. (2015) The extracellular matrix and insulin resistance. *Trends Endocrinol. Metab.* **26**, 357–366
71. Wasserman, D. H., Kang, L., Ayala, J. E., Fueger, P. T., and Lee-Young, R. S. (2011) The physiological regulation of glucose flux into muscle in vivo. *J. Exp. Biol.* **214**, 254–62
72. Yang, Y. J., Hope, I. D., Ader, M., and Bergman, R. N. (1989) Insulin transport across capillaries is rate limiting for insulin action in dogs. *J. Clin. Invest.* **84**, 1620–8
73. Chiu, J. D., Richey, J. M., Harrison, L. N., Zuniga, E., Kolka, C. M., Kirkman, E., Ellmerer, M., and Bergman, R. N. (2008) Direct administration of insulin into skeletal muscle reveals that the transport of insulin across the capillary endothelium limits the time course of insulin to activate glucose disposal. *Diabetes*. **57**, 828–35
74. Rorsman, P., and Braun, M. (2013) Regulation of Insulin Secretion in Human Pancreatic Islets. *Annu. Rev. Physiol.* **75**, 155–179
75. Shapiro, E. T., Tillil, H., Miller, M. A., Frank, B. H., Galloway, J. A., Rubenstein, A. H., and Polonsky, K. S. (1987) Insulin secretion and clearance. Comparison after oral and intravenous glucose. *Diabetes*. **36**, 1365–71
76. Bishop, J. S., Steele, R., Altszuler, N., Dunn, A., Bjerknes, C., and de Bodo, R. C. (1965) Effects of insulin on liver glycogen synthesis and breakdown in the dog. *Am. J. Physiol. Content*. **208**, 307–316
77. Moore, M. C., Coate, K. C., Winnick, J. J., An, Z., and Cherrington, A. D. (2012) Regulation of hepatic glucose uptake and storage in vivo. *Adv. Nutr.* **3**, 286–94
78. Ader, M., Stefanovski, D., Kim, S. P., Richey, J. M., Ionut, V., Catalano, K. J., Hucking, K., Ellmerer, M., Van Citters, G., Hsu, I. R., Chiu, J. D., Woolcott, O. O., Harrison, L. N., Zheng, D., Lottati, M., Kolka, C. M., Mooradian, V., Dittmann, J., Yae, S., Liu, H., Castro, A. V. B., Kabir, M., and Bergman, R. N. (2014) Hepatic insulin clearance is the primary determinant of insulin sensitivity in the normal dog. *Obesity (Silver Spring)*. **22**, 1238–45
79. Kim, S. P., Ellmerer, M., Kirkman, E. L., and Bergman, R. N. (2007) β-Cell "rest" accompanies reduced first-pass hepatic insulin extraction in the insulin-resistant, fat-fed canine model. *Am. J. Physiol. Metab.* **292**, E1581–E1589
80. Mittelman, S. D., Van Citters, G. W., Kim, S. P., Davis, D. A., Dea, M. K., Hamilton-Wessler, M., and Bergman, R. N. (2000) Longitudinal compensation for fat-induced insulin resistance includes reduced insulin clearance and enhanced beta-cell response. *Diabetes*. **49**, 2116–25
81. Erdmann, J., Kallabis, B., Oppel, U., Sypchenko, O., Wagenpfeil, S., and Schusdziarra, V. (2008) Development of hyperinsulinemia and insulin resistance during the early stage of weight gain. *Am. J. Physiol. Metab.* **294**, E568–E575
82. Ferrannini, E., Bjorkman, O., Reichard, G. A., Pilo, A., Olsson, M., Wahren, J., and DeFronzo, R. A. (1985) The disposal of an oral glucose load in healthy subjects. A quantitative study. *Diabetes*. **34**, 580–8

83. Stubbs, W., Kelly, D., Morgan, I., and Alberti, K. G. M. M. (1982) Insulin Clearance by Perfused Rat Lung. *Horm. Metab. Res.* **14**, 8–9
84. Kelbaek, H., Munck, O., Christensen, N. J., and Godtfredsen, J. (1989) Central haemodynamic changes after a meal. *Br. Heart J.* **61**, 506–9
85. Duckworth, W. C., Bennett, R. G., and Hamel, F. G. (1998) Insulin degradation: progress and potential. *Endocr. Rev.* **19**, 608–24
86. Rabkin, R., Ryan, M. P., and Duckworth, W. C. (1984) The renal metabolism of insulin. *Diabetologia*. **27**, 351–7
87. Liang, C., Doherty, J. U., Faillace, R., Maekawa, K., Arnold, S., Gavras, H., Hood, W. B., and Jr. (1982) Insulin infusion in conscious dogs. Effects on systemic and coronary hemodynamics, regional blood flows, and plasma catecholamines. *J. Clin. Invest.* **69**, 1321–36
88. Baron, A. D. (1994) Hemodynamic actions of insulin. *Am. J. Physiol.* **267**, E187-202
89. Laakso, M., Edelman, S. V, Brechtel, G., and Baron, A. D. (1990) Decreased effect of insulin to stimulate skeletal muscle blood flow in obese man. A novel mechanism for insulin resistance. *J. Clin. Invest.* **85**, 1844–52
90. Baron, A. D., and Brechtel, G. (1993) Insulin differentially regulates systemic and skeletal muscle vascular resistance. *Am. J. Physiol.* **265**, E61-7
91. Yki-Järvinen, H., and Utriainen, T. (1998) Insulin-induced vasodilatation: physiology or pharmacology? *Diabetologia*. **41**, 369–79
92. Rattigan, S., Clark, M. G., and Barrett, E. J. (1997) Hemodynamic actions of insulin in rat skeletal muscle: evidence for capillary recruitment. *Diabetes*. **46**, 1381–8
93. Coggins, M., Lindner, J., Rattigan, S., Jahn, L., Fasy, E., Kaul, S., and Barrett, E. (2001) Physiologic hyperinsulinemia enhances human skeletal muscle perfusion by capillary recruitment. *Diabetes*. **50**, 2682–90
94. Barrett, E. J., and Rattigan, S. (2012) Muscle perfusion: its measurement and role in metabolic regulation. *Diabetes*. **61**, 2661–8
95. Vincent, M. A., Clerk, L. H., Lindner, J. R., Klibanov, A. L., Clark, M. G., Rattigan, S., and Barrett, E. J. (2004) Microvascular recruitment is an early insulin effect that regulates skeletal muscle glucose uptake in vivo. *Diabetes*. **53**, 1418–23
96. Vincent, M. A., Clerk, L. H., Lindner, J. R., Price, W. J., Jahn, L. A., Leong-Poi, H., and Barrett, E. J. (2006) Mixed meal and light exercise each recruit muscle capillaries in healthy humans. *Am. J. Physiol. Metab.* **290**, E1191–E1197
97. Newman, J. M. B., Ross, R. M., Richards, S. M., Clark, M. G., and Rattigan, S. (2007) Insulin and contraction increase nutritive blood flow in rat muscle in vivo determined by microdialysis of L-[14C]glucose. *J. Physiol.* **585**, 217–29
98. Poole, D. C., Brown, M. D., and Hudlicka, O. (2008) Counterpoint: There is not capillary recruitment in active skeletal muscle during exercise. *J. Appl. Physiol.* **104**, 891–893
99. Clark, M. G., Rattigan, S., Barrett, E. J., and Vincent, M. A. (2008) Point:Counterpoint: There is/is not capillary recruitment in active skeletal muscle during exercise. *J. Appl. Physiol.* **104**, 889–891
100. Westerbacka, J., Wilkinson, I., Cockcroft, J., Utriainen, T., Vehkavaara, S., and Yki-Järvinen, H. (1999) Diminished wave reflection in the aorta. A novel physiological action of insulin on large blood vessels. *Hypertens. (Dallas, Tex. 1979)*. **33**, 1118–22
101. Renaudin, C., Michoud, E., Rapin, J. R., Lagarde, M., and Wiernsperger, N. (1998) Hyperglycaemia modifies the reaction of microvessels to insulin in rat skeletal muscle.

Diabetologia. **41**, 26–33
102. Chen, Y. L., and Messina, E. J. (1996) Dilation of isolated skeletal muscle arterioles by insulin is endothelium dependent and nitric oxide mediated. *Am. J. Physiol.* **270**, H2120-4
103. McKay, M. K., and Hester, R. L. (1996) Role of nitric oxide, adenosine, and ATP-sensitive potassium channels in insulin-induced vasodilation. *Hypertens. (Dallas, Tex. 1979)*. **28**, 202–8
104. Eringa, E. C., Stehouwer, C. D. A., Merlijn, T., Westerhof, N., and Sipkema, P. (2002) Physiological concentrations of insulin induce endothelin-mediated vasoconstriction during inhibition of NOS or PI3-kinase in skeletal muscle arterioles. *Cardiovasc. Res.* **56**, 464–71
105. Grover, A., Padginton, C., Wilson, M. F., Sung, B. H., Izzo, J. L., and Dandona, P. (1995) Insulin attenuates norepinephrine-induced venoconstriction. An ultrasonographic study. *Hypertens. (Dallas, Tex. 1979)*. **25**, 779–84
106. Feldman, R. D., and Bierbrier, G. S. (1993) Insulin-mediated vasodilation: impairment with increased blood pressure and body mass. *Lancet (London, England)*. **342**, 707–9
107. Steinberg, H. O., Brechtel, G., Johnson, A., Fineberg, N., and Baron, A. D. (1994) Insulin-mediated skeletal muscle vasodilation is nitric oxide dependent. A novel action of insulin to increase nitric oxide release. *J. Clin. Invest.* **94**, 1172–9
108. Zeng, G., and Quon, M. J. (1996) Insulin-stimulated production of nitric oxide is inhibited by wortmannin. Direct measurement in vascular endothelial cells. *J. Clin. Invest.* **98**, 894–8
109. Muniyappa, R., Montagnani, M., Koh, K. K., and Quon, M. J. (2007) Cardiovascular Actions of Insulin. *Endocr. Rev.* **28**, 463–491
110. Denninger, J. W., and Marletta, M. A. (1999) Guanylate cyclase and the ·NO/cGMP signaling pathway. *Biochim. Biophys. Acta - Bioenerg.* **1411**, 334–350
111. Cardillo, C., Nambi, S. S., Kilcoyne, C. M., Choucair, W. K., Katz, A., Quon, M. J., and Panza, J. A. (1999) Insulin stimulates both endothelin and nitric oxide activity in the human forearm. *Circulation*. **100**, 820–5
112. Halseth, A. E., Bracy, D. P., and Wasserman, D. H. (1998) Limitations to exercise- and maximal insulin-stimulated muscle glucose uptake. *J. Appl. Physiol.* **85**, 2305–2313
113. Pitkanen, O. P., Laine, H., Kemppainen, J., Eronen, E., Alanen, A., Raitakari, M., Kirvela, O., Ruotsalainen, U., Knuuti, J., Koivisto, V. A., and Nuutila, P. (1999) Sodium nitroprusside increases human skeletal muscle blood flow, but does not change flow distribution or glucose uptake. *J. Physiol.* **521 Pt 3**, 729–37
114. Nuutila, P., Raitakari, M., Laine, H., Kirvelä, O., Takala, T., Utriainen, T., Mäkimattila, S., Pitkänen, O. P., Ruotsalainen, U., Iida, H., Knuuti, J., and Yki-Järvinen, H. (1996) Role of blood flow in regulating insulin-stimulated glucose uptake in humans. Studies using bradykinin, [15O]water, and [18F]fluoro-deoxy-glucose and positron emission tomography. *J. Clin. Invest.* **97**, 1741–1747
115. Natali, A., Quiñones Galvan, A., Pecori, N., Sanna, G., Toschi, E., and Ferrannini, E. (1998) Vasodilation with sodium nitroprusside does not improve insulin action in essential hypertension. *Hypertens. (Dallas, Tex. 1979)*. **31**, 632–6
116. Natali, A., Bonadonna, R., Santoro, D., Galvan, A. Q., Baldi, S., Frascerra, S., Palombo, C., Ghione, S., and Ferrannini, E. (1994) Insulin resistance and vasodilation in essential hypertension. Studies with adenosine. *J. Clin. Invest.* **94**, 1570–6
117. Jamerson, K. A., Nesbitt, S. D., Amerena, J. V, Grant, E., and Julius, S. (1996)

Angiotensin mediates forearm glucose uptake by hemodynamic rather than direct effects. *Hypertens. (Dallas, Tex. 1979)*. **27**, 854–8
118. Baron, A. D., Steinberg, H., Brechtel, G., and Johnson, A. (1994) Skeletal muscle blood flow independently modulates insulin-mediated glucose uptake. *Am. J. Physiol.* **266**, E248-53
119. Baron, A. D., Steinberg, H. O., Chaker, H., Leaming, R., Johnson, A., and Brechtel, G. (1995) Insulin-mediated skeletal muscle vasodilation contributes to both insulin sensitivity and responsiveness in lean humans. *J. Clin. Invest.* **96**, 786–92
120. Barrett, E. J., Wang, H., Upchurch, C. T., and Liu, Z. (2011) Insulin regulates its own delivery to skeletal muscle by feed-forward actions on the vasculature. *Am. J. Physiol. Endocrinol. Metab.* **301**, E252-63
121. Ellmerer, M., Kim, S. P., Hamilton-Wessler, M., Hucking, K., Kirkman, E., and Bergman, R. N. (2004) Physiological Hyperinsulinemia in Dogs Augments Access of Macromolecules to Insulin-Sensitive Tissues. *Diabetes*. **53**, 2741–2747
122. Weinhandl, H., Pachler, C., Mader, J. K., Ikeoka, D., Mautner, A., Falk, A., Suppan, M., Pieber, T. R., and Ellmerer, M. (2007) Physiological hyperinsulinemia has no detectable effect on access of macromolecules to insulin-sensitive tissues in healthy humans. *Diabetes*. **56**, 2213–7
123. Fu, Z., Zhao, L., Aylor, K. W., Carey, R. M., Barrett, E. J., and Liu, Z. (2014) Angiotensin-(1-7) recruits muscle microvasculature and enhances insulin's metabolic action via mas receptor. *Hypertension*. **63**, 1219–27
124. Lillioja, S., Young, A. A., Culter, C. L., Ivy, J. L., Abbott, W. G., Zawadzki, J. K., Yki-Järvinen, H., Christin, L., Secomb, T. W., and Bogardus, C. (1987) Skeletal muscle capillary density and fiber type are possible determinants of in vivo insulin resistance in man. *J. Clin. Invest.* **80**, 415–24
125. Prior, S. J., Goldberg, A. P., Ortmeyer, H. K., Chin, E. R., Chen, D., Blumenthal, J. B., and Ryan, A. S. (2015) Increased Skeletal Muscle Capillarization Independently Enhances Insulin Sensitivity in Older Adults After Exercise Training and Detraining. *Diabetes*. **64**, 3386–3395
126. Bonner, J. S., Lantier, L., Hasenour, C. M., James, F. D., Bracy, D. P., and Wasserman, D. H. (2013) Muscle-specific vascular endothelial growth factor deletion induces muscle capillary rarefaction creating muscle insulin resistance. *Diabetes*. **62**, 572–80
127. Pries, A. R., and Secomb, T. W. (2014) Making microvascular networks work: angiogenesis, remodeling, and pruning. *Physiology (Bethesda)*. **29**, 446–55
128. Michel, C. C., and Curry, F. E. (1999) Microvascular permeability. *Physiol. Rev.* **79**, 703–61
129. Mann, G. E., Yudilevich, D. L., and Sobrevia, L. (2003) Regulation of Amino Acid and Glucose Transporters in Endothelial and Smooth Muscle Cells. *Physiol. Rev.* **83**, 183–252
130. Regittnig, W., Ellmerer, M., Fauler, G., Sendlhofer, G., Trajanoski, Z., Leis, H.-J., Schaupp, L., Wach, P., and Pieber, T. R. (2003) Assessment of transcapillary glucose exchange in human skeletal muscle and adipose tissue. *Am. J. Physiol. Endocrinol. Metab.* **285**, E241-51
131. Maggs, D. G., Jacob, R., Rife, F., Lange, R., Leone, P., During, M. J., Tamborlane, W. V, and Sherwin, R. S. (1995) Interstitial fluid concentrations of glycerol, glucose, and amino acids in human quadricep muscle and adipose tissue. Evidence for significant lipolysis in skeletal muscle. *J. Clin. Invest.* **96**, 370–377

132. FUCHI, T., ROSDAHL, H., HICKNER, R. C., UNGERSTEDT, U., and HENRIKSSON, J. (1994) Microdialysis of rat skeletal muscle and adipose tissue: dynamics of the interstitial glucose pool. *Acta Physiol. Scand.* **151**, 249–260
133. Aukland, K., and Reed, R. K. (1993) Interstitial-lymphatic mechanisms in the control of extracellular fluid volume. *Physiol. Rev.* **73**, 1–78
134. Sherwin, R. S., Kramer, K. J., Tobin, J. D., Insel, P. A., Liljenquist, J. E., Berman, M., and Andres, R. (1974) A model of the kinetics of insulin in man. *J. Clin. Invest.* **53**, 1481–92
135. Rasio, E. A., Mack, E., Egdahl, R. H., and Herrera, M. G. Passage of Insulin and Inulin Across Vascular Membranes in the Dog The biological activity of a hormone depends on its reaching the cell membrane of the target tissue in effective concentration. Small molecules diffuse easily across vascular endothelium, and their concentrations in. [online] http://diabetes.diabetesjournals.org/content/17/11/668.full-text.pdf (Accessed May 23, 2018)
136. Yang, Y. J., Hope, I. D., Ader, M., and Bergman, R. N. (1994) Importance of transcapillary insulin transport to dynamics of insulin action after intravenous glucose. *Am. J. Physiol.* **266**, E17-25
137. Sjostrand, M., Holmang, A., Lonnroth, P., Sjöstrand, M., Holmäng, A., and Lönnroth, P. (1999) Measurement of interstitial insulin in human muscle. *Am. J. Physiol.* **276**, E151-4
138. Miles, P. D., Levisetti, M., Reichart, D., Khoursheed, M., Moossa, A. R., and Olefsky, J. M. (1995) Kinetics of insulin action in vivo. Identification of rate-limiting steps. *Diabetes*. **44**, 947–53
139. Wagenmakers, A. J. M., Strauss, J. A., Shepherd, S. O., Keske, M. A., and Cocks, M. (2016) Increased muscle blood supply and transendothelial nutrient and insulin transport induced by food intake and exercise: effect of obesity and ageing. *J. Physiol.* **594**, 2207–22
140. Sarin, H. (2010) Physiologic upper limits of pore size of different blood capillary types and another perspective on the dual pore theory of microvascular permeability. *J. Angiogenes. Res.* **2**, 14
141. Bruns, R. R., and Palade, G. E. (1968) Studies on blood capillaries. I. General organization of blood capillaries in muscle. *J. Cell Biol.* **37**, 244–76
142. Simionescu, N. (1983) Cellular aspects of transcapillary exchange. *Physiol. Rev.* **63**, 1536–79
143. Clough, G., and Michel, C. C. (1981) The role of vesicles in the transport of ferritin through frog endothelium. *J. Physiol.* **315**, 127–42
144. Simionescu, M., and Simionescu, N. (1991) Endothelial transport of macromolecules: transcytosis and endocytosis. A look from cell biology. *Cell Biol. Rev.* **25**, 1–78
145. Gustavsson, J., PARPAL, S., KARLSSON, M., RAMSING, C., Thorn, H., Borg, M., Lindroth, M., PETERSON, K. H., Magnusson, K.-E. E., Strâlfors, P., and STRaLFORS, P. (1999) Localization of the insulin receptor in caveolae of adipocyte plasma membrane. *FASEB J.* **13**, 1961–71
146. Predescu, S. A., Predescu, D. N., and Malik, A. B. (2007) Molecular determinants of endothelial transcytosis and their role in endothelial permeability. *Am. J. Physiol. Lung Cell. Mol. Physiol.* **293**, L823-42
147. Rippe, B., Rosengren, B.-I., Carlsson, O., and Venturoli, D. (2002) Transendothelial Transport: The Vesicle Controversy. *J. Vasc. Res.* **39**, 375–390
148. Wagner, R. C., and Casley-Smith, J. R. (1981) Endothelial vesicles. *Microvasc. Res.* **21**,

267–298
149. BAR, R. S., HOAK, J. C., and PEACOCK, M. L. (1978) INSULIN RECEPTORS IN HUMAN ENDOTHELIAL CELLS: IDENTIFICATION AND CHARACTERIZATION [1]. *J. Clin. Endocrinol. Metab.* **47**, 699–702
150. King, G. L., and Johnson, S. M. (1985) Receptor-mediated transport of insulin across endothelial cells. *Science*. **227**, 1583–6
151. Bar, R. S., Boes, M., and Sandra, A. (1988) Vascular transport of insulin to rat cardiac muscle. Central role of the capillary endothelium. *J. Clin. Invest.* **81**, 1225–33
152. Wang, H., Liu, Z., Li, G., and Barrett, E. J. (2006) The vascular endothelial cell mediates insulin transport into skeletal muscle. *Am. J. Physiol. Endocrinol. Metab.* **291**, E323-32
153. Schnitzer, J. E., Oh, P., Pinney, E., and Allard, J. (1994) Filipin-sensitive caveolae-mediated transport in endothelium: reduced transcytosis, scavenger endocytosis, and capillary permeability of select macromolecules. *J. Cell Biol.* **127**, 1217–32
154. Wang, H., Wang, A. X., and Barrett, E. J. (2011) Caveolin-1 is required for vascular endothelial insulin uptake. *Am. J. Physiol. Endocrinol. Metab.* **300**, E134-44
155. Azizi, P. M., Zyla, R. E., Guan, S., Wang, C., Liu, J., Bolz, S.-S., Heit, B., Klip, A., and Lee, W. L. (2014) Clathrin-dependent entry and vesicle-mediated exocytosis define insulin transcytosis across microvascular endothelial cells. *Mol. Biol. Cell*. **26**, 740–50
156. Kubota, T., Kubota, N., Kumagai, H., Yamaguchi, S., Kozono, H., Takahashi, T., Inoue, M., Itoh, S., Takamoto, I., Sasako, T., Kumagai, K., Kawai, T., Hashimoto, S., Kobayashi, T., Sato, M., Tokuyama, K., Nishimura, S., Tsunoda, M., Ide, T., Murakami, K., Yamazaki, T., Ezaki, O., Kawamura, K., Masuda, H., Moroi, M., Sugi, K., Oike, Y., Shimokawa, H., Yanagihara, N., Tsutsui, M., Terauchi, Y., Tobe, K., Nagai, R., Kamata, K., Inoue, K., Kodama, T., Ueki, K., and Kadowaki, T. (2011) Impaired insulin signaling in endothelial cells reduces insulin-induced glucose uptake by skeletal muscle. *Cell Metab.* **13**, 294–307
157. Steil, G. M., Ader, M., Moore, D. M., Rebrin, K., and Bergman, R. N. (1996) Transendothelial insulin transport is not saturable in vivo. No evidence for a receptor-mediated process. *J. Clin. Invest.* **97**, 1497–503
158. Vicent, D., Ilany, J., Kondo, T., Naruse, K., Fisher, S. J., Kisanuki, Y. Y., Bursell, S., Yanagisawa, M., King, G. L., and Kahn, C. R. (2003) The role of endothelial insulin signaling in the regulation of vascular tone and insulin resistance. *J. Clin. Invest.* **111**, 1373–80
159. Konishi, M., Sakaguchi, M., Lockhart, S. M., Cai, W., Li, M. E., Homan, E. P., Rask-Madsen, C., and Kahn, C. R. (2017) Endothelial insulin receptors differentially control insulin signaling kinetics in peripheral tissues and brain of mice. *Proc. Natl. Acad. Sci.* **114**, E8478–E8487
160. Jansson, P.-A. A. E., Fowelin, J. P., von Schenck, H. P., Smith, U. P., Lönnroth, P. N., and Lonnroth, P. N. (1993) Measurement by Microdialysis of the Insulin Concentration in Subcutaneous Interstitial Fluid: Importance of the Endothelial Barrier for Insulin. *Diabetes*. **42**, 1469–73
161. Zawieja, S. D., Wang, W., Wu, X., Nepiyushchikh, Z. V., Zawieja, D. C., and Muthuchamy, M. (2012) Impairments in the intrinsic contractility of mesenteric collecting lymphatics in a rat model of metabolic syndrome. *Am. J. Physiol. Circ. Physiol.* **302**, H643–H653
162. Aird, W. C. (2007) Phenotypic heterogeneity of the endothelium: I. Structure, function,

and mechanisms. *Circ. Res.* **100**, 158–73
163. Aird, W. C. (2007) Phenotypic Heterogeneity of the Endothelium: II. Representative Vascular Beds. *Circ. Res.* **100**, 174–190
164. Durr, E., Yu, J., Krasinska, K. M., Carver, L. A., Yates, J. R., Testa, J. E., Oh, P., and Schnitzer, J. E. (2004) Direct proteomic mapping of the lung microvascular endothelial cell surface in vivo and in cell culture. *Nat. Biotechnol.* **22**, 985–92
165. Albelda, S. M., Sampson, P. M., Haselton, F. R., McNiff, J. M., Mueller, S. N., Williams, S. K., Fishman, A. P., and Levine, E. M. (1988) Permeability characteristics of cultured endothelial cell monolayers. *J. Appl. Physiol.* **64**, 308–22
166. Muñoz, P., Rosemblatt, M., Testar, X., Palacín, M., Thoidis, G., Pilch, P. F., and Zorzano, A. (1995) The T-tubule is a cell-surface target for insulin-regulated recycling of membrane proteins in skeletal muscle. *Biochem. J.* **312 (Pt 2)**, 393–400
167. Lauritzen, H. P. M. M. (2006) Imaging of Insulin Signaling in Skeletal Muscle of Living Mice Shows Major Role of T-Tubules. *Diabetes*. **55**, 1300–1306
168. Steinberg, H. O., Chaker, H., Leaming, R., Johnson, A., Brechtel, G., and Baron, A. D. (1996) Obesity/insulin resistance is associated with endothelial dysfunction. Implications for the syndrome of insulin resistance. *J. Clin. Invest.* **97**, 2601–10
169. Vollenweider, P., Randin, D., Tappy, L., Jéquier, E., Nicod, P., and Scherrer, U. (1994) Impaired insulin-induced sympathetic neural activation and vasodilation in skeletal muscle in obese humans. *J. Clin. Invest.* **93**, 2365–2371
170. Barton, M., Baretella, O., and Meyer, M. R. (2012) Obesity and risk of vascular disease: importance of endothelium-dependent vasoconstriction. *Br. J. Pharmacol.* **165**, 591–602
171. Van Guilder, G. P., Stauffer, B. L., Greiner, J. J., and DeSouza, C. A. (2008) Impaired endothelium-dependent vasodilation in overweight and obese adult humans is not limited to muscarinic receptor agonists. *Am. J. Physiol. Circ. Physiol.* **294**, H1685–H1692
172. Chadderdon, S. M. S. S. M., Belcik, J. T., Bader, L., Peters, D. M., Kievit, P., Alkayed, N. J., Kaul, S., Grove, K. L., Lindner, J. R. J., Laakso, M., Edelman, S., Brechtel, G., Baron, A., Coggins, M., Lindner, J. R. J., Rattigan, S., Dawson, D., Vincent, M., Barrett, E., Vincent, M., Barrett, E., Lindner, J. R. J., Clark, M., Rattigan, S., Vincent, M., Clerk, L., Lindner, J. R. J., Vincent, M., Clerk, L., Lindner, J. R. J., Vollus, G., Bradley, E., Roberts, M., Chadderdon, S. M. S. S. M., Belcik, J. T., Smith, E., Clerk, L., Vincent, M., Barrett, E., Lankford, M., Lindner, J. R. J., Clerk, L., Vincent, M., Jahn, L., Liu, Z., Lindner, J. R. J., Barrett, E., Kim, F., Pham, M., Maloney, E., Shim, C., Kim, S., Chadderdon, S. M. S. S. M., Chawengsub, Y., Gauthier, K., Campbell, W., Larsen, B., Miura, H., Hatoum, O., Mustafa, S., Sharma, V., McNeill, J., Ozkor, M., Quyyumi, A., Bellien, J., Iacob, M., Gutierrez, L., Knights, K., Rowland, A., Miners, J., Bremer, A., Stanhope, K., Graham, J., Chadderdon, S. M. S. S. M., Belcik, J. T., Bader, L., Tigno, X., Gerzanich, G., Hansen, B., Hansen, B., Bodkin, N., Kahn, S., Bellien, J., Remy-Jouet, I., Iacob, M., Fleming, I., Natarajan, R., Nadler, J., Spector, A., Norris, A., Clark, S., Fuchs, L., Miura, H., Wachtel, R., Liu, Y., Pfister, S., Falck, J., Campbell, W., Pritchard, K., Wong, P., Stemerman, M., Stapleton, P., Goodwill, A., James, M., Frisbee, J., Yu, Z., Huse, L., Adler, P., Chen, M., Yang, Z., Smith, K., Carter, J., Nadler, J., Natarajan, R., Gu, J., Rossi, J., Nunemaker, C., Chen, M., Pei, H., Bauersachs, J., Popp, R., Hecker, M., Sauer, E., Fleming, I., Busse, R., Kim, J., Montagnani, M., Koh, K., Quon, M., Amati, F., Dubé, J., Coen, P., Stefanovic-Racic, M., Toledo, F., Goodpaster, B., Shen, S., Reaven, G., Farquhar, J., Iyer, A., Kauter, K., and Alam, M. (2016) Temporal Changes in Skeletal Muscle Capillary Responses and

Endothelial-Derived Vasodilators in Obesity Related Insulin Resistance. *Diabetes*. **65**, db151574
173. Clerk, L. H., Vincent, M. A., Jahn, L. A., Liu, Z., Lindner, J. R., and Barrett, E. J. (2006) Obesity Blunts Insulin-Mediated Microvascular Recruitment in Human Forearm Muscle. *Diabetes*. **55**, 1436–1442
174. Clark, M. G. (2008) Impaired microvascular perfusion: a consequence of vascular dysfunction and a potential cause of insulin resistance in muscle. *Am. J. Physiol. Metab.* **295**, E732–E750
175. Frisbee, J. C., Wu, F., Goodwill, A. G., Butcher, J. T., and Beard, D. A. (2011) Spatial heterogeneity in skeletal muscle microvascular blood flow distribution is increased in the metabolic syndrome. *Am. J. Physiol. Regul. Integr. Comp. Physiol.* **301**, R975-86
176. Gavin, T. P., Stallings, H. W., Zwetsloot, K. A., Westerkamp, L. M., Ryan, N. A., Moore, R. A., Pofahl, W. E., and Hickner, R. C. (2005) Lower capillary density but no difference in VEGF expression in obese vs. lean young skeletal muscle in humans. *J. Appl. Physiol.* **98**, 315–21
177. Williams, I. M., Otero, Y. F., Bracy, D. P., Wasserman, D. H., Biaggioni, I., and Arnold, A. C. (2016) Chronic Angiotensin-(1-7) Improves Insulin Sensitivity in High-Fat Fed Mice Independent of Blood Pressure. *Hypertension*. **67**, 983–91
178. Reddy, K. G., Nair, R. N., Sheehan, H. M., and Hodgson, J. M. (1994) Evidence that selective endothelial dysfunction may occur in the absence of angiographic or ultrasound atherosclerosis in patients with risk factors for atherosclerosis. *J. Am. Coll. Cardiol.* **23**, 833–43
179. Deanfield, J. E., Halcox, J. P., and Rabelink, T. J. (2007) Endothelial function and dysfunction: testing and clinical relevance. *Circulation*. **115**, 1285–95
180. Muniyappa, R., and Sowers, J. R. (2013) Role of insulin resistance in endothelial dysfunction. *Rev. Endocr. Metab. Disord.* **14**, 5–12
181. Sansbury, B. E., and Hill, B. G. (2014) Regulation of obesity and insulin resistance by nitric oxide. *Free Radic. Biol. Med.* **73**, 383–99
182. Kim, F., Pham, M., Maloney, E., Rizzo, N. O., Morton, G. J., Wisse, B. E., Kirk, E. A., Chait, A., and Schwartz, M. W. (2008) Vascular inflammation, insulin resistance, and reduced nitric oxide production precede the onset of peripheral insulin resistance. *Arterioscler. Thromb. Vasc. Biol.* **28**, 1982–8
183. Predescu, D., Predescu, S., Shimizu, J., Miyawaki-Shimizu, K., and Malik, A. B. (2005) Constitutive eNOS-derived nitric oxide is a determinant of endothelial junctional integrity. *Am. J. Physiol. Cell. Mol. Physiol.* **289**, L371–L381
184. Kurose, I., Kubes, P., Wolf, R., Anderson, D. C., Paulson, J., Miyasaka, M., and Granger, D. N. (1993) Inhibition of nitric oxide production. Mechanisms of vascular albumin leakage. *Circ. Res.* **73**, 164–71
185. Yuan, S. Y. (2006) New insights into eNOS signaling in microvascular permeability. *Am. J. Physiol. Circ. Physiol.* **291**, H1029–H1031
186. Roy, D., Perreault, M., and Marette, A. (1998) Insulin stimulation of glucose uptake in skeletal muscles and adipose tissues in vivo is NO dependent. *Am. J. Physiol. Metab.* **274**, E692–E699
187. Vincent, M. A., Barrett, E. J., Lindner, J. R., Clark, M. G., and Rattigan, S. (2003) Inhibiting NOS blocks microvascular recruitment and blunts muscle glucose uptake in response to insulin. *Am. J. Physiol. Endocrinol. Metab.* **285**, E123-9

188. Shankar, R. R., Wu, Y., Shen, H. Q., Zhu, J. S., and Baron, A. D. (2000) Mice with gene disruption of both endothelial and neuronal nitric oxide synthase exhibit insulin resistance. *Diabetes*. **49**, 684–7
189. Duplain, H., Burcelin, R., Sartori, C., Cook, S., Egli, M., Lepori, M., Vollenweider, P., Pedrazzini, T., Nicod, P., Thorens, B., and Scherrer, U. (2001) Insulin Resistance, Hyperlipidemia, and Hypertension in Mice Lacking Endothelial Nitric Oxide SynthaseNote Added in Proof. *Circulation*. **104**, 342–345
190. Wang, H., Wang, A. X., Aylor, K., and Barrett, E. J. (2013) Nitric oxide directly promotes vascular endothelial insulin transport. *Diabetes*. **62**, 4030–42
191. Gudbjörnsdóttir, S., Sjöstrand, M., Strindberg, L., and Lönnroth, P. (2005) Decreased muscle capillary permeability surface area in type 2 diabetic subjects. *J. Clin. Endocrinol. Metab.* **90**, 1078–82
192. Halseth, A. E., Bracy, D. P., and Wasserman, D. H. (2000) Limitations to basal and insulin-stimulated skeletal muscle glucose uptake in the high-fat-fed rat. *Am. J. Physiol. Metab.* **279**, E1064–E1071
193. Kolka, C. M., Richey, J. M., Castro, A. V. B. de, Broussard, J. L., Ionut, V., and Bergman, R. N. (2015) Lipid-induced insulin resistance does not impair insulin access to skeletal muscle. *Am. J. Physiol. - Endocrinol. Metab.* 10.1152/ajpendo.00015.2015
194. Laine, H., Yki-Jarvinen, H., Kirvela, O., Tolvanen, T., Raitakari, M., Solin, O., Haaparanta, M., Knuuti, J., and Nuutila, P. (1998) Insulin resistance of glucose uptake in skeletal muscle cannot be ameliorated by enhancing endothelium-dependent blood flow in obesity. *J. Clin. Invest.* **101**, 1156–62
195. Ayala, J. E., Bracy, D. P., Julien, B. M., Rottman, J. N., Fueger, P. T., and Wasserman, D. H. (2007) Chronic treatment with sildenafil improves energy balance and insulin action in high fat-fed conscious mice. *Diabetes*. **56**, 1025–33
196. Bonner, J. S., Lantier, L., Hocking, K. M., Kang, L., Owolabi, M., James, F. D., Bracy, D. P., Brophy, C. M., and Wasserman, D. H. (2013) Relaxin treatment reverses insulin resistance in mice fed a high-fat diet. *Diabetes*. **62**, 3251–60
197. Clark, M. G., Rattigan, S., Clerk, L. H., Vincent, M. A., Clark, A. D., Youd, J. M., and Newman, J. M. (2000) Nutritive and non-nutritive blood flow: rest and exercise. *Acta Physiol. Scand.* **168**, 519–30
198. Berria, R., Wang, L., Richardson, D. K., Finlayson, J., Belfort, R., Pratipanawatr, T., De Filippis, E. A., Kashyap, S., and Mandarino, L. J. (2006) Increased collagen content in insulin-resistant skeletal muscle. *Am. J. Physiol. Endocrinol. Metab.* **290**, E560-5
199. Kang, L., Ayala, J. E., Lee-Young, R. S., Zhang, Z., James, F. D., Neufer, P. D., Pozzi, A., Zutter, M. M., and Wasserman, D. H. (2011) Diet-induced muscle insulin resistance is associated with extracellular matrix remodeling and interaction with integrin alpha2beta1 in mice. *Diabetes*. **60**, 416–26
200. Kang, L., Lantier, L., Kennedy, A., Bonner, J. S., Mayes, W. H., Bracy, D. P., Bookbinder, L. H., Hasty, A. H., Thompson, C. B., and Wasserman, D. H. (2013) Hyaluronan accumulates with high-fat feeding and contributes to insulin resistance. *Diabetes*. **62**, 1888–96
201. Abuissa, H., Jones, P. G., Marso, S. P., O'Keefe, J. H., and O'Keefe, J. H. (2005) Angiotensin-converting enzyme inhibitors or angiotensin receptor blockers for prevention of type 2 diabetes: a meta-analysis of randomized clinical trials. *J. Am. Coll. Cardiol.* **46**, 821–6

202. Taddei, S., Virdis, A., Ghiadoni, L., Mattei, P., and Salvetti, A. (1998) Effects of angiotensin converting enzyme inhibition on endothelium-dependent vasodilatation in essential hypertensive patients. *J. Hypertens.* **16**, 447–56
203. Gottlieb, S. S., Dickstein, K., Fleck, E., Kostis, J., Levine, T. B., LeJemtel, T., and DeKock, M. (1993) Hemodynamic and neurohormonal effects of the angiotensin II antagonist losartan in patients with congestive heart failure. *Circulation*. **88**, 1602–9
204. Ghiadoni, L., Virdis, A., Magagna, A., Taddei, S., and Salvetti, A. (2000) Effect of the angiotensin II type 1 receptor blocker candesartan on endothelial function in patients with essential hypertension. *Hypertens. (Dallas, Tex. 1979)*. **35**, 501–6
205. Vanhoutte, P. M., Auch-Schwelk, W., Biondi, M. L., Lorenz, R. R., Schini, V. B., and Vidal, M. J. (1989) Why are converting enzyme inhibitors vasodilators? *Br. J. Clin. Pharmacol.* **28 Suppl 2**, 95S–103S; discussion 103S–104S
206. Schindler, C., Bramlage, P., Kirch, W., and Ferrario, C. M. (2007) Role of the vasodilator peptide angiotensin-(1-7) in cardiovascular drug therapy. *Vasc. Health Risk Manag.* **3**, 125–37
207. Giani, J. F., Mayer, M. A., Muñoz, M. C., Silberman, E. A., Höcht, C., Taira, C. A., Gironacci, M. M., Turyn, D., Dominici, F. P., Munoz, M. C., Silberman, E. A., Hocht, C., Taira, C. A., Gironacci, M. M., Turyn, D., Dominici, F. P., Muñoz, M. C., Silberman, E. A., Höcht, C., Taira, C. A., Gironacci, M. M., Turyn, D., and Dominici, F. P. (2009) Chronic infusion of angiotensin-(1-7) improves insulin resistance and hypertension induced by a high-fructose diet in rats. *Am. J. Physiol. Endocrinol. Metab.* **296**, E262-71
208. Guimaraes, P. S., Oliveira, M. F., Braga, J. F., Nadu, A. P., Schreihofer, A., Santos, R. A. S., and Campagnole-Santos, M. J. (2014) Increasing angiotensin-(1-7) levels in the brain attenuates metabolic syndrome-related risks in fructose-fed rats. *Hypertension*. **63**, 1078–85
209. Marcus, Y., Shefer, G., Sasson, K., Kohen, F., Limor, R., Pappo, O., Nevo, N., Biton, I., Bach, M., Berkutzki, T., Fridkin, M., Benayahu, D., Shechter, Y., and Stern, N. (2013) Angiotensin 1-7 as means to prevent the metabolic syndrome: lessons from the fructose-fed rat model. *Diabetes*. **62**, 1121–30
210. Sjostrand, M., Gudbjornsdottir, S., Holmang, A., Lonn, L., Strindberg, L., and Lonnroth, P. (2002) Delayed Transcapillary Transport of Insulin to Muscle Interstitial Fluid in Obese Subjects. *Diabetes*. **51**, 2742–2748
211. Sandqvist, M., Strindberg, L., Schmelz, M., Lönnroth, P., and Jansson, P.-A. (2011) Impaired delivery of insulin to adipose tissue and skeletal muscle in obese women with postprandial hyperglycemia. *J. Clin. Endocrinol. Metab.* **96**, E1320-4
212. Broussard, J. L., Castro, A. V. B., Iyer, M., Paszkiewicz, R. L., Bediako, I. A., Szczepaniak, L. S., Szczepaniak, E. W., Bergman, R. N., and Kolka, C. M. (2016) Insulin access to skeletal muscle is impaired during the early stages of diet-induced obesity. *Obesity*. **24**, 1922–1928
213. Castillo, C., Bogardus, C., Bergman, R., Thuillez, P., and Lillioja, S. (1994) Interstitial insulin concentrations determine glucose uptake rates but not insulin resistance in lean and obese men. *J. Clin. Invest.* **93**, 10–6
214. Szendroedi, J., Frossard, M., Klein, N., Bieglmayer, C., Wagner, O., Pacini, G., Decker, J., Nowotny, P., Muller, M., and Roden, M. (2012) Lipid-Induced Insulin Resistance Is Not Mediated by Impaired Transcapillary Transport of Insulin and Glucose in Humans. *Diabetes*. **61**, 3176–3180

215. Kolka, C. M., Harrison, L. N., Lottati, M., Chiu, J. D., Kirkman, E. L., and Bergman, R. N. (2010) Diet-induced obesity prevents interstitial dispersion of insulin in skeletal muscle. *Diabetes*. **59**, 619–26
216. Ayala, J. E., Bracy, D. P., Malabanan, C., James, F. D., Ansari, T., Fueger, P. T., McGuinness, O. P., and Wasserman, D. H. (2011) Hyperinsulinemic-euglycemic clamps in conscious, unrestrained mice. *J. Vis. Exp.* 10.3791/3188
217. Kraegen, E. W., James, D. E., Jenkins, A. B., and Chisholm, D. J. (1985) Dose-response curves for in vivo insulin sensitivity in individual tissues in rats. *Am. J. Physiol.* **248**, E353-62
218. Ayala, J. E., Samuel, V. T., Morton, G. J., Obici, S., Croniger, C. M., Shulman, G. I., Wasserman, D. H., McGuinness, O. P., and Consortium, N. I. H. M. M. P. C. (2010) Standard operating procedures for describing and performing metabolic tests of glucose homeostasis in mice. *Dis Model Mech*. **3**, 525–34
219. Liu, F., Kohn, W. D., and Mayer, J. P. (2012) Site-specific fluorescein labeling of human insulin. *J. Pept. Sci.* **18**, 336–41
220. Kohn, W. D., Micanovic, R., Myers, S. L., Vick, A. M., Kahl, S. D., Zhang, L., Strifler, B. A., Li, S., Shang, J., Beals, J. M., Mayer, J. P., and DiMarchi, R. D. (2007) pI-shifted insulin analogs with extended in vivo time action and favorable receptor selectivity. *Peptides*. **28**, 935–948
221. Bagher, P., and Segal, S. S. (2011) The mouse cremaster muscle preparation for intravital imaging of the microcirculation. *J. Vis. Exp.* 10.3791/2874
222. Baatz, H., Steinbauer, M., Harris, A. G., and Krombach, F. Kinetics of white blood cell staining by intravascular administration of rhodamine 6G. *Int. J. Microcirc. Clin. Exp.* **15**, 85–91
223. Mempel, T. R., Scimone, M. L., Mora, J. R., and von Andrian, U. H. (2004) In vivo imaging of leukocyte trafficking in blood vessels and tissues. *Curr. Opin. Immunol.* **16**, 406–17
224. Otsu, N. (1979) A threshold selection method from gray-level histograms. *IEEE Trans. Syst. Man. Cybern.* **9**, 62–66
225. Crank, J. (1975) *The mathematics of diffusion*, 10.1016/0306-4549(77)90072-X
226. McClatchey, P. M., Keller, A. C., Bouchard, R., Knaub, L. A., and Reusch, J. E. B. (2016) Fully automated software for quantitative measurements of mitochondrial morphology. *Mitochondrion*. **26**, 58–71
227. Morgan, C. R., and Lazarow, A. (1963) Immunoassay of Insulin: Two Antibody System: Plasma Insulin Levels of Normal, Subdiabetic and Diabetic Rats. *Diabetes* . **12**, 115–126
228. Senanayake, P. D., Moriguchi, A., Kumagai, H., Ganten, D., Ferrario, C. M. M., Brosnihan, K. B. B., deS. Senanayake, P., Moriguchi, A., Kumagai, H., Ganten, D., Ferrario, C. M. M., and Brosnihan, K. B. B. (1994) Increased expression of angiotensin peptides in the brain of transgenic hypertensive rats. *Peptides*. **15**, 919–26
229. Weibel, E. R. (1969) Stereological principles for morphometry in electron microscopic cytology. *Int. Rev. Cytol.* **26**, 235–302
230. Steele, R., Wall, J. S., de Bodo, R. C., and Altszuler, N. (1956) Measurement of Size and Turnover Rate of Body Glucose Pool by the Isotope Dilution Method. *Am J Physiol -- Leg. Content*. **187**, 15–24
231. Cherrington, A. D., and Vranic, M. (1973) Effect of arginine on glucose turnover and plasma free fatty acids in normal dogs. *Diabetes*. **22**, 537–43

232. Hentz, N. G., Richardson, J. M., Sportsman, J. R., Daijo, J., and Sittampalam, G. S. (1997) Synthesis and Characterization of Insulin−Fluorescein Derivatives for Bioanalytical Applications. *Anal. Chem.* **69**, 4994–5000
233. Jaldin-Fincati, J. R., Pereira, R. V. S., Bilan, P. J., and Klip, A. (2018) Insulin uptake and action in microvascular endothelial cells of lymphatic and blood origin. *Am. J. Physiol. Metab.* 10.1152/ajpendo.00008.2018
234. Chen, A. K., Cheng, Z., Behlke, M. A., and Tsourkas, A. (2008) Assessing the sensitivity of commercially available fluorophores to the intracellular environment. *Anal. Chem.* **80**, 7437–44
235. Berlier, J. E., Rothe, A., Buller, G., Bradford, J., Gray, D. R., Filanoski, B. J., Telford, W. G., Yue, S., Liu, J., Cheung, C.-Y. C.-Y., Chang, W., Hirsch, J. D., Beechem, J. M., Haugland, R. P. R. P., Haugland, R. P. R. P., Beechem Rosaria P. Haugland, J. M., and Haugland, R. P. R. P. (2003) Quantitative Comparison of Long-wavelength Alexa Fluor Dyes to Cy Dyes: Fluorescence of the Dyes and Their Bioconjugates. *J. Histochem. Cytochem.* **51**, 1699–1712
236. Poole, D. C., Musch, T. I., and Kindig, C. A. (1997) In vivo microvascular structural and functional consequences of muscle length changes. *Am. J. Physiol. - Hear. Circ. Physiol.*
237. Lee, J.-F., Gordon, S., Estrada, R., Wang, L., Siow, D. L., Wattenberg, B. W., Lominadze, D., and Lee, M.-J. (2009) Balance of S1P1 and S1P2 signaling regulates peripheral microvascular permeability in rat cremaster muscle vasculature. *Am. J. Physiol. Heart Circ. Physiol.* **296**, H33-42
238. Magidson, V., and Khodjakov, A. (2013) Circumventing photodamage in live-cell microscopy. *Methods Cell Biol.* **114**, 545–60
239. Majumdar, S., Genders, A. J., Inyard, A. C., Frison, V., and Barrett, E. J. (2012) Insulin entry into muscle involves a saturable process in the vascular endothelium. *Diabetologia*. **55**, 450–6
240. Huxley, V. H., Curry, F. E., and Adamson, R. H. (1987) Quantitative fluorescence microscopy on single capillaries: alpha-lactalbumin transport. *Am. J. Physiol.* **252**, H188-97
241. Baxter, L. T., and Jain, R. K. (1989) Transport of fluid and macromolecules in tumors. I. Role of interstitial pressure and convection. *Microvasc. Res.* **37**, 77–104
242. Renkin, E. M. (1988) Transport Pathways and Processes. in *Endothelial Cell Biology in Health and Disease*, pp. 51–68, Springer US, Boston, MA, 10.1007/978-1-4613-0937-6_3
243. Schäffer, L., Brand, C. L., Hansen, B. F., Ribel, U., Shaw, A. C., Slaaby, R., and Sturis, J. (2008) A novel high-affinity peptide antagonist to the insulin receptor. *Biochem. Biophys. Res. Commun.* **376**, 380–3
244. Sjöstrand, M., Gudbjörnsdottir, S., Holmäng, A., Lönn, L., Strindberg, L., and Lönnroth, P. (2002) Delayed transcapillary transport of insulin to muscle interstitial fluid in obese subjects. *Diabetes*. **51**, 2742–8
245. Lee, W. L., and Klip, A. (2016) Endothelial Transcytosis of Insulin: Does It Contribute to Insulin Resistance? *Physiology*. **31**, 336–345
246. Bendayan, M., and Rasio, E. A. (1996) Transport of insulin and albumin by the microvascular endothelium of the rete mirabile. *J. Cell Sci.* **109 (Pt 7**, 1857–64
247. Vincent, M. A., Dawson, D., Clark, A. D. H., Lindner, J. R., Rattigan, S., Clark, M. G., and Barrett, E. J. (2002) Skeletal muscle microvascular recruitment by physiological hyperinsulinemia precedes increases in total blood flow. *Diabetes*. **51**, 42–8

248. Kang, L., Mokshagundam, S., Reuter, B., Lark, D. S., Sneddon, C. C., Hennayake, C., Williams, A. S., Bracy, D. P., James, F. D., Pozzi, A., Zent, R., and Wasserman, D. H. (2016) Integrin-Linked Kinase in Muscle Is Necessary for the Development of Insulin Resistance in Diet-Induced Obese Mice. *Diabetes*. **65**, 1590–1600
249. Kolka, C. M., and Bergman, R. N. (2012) The barrier within: endothelial transport of hormones. *Physiology (Bethesda)*. **27**, 237–47
250. Ellmerer, M., Hamilton-Wessler, M., Kim, S. P., Huecking, K., Kirkman, E., Chiu, J., Richey, J., and Bergman, R. N. (2006) Reduced Access to Insulin-Sensitive Tissues in Dogs With Obesity Secondary to Increased Fat Intake. *Diabetes*. **55**, 1769–1775
251. Wallis, M. G., Wheatley, C. M., Rattigan, S., Barrett, E. J., Clark, A. D. H., and Clark, M. G. (2002) Insulin-mediated hemodynamic changes are impaired in muscle of Zucker obese rats. *Diabetes*. **51**, 3492–8
252. Williams, I. M., Valenzuela, F. A., Kahl, S. D., Ramkrishna, D., Mezo, A. R., Young, J. D., Wells, K. S., and Wasserman, D. H. (2018) Insulin exits skeletal muscle capillaries by fluid-phase transport. *J. Clin. Invest.* **128**, 699–714
253. Lacorre, D.-A., Baekkevold, E. S., Garrido, I., Brandtzaeg, P., Haraldsen, G., Amalric, F., and Girard, J.-P. (2004) Plasticity of endothelial cells: rapid dedifferentiation of freshly isolated high endothelial venule endothelial cells outside the lymphoid tissue microenvironment. *Blood*. **103**, 4164–4172
254. Yen, T. T., Stienmetz, J., and Simpson, P. J. (1970) Blood volume of obese (ob-ob) and diabetic (db-db) mice. *Proc. Soc. Exp. Biol. Med.* **133**, 307–8
255. Cassuto, J., Dou, H., Czikora, I., Szabo, A., Patel, V. S., Kamath, V. V., Belin de Chantemele, E., Feher, A., Romero, M. J., and Bagi, Z. (2013) Peroxynitrite Disrupts Endothelial Caveolae Leading to eNOS Uncoupling and Diminished Flow-Mediated Dilation in Coronary Arterioles of Diabetic Patients. *Diabetes*. **63**, 1381–1393
256. Armstrong, S. M., Khajoee, V., Wang, C., Wang, T., Tigdi, J., Yin, J., Kuebler, W. M., Gillrie, M., Davis, S. P., Ho, M., and Lee, W. L. (2012) Co-Regulation of Transcellular and Paracellular Leak Across Microvascular Endothelium by Dynamin and Rac. *Am. J. Pathol.* **180**, 1308–1323
257. McClatchey, P. M., Frisbee, J. C., and Reusch, J. E. B. (2017) A conceptual framework for predicting and addressing the consequences of disease-related microvascular dysfunction. *Microcirculation*. **24**, e12359
258. Yang, Y., Smith, D. L., Keating, K. D., Allison, D. B., Nagy, T. R., and Nagy, T. R. (2014) Variations in body weight, food intake and body composition after long-term high-fat diet feeding in C57BL/6J mice. *Obesity (Silver Spring)*. **22**, 2147–55
259. Sader, M., and Celermajer, D. S. (2002) Endothelial function, vascular reactivity and gender differences in the cardiovascular system. *Cardiovasc. Res.* **53**, 597–604
260. Huxley, V. H., and Wang, J. (2010) Cardiovascular sex differences influencing microvascular exchange. *Cardiovasc. Res.* **87**, 230–42
261. Jackson, W. F., Boerman, E. M., Lange, E. J., Lundback, S. S., and Cohen, K. D. (2008) Smooth muscle alpha1D-adrenoceptors mediate phenylephrine-induced vasoconstriction and increases in endothelial cell Ca2+ in hamster cremaster arterioles. *Br. J. Pharmacol.* **155**, 514–24
262. Gurney, A. M., and Allam, M. (1995) Inhibition of calcium release from the sarcoplasmic reticulum of rabbit aorta by hydralazine. *Br. J. Pharmacol.* **114**, 238–44
263. Bursztyn, M., Raz, I., Mekler, J., and Ben-Ishay, D. (1997) Effect of acute N-nitro-L-

arginine methyl ester (L-NAME) hypertension on glucose tolerance, insulin levels, and [3H]-deoxyglucose muscle uptake. *Am. J. Hypertens.* **10**, 683–6
264. House, L. M., Morris, R. T., Barnes, T. M., Lantier, L., Cyphert, T. J., McGuinness, O. P., Otero, Y. F., and Otero, Y. F. (2015) Tissue inflammation and nitric oxide-mediated alterations in cardiovascular function are major determinants of endotoxin-induced insulin resistance. *Cardiovasc. Diabetol.* **14**, 56
265. Boesen, E. I., and Pollock, D. M. (2007) Effect of chronic IL-6 infusion on acute pressor responses to vasoconstrictors in mice. *Am. J. Physiol. Circ. Physiol.* **293**, H1745–H1749
266. Robinson, M. A., Welsh, D. C., Bickel, D. J., Lynch, J. J., and Lyle, E. A. (2003) Differential effects of sodium nitroprusside and hydralazine in a rat model of topical FeCl3-induced carotid artery thrombosis. *Thromb. Res.* **111**, 59–64
267. Griffith, O. W., and Kilbourn, R. G. (1996) Nitric oxide synthase inhibitors: amino acids. *Methods Enzymol.* **268**, 375–92
268. Kvietys, P. R., and Granger, D. N. (2012) Role of reactive oxygen and nitrogen species in the vascular responses to inflammation. *Free Radic. Biol. Med.* **52**, 556–592
269. Rumbaut, R. E., Wang, J., and Huxley, V. H. (2000) Differential effects of l -NAME on rat venular hydraulic conductivity. *Am. J. Physiol. Circ. Physiol.* **279**, H2017–H2023
270. O'Callaghan, C. J., Komersova, K., and Louis, W. J. (1998) Acute effects of blood pressure elevation on insulin clearance in normotensive healthy subjects. *Hypertens. (Dallas, Tex. 1979)*. **31**, 104–9
271. Deibert, D. C., and DeFronzo, R. A. (1980) Epinephrine-induced insulin resistance in man. *J. Clin. Invest.* **65**, 717–21
272. Beyer, A. M., Guo, D.-F., and Rahmouni, K. (2013) Prolonged treatment with angiotensin 1-7 improves endothelial function in diet-induced obesity. *J. Hypertens.* **31**, 730–8
273. Andrade, J. M. O., Lemos, F. de O., da Fonseca Pires, S., Millán, R. D. S., de Sousa, F. B., Guimarães, A. L. S., Qureshi, M., Feltenberger, J. D., de Paula, A. M. B., Neto, J. T. M., Lopes, M. T. P., Andrade, H. M. de, Santos, R. A. S., and Santos, S. H. S. (2014) Proteomic white adipose tissue analysis of obese mice fed with a high-fat diet and treated with oral angiotensin-(1–7). *Peptides*. **60**, 56–62
274. Winzell, M. S., Ahrén, B., and Ahren, B. (2004) The High-Fat Diet-Fed Mouse: A Model for Studying Mechanisms and Treatment of Impaired Glucose Tolerance and Type 2 Diabetes. *Diabetes*. **53 Suppl 3**, S215-9
275. Echeverría-Rodríguez, O., Del Valle-Mondragón, L., and Hong, E. (2014) Angiotensin 1-7 improves insulin sensitivity by increasing skeletal muscle glucose uptake in vivo. *Peptides*. **51**, 26–30
276. Gironacci, M. M., Adamo, H. P., Corradi, G., Santos, R. A., Ortiz, P., and Carretero, O. A. (2011) Angiotensin (1-7) Induces Mas Receptor Internalization. *Hypertension*. **58**, 176–181
277. Cavaghan, M. K., Ehrmann, D. A., Byrne, M. M., and Polonsky, K. S. (1997) Treatment with the oral antidiabetic agent troglitazone improves beta cell responses to glucose in subjects with impaired glucose tolerance. *J. Clin. Invest.* **100**, 530–537
278. Zinker, B. A., Lacy, D. B., Bracy, D. P., and Wasserman, D. H. (1993) Role of glucose and insulin loads to the exercising limb in increasing glucose uptake and metabolism. *J. Appl. Physiol.* **74**, 2915–2921
279. Abdul-Ghani, M. A., Williams, K., DeFronzo, R., and Stern, M. (2006) Risk of Progression to Type 2 Diabetes Based on Relationship Between Postload Plasma Glucose

and Fasting Plasma Glucose. *Diabetes Care*. **29**, 1613–1618
280. Lorenzo, C., Wagenknecht, L. E., Hanley, A. J. G., Rewers, M. J., Karter, A. J., and Haffner, S. M. (2010) A1C Between 5.7 and 6.4% as a Marker for Identifying Pre-Diabetes, Insulin Sensitivity and Secretion, and Cardiovascular Risk Factors: The Insulin Resistance Atherosclerosis Study (IRAS). *Diabetes Care*. **33**, 2104–2109
281. Laakso, M., and Kuusisto, J. (2014) Insulin resistance and hyperglycaemia in cardiovascular disease development. *Nat. Rev. Endocrinol.* **10**, 293–302
282. Henriksen, E. J., and Prasannarong, M. (2013) The role of the renin-angiotensin system in the development of insulin resistance in skeletal muscle. *Mol. Cell. Endocrinol.* **378**, 15–22
283. Coimbra, C. C., Garofalo, M. A., Foscolo, D. R., Xavier, A. R., and Migliorini, R. H. (1999) Gluconeogenesis activation after intravenous angiotensin II in freely moving rats. *Peptides*. **20**, 823–7
284. Takeda, M., Yamamoto, K., Takemura, Y., Takeshita, H., Hongyo, K., Kawai, T., Hanasaki-Yamamoto, H., Oguro, R., Takami, Y., Tatara, Y., Takeya, Y., Sugimoto, K., Kamide, K., Ohishi, M., and Rakugi, H. (2013) Loss of ACE2 exaggerates high-calorie diet-induced insulin resistance by reduction of GLUT4 in mice. *Diabetes*. **62**, 223–33
285. Prasannarong, M., Santos, F. R., and Henriksen, E. J. (2012) ANG-(1-7) reduces ANG II-induced insulin resistance by enhancing Akt phosphorylation via a Mas receptor-dependent mechanism in rat skeletal muscle. *Biochem. Biophys. Res. Commun.* **426**, 369–73
286. Kang, L., Mayes, W. H., James, F. D., Bracy, D. P., and Wasserman, D. H. (2014) Matrix metalloproteinase 9 opposes diet-induced muscle insulin resistance in mice. *Diabetologia*. **57**, 603–13
287. Tran, L. T., Yuen, V. G., and McNeill, J. H. (2009) The fructose-fed rat: a review on the mechanisms of fructose-induced insulin resistance and hypertension. *Mol. Cell. Biochem.* **332**, 145–59
288. Leto, D., and Saltiel, A. R. (2012) Regulation of glucose transport by insulin: traffic control of GLUT4. *Nat. Rev. Mol. Cell Biol.* **13**, 383–96
289. Shiuchi, T., Cui, T.-X. T.-X. T.-X., Wu, L., Nakagami, H., Takeda-Matsubara, Y., Iwai, M., and Horiuchi, M. (2002) ACE Inhibitor Improves Insulin Resistance in Diabetic Mouse Via Bradykinin and NO. *Hypertension*. **40**, 329–34
290. Sano, H., Kane, S., Sano, E., Mîinea, C. P., Asara, J. M., Lane, W. S., Garner, C. W., and Lienhard, G. E. (2003) Insulin-stimulated Phosphorylation of a Rab GTPase-activating Protein Regulates GLUT4 Translocation. *J. Biol. Chem.* **278**, 14599–14602
291. Muñoz, M. C., Giani, J. F., Burghi, V., Mayer, M. A., Carranza, A., Taira, C. A., and Dominici, F. P. (2012) The Mas receptor mediates modulation of insulin signaling by angiotensin-(1-7). *Regul. Pept.* **177**, 1–11
292. Muñoz, M. C., Giani, J. F., and Dominici, F. P. (2010) Angiotensin-(1-7) stimulates the phosphorylation of Akt in rat extracardiac tissues in vivo via receptor Mas. *Regul. Pept.* **161**, 1–7
293. Santos, S. H. S., Giani, J. F., Burghi, V., Miquet, J. G., Qadri, F., Braga, J. F., Todiras, M., Kotnik, K., Alenina, N., Dominici, F. P., Santos, R. A. S., and Bader, M. (2014) Oral administration of angiotensin-(1-7) ameliorates type 2 diabetes in rats. *J. Mol. Med. (Berl).* **92**, 255–65
294. Larance, M., Ramm, G., Stöckli, J., van Dam, E. M., Winata, S., Wasinger, V., Simpson,

F., Graham, M., Junutula, J. R., Guilhaus, M., and James, D. E. (2005) Characterization of the role of the Rab GTPase-activating protein AS160 in insulin-regulated GLUT4 trafficking. *J. Biol. Chem.* **280**, 37803–13
295. Santos, R. A. (2014) Angiotensin-(1-7). *Hypertension*. **63**, 1138–47
296. Mendes, A. C. R., Ferreira, A. J., Pinheiro, S. V. B., and Santos, R. A. S. (2005) Chronic infusion of angiotensin-(1–7) reduces heart angiotensin II levels in rats. *Regul. Pept.* **125**, 29–34
297. Passos-Silva, D. G., Verano-Braga, T., and Santos, R. A. S. (2013) Angiotensin-(1–7): beyond the cardio-renal actions. *Clin. Sci.* **124**, 443–456
298. Simionescu, N., Siminoescu, M., and Palade, G. E. (1975) Permeability of muscle capillaries to small heme-peptides. Evidence for the existence of patent transendothelial channels. *J. Cell Biol.* **64**, 586–607
299. WAGNER, R., MODLA, S., HOSSLER, F., and CZYMMEK, K. (2012) Three-Dimensional Analysis and Computer Modeling of the Capillary Endothelial Vesicular System with Electron Tomography. *Microcirculation*. **19**, 477–484
300. Prager, R., Wallace, P., and Olefsky, J. M. (1986) In vivo kinetics of insulin action on peripheral glucose disposal and hepatic glucose output in normal and obese subjects. *J. Clin. Invest.* **78**, 472–81
301. Erdei, N., Tóth, A., Pásztor, E. T., Papp, Z., Édes, I., Koller, A., and Bagi, Z. (2006) High-fat diet-induced reduction in nitric oxide-dependent arteriolar dilation in rats: role of xanthine oxidase-derived superoxide anion. *Am. J. Physiol. Circ. Physiol.* **291**, H2107–H2115
302. Pacher, P., Beckman, J. S., and Liaudet, L. (2007) Nitric Oxide and Peroxynitrite in Health and Disease. *Physiol. Rev.* **87**, 315–424
303. Ghosh, K. K., Burns, L. D., Cocker, E. D., Nimmerjahn, A., Ziv, Y., Gamal, A. El, and Schnitzer, M. J. (2011) Miniaturized integration of a fluorescence microscope. *Nat. Methods*. **8**, 871–878
304. Llewellyn, M. E., Barretto, R. P. J., Delp, S. L., and Schnitzer, M. J. (2008) Minimally invasive high-speed imaging of sarcomere contractile dynamics in mice and humans. *Nature*. **454**, 784–8
305. Levick, J. R., and Michel, C. C. (2010) Microvascular fluid exchange and the revised Starling principle. *Cardiovasc. Res.* **87**, 198–210

APPENDIX

ImageJ Image Analysis Scripts

For the scripts below, commands are bolded and comments describing each step are italicized. These scripts were developed for specific image file types. While the analysis procedures will work on any images, slight adjustments to the scripts may need to be made to handle different file types.

Automated CD31+ structure quantification with ImageJ

```
//define a function called action which can be looped over for each image in a directory
function action(input, filename){
        open(input + filename);

//improve contrast by histogram stretching
run("Enhance Contrast", "saturated=0.35");

//de-convolve hematoxylin, eosin, and DAB stains
        run("Colour Deconvolution", "vectors=[H&E DAB] hide");

//CD31+ structures are stained by DAB which is Colour 3 by this plugin
selectWindow(filename+"-(Colour_3)");

//use Intermodes thresholding method to identify CD31+ structures, thresholding method determined empirically
        setAutoThreshold("Intermodes");
        run("Threshold...");
        selectWindow(filename+"-(Colour_3)");

//use particle analysis to count thresholded structures, criteria for determining a structure determined empirically
        run("Analyze Particles...", "size=100-Infinity display summarize");
        run("Close All");
}

//use batch mode to improve the speed of the macro
setBatchMode(true);

//ask user to choose an input directory
input=getDirectory("Choose a Directory");
```

```
//set a variable that contains the list of files in the directory
list=getFileList(input);

//run function defined above for every file in the directory
for(i=0; i < list.length; i++)
        action(input, list[i]);
setBatchMode(false);
```

Automated vascular and interstitial segmentation with Image J

```
//use batch mode to improve the speed of the macro
setBatchMode(true);

//store title of image as a variable called ‘”name”’
name=getTitle();

//determine the measurements you will eventually make on the vessels
run("Set Measurements...", "area mean redirect=None decimal=3");

//split stack into separate channels for rho-dex and ins-647
run("Split Channels");

//determine properties of the image stack
Stack.getDimensions(width, height, channels, slices, frames);

//set up loop for all frames and slices
for (i=1; i<frames+1; i++) {
        for (j=1; j<slices+1; j++){

//make sure you are on the right slice and frame; start with the rho-dex channel
        selectWindow("C1-"+name+"");
        setSlice(j);
        selectWindow("C2-"+name+"");
        setSlice(j);
        selectWindow("C1-"+name+"");
        Stack.setFrame(i);
        selectWindow("C2-"+name+"");
        Stack.setFrame(i);

//use Otsu-thresholding to demarcate vessels
        run("Auto Threshold", "method=Otsu white");

//create a mask of these thresholded vessels
        run("Create Mask");
```

```
//perform some basic morphometric operations on these vessels to make them smoother and more continuous
        run("Close-");
        run("Open");
        run("Median...", "radius=4");

//have ImageJ only choose vessels with certain characteristics (determined empirically)
        run("Analyze Particles...", "size=50.00-Infinity circularity=0.00-0.50
        show=Masks");

//create new mask of the vessels
        selectWindow("Mask of mask");
        run("Create Selection");

//apply mask to insulin-647 channel
        selectWindow("C1-"+name+"");
        run("Restore Selection");

//measure insulin-647 in the vessels
        run("Measure");

//go back to original vascular mask and dilate it to segment interstitial spaces
        selectWindow("Mask of mask");
        run("Enlarge...", "enlarge=1");
        selectWindow("C1-"+name+"");

//move dilated mask back to insulin-647 channel
        run("Restore Selection");

//measure insulin-647 in this interstitial segment
        run("Measure");

//repeat this procedure for additional interstitial spaces out to 3µm from the vessel
        selectWindow("Mask of mask");
        run("Enlarge...", "enlarge=0.5");
        selectWindow("C1-"+name+"");
        run("Restore Selection");
        run("Measure");
        selectWindow("Mask of mask");
        run("Enlarge...", "enlarge=0.5");
        selectWindow("C1-"+name+"");
        run("Restore Selection");
        run("Measure");
        selectWindow("Mask of mask");
        run("Enlarge...", "enlarge=0.5");
```

```
        selectWindow("C1-"+name+"");
        run("Restore Selection");
        run("Measure");
        selectWindow("Mask of mask");
        run("Enlarge...", "enlarge=0.5");
        selectWindow("C1-"+name+"");
        run("Restore Selection");
        run("Measure");

//close all open windows
        selectWindow("Mask of mask");
        close();
        selectWindow("mask");
        close();
        }
        }
run("Close All");
```

MATLAB Mathematical Modeling Scripts and Functions

For MATLAB scripts, comments are in green and follow '%' signs. The optimization script and "lack of fit" functions change slightly depending on the specific mathematical model the imaging data are being fit to. The optimization script and "lack of fit" function shown below were used for fitting data to the fluid-phase transport model.

Optimization Script

```
%Optimization script for regressing simulated data against experimental measurements.

clear; %clears workspace
close all; %closes any figures that are open
D=1; F=0.1; k=0.00001; t0=0.25; %initial parameter guesses for fluid-phase transport
%model. Initial parameter values are different for diffusion and Michaelis-Menten
%models.
folder = uigetdir;%prompt user to select directory where data files are
cd(folder) %change folder to this new folder
files=dir('*.xlsx'); %pull out the excel files into a structure
files=extractfield(files, 'name'); %pull the filenames out of the structure
% and into a cell array
len=length(files);

fit_start = 1; %distance at which you want to start fitting data (µm from
%capillary)
fit_end = 3; %end fitting distance (µm from capillary)


%Read in data from excel files and format
for i = 1:len,
    [data{i}, txt, raw{i}] = xlsread(files{i});%read excel file; store numerical
    % data and text headers in separate cell arrays
    [x_length, t_length] = size(txt); %get dimensions of data set
    data{i} = cell2mat(raw{i}([2,2*fit_start+1:2*fit_end+1],2:t_length))';  %transpose
%numerical data and create matrices with experimental measurements

end

%Pull out information from the headers in the excel spreadsheets
[tok,rem]=strtok(txt); %takes the string data from the header and splits it
% into 2 cell arrays, tok and rem. tok is the 1st part of the header
%(the numeric value) and rem is the 2nd part of the header (units) after
% some kind of delimiter (i.e. space).

t = str2double(tok(1,2:end)'); %construct time vector by selecting the
% numeric values of the time heading, converting them from a string to a
% double-precision value (number) and then transposing this matrix

x = str2double(tok([1+2*fit_start:2*fit_end+1],1)); %construct position
% vector by selecting the numeric values of the position heading and
% converting them from a string to a double-precision value (number)

tunit=rem{1,2}; %store time units as a character
xunit=rem{2,1}; % store position units as a character
```

```
data = cat(3,data{:}); %create measurement matrix by concatenating data from
%each of the files along the third dimension (z). Each matrix is a 2D
%matrix (space by time). In order to operate on all of the data at the same
%time, you stack these matrices on top of each other in the 3rd dimension
%(i.e. in z).

sd = std(data,0,3); %create standard deviation matrix by taking the standard
%deviation of the data sets with no weighting factor (0) along the 3rd
%dimension (3)

sdbar = nanmedian(sd(:)); %find median of standard deviation matrix and store
%it as sdbar

sd(:) = sdbar; %new standard deviation matrix is a standard deviation matrix
%fully populated by the median sd. We decided to give all the points equal weight by
%using the median SD value points with high SD will essentially get ignored during the
%fitting process and the points with low SD will dominate. The measurements with the
%highest SD in our case are the very early time points near the capillary, which are
%our most important measurements.

datanan = data(:,:,any(all(isnan(data),2))); %move data sets with NaNs (missing
%values) to a new list. This list contains only data sets with NaNs

data(:,:,any(all(isnan(data),2)))=[]; %remove data sets with NaNs from
%original list. This list of matrices is now only matrices with no NaNs

[m,n,len] = size(data); %get dimensions of non-NaN data set

pout = zeros(5+m,len); %initialize parameter matrix - memory pre-allocation.
%It's good practice in MATLAB to specify the end dimensions of a matrix
%that will grow as more calculations are made

chi2 = zeros(1,len); %initialize chi^2 vector, the sum of squares of the weighted
%residuals.

p0=[D;F;k]; %set up initial parameter vector;

%Randomize initial parameter guesses
lb = log10(p0) - 3;
ub = log10(p0) + 3;
p0a = 10.^(lb + rand(size(p0)).*(ub-lb));

%Optimization
for i=1:len,%loop through all the non-NaN files you read in
    cp=data(:,1,i); %get plasma ins-647 intensity by calling the first column
    %of data from each matrix
    p0=[p0a;t0;cp(1);cp]; %include plasma ins-647 values as an adjustable parameter
%because the time at which they were measured is not known exactly; we will also
%let the initial time (t0) vary because there is a slight delay between the time of
%injection and the time at which the first image is collected
    plb=zeros(size(p0)); %set lower bounds on parameters
    pub=inf(size(p0)); %set upper bounds on parameters
    pub(4) = 1; % set max t0 to 0.25 min
    cdata = data(:,:,i); %pick ith data set
    cwt = sd; %this is the standard deviation matrix used for weighting residuals
    options = optimoptions(@lsqnonlin, 'MaxFunctionEvaluations', 50000,
'MaxIterations',5000);
    [pout(:,i),chi2(i),r] =
lsqnonlin(@(p)lof_conv(p,x,t,cdata,cwt),p0,plb,pub,options);
%This is the optimizer, it will find the best-fit parameter estimates which minimize
%the difference between experimental measurements and simulated data. The optimizer
%uses a gradient descent algorithm. The first input is @(p)lof(p,x,t,cdata,cwt). This
```

```
% 'lof' function ('lack of fit') is the function to be minimized. The outputs of this
%function (parameters) are stored to the parameter matrix, the norm of the residual is
%stored to the chi2 vector, and the residuals are stored to the r vector

    r=reshape(r,m,n); %reshape residual vector into a matrix

    [cout,xout,tout]=sim_conv(x,t,pout(:,i)); %use parameters estimated from
    %optimization to feed to the model equation to simulate a c(x,t) profile


%%%Optimization for data sets with missing values


[m2, n2, len2]=size(datanan); %get dimensions of NaN-containing matrix
[num_nan_total] = size(find(any(isnan(datanan),2)),1); %find total number of NaNs


 poutb_final = zeros(m+5, len2); %initialize final parameter matrix for
 %NaN-containing matrices. This matrix is the same size as the one used for
 %matrices without NaNs so that they can be merged later
 chi2b=zeros(1,len2); % initialize chi square array for matrices w NaNs

for i=1:len2,%loop through all the files you read in
    cdata = datanan(:,:,i); %pick ith data set
    [num_nan_ind] = size(find(any(isnan(cdata),2)),1); %find number of NaNs in the
%specific matrix
    [timenan] = zeros(1, num_nan_total); %initialize vector to store location of NaNs
    timenan(i:i + num_nan_ind-1) = find(any(isnan(cdata),2)); %locate NaNs and store
%them inpre-specified vector from step above
    t = str2double(tok(1,2:end)'); %original time vector
    t(timenan(i:i+num_nan_ind-1))=[];  %remove time point that's missing from
%experimental data from the time vector. This will tell the simulation function only
%to simulate at time points for which we have data

    cdata(any(isnan(cdata),2),:) = []; % Trim NaNs from matrices
    [m3, n3, len3] = size(cdata); % get size of matrix after removing NaNs
    poutb = zeros(5+m3,len3);%initialize parameter array for matrices with
    %NaNs. This parameter matrix only accounts for the size of the
    %trimmed matrix. This allows lsqnonlin to work. Will resize later after
    %fitting.
    cp=cdata(:,1);
    p0=[p0a;t0;cp(1);cp];
    plb=zeros(size(p0));
    pub=inf(size(p0));
    pub(4) = 1;
    cwt = sd;

%Optimization
    options = optimoptions(@lsqnonlin, 'MaxFunctionEvaluations', 50000,
'MaxIterations',5000);
    [poutb(:,i),chi2b(i),r]                                                    =
lsqnonlin(@(p)lof_conv(p,x,t,cdata,cwt),p0,plb,pub,options);


%Parameter matrix formation for NaN-containing matrices
    poutb_size=zeros(m+5, 1);
    poutb_sizeb=zeros(m+5, 1); %similar to step above but has NaNs instead of
    %zeros. Explanation to follow
    poutb_size(timenan(i:i+num_nan_ind-1)+5)=true; %indicate the place in the re-sized
    %parameter matrix where there will be a missing value
    poutb_size = logical(poutb_size); %turn poutb_size into a logical array
    poutb_sizeb(poutb_size)=nan; %populate the place specified in the step
    %above with NaN
```

```
    poutb_sizeb(~poutb_size) = poutb(:,i); %populate the rest of the matrix
    %with the rest of the parameters
    poutb_final(:,i)=poutb_sizeb; %add this single parameter array to the
    %total parameter array for all the NaN-containing matrices;


    r=reshape(r,m3,n3); %reshape residual vector into a matrix

    [cout,xout,tout]=sim_conv(x,t,poutb(:,i)); %use parameters estimated from
    %lsqnonlin to get c(x,t) profile


pout_final=cat(2,pout,poutb_final); %concatenate parameter matrices
chi2f = cat(2, chi2, chi2b); %concatenate chi2 matrices

pav = nanmean(pout_final,2); % average parameter estimates
psd = nanstd(pout_final,0,2); % standard deviation of parameter estimates
dof = m*n - length(p0); % degrees of freedom
disp('');
disp(['chi2 = ',mat2str(chi2f,5)]); % display outputs
disp(['Expected            chi2            (95%            confidence)            =
',mat2str(chi2inv([0.025,0.975],dof),5)]);%computes the chi-square inverse cumulative
%distribution function for a certain number of degrees of freedom. This is the
%expected residual errors for the number of variables we have.

%Display mean and standard deviation of parameter estimates
disp(['D               =               ',num2str(pav(1)),'               ',char(177),'
',num2str(psd(1)),xunit,'^2/',tunit(2:end),'; cv=', num2str(psd(1)/pav(1)*100),'%']);
disp(['F               =               ',num2str(pav(2)),'               ',char(177),'
',num2str(psd(2)),xunit,'/',tunit(2:end),'; cv=', num2str(psd(2)/pav(2)*100),'%']);
disp(['k  =  ',num2str(pav(3)),'  ',char(177),'  ',num2str(psd(3)),'  1/',tunit(2:end),';
cv=', num2str(psd(3)/pav(3)*100),'%']);
disp(['t0 = ',num2str(pav(4)),' ',char(177),' ',num2str(psd(4)),tunit]);
disp(['%                    within                    range                    =
',num2str(nnz(chi2f<chi2inv([0.975],dof))/size(chi2f,2)*100),'%']);
```

Lack of fit function

```
%Lack of fit function. Calculate lack-of-fit between experimental and simulated
measurements.

function r = lof_conv(p,x,t,cdata,cwt)

[n1 n2] = size(cdata); n3=n2-1; %Get size of the experimental data matrix
%being passed in from lsqnonlin (optimizer).
t=t(1:n1); x=x(1:n3); %Reshape time and space vectors accordingly.
cpred = sim_conv(x,t,p); %Simulate intensity-space-time profile from model equation
%(in this case fluid-phase transport model) based on parameters passed from lsqnonlin.

cwt2 = cwt(1:n1, 1:n2); %Reshape weighting matrix according to size of
%incoming data matrix.

r  =  (cpred(:)-cdata(:))./cwt2(:);%  Simulated  data  (cpred)  minus  experimental
%measurements (cdata)divided by the weigthing (median standard deviation) matrix.
%These weighted residuals will then be passed back to the optimizer.
```

Diffusion model simulation

```
%Simulate insulin concentration as a function of distance from capillary (x) and time
%following injection (t) using the diffusion model equation and parameters from
%optimizer.

function [cout,xout,tout] = sim_dif(x1,t1,p) %Create a function called
% 'sim_dif' which takes space, time, and model parameters as inputs and generates an
%insulin concentration-space-time matrix.

D = p(1); P = p(2); k = p(3); t0 = p(4); cp1 = p(5:end); %Unpack parameters from
%parameter vector.

L=max(x1); T=L^2/D; C=max(cp1); %Define scaling factors.

x = x1/L; t=[0;t1+t0]/T; cp=cp1/C; %Scale data by the scaling factors defined above.

b = P*L/D; d = k*L^2/D; %Combine parameters and scaling factors in such a way that
$non-dimensionalizes the parameters (i.e. their units cancel).

dt=diff(t)'; %Time interval.

[x,t] = meshgrid(x,t); %Create coordinate system over which you can evaluate and
$visualize a function of two variables with different ranges.

[m,n] = size(x); % Get dimensions of the coordinate system you just created.

cp=cp(:,ones(1,n)); %Make cp vector match the size of both x and t. In order to later
%computed the integrand the arrays must be the same size.

c=zeros(m-1,n); %Pre-allocate memory by initializing insulin concentration vector.


for i = 2:m  %Loop over time points greater than zero.

    z=t(i(ones(i,1)),:) - t(1:i,:); %Calculate the convolution integral time shift(t-
%tau.

f = b*exp(-d*z).*(exp(-x(1:i,:).^2./(4*z))./sqrt(pi*max(z,eps))...
   -b*exp(b*x(1:i,:)+b^2*z).*erfc(0.5*x(1:i,:)./sqrt(z)+b*sqrt(z)));
%Evaluate the exponential terms of the final non-dimensionalized solution to the
%diffusion model.

y = cp(1:i,:).*f; %Compute full integrand.

c(i-1,:) = 0.5*dt(1:i-1)*(y(1:i-1,:) + y(2:i,:)); %Use trapezoidal integration to
%evaluate the integral.

end

[xout,tout] = meshgrid([0;x1],t1+t0); %Create an output matrix for the data you just
%simulated.

cout = [cp1(2:end) C*c]; %Populate output concentration matrix with simulated data.
```

Michaelis-Menten model simulation

```
%Simulate insulin concentration as a %function of distance from capillary (x) and time
following injection (t) using the %Michaelis-Menten model equation and parameters from
optimizer.

function [cout,xout,tout] = sim_mm(x1,t1,p) %Create a function called
% 'sim_dif' which takes space, time, and model parameters as inputs and generates an
%insulin concentration-space-time matrix.

D = p(1); Vmax = p(2); Km = p(3); k = p(4); t0=p(5); cp1 = p(6:end); %Unpack
$parameters from %parameter vector.

L=max(x1); T=L^2/D; C=max(cp1); %Define scaling factors.

x = x1/L; t=[0;t1+t0]/T; cp=cp1/C; %Scale data by the scaling factors defined above.

g = (Vmax*L)/(D*C); r = Km/C; d = k*L^2/D; %Combine parameters and scaling factors in
%such a way that $non-dimensionalizes the parameters (i.e. their units cancel).

dt=diff(t)'; %Time interval.

[x,t] = meshgrid(x,t); %Create coordinate system over which you can evaluate and
$visualize a function of two variables with different ranges.

[m,n] = size(x); % Get dimensions of the coordinate system you just created.

cp=cp(:,ones(1,n)); %Make cp vector match the size of both x and t. In order to later
%computed the integrand the arrays must be the same size.

c=zeros(m-1,n); %Pre-allocate memory by initializing insulin concentration vector.

for i = 2:m  %Loop over time points greater than zero.

    z=t(i(ones(i,1)),:) - t(1:i,:); %Calculate the convolution integral time shift(t-
%tau.

f = (g./(pi*z)).*exp((d.*z)+ (-x(1:i,:).^2./(4*z)));
   f(isnan(f))=0;
%Evaluate the exponential terms of the final non-dimensionalized solution to the
%Michaelis-Menten model.

y = cp(1:i,:)./(r+cp(1:i,:)).*f; %Compute the full integrand.

c(i-1,:) = 0.5*dt(1:i-1)*(y(1:i-1,:) + y(2:i,:)); %Use trapezoidal integration to
evaluate the integral.

end

[xout,tout] = meshgrid([0;x1],t1+t0); %Create an output matrix for the data you just
%simulated.

cout = [cp1(2:end) C*c]; %Populate output concentration matrix with simulated data.
```

Fluid-phase transport model simulation

```
%Simulate insulin concentration as a function of distance from capillary (x) and time
%following injection (t) using the fluid-phase transport model equation and parameters
%from optimizer.

function [cout,xout,tout] = sim_conv(x1,t1,p) %Create a function called
% 'sim_conv' which takes space, time, and model parameters as inputs and generates an
%insulin concentration-space-time matrix.

D = p(1); F = p(2); k = p(3); t0 = p(4); cp1 = p(5:end); %Unpack parameters from
%parameter vector.

L=max(x1); T=L^2/D; C=max(cp1); %Define scaling factors.

x = x1/L; t=[0;t1+t0]/T; cp=cp1/C; %Scale data by the scaling factors defined above.

b = F*L/D; d = k*T; %Combine parameters and scaling factors in such
% a way that non-dimensionalizes the parameters (i.e. their units cancel
% out.

dt=diff(t)'; %Time interval.

[x,t] = meshgrid(x,t); %Create coordinate system over which you can evaluate and
%visualize a function of two variables with different ranges.

[m,n] = size(x); % Get dimensions of the coordinate system you just created.

cp=cp(:,ones(1,n)); %Make cp vector match the size of both x and t. In order to later
%computed the integrand the arrays must be the same size.

c=zeros(m-1,n); %Pre-allocate memory by initializing insulin concentration vector.

for i = 2:m  %Loop over time points greater than zero.

    z=t(i(ones(i,1)),:) - t(1:i,:); %Calculate the convolution integral time shift(t-
%tau.

f = b*exp(-d*z).*(exp(-x(1:i,:).^2./(4*z))./sqrt(pi*max(z,eps)));

%Evaluate the exponential terms of the final non-dimensionalized solution to the
%fluid-phase transport model.

y = cp(1:i,:).*f; %Compute full integrand.

c(i-1,:) = 0.5*dt(1:i-1)*(y(1:i-1,:) + y(2:i,:)); %Use trapezoidal integration to
%evaluate the integral.

end

[xout,tout] = meshgrid([0;x1],t1+t0);%Create an output matrix for the data you just
%simulated.

cout = [cp1(2:end) C*c]; %Populate output concentration matrix with simulated data.
```

Intravital insulin-647 imaging protocol

Imaging materials checklist

1. Fasting buckets
2. Large white absorbent pad and 1 small one (per mouse)
3. Tools: fine-tipped forceps, scissors, hemostats (with and without silicone tubing)
4. Styrofoam pad for taking tissues
5. Kimwipes and gauze
6. Gloves
7. Blunted injection needles (at least 5 per mouse)
8. 8 cm micro-renathane tubing with connector for injections
9. Alcohol swabs
10. Ketamine/xylazine/acepromazine cocktail
11. Razor
12. Custom stage mount
13. Duct tape
14. Tetramethylrhodamine-dextran
    a. Make 5 mg/ml stock solution in 0.9% NaCl
    b. Sonicate and spin down to get rid of aggregates
    c. Aliquot and freeze at -20°C
    d. Dilute 5X in 50uL 0.9% saline (10 uL dextran into 40uL saline)
15. Insulin-647
    a. Make 1mg/ml stock solution in insulin storage buffer + 1% TX (insulin storage buffer: 16mg/ml glycerol, 2.5mg/ml m-cresol, 20mM Tris Hcl, pH 7.5)
    b. Add 34 µL 10% TX-100 to 306µL insulin storage buffer
    c. Add 170µL ins storage buffer + TX to 1 vial of insulin-647 (should be 0.17mg mass)
    d. Wrap in aluminum foil and shake for 30 minutes
    e. Transfer to Eppendorf tube, transfer label, sonicate in water bath sonicator for 1 hour
    f. Spin down for 10 min @ 13,000rpm to ensure no aggregation
    g. Dilute 1:100 in 0.9% saline and check absorbance
        i. Use quartz cuvette
        ii. Blank should be 1:100 ins storage buffer + 1% TX in 0.9% NaCl
        iii. Absorbance should be in the 0.25 – 0.35 range
        iv. Calculate insulin concentration in U/ml using the equation: Abs*100/239,000*10^6/6
            1. This is just Beer's law; 100 – dilution factor, 239,000 – molar absorptivity coefficient of Alexa Fluor-647; 10^6/6 – unit conversion
    h. Check fluorescence on fluorometer with an emission scan (Ex: 633, Em: 650-750)
        i. Emission intensity peak should be over 1 million
    i. Dilute insulin-647 to appropriate concentration based on dose and mouse body weight using spreadsheet
16. [^{14}C]2DG
    a. Dry down tracers

17. 0.1% BSA in saline
18. 0.9% injectable saline
19. Peristaltic pump
20. 5% CO_2/95%N_2
21. Bicarbonate-buffered physiological saline solution (PSS; make working solution day of experiments – 250mL per mouse)
    a. Stock 1 20x (2.638M NaCl, 94mM KCl, 40mM $MgSO_4$, 23.4 mM $CaCl_2$)
    b. Stock 2 20X (360mM $NaHCO_3$)
    c. Mix 12.5ml Stock 1, 12.5ml Stock 2, 225ml H20 per mouse filter
22. Beaker + stir bar
23. Heating block
24. Vacuum setup (Sidearm flask, tubing)
25. Electric blanket/temperature device
26. LN_2
27. Styrofoam LN_2 bucket
28. Labeled tubes for tissues (Soleus, gastrocnemius, vastus, liver, epididymal fat, heart, brain)
29. Labeled tubes for probes/samples (rhodamine dextran, insulin-647, 2DG standard, plasma, treatment)
30. Heparinized capillary tubes for blood collection
31. Sharps box
32. Glucose strips
33. Timer
34. Lab notebook
35. ddH_2O water bottle
36. Other potential items depending on the study: hematocrit tubes / clay, syringe pump, 3 ways, syringes with red tops, additional micro-renathane tubing

Room set-up

1. Set up body temperature on top shelf of cart control unit and turn on
2. Put peristaltic pump on top of temperature unit
3. Put heating block just to the left of the peristaltic pump
4. Heat PSS to 37°C on heating block and mix
5. Put influent line of peristaltic pump into PSS
6. Hook up tubing to 95%N_2/5%CO_2; put pipette tip end into PSS and bubble for ~5 minutes before starting experiment
    a. Tape gas tubing to PSS bottle
7. Set-up vacuum trap
    a. Sidearm connected to vacuum line with tubing
    b. Vertical arm (serological pipette) connected to port on stage mount with tubing
    c. Turn on vacuum
8. Clean coverglass with water, sparkle, water, then dry with kimwipes
9. Take off condenser with screwdriver and set to the left
10. Move objective to lowest position (rotate focus knob towards you)
11. Clean 20X W 0.8NA lens gently with lens paper and cotton-tipped applicator
12. Put custom stage mount in the correct holder on the microscope

13. Tape effluent line to stage mount so that pipette tip releases PSS at the bottom right corner of coverglass
14. Put everything for mouse preparation and tissue collection on table
    a. Plug in razor
15. Put liquid nitrogen, Styrofoam bucket, and freezer clamps under table

Probe preparation

1. Dilute 2Mda tetramethylrhodamine-dextran (5mg/ml) 5x in 50uL saline (10 uL dex into 40 uL saline)
2. Make insulin-647 in 0.1% BSA according to dilution spreadsheet
3. Store on ice and covered in tinfoil until use

Microscope set-up

1. Turn on switches in the order that they are labeled:
    a. Main power source (1)
    b. Main power key (2)
    c. Argon laser control (3a)
    d. Argon laser power supply (3b)
    e. Components power supply (4)
    f. PC power supply (5)
    g. Argon laser – turn from standby to on, turn knob to the right until red light comes on then turn back down until it becomes green (6)
    h. Mercury lamp (7)
2. Use touch pad to ensure that 20X W 0.8NA lens is selected
3. Move objective to lowest Z position
4. Open Zen software
    a. Have to also click "Start System"
5. Turn on lasers
    a. Acquisition tab → Laser dialog box → switch DPSS-561 and HeNe633 to "on"
6. Load settings
    a. Depends on the experiment being run (either 1, 2, or 4U/kg insulin-647)

Syringes

1. Fill up 2 syringes with 0.9% NaCl
    a. Connect 1 to 8 cm microrenathane tubing with connector (flush line)
2. Fill up rhodamine-dextran syringe
3. Fill up insulin-647/2DG syringe - combined

Mouse preparation and mounting

1. Hook up micro-renathane tubing + connector to venous catheter; check to see if it is drawing/infusing with saline
2. Anesthetize mouse with ketamine/xylazine/acepromazine cocktail
    a. Inject ~40ul (obese) or ~30ul (lean) per mouse to start
    b. Give 20µL before putting mouse on stage
    c. Give 20µL ~3 minutes before experiment
    d. Give additional boosters as necessary

3. Lay mouse on heating blanket
    a. Try to keep mouse on heating pad as much as possible but may have to take off for certain procedures
4. Shave right leg
    a. Wipe away hair with gauze / alcohol swabs
    b. Very important to make sure there is absolutely no hair anywhere near the prep
5. Expose lateral gastrocnemius on left leg
    a. Make notch in skin near Achilles tendon
    b. Grab notch with hemostat and pull skin off of the leg
    c. Cut away skin
    d. The muscle you are looking for is lateral to the tibia (lateral gastroc); it forms a triangular region on the side of the leg
    e. Remove fascia with fine tipped forceps and scissors so that fibers are exposed (check under dissecting microscope if necessary)
        i. Pull up fascia and make an incision, there is a pocket underneath
        ii. Cut out the fascia from the entire lateral gastrocnemius
        iii. Be sure not to nick blood vessel towards the bottom of the exposed tissue region
    f. During gastrocnemius preparation, keep leg hydrated with 0.9% saline
6. Situate mouse on coverslip platform
    a. Start superfusion
    b. Lay mouse on its side so the exposed lateral gastrocnemius is flush against the coverslip
    c. You want as much of the body of the mouse off the stage mount as possible (helps with breathing-induced motion artifacts
    d. Try to get the heel situated so that it is fully on the coverslip; trap the toes against the side of the coverglass so that the leg can't raise up
        i. Can tape down leg if necessary
7. Insert rectal probe
    a. Grab by the flexible part; run down at the same angle as the tail to insert into rectum
    b. Tape down
8. Put heating blanket on top of the mouse
    a. Get nice wrap around mouse by fitting the edge of the heating blanket into the back of the stage mount
    b. Put ~1/2-filled water glove (not too heavy) on top of heating blanket to further stabilize mouse

Locating vessels

1. Select **Locate** tab in the top left
2. Select the **GFP** filter
3. Turn on reflected light to desired intensity (12%)
4. Bring objective down away from the mouse and look underneath the coverglass to get in the approximate area of the tissue (will look whitish under the blue light)
5. Bring objective close to the coverslip
6. Use eyepieces to ensure quality of preparation and mouse situation

   a. Exposed tissue should be in the same focal plane (roughly)
   b. Not too much movement
   c. If you don't meet either of these criteria, I would recommend re-situating the mouse to get its leg pressed and held down more securely against the coverslip
7. Turn off reflected light
8. Inject rhodamine-dextran and chase with saline
9. Select **FS43 HE** filter to view the red dextran and turn on reflected light
10. Focus up and down and select a region with parallel capillaries that can be seen clearly
   a. Capillaries should be sharp – should be able to see blood flowing
   b. Go above and below the focus plane to make sure there are no large feeder vessels in the vicinity
   c. Make sure there are no hairs
   d. Region with vessels in several different focal planes is ideal
11. A good area for lots of clear vessels can be found by going to the far left of the exposed gastrocnemius, locating some big post-capillary venules and then looking below them and to the right

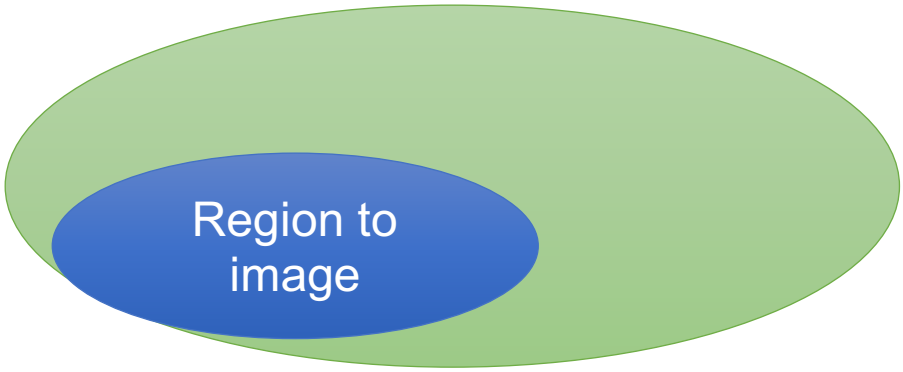

Imaging

1. Switch to **Acquisition tab**
2. There are at least 3 different imaging settings saved (depends on dose of insulin-647 you use)
   a. For any given experiment, use the same imaging settings for all the mice in that experiment
3. In the "channels" dialog box uncheck the AF647 track, leaving only the Rhod channel checked
4. Scan Rhod channel in **Live** mode to view vessels
5. Set up z-stack
   a. Focus up to the coverslip (focus knob towards you) and then back down to the first vessels (focus knob away from you) that appear; click **set first**
   b. Move down (focus knob away from you) 16µm and click **set last -** this will depend on the specific experiment – some experiments will have larger depths than others
   a. Interval should be set to half of the pinhole width (usually 4µm)
   b. Make sure you have 4 slices (depends on experiment)
12. Click **Start experiment** to acquire dextran image + insulin-647 background

Imaging

1. Inject insulin-647/2DG slowly; chase with ~30uL of saline
2. Manually acquire z-stack every minute for 15 minutes
    a. Acquire image ~ 10 seconds before the minute (i.e. 50 sec, 1min 50 sec, etc) – **Start Experiment**,
    b. **Split, Save, Close previous point, open new blank image**
    c. Make sure sufficient "New Acquisition Documents" are open and ready at all times
    d. Make sure you are saving the correct image in the right hand panel
    e. Can scan in live mode to make sure focal plane hasn't drifted. This is done by finding a distinctive feature in the image and keeping that in focus throughout the time course

Taking tissues and plasma

1. Take ~ 200-300 uL whole blood from tail vein into microvettes
2. Excise soleus, gastrocnemius, vastus, liver, epididymal fat, heart, and brain
    a. Freeze clamp and place in LN_2

Cleaning up prior to next experiment

1. Wrap up mouse carcass in absorbent pad and put in fasting bucket
2. Wipe off tools with alcohol swab
3. Clean off coverglass with water, sparkle, water